PhD Thesis

Exploring the formation mechanism of star clusters in molecular clouds:
The role of physical processes and gas-to-star conversion factors

Submitted in partial fulfillment of the requirements
of the degree of

Doctor of Philosophy

by

Vineet Rawat
(Roll No. 19330021)

Under the guidance of

Dr. Manash Ranjan Samal
Astronomy and Astrophysics Division
Physical Research Laboratory, Ahmedabad, India

Department of Physics
INDIAN INSTITUTE OF TECHNOLOGY GANDHINAGAR

2024

Dedicated to my beloved family

Declaration

I, Vineet Rawat, declare that this written submission represents my ideas in my own words and where others' ideas or words have been included, I have adequately cited the original sources. I also declare that I have adhered to all principles of academic honesty and integrity and have not misrepresented or fabricated or falsified any idea/data/fact/source in my submission. I understand that any violation of the above will be cause for disciplinary action by the Institute and can also evoke penal action from the sources which have thus not been properly cited or from whom proper permission has not been taken when needed.

Vineet Rawat
(Roll. No. 19330021)

Date: 25-02-2025

Certificate

It is certified that the work contained in the thesis entitled **"Exploring the formation mechanism of star clusters in molecular clouds: The role of physical processes and gas-to-star conversion factors"** submitted by Mr Vineet Rawat (Roll no: 19330021) to Indian Institute of Technology, Gandhinagar has been carried out under my supervision at the Astronomy & Astrophysics Division, Physical Research Laboratory, Ahmedabad and that this work has not been submitted elsewhere for any degree or diploma.

(Dr. Manash Ranjan Samal)
Thesis Supervisor
Associate Professor
Astronomy & Astrophysics Division
Physical Research Laboratory
Unit of Department of Space, Govt. of India
Ahmedabad-380009, Gujarat, India.

Date: 25-02-2025

Acknowledgement

" Nothing in life is to be feared, it is only to be understood. Now is the time to understand more, so that we may fear less "

– Marie Curie, 1867–1934

Embarking on a PhD journey is akin to setting out on a long, uncharted voyage. It's a path defined by a blend of rigorous academic inquiry, personal growth, and an unwavering quest for knowledge. As I reach the culmination of my PhD journey, I am filled with an overwhelming sense of joy and gratitude. Throughout this journey, I have encountered numerous challenges and obstacles. There were times of intense doubt and moments when the path ahead seemed uncertain. I feel very fortunate and grateful to god that I was surrounded by motivating and inspiring people who always encouraged me to complete this journey successfully. Now, here is the time I acknowledge all of them who not only supported me in these five years but also helped me to develop my personality and inspired me to become a better human being.

First and foremost, I would like to express my deepest gratitude to my thesis advisor, *Dr. Manash Ranjan Samal*, for his invaluable guidance, support, and encouragement throughout my PhD journey. During my PhD coursework, *Dr. Samal* instructed us in a course on "Star Formation." This course sparked my interest in the field, prompting me to explore this topic further. *Dr. Samal* gave me all the freedom to work and was consistently available to discuss any problems or progress in my research. I learned a lot from him, not only in academics but also in maintaining a work-life balance, developing essential skills, and essence of collaborative research when required. I extend my sincere gratitude to my Doctoral studies committee members, *Prof. Sachindra Naik, Dr. Lokesh Kumar Dewangan, and Dr. Amitava Guharay*, for their constructive feedback, suggestions, and encouragement during DSC meetings and personal interactions throughout my PhD journey. Their invaluable suggestions have greatly helped me to improve the quality of the thesis. I extend my gratitude to all the faculty members in the Astronomy and Astrophysics division of the Physical Research Laboratory (PRL) for their support and insightful discussions during division seminars that groomed me as a researcher and improved my communication skills. I am also profoundly thankful to my collaborators, *Prof. D.K. Ojha, Dr. Daniel Walker, Prof. Annie Zavagno, Prof. Anandmayee Tej, Dr. Davide Elia, Dr. Jessy*

Jose, Dr. Eswaraiah Chakali, Dr. Gabor Marton, Prof. W.P. Chen, Dr. C.P Zhang, Dr. Jia-Wei Wang, Dr. Ramkesh Yadav, Dr. Somnath Dutta, Dr. Brajesh Kumar, Dr. Saurabh Sharma, and Prof. Ram Sagar, whose invaluable suggestions and guidance has helped to improve the quality of my work and complete the projects. I express my profound gratitude to the Director, PRL, *Prof. Anil Bhardwaj*, the Dean, PRL, *Prof. Pallam Raju*, the division head, A&A, PRL, *Prof. Abhijit Chakraborty*, and all the academic committee members for their support. Additionally, I am thankful to the *Time Allocation Committee (TAC) members* at the Devasthal Observatory, Mount Abu Observatory, and James Clerk Maxwell Telescope facility for providing ample observation time and all the necessary support during the observations. I wish to express my gratitude to *Dr. Eugenio Schisano* for providing the *Herschel* Hi-Gal column density and dust temperature maps. I am also grateful to *Prof. S.N. Longmore* for sharing the data of massive molecular clouds, pressure lines, and other critical parameters used in their work to compare them with ours. I thank *Dr. Eric Koch* and *Dr. Catherine Zucker*, for the discussion on using the FILFINDER and RADFIL packages. I am also grateful to my Bachelor's faculties at the University of Delhi, *Dr. Debjani Banerjee*, *Dr. Vishal Chaudhary*, and *Dr. S.S Gaur*, who always guided and motivated me to pursue research in physics with commitment and integrity.

My PhD journey would not have been possible without the support of my colleagues and friends at PRL. I express my heartfelt thanks to my senior, *Dr. Namita Uppal*, for her warm, joyful, and inspiring presence. I am truly fortunate to have had her as a senior, from whom I learned to overcome any obstacle with a smile. She was always there to help and encourage me whenever I needed support, whether discussing new results, PhD work, or personal issues. I extend my gratitude to *Archita, Aravind, Naval, and Akanksha* for their invaluable suggestions and discussions on various topics. Thanks to all my other seniors in the department, *Sandeep, Neeraj, Sushant, Abhay, Biswajeet, Vipin, Abhijit, Shanwlee, Ruchi, Sadhana, Ranjan, Alaxender, Ekta, and Jayanand*, for being a continuous source of inspiration and learning and guiding me at various stages of my PhD journey. I also thank my seniors from other departments, *Anshika, Ankit, Sana, Priyank, Yash, Dayanand, Pranav, Monika, Deepak Rai, Sanjit, Vikas, Meghna, and Sunil*, for all their advice and assistance with academics and hostel issues.

Spending five years in the same place is a significant time to create memories and friends. I will never forget the time which I spent in the Thaltej hostel. The credit goes to my friends – *Trinesh, Sanjay, Aditya, Arup Maity, Arup Chakraborty, Malika, Wafikul, Goldy, Arijit, Varsha, Kiran, Shreya, Soumik, and Dibyendu*, with whom I shared a close bond of friendship. They were always a source of fun and light-hearted conversations that helped me relieve stress and enjoy my life as a researcher. They were my family far away from home, who were there in my good and bad times. I enjoyed organizing random fun events, rooftop late-night parties, birthdays, fresher parties, and other recreational activities with them. I also want to thank my other juniors, *Ashish, Narendra, Akash, Shubhendra, Omkar, Priyadarshee, Kushagra, and Ritik*. It was a pleasure to know such enthusiastic and talented individuals. Finally, I express my gratitude to my batchmates, the batch 'JRF-2019', *Birendra, Kimi, Somu, Santunu, Neha, Sandipan, Swagatika, Tanya, Vardaan, Ritvik, Ajayeta, Gourav, Kshitiz, Bijoy, Bharathi, Saurabh, Yogesh, and Satyam*, with whom I shared and enjoyed the early days of my PhD and every moment of my life. I will never forget the difficult times we endured together during COVID, taking care of each other with precautions and celebrating each day like an achievement. Thanks to these incredible people, I was able to face the lockdown with positivity and embrace life to the fullest. I cherish the hours spent on random talks and stories, late-night parties, movie nights, festivals, and playing games in the hostel. Thanks to my lunch group, *Harish, Shivani, Subham, Deepali, Anil, Akanksha, Birendra, Kimi, Neha, Trinesh, Sanjay, and Aditya*, with whom having lunch every day was an event. We used to pour our hearts out at the lunch table, which helped relieve the pressure of the PhD.

Apart from PRL, I always had a constant life support system from my family and friends. I am deeply in debt to my family, who have been my pillar of strength throughout my whole journey. Despite not having an idea of what I am doing, their love and encouragement have always been unwavering. Firstly, I would like to express my gratitude to my uncle, *Tajbar Singh Khatri*, who was my first teacher and consistently motivated me to excel academically from my early education to the present. He was the person I always sought advice from before making any major decisions in my life. I want to express my heartfelt love to my dear *Nana* and *Nani*. I am eternally grateful to my parents for their sacrifices and unconditional love. They have provided me with all the facilities, freedom, and environment to bloom and become an independent person. I am fortunate to have an elder brother, *Amit*, who has supported me both financially and emotionally and taught me to always keep moving forward in life. My heartfelt thanks also go to the new members of my family – my sister-in-law, *Monika*, and the adorable little one, *Seenu*, whose smile and sweet giggling voice always brought a smile on my face, even during the most frustrating times. I am also deeply thankful to *Neha Negi*, my close friend, for her warm presence and constant encouragement. Although she is from a different field, she has always understood me well and

supported me through every challenging situation with her bright positivity and smile. Even without physical presence, she stood by my side and walked with me through the challenges of life. I extend my thanks to my school and college friends – *Dhyani, Istwal, Ambika, Aman, Saurav, Ankit, Aakanksha Rawat, Pawan, Shailesh, Sourabh, Anant, Anshul, Abhay, Sambhav, Roopesh, Shivam, and Vishal*, for their immense love and care. Lastly, to all those who have contributed in big or small ways, I extend my heartfelt gratitude to each and every one of you for your invaluable support and encouragement. Whether through your guidance, friendship, or assistance, your contributions have been essential to my success. The lessons I've learned and the memories we've created together will forever hold a special place in my heart. Your collective impact has not only shaped my academic achievements but also enriched my personal growth in immeasurable ways. I will always cherish the positive influence you have had on my journey, and for that, I am eternally thankful.

Abstract

One of the outstanding problems of astrophysics is how gas is converted into stars, which is still not fully understood because of the different physical factors involved and the span of huge spatial scales. Moreover, it is well known that most of the stars in molecular clouds form in clusters. Rich and massive clusters are not only important laboratories for understanding stellar evolution, but also their impact on the interstellar medium and star-formation processes of the host galaxy is immense. Despite their importance, there are many key unanswered questions related to them, like how intermediate-to-massive bound stellar clusters form in giant molecular clouds, what are the roles of different physical factors in cluster formation and early evolution, and whether their formation is controlled by some galaxy-wide processes or sensitive to the local environment of the region, where they form. Addressing these questions is crucial for understanding the formation mechanisms of bound stellar clusters across the full mass range.

To answer the aforementioned questions, this thesis conducted an in-depth case study of a giant molecular cloud, G148.24+00.41, characterizing its properties, with a specific focus on its cluster formation potential and scenarios. In addition to the global properties, physical structure, and kinematics of the cloud, the thesis also explores the cloud's central region to investigate the magnetic field structure and its relative role in comparison to gravity and turbulence in the star formation process. It also explores the properties of the emerging cluster in the cloud and its likely fate. This thesis also presents a statistical study of 17 nearby cluster-forming clumps to examine the connection between star formation rate and gas mass at the clump scale, thus, the role of local versus global factors in making stars or star clusters in molecular clouds.

Clouds more massive than about 10^5 $M_\odot$ are potential sites of massive cluster formation. Studying the properties of such clouds in the early stages of their evolution offers an opportunity to test various cluster formation processes, and G148.24+00.41 is one such cloud. Our results show the cloud to be of high mass ($\sim 10^5$ $M_\odot$), low dust temperature ($\sim$14.5 K), nearly circular (projected radius $\sim$26 pc), and gravitationally bound with a dense gas fraction of $\sim$18%. The central area of the cloud is actively forming protostars and is moderately fractal with a Q-value of ~0.66. It is found that the cloud has undergone hierarchical fragmentation, with massive and younger protostars forming towards the cloud centre. Also, evidence of primordial mass segregation has been found in the cloud, with a degree of mass segregation ~3.2. The CO (1−0) isotopologues molecular line data was used to study the gas properties and kinematics of G148.24+00.41. Six likely velocity coherent filaments are identified in the cloud having length ~14−38 pc and mass ~(1.3−6.9) × 10^3 $M_\odot$. The filaments are found to be converging towards the central area of the cloud, forming a hub at their junction, and inflowing matter at a rate of ~26−264 $M_\odot$ Myr^{-1} towards the central area. The cloud has fragmented into 7 clumps having mass in the range of ~260−2100 $M_\odot$, out of which the most massive clump is located at the hub of the filamentary structures. Three filaments are found to be directly connected to the massive clump and transferring matter at a rate of ~675 $M_\odot$ Myr^{-1}. The clump is found to be the host of a near-infrared cluster, FSR 655. High-resolution dust polarization observations at 850 μm around the most massive clump using SCUBA-2/POL-2 at the James Clerk Maxwell Telescope show the decreasing trend of polarization towards the denser regions. Our observations have resolved the massive clump into multiple substructures. The magnetic field strengths of the Central clump and Northeastern elongated structure are found to be ~24.0 ± 6.0 μG and 20.0 ± 5.0 μG, respectively. Both regions are magnetically transcritical/supercritical and trans-Alfvénic. In the central clump/hub region of G148.24+00.41, virial analysis suggests that gravitational energy currently has an edge over magnetic and kinetic energies, suggesting that the clump will continue to form stars under the effect of gravity.

The young embedded cluster, FSR 655, located in the hub of G148.24+00.41, is studied in detail using near-infrared observations done with the TANSPEC instrument mounted on the 3.6-m Devasthal Optical Telescope. The present stellar mass of the cluster is around ~180 $M_\odot$, and the cluster is currently forming stars at a rate of 330 $M_\odot$ Myr^{-1}, with an efficiency of ~19%. From these findings, this thesis suggests that large-scale filamentary accretion flows towards the central region are crucial for supplying the matter needed to form the central high-mass clump and subsequent stellar cluster. Also, discuss that the clump being connected to an extended gas reservoir via a filamentary network, the cluster has the potential to become a richer cluster of mass ~1000 $M_\odot$ within a few Myr of time. Broadly, this thesis suggests that in this massive cloud, the most massive clump (i.e. the clump located at the hub) can only make a cluster of mass ~1000 $M_\odot$. Thus, a single clump may not give rise to a massive cluster, but the whole cloud has the potential to form a cluster in the mass range ~2000–3000 $M_\odot$ through dynamical hierarchical collapse and assembly of both gas and stars.

The statistical study of 17 cluster-forming clumps shows that the star formation rate surface density varies with gas mass surface density as a power-law of index $\sim 1.60 \pm 0.29$. The volumetric star formation relation even shows a better correlation with the power-law index of $\sim 1.00 \pm 0.16$. The median star formation efficiency in our sample of clumps is around 0.22, which is the first robust analysis of the star formation efficiency of cluster-forming clumps and will be highly beneficial for numerical simulations of cloud collapse and evolution. This study finds that the star formation rate−gas mass relation at the clump scale lies much above the volumetric scaling law for extragalactic and cloud scales, with a free-fall efficiency of ~0.2. The thesis discusses these results in the context of the role of local versus global processes in star formation within the clumps and the emergence of bound clusters.

List of Publications

Peer - Reviewed Journals

Part of the thesis

1. **Rawat V.**, Samal M. R., Walker D. L., et al. 2023, Probing the global dust properties and cluster formation potential of the giant molecular cloud G148.24+00.41, MNRAS, 521, 2786.
   DOI: 10.1093/mnras/stad639

2. **Rawat V.**, Samal M. R., Walker D. L., et al. 2024, The Giant Molecular Cloud G148.24+00.41: gas properties, kinematics, and cluster formation at the nexus of filamentary flows, MNRAS, 528, 2199.
   DOI: 10.1093/mnras/stae060

3. **Rawat V.**, Samal M. R., Eswaraiah C, et al. 2024, Understanding the relative importance of magnetic field, gravity, and turbulence in star formation at the hub of the giant molecular cloud G148.24+00.41, MNRAS, 528, 1460.
   DOI: 10.1093/mnras/stae053

4. **Rawat V.**, Samal M. R., Ojha D. K., et al. 2024, Peering into the heart of the giant molecular cloud G148.24+00.41: A deep near-infrared view of the newly hatched cluster FSR 655, AJ, 168, 136.
   DOI: 10.3847/1538-3881/ad630d

Under preparation

5. **Rawat V.**, Samal M. R., et al. 2024, Star formation-gas mass scaling relation in young clusters.

Other publications

1. Maurya, J., Joshi, Y. C., Samal, M. R., **Rawat, V.**, & Gour, A. S. 2023, Statistical analysis of dynamical evolution of open clusters, Journal of Astrophysics and Astronomy, 44, 71. DOI: 10.1007/s12036-023-09959-3

Conferences and talks

Poster presentations

1. **ASI 2021** - Near-infrared and radio analysis of IRAS 23545+6508: a cluster in the process of making - **Vineet Rawat et al.**, hosted jointly by ICTS - TIFR Bengaluru, IISER Mohali, IIT Indore, and IUCAA Pune from 18 - 23 February 2021 (online).

2. **ASI 2022** - Understanding the cluster formation potency of massive dark clouds - **Vineet Rawat et al.**, hosted jointly by IIT Roorkee and ARIES Nainital during 25 - 29 March 2022 (hybrid).

3. **Ph.D. Research Showcase 2023** - Understanding the dust properties and clustering structure of a Giant Molecular Cloud G148.24+00.41 - **Vineet Rawat et al.**, hosted by IIT-Gandhinagar on 27 January 2023.

4. **ASI 2023** - How do massive star clusters form? A case study on Galactic Molecular Cloud G148.24+00.41 - **Vineet Rawat et al.**, hosted by Indian Institute of Technology Indore during 1 - 5 March 2023.

5. **Magnetic Fields from Clouds to Stars (Bfields-2024)** - Understanding the relative importance of magnetic field, gravity, and turbulence in star formation at the hub of the GMC G148.24+00.41 - **Vineet Rawat et al.**, held at Mitaka Campus, National Astronomical Observatory of Japan, Tokyo, Japan during 25 - 29 March 2024.

Oral presentations

1. Delivered a talk titled **“Understanding the cluster formation potency of massive dark clouds"** at the 3rd Meeting on Star Formation held at ARIES - Nainital, between 04 - 07 May 2022.

2. Delivered a talk titled **“Role of magnetic field in cluster formation: A case study of G148.24+00.41 with JCMT SCUBA-2/ POL-2"** at the JCMT users meeting 2023, between 30 May - 1 June 2023 (online).

3. Delivered a talk titled **“Exploring the interplay of magnetic fields, gravity, and turbulence in star formation at the hub of the GMC G148.24+00.41"** at the 42nd Annual Meeting of the Astronomical Society of India (ASI) held at IISc Bengaluru, between 31 Jan - 4 Feb 2024.

Seminar details

Division seminars

1. **Topic :** Understanding the Connection Between Star Formation Rate and Gas in Galactic Molecular Clouds.
   Date : 05th July 2021.

2. **Topic :** Understanding the connection between star formation and Gas of the Molecular Cloud G148.24+00.41.
   Date : 29th April 2022.

3. **Topic :** Gas Properties, Kinematics, and Cluster Formation at the Nexus of Filamentary Flows: G148.24+00.41.
   Date : 21st July 2023.

4. **Topic :** Exploring the interplay of magnetic fields, gravity, and turbulence in star formation at the hub of the GMC G148.24+00.41

Date : 19th March 2024.

DSC seminars

1. 29th January 2021; DSC seminar 1
2. 30th July 2021; DSC seminar 2
3. 28th January 2022; DSC seminar 3
4. 29th April 2022; DSC seminar 4
5. 9th January 2023; DSC seminar 5
6. 31st July 2023; DSC seminar 6
7. 26th December 2023; DSC seminar 7

Contents

List of Figures

List of Tables

List of Abbreviations

ALMA	Atacama Large Millimeter/submillimeter Array
AU	Astronomical Unit
CMF	Core Mass Function
CMZ	Central Molecular Zone
DCF	Davis-Chandrasekhar-Fermi
DOT	Devasthal Optical Telescope
DSS2	Digitized Sky Survey II
FIR	Far-Infrared
FWHM	Full Width at Half Maximum
GC	Globular clusters
GHC	Global Hierarchical Collapse
GLIMPSE	*Spitzer* Galactic Legacy Infrared Mid-Plane Survey Extraordinaire
GMC	Giant Molecular Cloud
GPS	Galactic Plane Survey
HFS	Hub Filament System
Hi-GAL	Herschel Infrared Galactic Plane Survey
IG	Intensity Gradients
IMF	Initial Mass Function
IR	Infrared
IRDC	Infrared Dark Cloud
IRAS	Infrared Astronomical Satellite

ISM	Interstellar Medium
JCMT	James Clerk Maxwell Telescope
kpc	kilo-parsec
KS	Kennicutt-Schmidt relation
LG	Local Gravity
LOS	Line Of Sight
LSR	Local Standard of Rest
LTE	Local Thermodynamic Equilibrium
MHD	Magneto Hydrodynamics
MID	Mid-Infrared
mm	Millimeter
MNRAS	Monthly Notices of the Royal Astronomical Society
MST	Minimum Spanning Tree
MYSO	Massive Young Stellar Object
MWISP	Milky Way Imaging Scroll Painting
NIR	Near-Infrared
OC	Open clusters
PACS	Photoconductor Array Camera and Spectrometer
pc	parsec
PDF	Probability Density Function
PMO	Purple Mount Observatory
PNICER	Probability densities Near-Infrared Color Excess Revisited
POS	Plane Of Sky
PPV	Position-Position-Velocity
PPMAP	Point Processing Mapping
PSF	Point Spread Function

PV	Position-Velocity
RAT	Radiative Alignment Torque
RMS	Red MSX Source
SCUBA-2	Submillimetre Common User Bolometer Array-2
SED	Spectral Energy Distribution
SFE	Star Formation Efficiency
SFOG	Star Formation in the Outer Galaxy
SFR	Star Formation Rate
SPIRE	Spectral and Photometric Imaging Receiver
Submm	Sub-Millimeter
TANSPEC	TIFR-ARIES Near infrared Spectrometer
2MASS	Two Micron All Sky Survey
UKIDSS	UKIRT Infrared Deep Sky Survey
UV	Ultraviolet
VCF	Velocity Coherent Filaments
WISE	Wide Field Infrared Survey Explorer
YMC	Young Massive Cluster
YSO	Young Stellar Object

Chapter 1

Introduction

" The Milky Way is nothing else but a mass of innumerable stars planted together in clusters "

– Galileo Galilei, 1564–1642

On dark nights, one can see that the sky is full of billions and trillions of speckling stars. These are the stars visible to the naked eye, but there are also numerous fainter stars that we cannot see, as well as very young stars that emit most of their light in the infrared spectrum. Depending upon the total amount of light they emit, which is called the luminosity, different classes of stars are defined, mainly dwarfs, subgiants, giants, supergiants, and bright supergiants. The Universe consists of very young stars that are only a few million years old and some of the oldest stars, which are believed to be formed 100 million to 250 million years after the Big Bang (Bromm & Larson, 2004; Bromm, 2013). Since the dawn of civilization, humankind has always wondered about these stars twinkling in the night sky. The Hipparchus of Nicaea, a Greek astronomer, has been given the credit for producing the first stellar catalogue in the second century BCE, consisting of around 850 stars. Ever since, astronomers have wondered about the formation of stars and have started to explore questions like, *when*, *where*, and *how* these stars form. Figure 1.1 shows astrometry through the ages, i.e. over the time period of II century BCE to the GAIA era, which discovered enormous stars in the sky.

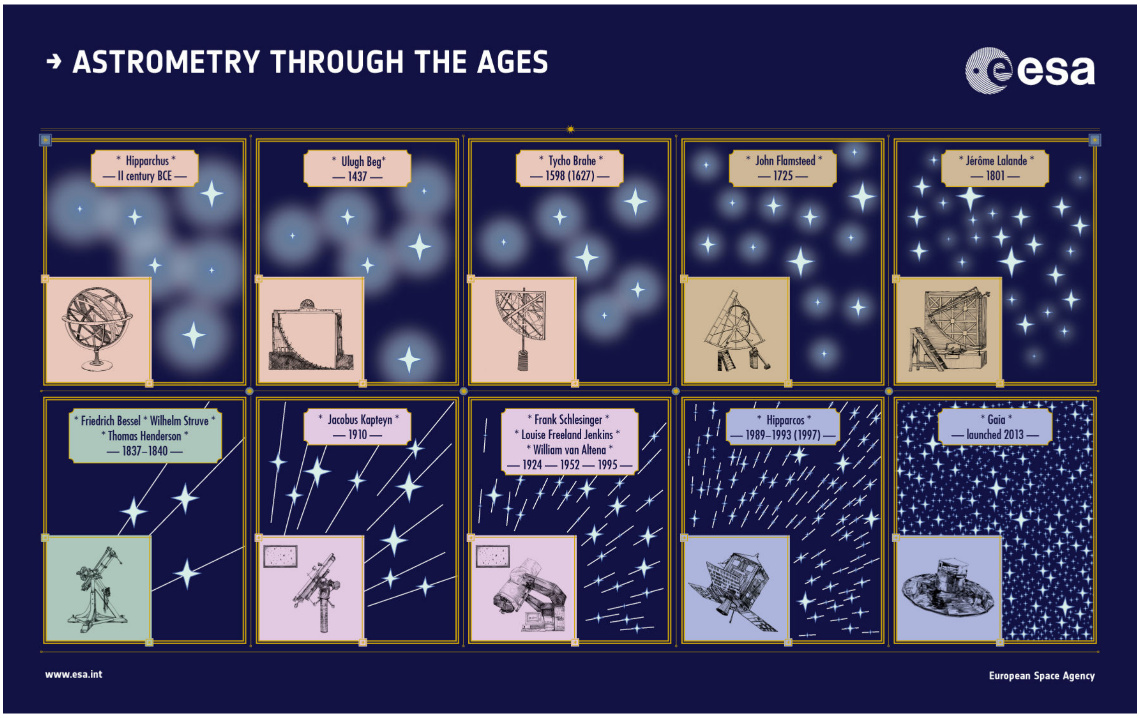

Figure 1.1: Astrometry through the ages. *Credit: ESA*.

In earlier times, stars, once believed to be eternal, served as a navigation system for sailors long before the advent of sophisticated instruments. In reality, stars are not eternal, they take birth, evolve over time, and then die by releasing an immense amount of energy and matter. That matter, generally referred to as cosmic dust, is then thrown into space, forming the basis for the birth of new stars, planets, and other cosmic bodies. Stars take birth in the darkest and dust-embedded regions of the universe, and that's why they are not visible to the naked eye. When stars become visible to the naked eye (the brighter ones), it means they have already formed and are in the advanced stage of stellar evolution. It requires modern telescopes, robust instruments, and advanced observational techniques at different wavelengths to see the early stages of star formation.

In the 20th century, with the advancement of modern-day telescopes and space-based observatories, astronomers have revealed many insightful and exciting results about the formation of stars and their properties, like mass, luminosity, temperature, and age. In the late 20th century and mainly in the 21st century, a huge leap has been seen in the field of star formation and understanding of their birthplace, thanks to facilities such as the Hubble Space Telescope

(HST), Spitzer Space Telescope, Herschel Space Observatory, and James Webb Space Telescope (JWST) and many ground-based optical, infrared (IR), sub-millimetre, and radio telescopes. For example, the whole sky astronomical surveys like the Two Micron All-Sky Survey (2MASS) have immensely helped astronomers to reveal and study the early phases of star and star-cluster formation.

The following sections provide an introduction to the composition of the interstellar medium and regions where stars or groups of stars form. Furthermore, the theory of different physical processes involved in star formation and the various observational tools that are generally used are briefly discussed. Additionally, the sections address the motivation behind the research, the broad objectives of the thesis, and its outline.

1.1 Interstellar medium (ISM)

The interstellar medium (ISM) is the matter that exists in the space between the stars within a galaxy. In 1922, Hubble mentioned that the starlight gets scattered from the dust present between the stars and shines as a reflection nebula (Hubble, 1922). The ISM serves as the reservoir for the raw materials from which new stars and planetary systems form. It is composed of gas (mostly hydrogen and helium) in the form of atoms, ions, and molecules, as well as dust grains. The typical composition of the ISM is hydrogen (70%), helium (28%), and the rest are heavier elements, preferentially called metals in Astronomy. Overall, approximately 99% of the interstellar matter is in the gaseous phase, with the remaining 1% in the solid form that is called dust.

Stars form in the densest regions of the ISM through condensation and gravitational collapse of gas clouds, and they eject some of their material back into the ISM via stellar winds. When stars die, depending on their masses, they become white dwarfs, neutron stars, and black holes. Massive stars evolve into Supergiants, which explode once their nuclear fuel runs out and not enough to balance against the force of gravity, known as a supernova explosion. While the low-mass stars evolve into white dwarfs, which also eject material from their outer envelope and through *nova* events. The heavier elements in the material ejected by the stars, once cool, condense into the interstellar grains and disperse along with the gas. This ejected material in the

ISM contributes to the formation of a new generation of stars. This process is believed to be the reason why heavier elements (e.g., iron) are found in low-mass stars, planets, and other smaller bodies, as they cannot produce such elements on their own. These heavier elements can only be formed in massive stars through nucleosynthesis. Figure 1.2 shows the basic schematic of the recycling of gas and stars in the ISM.

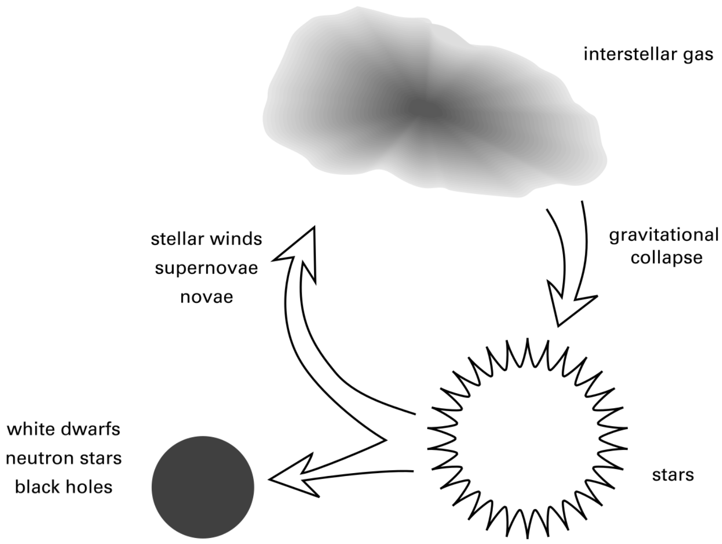

Figure 1.2: Recycling of material in the ISM. *Credit: The Formation of Stars (Stahler & Palla, 2004).*

The ISM has different phases depending upon their density and temperature: hot ionized medium (3×10^{-3} cm^{-3} and 5×10^{5} K), warm ionized medium (0.3 cm^{-3} and 8×10^{3} K), warm neutral medium (WNM, 0.5 cm^{-3} and 8×10^{3} K), cold neutral medium (CNM, 50 cm^{-3} and 80 K), and molecular clouds (> 300 cm^{-3} and 10 K) (see Stahler & Palla, 2004; Kalberla & Kerp, 2009). Atomic hydrogen (H I) is the most abundant baryonic component of the Universe and is a gas reservoir that makes the molecular clouds, the birthplace of stars. The radio observations show that the atomic hydrogen in our Milky Way is mostly confined to the disk with a scale height of around 100−200 pc between the galactocentric distance (R_{gal}) of ∼4 to 8.5 kpc (Stahler & Palla, 2004; Kalberla & Kerp, 2009; McClure-Griffiths et al., 2023). By mass fraction, the neutral hydrogen has the highest percentage in the ISM. The ionized phase (H II), though relatively small in mass, occupies most of the volume of the ISM and is very important in identifying the massive star-forming regions. The temperature and density of neutral hydrogen medium (or diffused atomic clouds) are not adequate for the formation of stars. The stars form in a more dense and cold environment of ISM, i.e. the molecular regions.

1.1.1 Molecular gas and its detection

The molecular fraction of the ISM is only < 1% of the total volume but around 13% by mass. The distribution of molecular gas in the Milky Way shows a peak around the central few hundred parsecs (Central Molecular Zone), drops between 0.5 to 3 kpc and again rises around 4 to 6 kpc (Molecular ring), and then drops exponentially up to 12−13 kpc (see Stahler & Palla, 2004; Ballesteros-Paredes et al., 2020, and references therein). It is mostly confined to the Galactic plane with a scale height of around 50−60 pc. The molecules are mostly concentrated in the dense regions of ISM called molecular clouds. These are cold and dark regions, where molecules are shielded from UV radiation, allowing star formation to occur.

Though H_2 is the most abundant molecule, being a homonuclear diatomic (or symmetric) molecule, it has no permanent dipole moment, and hence, its rotational dipole transitions are forbidden. The quadrupole transitions are possible for H_2, but they require a high excitation temperature of around 540 K. The lowest vibrational transitions for H_2 are even more difficult, as the temperature required for these transitions is nearly 6471 K (see the review article by Bolatto et al., 2013). Since H_2 emission is not prominent in cold clouds, other surrogate tracers are used, like Carbon monoxide (CO) isotopologues, which is the second most abundant molecule in the clouds. The CO has a weak permanent dipole moment of around 0.1 Debye, and the lowest rotational (J = 1−0) transitions are possible in molecular clouds at a temperature of 5.5 K. It has been widely used as a tracer of molecular hydrogen column density and mass of molecular clouds. The ^{12}CO is the most abundant isotope but is relatively optically thick and, thus, only better probes the outer low-density envelope of the clouds. The ^{13}CO and C^{18}O, being relatively optically thin, are better tracers of inner dense structures of the cloud. The excitation of CO mostly happens due to the collisions with H_2 in the ambient medium. If the density of a region is higher than the critical density, then frequent collisions can happen, and the lower rotational energy levels of CO will thermalise with H_2. In this case, the CO molecule comes into local thermodynamic equilibrium (LTE), and its excitation temperature becomes nearly equal to the kinetic temperature. The critical density can be defined as the volume density required to collisionally excite a transition and is the ratio of Einstein's spontaneous decay rate to the collisional de-excitation rate per molecule. The emission from CO (J = 1−0) isotopologues comes in the millimetre wavelengths, i.e. 2.6, 2.7, and 2.1 mm for ^{12}CO, ^{13}CO, and C^{18}O, respectively.

The column density of CO isotopologues can be derived by assuming the same excitation temperature for ^{12}CO, ^{13}CO, and C^{18}O under the LTE condition and using the optical depth and total integrated emission of the species. The relation between the aforementioned terms is known as the *detection equation*, which is basically derived from the radiative transfer equations and is given as

$$T_{B_0} = T_0[f(T_{ex}) - f(T_{bg})][1 - \exp(-\Delta\tau_0)], \tag{1.1}$$

where $f(T) = \frac{1}{\exp(T_0/T)-1}$, T_{B_0} is the brightness temperature at the line centre, T_{ex} is the excitation temperature, T_{bg} is the background temperature that is generally taken as 2.73 K for Cosmic Microwave Background Radiation (CMBR), and $\Delta\tau_0$ is the optical thickness of the cloud. Here, $T_0 = h\nu/k$, where h is the Planck's constant, ν is frequency, and k is the Boltzmann constant. For ^{13}CO and C^{18}O, in general, the total integrated emission is proportional to the total column density. However, this is not valid for ^{12}CO, as it can be optically thick in dense regions, but a conversion "$X_{\rm CO}$ or CO-to-H$_2$ conversion" factor is widely used to obtain H$_2$ column density, N(H$_2$), directly from the total integrated intensity of ^{12}CO. While ^{13}CO and C^{18}O column density (N(^{13}CO) and N(C^{18}O)) can be transformed to N(H$_2$) using H$_2$-to-CO abundance ratios. This X_{CO} factor has been observationally derived mostly in the range of ~0.9−4.8 × $10^{20}\,\mathrm{cm^{-2}\,K^{-1}\,km^{-1}\,s}$ from different methods, like detection of gamma rays (Bloemen et al., 1986), the virial mass of molecular clouds (Solomon et al., 1987), dust emission (Dame et al., 2001; Frerking et al., 1982), and extinction maps (Lombardi et al., 2006). The average X_{CO} value is around $2 \times 10^{20}\,\mathrm{cm^{-2}\,K^{-1}\,km^{-1}\,s}$ with an uncertainty of 0.1 dex (Bigiel et al., 2008; Bolatto et al., 2013).

Apart from CO, there are also less abundant molecules present in the ISM and clouds, like some high-density tracers, NH$_3$, HCN, N$_2$D$^+$, N$_2$H$^+$, and others are OH, H$_2$O, CH$_3$OH, CN and many more complex molecules, which are used to trace the properties and structure of dense regions in molecular clouds. The amount of dust in the ISM is very small (~1%). However, it is one of the best proxies for tracing the molecular cloud structure, its properties, and the stars within it, as the thermal emission from dust is mostly optically thin across the majority part of the electromagnetic spectrum.

1.1.2 Interstellar dust

In 1785, William Herschel published a paper highlighting the "holes in the sky" in Scorpius, the regions which were deficit of stars. Later, in 1930, R.J. Trumpler confirmed these holes, which were present in the whole sky, as the effect of interstellar dust present along the line-of-sight (LOS) that is obscuring the starlight (Trumpler, 1930). The interstellar dust mainly consists of silicates, amorphous carbon, and small graphite particles at the core, which is surrounded by icy mantles consisting of water ice and other organic molecules (see Draine, 2003). The dust forms from the heavy elements that condense out of the gaseous phase at temperatures below 2000 K. These heavy elements are ejected by the expanding outer layers of evolved stars (e.g. asymptotic giant branch stars) and supernova events. The ISM consists of large dust grains with sizes in the range of ~0.01 to 0.1 μm, as well as smaller grains with sizes in the range of ~0.001 to 0.01 μm. The generally adopted average size of the dust grain in the ISM is around 0.1 μm (Draine, 2003).

Dust plays a very important role in the thermodynamics and chemistry of gas and the dynamics of star formation. One of the prominent effects of dust grains is to obstruct and attenuate the light coming from distant stars. The scattering and absorption of the background stars by the dust grains is known as *Extinction*. Extinction has a wavelength dependency of the form, $A_\lambda/A_\mathrm{V} \propto \lambda^{-\beta}$ (Cardelli et al., 1989), where A_V is the extinction in V-band, i.e. visual extinction. Here, $A_\lambda = 2.5\log(F_\lambda^0/F_\lambda)$ is the extinction at wavelength λ, where F_λ^0 is the flux without extinction and F_λ is the observed flux. In general, the extinction is more at shorter wavelengths (optical and UV) in comparison to longer wavelengths (infrared). Blue light scatters the most in comparison to red light, which makes the stars appear redder, and this phenomenon is known as *reddening*. Figure 1.3 shows the images of globule Barnard 68 at different wavelengths (0.44 – 2.16 μm), where one can clearly see the dark patch at the shorter wavelengths due to high dust extinction, whereas at longer wavelengths, stars become visible because these wavelengths suffer less extinction. A part of the radiation is absorbed by the dust grains and re-radiated thermally at the longer wavelengths. Therefore, the observed flux or magnitude of stars must be corrected for extinction. The color excess due to dust extinction can be calculated as,

$$E(A_{\lambda 1} - A_{\lambda 2}) = (m_{\lambda 1} - m_{\lambda 2})_{obs} - (m_{\lambda 1} - m_{\lambda 2})_{int}, \tag{1.2}$$

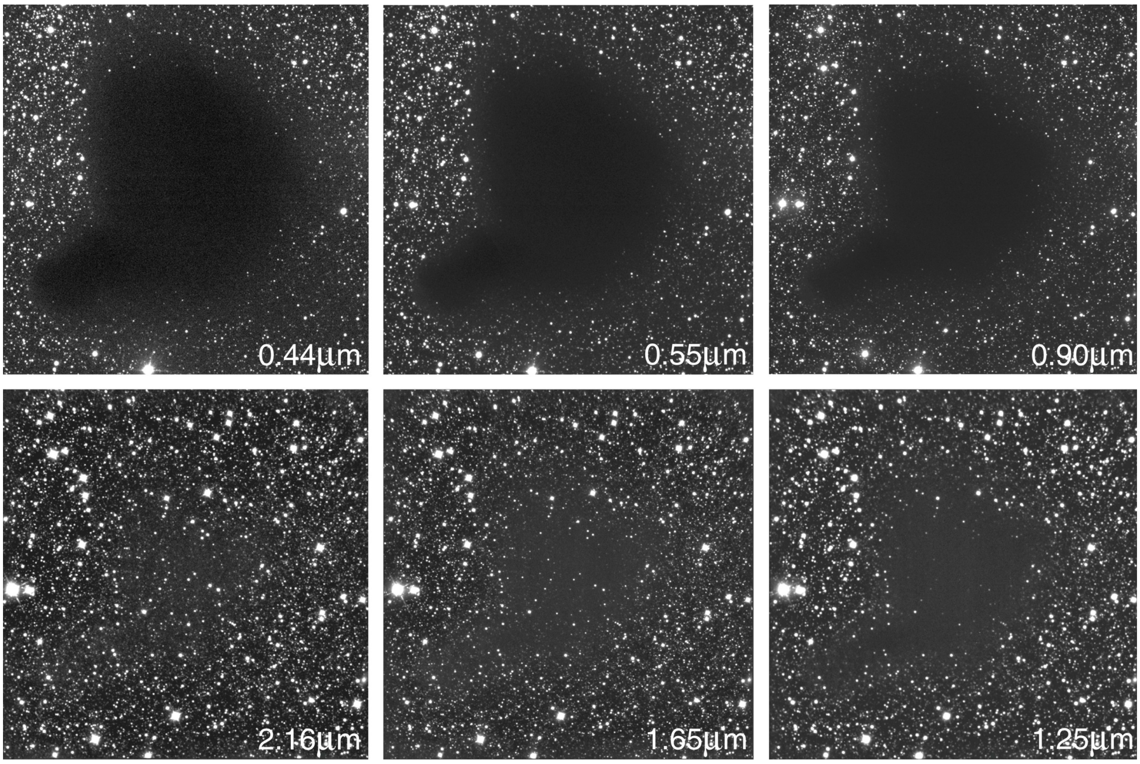

Figure 1.3: Images of the globule Barnard 68 in Optical (BVI) and infrared (JHK_s) bands adopted from Lada et al. (2007), and were taken from ESO's VLT and NTT (Alves et al., 2001).

where the first term on the righthand side is the observed color, the second term is the intrinsic color, and m_λ is the apparent magnitude of a star at λ wavelength. The ratio of visual extinction to color excess in blue and visible filters is known as *total-to-selective extinction ratio* at the visible (V) band, which is generally used to determine the extinction of a region and is given as

$$R_V = \frac{A_V}{E(B-V)}. \tag{1.3}$$

The value of R_V in the diffused ISM is generally taken as 3.1 (Bohlin et al., 1978), however, it can vary depending upon the density of the regions (see Cardelli et al., 1989, and references therein). The empirical relation between color excess and hydrogen column density, $N(H)$, is given by (Stahler & Palla, 2004)

$$\frac{E(B-V)}{N(H)} = 1.7 \times 10^{-22}\,\mathrm{mag\,cm^2}. \tag{1.4}$$

The above relation has been found by measuring the $N(H)$ from the Lyα absorption lines excited by OB stars located behind the diffuse clouds and the color excess of the same OB stars due to extinction caused by dust in the diffuse cloud (see Bohlin et al., 1978, for details). By combining equation 1.3 and 1.4 and taking $R_V = 3.1$ and $N(H_2) = N(H)/2$, the relation between A_V and $N(H_2)$ can be expressed as

$$N(H_2) = A_V \times 9.4 \times 10^{20} \mathrm{cm}^{-2} \,. \tag{1.5}$$

As already mentioned above, the dust grains also absorb the starlight at shorter wavelengths and emit continuum radiation thermally at longer wavelengths and, therefore, are used as a tool to study the molecular clouds where dust is ubiquitous. Since the temperature in molecular clouds is 10−20 K, most of the emission comes in the longer wavelength, i.e. in (sub)-millimetre. The light propagation through the dust medium can be understood via the radiative transfer equation given by

$$I_\nu = I_\nu(0)e^{-\tau_\nu} + S_\nu(1-e^{-\tau_\nu}), \tag{1.6}$$

where I_ν is the intensity at frequency ν, $I_\nu(0)$, is the background intensity which is attenuated by the optical depth τ_ν, and S_ν is the source function, which is the ratio of emission (j_ν) and absorption (α_ν) coefficient. For the continuum emission at the longer wavelength, the background intensity will be negligible such that $I_\nu = S_\nu(1-e^{-\tau_\nu})$. For optically thin medium ($\tau_\nu << 1$), which is generally the case for dust emission in molecular clouds and assuming that the dust is emitting like a blackbody such that $S_\nu \approx B_\nu(T_D)$, the above equation will become

$$I_\nu = \tau_\nu B_\nu(T_D), \tag{1.7}$$

where $B_\nu(T_D)$ is the blackbody radiation at dust temperature (T_D) given as $B_\nu(T_D) = \frac{2h\nu^3}{c^2}\frac{1}{e^{h\nu/kT_D}-1}$. The optical depth depends upon the matter along the line of sight, i.e. the column density, as $\tau_\nu = N_D\sigma_D Q_\nu$. Here, N_D is the dust column density, σ_D is the geometric cross-section of a typical grain, and Q_ν is the extinction efficiency factor. Thus, if there are enough measurements of dust emission at different wavelengths, one can determine the dust temperature and the optical depth of the cloud, and hence the column density of the cloud. At the longer wavelength limit, the τ_ν is well expressed as $\tau_\nu = \tau_{\nu_0}\left(\frac{\nu}{\nu_0}\right)^\beta$, where τ_{ν_0} is the optical depth at some reference frequency ν_0 and β is the dust opacity index. This methodology has been adopted to derive the physical conditions and column density of Galactic clouds using multi-band far-infrared (FIR) dust continuum data (e.g. André et al., 2010).

Dust also plays a very important role in the formation of molecules in the ISM. The intense ultraviolet radiation coming from massive stars, like OB-type stars, can photodissociate the molecules very easily. The dust obscures the incoming starlight, i.e. extinction, and thus shields the regions and suppresses the photodissociation of molecules. The dust grain surface also acts as a catalyst and a formation site for molecules. The formation of H_2 molecules through gas-phase reactions ($H + H \longrightarrow H_2$) and radiative association (H^+ and H^- radicals) are limited due to small rate reactions, which are relevant only in the low metalicity gas of the early universe (see Ballesteros-Paredes et al., 2020, and references therein). However, in the present-day ISM, dust efficiently absorbs radiation, enabling molecules to form in the densest parts of the clouds while those near the surface may be destroyed. It has been proposed and demonstrated that interstellar molecular hydrogen forms efficiently on the surfaces of dust grains (Hollenbach et al., 1971; Cazaux & Tielens, 2002; Vidali et al., 2009; Draine, 2011; Wakelam et al., 2017), essentially in present-day galaxies. The dust is also responsible for the polarization of background starlight through scattering and absorption (Hall, 1949; Hiltner, 1949). This polarization signal is used to indirectly trace the plane-of-sky (POS) component of the magnetic field in the ISM and star-forming regions.

Figure 1.4 shows the maps of the Milky Way disk at different wavelengths: radio, submillimetre, infrared, near-infrared (NIR), and optical. The radio surveys of 21 cm line emission show the distribution of atomic hydrogen in the disk. The submillimetre emission at 115 GHz from CO (J = 1−0) shows the molecular hydrogen column density distribution. It is a standard tracer to see the distribution of cold molecular clouds in the disk. The infrared map (12, 60, and 100 μm) shows mostly the thermal emission from the interstellar dust heated by lights from the stars. The NIR map (1.25, 2.20, and 3.50 μm) shows a part of the emission from stars (redder wavelength) that is capable of penetrating interstellar dust. The optical map (0.4−0.6 μm) shows the visible light from stars obscured by the intervening interstellar dust. The dust extinction based column density of a cloud can be derived using the dust extinction law and dust-to-gas ratio. The color excess obtained for an ample number of background stars to the cloud can be

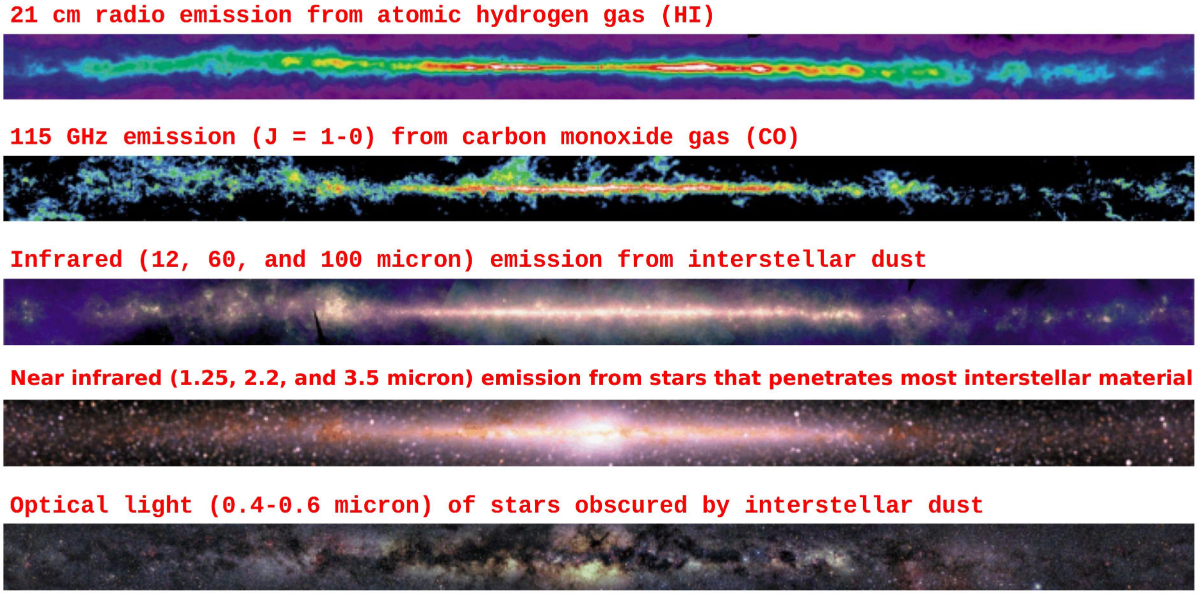

Figure 1.4: Maps of the Galactic disk at different wavelengths. The images are taken from the NASA site: *https://asd.gsfc.nasa.gov/archive/mwmw/*.

converted into molecular hydrogen column density by using equation 1.3 and 1.5. The extinction map provides a better measurement of the total amount of gas present in the clouds because of its small uncertainty compared to other methods. However, the resolution of the extinction map is limited by the number of observed background stars in a given region. Consequently, extinction maps tend to saturate in high-density regions where the optical depth is too high to observe background stars.

The dust continuum based column density estimation depends upon the dust temperature, gas-to-dust ratio and dust opacity index. The dust mass (M_d) can be calculated from the total flux emitted by dust (F_ν) using the following equation (Hildebrand, 1983)

$$M_d = \frac{F_\nu D^2}{\kappa_\nu B_\nu(T_D)}, \tag{1.8}$$

where κ_ν is the dust mass opacity coefficient, defined as $\kappa_\nu = \frac{3Q_\nu}{4a\rho_d}$. Here, Q_ν, a, and ρ_d are the extinction efficiency factor, dust grain size, and dust density, respectively. Then, the dust mass of the cloud can be transformed into its gas mass by assuming a gas-to-dust ratio and dust opacity index.

1.2 Molecular clouds: the birthplace of stars

As already discussed, molecular clouds are the densest parts of the ISM, where star formation occurs. Both gas and dust are present in molecular clouds in which H_2 is the most abundant molecule. Thus, it is crucial to study the properties and dynamics of molecular clouds in order to understand star formation. There are several mechanisms proposed for the formation of molecular clouds, but they are broadly divided into two categories i.e. *top-down approach* and *bottom-up approach*, after the WNM contracts and converts to the CNM likely due to thermal instability caused by the atomic cooling of the ISM (Ballesteros-Paredes et al., 2020). In the *top-down approach*, the large diffuse atomic clouds are thought to be compressed into dense molecular clouds due to gravitational instability, while in the *bottom-up approach*, the agglomeration of small diffuse atomic (or molecular) clouds, known as H I streams are thought to be the cause of molecular cloud formation. These H I streams can be produced by the expansion of H II regions, supernovae explosions, spiral arm passage, and cloud-cloud collision. The details on molecular cloud formation are given in Ballesteros-Paredes et al. (2020).

In general, a cloud is considered to be gravitationally bound if its gravitational pressure is higher than the surface pressure, which is mostly the case for molecular clouds. Whereas if the surface pressure exceeds the gravitational pressure, as seen in CNM or some diffuse atomic clouds, the cloud is confined by this pressure. However, the molecular clouds are not distinctly separated from the ISM but are surrounded by diffused molecular and atomic gas. The giant molecular clouds (GMCs) having a size of $\gtrsim$ 30 pc to 100 pc and masses of $\gtrsim 10^5$ $M_\odot$ are the reservoir of most of the molecular gas in the Milky Way (Stahler & Palla, 2004; Miville-Deschênes et al., 2017). Although the lifetime of molecular clouds and the impact of stellar feedback on them are complex and highly debated problems, the typical lifetime of a GMC has been estimated to be in the range of 10−50 Myr (Murray, 2011; Jeffreson & Kruijssen, 2018). Lada & Lada (2003) discuss that once the massive stars form, their feedback can disperse the natal cloud in ~3−5 Myr. Ballesteros-Paredes et al. (1999) have found short-lived GMCs having ages less than 3 Myr in their study of molecular clouds in the solar neighbourhood.

1.3 Star formation in a nutshell

The star formation process occurs under the effect of gravity and covers a wide range of spatial scales, depending upon the role of different physical factors like thermal pressure, rotation, turbulence, and magnetic field. The stellar feedback, like photoionization, stellar winds, and outflows, can also significantly affect the rate of star formation, as they can quickly disperse the natal star-forming gas. Star formation happens in the dense regions of molecular clouds, such as clumps and cores, where the molecules are shielded from UV radiation. The typical size of the clumps is around 0.5−1 pc, which further fragments to form denser entities with even higher volume densities, known as cores. The size of cores is ~0.1 pc, where single and binary stars can form (McKee & Ostriker, 2007) and a whole gravitationally unstable clump forms a stellar cluster.

The different physical factors dictate the stability of the system or molecular clouds, which can be explained theoretically using the virial theorem. Considering the cloud is in virial equilibrium, then all the forces are related by virial theorem:

$$\frac{1}{2}\frac{d^2\mathcal{I}}{dt^2} = 2\mathcal{U} + 2\mathcal{T} + \mathcal{M} + \mathcal{W}, \tag{1.9}$$

where $\mathcal{I}$ is the moment of inertia, $\mathcal{U}$ is the thermal energy due to random thermal motion, $\mathcal{T}$ is the total kinetic energy of the bulk motion of the cloud, $\mathcal{M}$ is the magnetic energy, and $\mathcal{W}$ is the gravitational potential energy. In the classical collapse scenario of Jeans (Jeans, 1902), a spherical cloud will collapse if $\mathcal{W} > 2\mathcal{U}$, neglecting the other force terms in equation 1.9, and factors like turbulence, external pressure, and complex geometry of the clouds. This condition of cloud collapse is popularly known as *Jeans criteria*, and the corresponding mass is known as *Jeans mass*, given as

$$M_J = \sqrt{\frac{3}{4\pi\rho}}\left(\frac{5kT}{GM}\right)^{3/2}, \tag{1.10}$$

where ρ, M, and T are the density, mass, and temperature of the cloud, respectively, and G is the gravitational constant. Initially, the cloud collapses almost isothermally and in a pressureless regime. As the density increases, the Jeans mass decreases, causing small inhomogeneities within the cloud to collapse independently, and the cloud then fragments into smaller structures. With fragmentation, at some point, these structures become dense enough such that their optical depth increases, resulting in a rise in temperature. This increase in temperature makes the cloud nearly adiabatic, causing the Jeans mass to become directly proportional to the density. Consequently, the cloud reaches the nearly adiabatic contraction phase, and a further increase in density raises the Jeans mass limit, halting further fragmentation. The Jeans classical collapse is a very simplified scenario to understand the overall collapse of a cloud, building substructures and star formation within them. However, the star formation process from cloud to core is a much more complex process due to the significant effect of other factors like magnetic field, rotation, turbulence, and feedback from the newly born stars, and their role changes with scale size and time. Otherwise, if the cloud were collapsing under the effect of gravitational force only, then the Galactic star formation rate (SFR) would have been very high (e.g. 300−500 $M_\odot$ Myr^{-1}), but observationally, it has been found that the Galactic SFR is very small ~1−2 $M_\odot$ Myr^{-1} (see Chomiuk & Povich, 2011; Elia et al., 2022, and references therein) and the star formation is, in fact, an inefficient process. The star formation efficiency (SFE), as has been found in the nearby star-forming regions, lies in the range of 2−6% (Evans et al., 2009; Lada et al., 2010; Heiderman et al., 2010; Lee et al., 2016). It means that other physical factors are significantly affecting and regulating the star formation process with the evolution of the cloud. Also, in reality, the clouds are not at all spherical and homogeneous, they are highly fragmented and of irregular shapes. In fact, the dust continuum images in far-infrared from *Herschel* show that the molecular clouds are filamentary in structure (André et al., 2010, 2014; Molinari et al., 2010), and these filaments play a crucial role in the star and star cluster formation (Heitsch et al., 2008; Myers, 2009; André et al., 2010; Schneider et al., 2012). Figure 1.5 shows the color-composite image of the Taurus molecular cloud taken with *Herschel* at far-infrared wavelengths (160, 250, 350, and 500 μm), revealing its filamentary structures. The filaments and their role in star formation will be again discussed in chapter 3. Here, we briefly discuss the role of the basic physical factors apart from gravity that impact the dynamic stability of the molecular cloud and substructures within it.

Figure 1.5: The filamentary structure of Taurus molecular cloud observed from *Herschel* at far-infrared wavelengths, from 160 to 500 μm. *Credit: ESA/Herschel/NASA/JPL-Caltech CC BY-SA 3.0 IGO; Acknowledgement: R. Hurt (JPL-Caltech).*

1.3.1 Rotation

Molecular clouds are not static; they carry angular momentum from the ISM or from the galactic rotation. However, small clumps and cores can have random spin axis orientations depending upon the internal interaction and turbulence. The rotation of the cloud exerts a centrifugal force in opposition to the gravitational force that provides stability to the cloud against the gravitational contraction. However, the rotation at the cloud scale is very slow and not significant enough to balance the cloud against gravity. The rotation speed increases with the collapse of the cloud from 3×10^{-15} s^{-1} to $(0.3-3) \times 10^{-14}$ s^{-1} at the clump scale, and further increases to $(1-10) \times 10^{-13}$ s^{-1} at the core scale, due to angular momentum conservation (Phillips, 1999). The rotation of the cloud causes it to be flattened along the axis perpendicular to the rotation axis, and that flattened geometry becomes more prominent at the core scale, which can be a seed for an accretion disk around the young star.

For the same simplified scenario of a spherical cloud as discussed in the previous section, the rotational kinetic energy to gravitational potential energy ratio is given by $\frac{\omega^2 R^3}{3GM}$, where ω and R are the angular velocity and radius of the cloud, respectively. With the collapse of the cloud, the angular velocity increases and as the dense cores continue to contract, they rotate more rapidly, potentially preventing further collapse. The magnetic field plays here a critical role in slowing down the rotating cloud cores, which is known as *magnetic braking*. Magnetic field lines, which are frozen with the matter (ionized particles) in the rotating clouds, behave like rubber bands or springs that are tied to the larger Galactic magnetic field. Therefore, as these magnetic field lines get twisted with the rotation, a restoring torque due to magnetic tension is generated in the opposite direction of the rotation, which slows down the rotating cloud cores. In this way, the magnetic field carries away the excess angular momentum from the cloud to the ambient medium through torsional Alfvén waves.

1.3.2 Magnetic field

The magnetic field is also ubiquitous in the ISM. The origin of magnetic fields in the universe is not very clear, but the current picture suggests that they originate from galactic scale dynamo amplification of weak seed fields generated by Biermann batteries in Population III stars and/or in early Active Galactic Nuclei (AGNs) (J. Rees, 2005; Beck et al., 2012; Pakmor et al., 2014; Martin-Alvarez et al., 2018; Attia et al., 2021). The magnetic field is then seeded into molecular clouds during their formation and sustained due to ionization caused by radiation from stars and *cosmic rays*, and evolves with cloud evolution. In the dense regions of the molecular cloud where there is no other source of ionization is present, the *cosmic rays* can penetrate even in the very optically thick clouds and provide a minimum degree of ionization ($\sim 10^{-8} - 10^{-9}$), which is enough to sustain the small magnetic field in clouds. With the contraction of clouds, the magnetic field strength increases, i.e. from clouds to cores.

Magnetic field plays a very significant role in the dynamics of clouds, clumps, and cores, as well as in the formation of stars. The average magnetic field strength in the ISM is a few microgauss, while in molecular clouds, it is around 10–20 microgauss. The magnetic field contributes to the total pressure that supports the cloud against the gravitational collapse (see equation 1.9). Including only magnetic and gravitational potential energy terms in equation 1.9 and taking $\mathcal{M} = \frac{B^2}{8\pi}\frac{4}{3}\pi R^3$ and $\mathcal{W} = \frac{3}{5}\frac{GM^2}{R}$, one can determine the maximum mass that the magnetic field alone can support against the gravitational collapse as

$$M_\phi = \frac{\sqrt{5}}{3\pi\sqrt{2}G^{1/2}}\phi \sim 0.17\frac{\phi}{G^{1/2}}, \tag{1.11}$$

where ϕ is the magnetic flux and B is the magnetic field. The equation 1.11 is mostly used in the form of mass-to-flux ratio (λ_B), which is the ratio of column density ($N(H_2)$) to the magnetic field, in order to check the stability of regions.

$$\lambda_B = 2\pi\sqrt{G}\mu m_H\left(\frac{N(H_2)}{B}\right), \tag{1.12}$$

where μ is the mean molecular weight per hydrogen molecule. As discussed in the previous section, if the large-scale magnetic field at the cloud scale is inherited down to the core scale, it will help in removing the excess angular momentum due to magnetic freezing (Li et al., 2014b). The magnetic field also plays a very crucial role in the dynamic stability of the cores. In the case of the strong magnetic field at the core scale, due to magnetic freezing, ionized particles are not free to move across the strong magnetic field lines but can move along the field lines. As a result, the core initially contracts preferentially along the field lines and consequently acquires a flattened geometry. Initially, the high density of ionized particles prevents neutral particles from moving freely across the magnetic field lines, as they continuously collide with ionized particles. This is known as ion-neutral coupling. Therefore, the magnetic field lines initially oppose the collapse of the core, i.e. magnetically supported (subcritical region, $\lambda_B < 1$). However, since the matter can flow along the field lines, mass accumulates at a higher rate than the increase in the magnetic field. Once the core gets sufficient mass and the ionization fraction becomes low, the ion-neutral coupling breaks down, and the neutrals drift through the field lines, falling into the gravitational potential well. This drift between ions and neutrals is known as *ambipolar diffusion*. Thus, due to *ambipolar diffusion*, the core will become unstable (supercritical region, $\lambda_B > 1$) and eventually collapse under its own gravity. Due to the pinching of magnetic field lines by the inflow of matter, the magnetic field structure acquires an hour-glass geometry (Girart et al., 2006; Qiu et al., 2014; Beltrán et al., 2019). A more detailed discussion on the role of the magnetic field is given in Section 1.5.2 and Chapter 4.

As discussed in Section 1.1.2, the POS component of the magnetic field can be indirectly traced by measuring the dust scattering and emission polarization of the background starlight (linear polarization). The light coming from the background stars gets scattered from the dust and becomes partially polarized in the direction of the magnetic field, which mostly comes in the optical and NIR domains. Whereas in emission polarization, the light is polarized in a perpendicular direction to the magnetic field (for details, see the review article by Crutcher, 2012; Pattle et al., 2022). The emission polarization is important in studying the dense star-forming regions, like the distant clouds, clumps, and cores, where the optical signal is significantly attenuated due to high optical depth. The first reported observations of emission polarization were in FIR by Cudlip et al. (1982). A significant advancement in the FIR and submillimetre polarization studies resulted from observations made by the *Planck* satellite, which produced an all-sky 353 GHz (850 μm) dust polarization-based magnetic field map (Planck Collaboration et al., 2015) (shown in Figure 1.6). The ground-based observatories have also majorly contributed to observing the polarization signals at longer wavelengths and different spatial scales (clouds to cores), like the James Clerk Maxwell Telescope (JCMT), Atacama Large Millimeter/submillimeter Array (ALMA), Atacama Pathfinder Experiment (APEX), and Submillimeter Array (SMA).

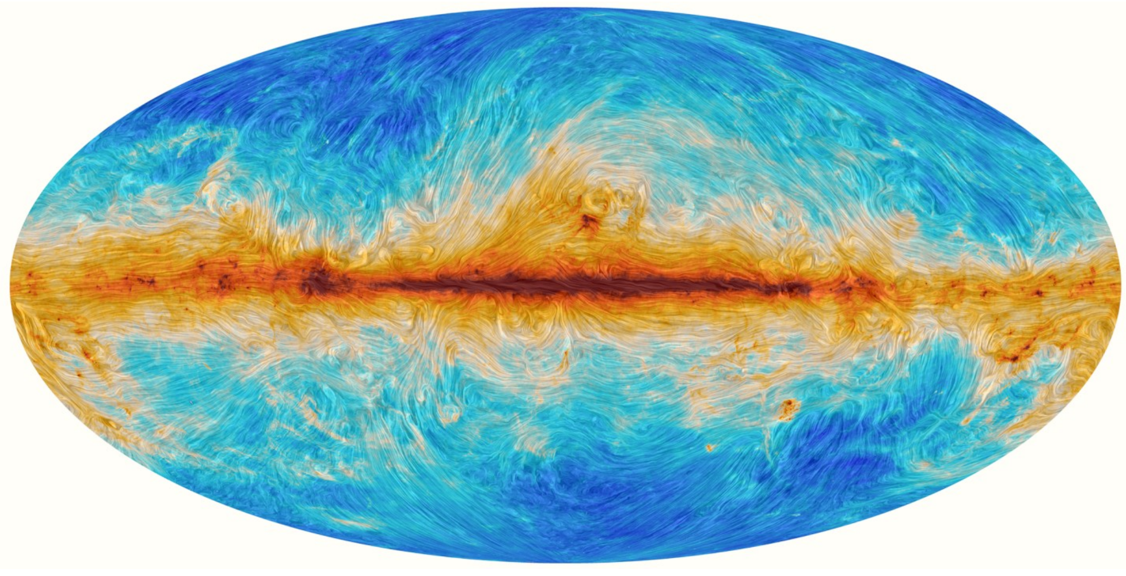

Figure 1.6: The all-sky magnetic field map of Milky Way traced by dust polarization at 353 GHz (850 μm) from *Planck*. *Credit: ESA and the Planck Collaboration (Planck Collaboration et al., 2015).*

The detection and measurement of polarization signals to trace the POS magnetic field is discussed in Chapter 4. The LOS component can be traced directly by measuring the Zeeman splitting of spectral lines of molecules (e.g. OH, CN, and SO), both in absorption or emission. The shift in the spectral lines is proportional to the strength of the magnetic field ($\Delta\nu \propto \mu_B B$), where μ_B is the Bohr magneton. The Zeeman observations of H I emission trace the low-density regions ($\sim 10^0 - 10^2$ cm^{-3}), OH emission and H I absorption trace the moderate densities ($\sim 10^2 - 10^4$ cm^{-3}), and CN traces the relatively high-density regions ($\sim 10^5 - 10^6$ cm^{-3}) (Pattle et al., 2022).

1.3.3 Turbulence

Apart from thermal pressure, rotation, and magnetic field, turbulence is another factor that significantly affects star formation in molecular clouds. Reynolds number is used to differentiate between the nature of fluid flow, i.e. laminar or turbulent. Turbulence can be generated by a variety of mechanisms, such as galactic shear, feedback from massive stars, supernovae shocks, protostellar outflows, large-scale gravitational instabilities, and cloud-cloud collisions. The kinetic energy at a large scale can either dissipate into heat due to viscosity or feed into turbulence due to some instabilities, like Kelvin-Helmholtz instability (Chandrasekhar, 1961). In fluid dynamics, these flow instabilities or shear flow generate swirling motions (vortices and eddies) of different scale sizes. The energy cascades from large-scale to small-scale structures or eddies and eventually dissipates into thermal energy at the Kolmogorov length scale (see Mac Low & Klessen, 2004, and references therein).

In molecular clouds, a larger velocity dispersion, which simply can not be explained only due to thermal broadening, is generally believed to be partly contributed by turbulence. In simple terms, turbulence can be thought of as the chaotic and irregular gas motions that may cause local density enhancements in the cloud. The linewidth ($\Delta\nu$) of the cloud scales with its size (R) as $\Delta\nu \propto R^{0.5}$, which is known as Larson's linewidth-size relation (Larson, 1981). The ratio of the flow velocity to the speed of sound is defined as the Mach number. Depending upon the Mach number, the turbulence can be hypersonic, supersonic, transonic, and subsonic. If the flow speed in a medium is higher than the sound speed, it generates shocks. The turbulence cascades down from large-scale clouds to small-scale clumps and cores. At the cloud scale, turbulence can provide support like the magnetic field against gravitational collapse, but not for long; it has been found that generally, the external turbulence decays in one dynamical time of the cloud (Vázquez-Semadeni et al., 2019). There must be some source of internal turbulence in the cloud, like protostellar outflows and stellar winds.

Another observational diagnostic of the presence of turbulence in a GMC is the density profile of the cloud. Whether a cloud is dominated by gravity or turbulence can be seen from its column density-probability density function (N-PDF). The shape of the density/column density is expected to tell about the underlying physics of the cloud and its star formation activity. The log-normal density distribution shows the effect of turbulence, and the cloud with active star formation takes the form of a power-law, which shows the dominance of self-gravity (McKee & Ostriker, 2007; Schneider et al., 2015a,b). Studies show that the N-PDF of molecular clouds consists of a lognormal distribution at lower density and a power-law tail at higher density (Schneider et al., 2015a,b, 2016), which suggests that molecular clouds are turbulent in nature, whereas gravity becomes dominant in high-density regions.

1.4 A star cluster

A star cluster is a group of stars that are gravitationally bound to one another and share a common origin. Being born in the same parental molecular cloud, they have similar distances. Star clusters form in the densest regions of molecular clouds, i.e. clumps. During the early phases of their formation and evolution, they are heavily obscured by the dust and, therefore, mostly visible at infrared wavelengths. In the literature, the morphological criteria to define a cluster is that its stellar density should be at least 3−5-sigma of the background stellar density (see Ascenso, 2018, and references therein). Here, sigma is the standard deviation of the background stellar density. Dynamically, Lada & Lada (2003) define a cluster as a group of at least 35 stars whose stellar mass density is higher than 1 $M_{\odot}$ pc^{-3}, a threshold required for a cluster to survive tidal disruptions and evaporation for at least 10^8 yr. McKee et al. (2015) define a cluster as a group of stars having a density significantly higher than their mean local background (for e.g. 0.1 $M_{\odot}$ pc^{-3}; near solar neighbourhood). However, Krumholz et al. (2019) define the star clusters in a more general way, i.e. a group of at least 12 stars with a density of a few times larger than the local background.

It is believed that the majority of the stars, if not all, form in a clustered environment (Lada & Lada, 2003). The crowded environment in which stars form determines the properties of stars themselves – the initial mass function (IMF), stellar multiplicity distributions, and probably their planetary properties as well. However, the formation and early evolution of star clusters remain enigmatic and mysterious even after nearly 400 years since Galileo's first observations. Star clusters can either be gravitationally bound or unbound, with the unbound clusters sometimes referred to as associations (Krumholz et al., 2019). In this thesis, we tried to explore how bound clusters may form and the different possible mechanisms by which a massive molecular cloud can give birth to an intermediate-to-massive bound stellar cluster.

The stellar clusters span a huge range of mass (hundreds to millions of $M_\odot$) and age (few Myr to $\geq$ 10 Gyr). Some clusters are compact and dense, whereas others are sparse and extended. There are different categories of clusters depending on their size, stellar population, and composition, namely *embedded clusters*, *open clusters*, and *globular clusters*. Embedded clusters are the youngest clusters that are still nested in the dense dust and gas environments of their parental molecular cloud, such that they are hardly visible in optical and, therefore, can only be seen at longer wavelengths such as IR. Being the host of young stars, which share the properties of their parent clump, these clusters are the sites to study the early phases of star formation. Figure 1.7 (left panel) shows an embedded cluster, S255-IR, which is part of a larger complex in Gemini OB association located at a distance of ~2.5 kpc (Ojha et al., 2011). The typical age of an embedded cluster is less than 5 Myr (Ascenso, 2018).

Open clusters (OCs) are evolved and older than embedded clusters, consisting of anywhere from tens to thousands of stars. The open clusters are mostly found in the Galactic disk and are irregular in shape and loosely packed, therefore stars in these clusters can disperse after a few billion years. Most of the open clusters are less than 1 billion years old, while the older ones are located farther from the Galactic centre. Figure 1.7 (right panel) shows NGC 3766, also known as Caldwell 97, is an open cluster in the southern constellation Centaurus located at a distance of ~1.7 kpc. An embedded cluster such as S255-IR might evolve to become an open cluster after clearing its natal cloud material.

Globular clusters (GCs) are bigger and older than OCs and consist of hundreds of thousands of stars held together by gravitational force. These clusters are mostly found in the Galactic halo region and consist of the older population of stars (i.e. population II stars). Globular clusters are big in size (can reach up to 300 light years in diameter) and symmetrical in shape due to high gravitational attraction. The globular clusters are believed to be formed during the epoch of

Figure 1.7: Left panel: The color-composite image of an embedded cluster, S255-IR, taken in J (blue), H (green), and K_s (red) bands from 2.2-m University of Hawaii telescope. The figure is adopted from Ojha et al. (2011) in which the massive young stars are also marked by green open circles. Right panel: Image of an open cluster NGC 3766 obtained in B (451 nm), V (539 nm), and I (783 nm) bands through MPG/ESO 2.2-metre telescope using Wide Field Imager (WFI). *Credit: ESO*.

extreme star formation in the early universe and show a wide range of metallicities and multiple stellar populations. Specifically, they show a bimodal metallicity distribution, i.e. a metal-poor population and a metal-rich population, observed not only in the Milky Way but also in other galaxies (Brodie & Strader, 2006; Bastian & Lardo, 2018; Beasley, 2020; Fahrion et al., 2020). Globular clusters are important sites for studying stellar and galaxy evolution. Figure 1.8 shows Omega Centauri, which is a globular cluster in the constellation of Centaurus located at a distance of ~5.2 kpc and consists of millions of stars.

However, with new better quality data, the distinctions between globular and open clusters are diluting, and some of their properties, like metallicity and density, are overlapping. In the context of the Milky Way galaxy, the mass and age of most of the open clusters are $\lesssim$ 5000 $M_\odot$ and $\lesssim$ 6 Gyr, respectively, while globular clusters have masses $\gtrsim 10^4$ $M_\odot$ and ages $\gtrsim$ 6 Gyr (Kharchenko et al., 2013). There is another intriguing and relatively less explored category of clusters that are much younger and, in terms of mass and size, mostly lie in between open and globular clusters; these are known as the young massive clusters (YMCs) (see Figure 2 of Portegies Zwart et al., 2010).

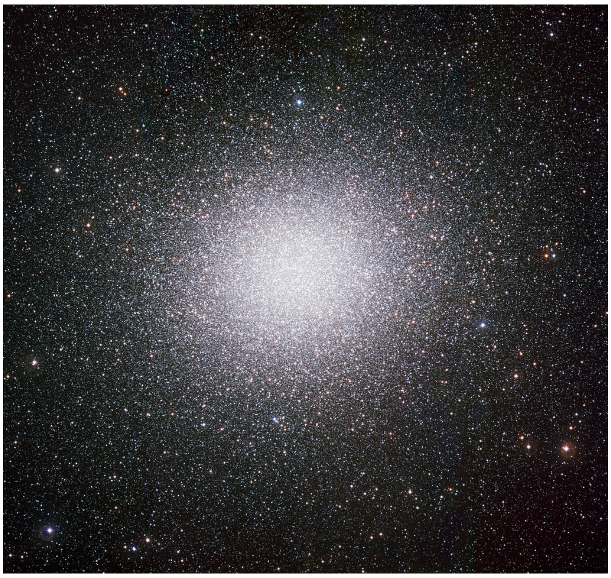

Figure 1.8: The color composite image of a globular cluster Omega Centauri obtained in B (451 nm), V (539 nm), and I (783 nm) bands, taken with the WFI camera from ESO's La Silla Observatory. *Credit: ESO*.

1.4.1 Young massive clusters

The young massive clusters are broadly classified as clusters having mass $\gtrsim 10^4$ $M_\odot$ and age less than 100 Myr (Portegies Zwart et al., 2010). The YMCs are thought to be the potential modern-day analogues of globular clusters that formed in the early Universe. It has also been suggested that understanding the formation of massive clusters like YMCs can provide insights into how GCs might have formed in the distant past of the Milky Way Galaxy (Elmegreen & Efremov, 1997). Determining their formation mechanism will better constrain the different cluster formation models over the full mass range of clusters. Figure 1.9 shows the *Hubble* image of Arches, a massive star cluster located towards the Galactic centre, and has mass ~2×10^4 $M_\odot$, size ~0.4 pc, and age ~2.5−4 Myr (see Espinoza et al., 2009, and references therein).

1.5 Motivation of the thesis

Massive to intermediate-mass clusters play a dominant role in the overall evolution and chemical enrichment of the Galaxy via stellar feedback such as photoionization, stellar winds, and

Figure 1.9: Image of Arches massive star cluster taken with NASA/ESA Hubble space telescope. Arches is located in the Central Molecular Zone (CMZ), i.e. within 200 pc of the Galactic centre.

supernovae (e.g. Geen et al., 2015, 2016; Kim et al., 2018). As they contain a large number of stars from the same parental cloud, they also serve as an important astrophysical laboratory for studying the stellar initial mass function, stellar evolution, and stellar dynamics. Moreover, it is also believed that most of the massive stars (> 20 $M_\odot$) form in massive clusters ($\gtrsim$ 1000 $M_\odot$) (Weidner et al., 2010, 2013; Yan et al., 2017, 2023). Thus, these massive clusters are often explored to study the formation and evolution of massive stars as well as to see their effect on the surrounding environment. Therefore, understanding cluster formation, in particular the formation of intermediate-mass ($10^3 - 10^4$ $M_\odot$; Weisz et al., 2015) to high-mass clusters (> 10^4 $M_\odot$; Portegies Zwart et al., 2010) is crucial and one of the key problems in modern astrophysics (e.g. Longmore et al., 2014; Krause et al., 2020). Especially the clusters of mass around 10^4 $M_\odot$ or more, as YMCs are rare, for e.g. only 12 YMCs have been found in the Milky Way so far (see Table 4 of Krumholz et al., 2019), despite the fact that our Galaxy contains a large number of massive molecular clouds (> 10^5 $M_\odot$). Thus formation of massive clusters like YMCs perhaps requires specific initial conditions, environment and mode of star formation in a given molecular cloud. In addition to the structure and physical process, it is believed that the formation of bound clusters also depends upon the efficiency by which the gas in molecular clouds or clumps gets converted into stars. The fact that makes the formation of massive clusters a difficult task is the very low SFE of 2−6% that has been found in molecular clouds (Evans et al., 2009; Lada et al., 2010; Heiderman et al., 2010; Evans et al., 2014). So, to form intermediate-to-massive bound clusters, simulations suggest either a high mass gas assembly with a high SFE ($\gtrsim 30\%$) is required before the stellar feedback becomes significant (Longmore et al., 2014; Banerjee & Kroupa, 2015; Krumholz et al., 2019), or they can form through a gradual gas assembly and hierarchical merger of small sub-clusters (Longmore et al., 2014; Sills et al., 2018a; Krumholz et al., 2019; Polak et al., 2023) or a combination of both. Therefore, investigating a massive molecular cloud's dust and gas properties, gas kinematics, SFR, and SFE, along with various physical factors, is essential for assessing the cluster formation potential of the cloud. Also, despite the fact that most stars form in clusters, only a few clusters remain bound after 10^8 years (Lada & Lada, 2003). The massive clusters, like GCs, which are still gravitationally bound must be the consequence of their different star formation histories that are not fully known. In this regard, factors like SFR, SFE, and the timescales in which gas is converted into stars to form bound stellar clusters are of great interest in the context of molecular cloud evolution and cluster formation.

1.5.1 Understanding the formation mechanisms of intermediate to massive clusters

It is well established that star and star clusters form in the dense clumps of GMCs. However, how exactly stellar clusters form, in particular intermediate to massive clusters, remains largely unknown and has been the subject of several reviews (Longmore et al., 2014; Krumholz et al., 2019; Adamo et al., 2020; Krause et al., 2020). How does the matter gather in star-forming regions to form these young clusters, i.e. whether enough matter is already present in the clump or it continuously accumulates from the ambient cloud to become more massive over time? Based upon that, it's debated whether they form monolithically in a single gravitational collapse event or through a hierarchical process involving gas accretion onto protoclusters while stars form concurrently (Longmore et al., 2014; Krumholz & McKee, 2020; Krause et al., 2020). Does the clump undergo rapid global collapse to form a star cluster, or is the process much slower, allowing the clump to be in quasi-equilibrium, perhaps regulated by turbulence (Nakamura & Li, 2014)?

Simulations suggest that a high-mass cluster may form: (a) if the cloud collapses to form a centrally condensed massive dense clump, which fragments to form stars at a high efficiency (Banerjee & Kroupa, 2015, 2018). By doing so, the clump may produce a rich cluster in a short span of time before the stellar feedback commences and the process is called as *monolithic* or *in-situ* mode of cluster formation (e.g. Banerjee & Kroupa, 2015; Walker et al., 2015). In this scenario, the cluster forms at higher initial stellar densities and then relaxes to its final state after expelling the gas. In a recent work, Polak et al. (2023) simulated clouds of different mass with different surface densities and found that GMCs of mass $\geq 10^5$ $M_\odot$ can form massive clusters of mass $\geq 10^4$ $M_\odot$ with a high SFE.

(b) In the literature, many large-scale dynamical models involving the evolution of molecular clouds over an extended period of time have been proposed for making massive clusters. These includes flow-driven models like *global hierarchical collapse* (GHC; Vázquez-Semadeni et al., 2019), *conveyor-belt collapse* (CB; Longmore et al., 2014; Walker et al., 2016; Barnes et al., 2019; Krumholz & McKee, 2020), and *inertial inflow model* (I2; Padoan et al., 2020). All these models have some similarities and differences (for details, see the review article by Vázquez-Semadeni et al., 2019; Krumholz & McKee, 2020). The GHC and CB models differ in their respective assumptions regarding the evolution of central clumps or hubs over time and the physical parameters responsible for the acceleration in star formation. In the CB model, the hub nearly remains at a constant density over many free-fall times, and therefore, acceleration in star formation happens because of increasing mass. While in the GHC, the hub collapses dynamically, with density rising over time, which explains the increase in SFR. The I2 model differs from the GHC model in terms of the origin of the large-scale flow from the ambient cloud towards the central clump/hub, which is turbulence-driven in I2 and gravity-driven in GHC. Broadly, these models point to the formation, evolution, and coalescence/convergences of substructures within a molecular cloud into a more massive structure driven by global collapse, leading to the formation of massive stars and associated clusters.

The above two scenarios *monolithic* and flow-driven models differed on the basis of whether the mass gathers before the onset of star formation or gathers concurrently along with ongoing star formation. The aforementioned models give different predictions of the outcomes of star and star cluster formation, basically the kinematic signatures and spatial structures. These predictions can be used to explore which model better explains the observational signatures of cluster formation in a GMC.

1.5.2 Relative role of magnetic field in cluster formation

One fundamental question that is still not fully understood even after decades of research is "what drives the star formation process?" One of the reasons that the lifetime of molecular clouds is larger than their free-fall times (typically $\sim 10^6$ yr; Hartmann et al., 2001; Palla & Stahler, 2002) is the role of the magnetic field in the dynamic stability of clouds, clumps, and cores (see Section 1.3). The star formation happens in filamentary molecular clouds (Könyves et al., 2015; André, 2017). Within these immense structures of cold gas and dust, the gravity, turbulence, and magnetic fields dictate the process of star formation at different scales, from large scale (cloud and filaments) to small scale (clumps and dense cores) (Klessen et al., 2000; Ballesteros-Paredes et al., 2007; Federrath, 2015; Tang et al., 2019; Wang et al., 2020b; Pattle et al., 2022). However, their relative role during the different stages of cloud evolution is still unclear and a topic of debate (Li et al., 2014a). The knowledge of physical processes that convert gas into stars is very important to develop the theory of star formation and evolution at different scales.

The magnetic field exists throughout star-forming molecular clouds across various scales (see the review article by Pattle et al., 2022) and plays a crucial role in the formation of molecular clouds and filamentary structures (Soler et al., 2013; Hennebelle & Inutsuka, 2019). Numerical simulations show that the strong magnetic fields play an important role in the magnetically channelled gravitational collapse of clouds (Nakamura & Li, 2008; Gómez et al., 2018), and can channel turbulent flows along the filaments (Li & Houde, 2008; Soler et al., 2013; Zamora-Avilés et al., 2017), guide the accreting matter (Seifried & Walch, 2015; Shimajiri et al., 2019), and dynamically influence the formation of cores along the dense ridges of the filamentary clouds (e.g. Koch et al., 2014; Zhang et al., 2014; Cox et al., 2016; Pattle et al., 2017; Soam et al., 2018; Liu et al., 2019; Eswaraiah et al., 2021). At parsec (or few parsec) scale, the magnetic field typically shows an ordered structure, mostly aligned with the long axis of the low-density elongated gas structures such as striations, while in high-density filaments, the magnetic field lines are preferentially perpendicular to the long axes of filaments (e.g. Cox et al., 2016; Planck Collaboration et al., 2016; Soler et al., 2017; Ward-Thompson et al., 2017; Tang et al., 2019; Soam et al., 2019; Doi et al., 2020). At sub-parsec scales, the magnetic field can be very complex depending upon the turbulent nature of the magnetic field and stellar feedback (e.g. Hull et al., 2017; Eswaraiah et al., 2020; Eswaraiah et al., 2021). Dust polarization studies at small scales have revealed a variety of magnetic field morphologies in dense clumps and cores, and the results suggest that the magnetic field is scale-dependent and varies with the environment (e.g. Girart et al., 2013; Hull et al., 2017; Ward-Thompson et al., 2017; Pattle et al., 2018; Eswaraiah et al., 2020; Eswaraiah et al., 2021).

Moreover, it is not clear whether it is turbulence or magnetic field along with gravity that dominates the star formation process. The role of gravity has long been recognised as the primary factor driving the collapse of dense regions and initiating the birth of protostellar cores. On the other hand, turbulence, the chaotic and ubiquitous motion of gas within these massive clouds, influences the fragmentation of the collapsing gas. However, the role of magnetic field, in comparison to turbulence and gravity, is relatively less understood at various stages of star formation. The "strong magnetic field" theory of star formation stresses the importance of the magnetic field in the formation and evolution of clouds and subsequent structures (Mouschovias et al., 2006; Tan et al., 2013; Hennebelle, 2018). This theory suggests that the magnetic field is strong enough to support the core against gravity, which makes the core magnetically sub-critical (Mouschovias et al., 2006). The magnetic support gradually dissipates due to ambipolar diffusion, and the core becomes magnetically supercritical and ultimately collapses under its self-gravity and forms stars (see Section 1.3.2). Conversely, the "weak magnetic field" theory suggests that turbulent flows control the formation and evolution of clouds and cores, and create the compressed regions where stars form (Padoan & Nordlund, 2002; Mac Low & Klessen, 2004; Federrath & Klessen, 2012). The gravoturbulent theory (Mac Low & Klessen, 2004; Federrath & Klessen, 2012) suggests that turbulence plays a dual role, providing stability to the clouds against gravitational contraction at a large scale, and generating the shocks that compress the gas in dense structures to trigger the star formation at a small scale. Observationally also, in some high-mass star-forming regions, it has been found that the turbulent energy is more dominant or comparable to magnetic energy (e.g. Beuther et al., 2010; Girart et al., 2013; Beuther et al., 2020; Wang et al., 2020b). In contrast, other studies found magnetic energy to be more dominant than turbulent energy (e.g. Girart et al., 2009; Beuther et al., 2018; Eswaraiah et al., 2020; Chung et al., 2023). Therefore, more observational evidence is required at the early stages of star formation to better constrain the theoretical models and relative roles of gravity, magnetic field, and turbulence in the star-forming regions.

1.5.3 Understanding the star formation scaling laws at clump scale

The processes that regulate the conversion of gas into stars in molecular clouds, as well as the mechanisms of cluster formation, are still the least understood. To understand the formation of stellar clusters, it is required to follow the sequence of interstellar processes from molecular clouds to clumps/cores. However, in reality, this sequential process of star formation is much more complex, involving filamentary structures of molecular clouds and the relative role of gravity, turbulence, magnetic field, and stellar feedback that too varies with the scale size, i.e. from clouds to cores. Along with the aforementioned factors, the radiation pressure from newly formed stars (acting mostly on dust) or enhanced thermal pressure from photoionized regions can halt the mass accretion to the clump and may eventually unbound the cluster by violent gas expulsions (Krumholz et al., 2019). So, inquiring about the rate of star formation and how it changes at different stages of cloud evolution is a topic of interest, as it is essential to develop a complete and universal description of star formation in the galaxy. In short, the quest is to understand whether the star formation is regulated by some large galactic scale process or depends on the local conditions of the star-forming gas material in the region.

The SFE is defined as the ratio of the total stellar mass to the total mass of a star-forming region, i.e., stellar mass plus present-day gas mass. Simulations suggest that the SFE of a star-forming region plays a very crucial role in making a bound cluster. Some young massive clusters in the Milky Way and the Magellanic Clouds show a lack of age spread, which might be a cause of a single episodic star formation event (Banerjee & Kroupa, 2015). However, simulations also suggest that a cluster can also become massive in 1 Myr through a merger of smaller sub-clusters that are closely located at birth (Banerjee & Kroupa, 2015; Sills et al., 2018a). Therefore, it is important to investigate the conditions under which the embedded clusters survive the violent gas expulsions and remain bound, like the Arches and Quintuplet clusters.

The connection between star formation rate and the gas mass that forms the stars is known as star formation scaling laws. To have a better understanding of the physics responsible for the star and cluster formation, the star formation-gas mass relation needs to be explored at scales of clouds/clumps in the Milky Way across different environments, densities, and sizes. Below is a brief summary of some theoretical and observational studies that have been done so far to examine the scaling laws at different spatial scales, along with our motivation to carry forward these studies.

1.5.3.1 Current understanding of Scaling laws

Galaxy-scale studies have led to a number of empirical relations between SFR and gas mass (Schmidt, 1959; Kennicutt, 1998b; Gao & Solomon, 2004; Wu et al., 2005; Bigiel et al., 2008). Schmidt (1959) first time established the relation between SFR of the stars perpendicular to the galactic plane and local hydrogen atomic gas in the interstellar medium. Schmidt (1959) found that the SFR density is proportional to the square of the density of the gas. Later on, the molecular hydrogen gas is also included and further studies were expanded to extragalactic scale (Kennicutt, 1989). Kennicutt (1998b) investigated a global Schmidt law for a sample of galaxies by measuring their projected SFR surface densities ($\Sigma_{\rm SFR}$) and gas mass surface densities ($\Sigma_{\rm gas}$), which is given by

$$\Sigma_{\rm SFR} \propto \Sigma_{\rm gas}^{N}, \tag{1.13}$$

where N is a power-law index. Kennicutt (1998b), studied 61 normal galaxies with Hα, H I, and CO observations to study the relation between average disk SFRs and average gas (atomic plus molecular) densities, and found $N = 1.4$, which is known as “Kennicutt-Schmidt (KS) relation” (Schmidt, 1959; Kennicutt, 1998b). The KS relation is well established at the extragalactic scales. de los Reyes & Kennicutt (2019) revisited the scaling relation by increasing the sample to 169 spiral galaxies and 138 dwarf galaxies, and found $N = 1.41 \pm 0.07$. However, the authors found that the correlation between SFR and gas mass is stronger and linear with molecular hydrogen compared to atomic hydrogen. Figure 1.10 shows the global Schmidt law for galaxies adopted from Kennicutt & Evans (2012), which also includes the sample of galaxies from (Kennicutt, 1998b).

Apart from the KS relation, the other observational studies based on either radial or point-by-point measurements (Martin & Kennicutt, 2001; Zhang et al., 2001; Wong & Blitz, 2002; Heyer et al., 2004; Komugi et al., 2005) have found values of N to be between 1 and 2. However, the studies of SFR−gas mass relation in single galaxies at the sub-kpc scales have found slightly lower power-law index values of ∼0.8−1.6 (Kennicutt et al., 2007; Thilker et al., 2007; Braun et al., 2009; Blanc et al., 2009; Verley et al., 2010). Bigiel et al. (2008) also found a

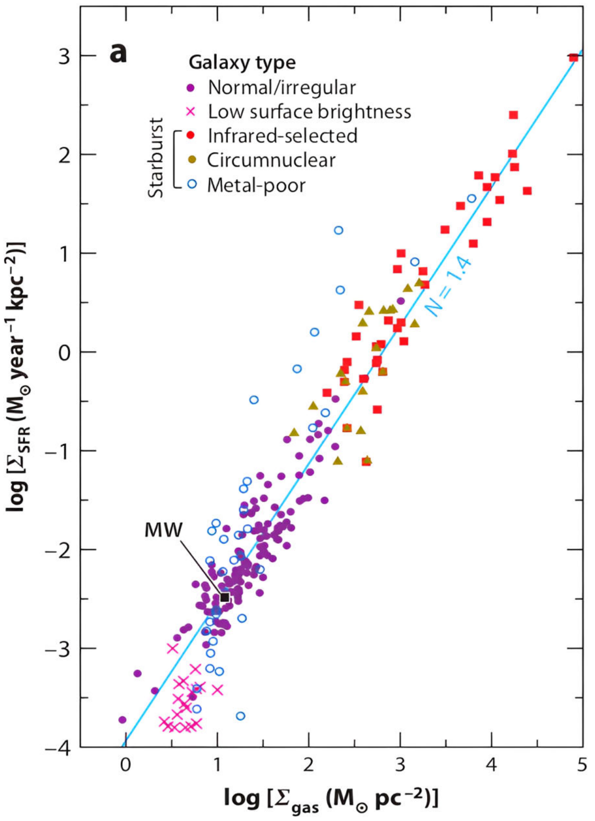

Figure 1.10: The relation between the disk-averaged surface density of SFR and gas mass (atomic and molecular) for different galaxies. The figure is adopted from Kennicutt & Evans (2012).

linear relation between Σ_{SFR} and Σ_{gas} (3−50 $M_{\odot}$ pc^{-2}) at ∼750 pc scales for 18 nearby galaxies with index $N = 1.0 \pm 0.2$.

In contrast, at the molecular cloud scale, the star formation−gas mass relations show poor correlations, which were analyzed using CO and near/far infrared luminosities or massive stars luminosity or radio continuum emission for proxy determination of gas mass and SFR, respectively (Mooney & Solomon, 1988; Onodera et al., 2010; Kruijssen & Longmore, 2014; Vutisalchavakul et al., 2016). For nearby molecular clouds, the star count method has been used to study scaling relations in different forms, like SFR−gas mass relation with free-fall, depletion, and orbital time scales, but they all show scatteredness at the cloud scale and lie well above the KS relation (Evans et al., 2009; Heiderman et al., 2010; Kennicutt & Evans, 2012; Evans et al., 2014). Evans et al. (2009) compared the SFR−gas mass relation for Galactic molecular clouds from the *Spitzer* Cores to Disks (c2d) survey and found that SFRs of Galactic clouds lie almost ∼20 times above the KS relation. Heiderman et al. (2010) studied nearby molecular clouds from the c2d survey (Evans et al., 2009) and Gould Belt (GB) survey (Dunham et al., 2013) and found similar results, with their $\Sigma_{\rm SFR}$ value being higher by a factor of 30 than the expected value from the KS relation. Krumholz et al. (2012) suggested a volumetric star formation model to reduce the scatter in SFR−gas mass relation by arguing that the scatter could be due to variation in local free-fall timescales. The authors argued that if a time scale is involved like free-fall time in the SFR−gas mass relation, which is proportional to the gas mass divided by one free-fall time, then $t_{\rm ff} \propto \rho_{\rm gas}^{-0.5}$ and the relation becomes $\rho({\rm SFR}) \propto \rho_{\rm gas}^{1.5}$ (Krumholz & McKee, 2005; Krumholz & Tan, 2007). Thus, for a constant scale height, the slope is similar to the index value of the KS relation (1.4 ± 0.15). Evans et al. (2014) tested the volumetric star formation model for 29 nearby molecular clouds compiled from the *Spitzer* c2d and GB survey, and they argued that involving free-fall time does not reduce the scatter in $\Sigma_{\rm SFR} - \Sigma_{\rm gas}$ relation.

Interestingly, Heiderman et al. (2010); Lada et al. (2010) in their studies found that the rate of star formation increases rapidly above a certain threshold gas surface density ($\sim$130 $M_\odot$ pc^{-2}), above which the $\Sigma_{\rm SFR} - \Sigma_{\rm gas}$ relation shows a better correlation. The authors discussed that star formation has been observed to be more concentrated in high surface mass density regions. Lada et al. (2012) proposed that the total SFR in a molecular cloud or galaxy is linearly proportional to the dense gas mass within the cloud or galaxy. They found a better correlation between SFR and gas mass above a K-band extinction threshold of 0.8 mag (or N(H_2) $\sim 6.7 \times 10^{21}$ cm^{-2}), i.e. dense gas mass, and included dense gas fraction (f_{DG}, ratio of dense gas mass to total gas mass) in the $\Sigma_{\rm SFR} - \Sigma_{\rm gas}$ relation. In fact, studies of some normal and starburst galaxies (Gao & Solomon, 2004) and Galactic dense cores (Wu et al., 2005) using HCN as a dense gas tracer and infrared luminosity as an SFR tracer have also revealed linear and tighter correlations in scaling relations in comparison to that from total gas density. However, Gutermuth et al. (2011), in their study of nearby molecular clouds, did not find any such threshold density for star formation to occur and reported a square dependence of $\Sigma_{\rm SFR}$ on $\Sigma_{\rm gas}$ at lower densities also. The negation of any threshold density is also supported by Burkhart et al. (2013), which argued that a better correlation between $\Sigma_{\rm SFR} - \Sigma_{\rm gas}$ above a certain threshold density is just a consequence of larger gravitational influence at higher densities.

The possible reasons for scatter in the KS relation at a small scale can be an actual scatter due to some localized physical factors (Lee et al., 2016), or it can be a limitation due to some observational biases, like undersampling of the mass distribution function, an incomplete sample of young stellar objects (YSOs), and use of massive stars luminosity to determine the SFR. For example, the use of massive stars' luminosity as a tracer of star formation at a small scale may underestimate the SFR for young star-forming clouds (< 5 Myr; Krumholz & Tan, 2007; Calzetti et al., 2012), due to the lack of massive stars, as they mostly form late in comparison to low-mass stars in the cloud (Vázquez-Semadeni et al., 2009; Foster et al., 2014; Vázquez-Semadeni et al., 2019). In contrast, for older clouds, the massive stars will rapidly disperse the star-forming gas material, and hence, the gas tracers will underestimate the gas mass (Calzetti et al., 2012). Therefore, the scarcity of massive stars in young clouds and their gas dispersal effect makes it inappropriate to use the luminosity of massive stars as a tracer of SFR in clouds. Secondly, averaging over the whole galaxy for gas mass, where gas contained both in molecular clouds that are active in star formation and diffused gas regions that are quiescent, are included in total gas mass may underestimate the $\Sigma_{\rm SFR}$. For example, Goldsmith et al. (2008) found a significant amount of diffuse ^{12}CO gas in the Taurus molecular cloud where no young stars were found.

On the other hand, if the scatter in the KS relation is real due to the effect of local environment and physical factors like magnetic field, turbulence, protostellar outflows, and stellar feedback (Krumholz & McKee, 2005; Krumholz et al., 2014), it points that star formation at a small scale is not regulated by the galaxy-wide global process but by the local conditions of the gas from which star forms. The limitation of these aforementioned factors and uncertainties averages out at the extragalactic scale and does not affect the scaling relations, hence a strong correlation between $\Sigma_{\rm SFR} - \Sigma_{\rm gas}$ at the extragalactic scale. Because at the extragalactic scale, the average of a large number of clouds within a galaxy, each at a different evolutionary stage, is taken into consideration, causing their individual uncertainties to cancel out. However, the effect of physical factors and observational constraints can be significant at cloud or clump scale and can create a large scatter in scaling relations (Kruijssen & Longmore, 2014).

Recently, Pokhrel et al. (2020, 2021) studied the KS relation in 12 nearby molecular clouds by using better-quality Spitzer Extended Solar Neighborhood Archive (SESNA) YSO catalogue (Gutermuth et al., 2019), high dynamic range gas column densities, and reducing various observational uncertainties. The authors find a tight correlation between $\Sigma_{\rm SFR}$ and $\Sigma_{\rm gas}$ with an index of ~2. The authors also tested the volumetric scaling relation by including the free-fall timescale and found a tighter correlation when measuring the cloud-to-cloud KS relation. In summary, overall the $\Sigma_{\rm SFR} - \Sigma_{\rm gas}$ power-law index changes from 1.0−1.5 at extragalactic scales (Bigiel et al., 2008; Kennicutt & Evans, 2012; de los Reyes & Kennicutt, 2019) to 1.5−2.0 at molecular cloud scales (Gutermuth et al., 2011; Lada et al., 2013; Evans et al., 2014; Pokhrel et al., 2021).

As also discussed previously, the SFE found in nearby molecular clouds is around 2−6%, while the SFE in cores that is indirectly scaled from the similarity between the stellar initial mass function and the core mass function is around 30 ± 10% (Könyves et al., 2015). However, no robust scaling laws have been derived at the clump scale so far, as only very few studies have been done in the literature. Our broad aim is to investigate the scaling laws in young nearby star clusters, in order to examine the $\Sigma_{\rm SFR} - \Sigma_{\rm gas}$ relation at clump scale and also to establish the evolution of SFR and SFE from cloud to core scales.

1.6 Sample selection, data sets, and methodology

This thesis addresses two broad problems in the formation and early evolution of star clusters:

i) understanding the cluster formation potential of massive GMCs by investigating the dust and gas properties, gas kinematics, and the influence of various physical factors on star and star cluster formation and ii) what are the SFR and SFE of cluster forming clumps within molecular clouds, and how these parameters correlate with the gas mass of the clumps. In order to address the first question, an in-depth study of a carefully selected GMC using multiwavelength data sets was conducted, including infrared, sub-millimetre, and millimetre. For the second goal, 17 cluster-forming clumps were studied, and their various parameters, like SFR and SFE, were determined. These results are discussed in the context of cluster formation and the potential to remain bound. Details of the selection of the studied GMC and cluster-forming clumps are elucidated below.

1.6.1 Detailed characterization of G148.24+00.41: a giant molecular cloud

To explore the first goal, we carefully chose the G148.24+00.41 cloud for the following reasons. Clouds more massive than about 10^5 $M_\odot$ are potential sites of massive cluster formation. Studying the properties of such clouds in the early stages of their evolution offers an opportunity to test various cluster formation processes because (i) a massive bound cloud with a significant dense gas reservoir is required to form a high-mass cluster, and (ii) once star formation is underway, the massive members of the cluster can erase/alter the initial conditions and structure of the parental gas on a very short time-scale via feedback such as radiation, jets, and stellar winds. The molecular cloud – G148.24+00.41, is one such cloud whose temperature, as estimated by Planck, is around 13.5 K, while its mass, as estimated by Miville-Deschênes et al. (2017) using low spatial resolution CO data ($\sim$8′) is $\sim$1.3 × 10^5 $M_\odot$, suggesting that G148.24+00.41 is a massive cold cloud. The cloud region also includes the dark cloud "TGU 942P7", identified by Dobashi et al. (2005) based on the digitized sky survey extinction map. The Infrared Astronomical Satellite (IRAS) also identified a source "IRAS 03523+5343" in the direction of G148.24+00.41 close to TGU 942P7. The peak velocity of the various molecular gas associated with the IRAS 03523+5343 source and its immediate vicinity, estimated by different authors, lies mostly in the range $\sim$−33 to −35 km s^{-1} (e.g. Wouterloot & Brand, 1989; Yang et al., 2002; Urquhart et al., 2008; Miville-Deschênes et al., 2017). The kinematic distance of the cloud, as found in the literature, lies in the range 3.2–4.5 kpc (Yang et al., 2002; Cooper et al., 2013; Maud et al., 2015; Miville-Deschênes et al., 2017). In the direction of the cloud, the signature of star formation in terms of YSOs (Winston et al., 2020) and cold cores (Yuan et al., 2016; Zhang et al., 2018) have been identified. The cloud is still in the early stages of its evolution, such that stellar feedback is not yet significant, as no evidence of H II regions or bubbles has been found in the cloud. Despite the fact that G148.24+00.41 is a cold massive cloud, its global properties, structure, physical conditions, and stellar content have not been studied in detail.

1.6.2 Measuring star formation properties of a sample of 17 nearby young clusters

For the statistical work of studying the relation between SFR surface density and gas mass surface density at the clump scale, 17 young cluster-forming clumps were carefully selected within a distance of $\sim$2.5 kpc. Those clusters are included in the sample, which have deep NIR data from UKIRT Infrared Deep Sky Survey (UKIDSS; Lawrence et al., 2007) and dust continuum data from *Herschel* (details of the data are given in the next section). The clustering of stars in the clusters is first inspected by visualizing the 2MASS, *WISE*, and *Spitzer* images, and also their association with the cold dust emission from AKARI and *Herschel* is checked, which ensures that the cluster is young such that the gas dispersal is not yet happened. The cluster sample is constrained within a distance limit of 2.5 kpc, taking into account the typical extinction in the direction of the cluster-forming clumps (i.e., A_V ~5−11 mag) and the typical point source completeness of the UKDISS survey (K ~18 mag). The data would be sensitive to detect the cluster members down to 0.1−0.2 $M_\odot$, which is essential to estimate the total stellar mass of the cluster. In some cases, where extinction is higher, it is ensured that the stars are detected at least down to 0.5 $M_\odot$, for estimating the stellar mass using the functional form of the IMF and integrating it down to 0.1 $M_\odot$. The IMF is the distribution of stars at the time of birth and is generally characterised using the Kroupa (Kroupa, 2001) and Chabrier (Chabrier, 2003) functional forms.

1.6.3 Data sets

To achieve the above goals, we have used multiwavelength data sets from the public archive as well as by conducting our own observations. Below, we briefly outline these data sets. More details are given in the individual chapters.

To investigate the dust properties of the cloud and clumps, and the distribution of young embedded stellar sources, this thesis utilised FIR data taken from the Herschel space observatory. The Herschel Space Observatory is a 3.5-m telescope which was built and operated by the European Space Agency (ESA) and was active from 2009 to 2013. For this work, we have used imaging data between 70 to 500 μm (spatial resolution ~8.5 to 36.3 arcsec) as well as the Herschel Infrared Galactic Plane Survey (Hi-Gal) data products such as dust temperature and column density maps derived from multi-band imaging observations. These observations are taken with the Photodetector Array Camera and Spectrometer (PACS; Poglitsch et al., 2010) and the Spectral and Photometric Imaging Receiver (SPIRE; Griffin et al., 2010) instruments onboard on *Herschel*. The PACS is a photometer and medium-resolution spectrometer (R = 1000−5000) that operates in wavelengths 70, 100, and 160 μm for imaging and 55−210 μm for spectroscopy. The SPIRE is also a photometer and low-to-medium resolution spectrometer (R = 20−1000) that operates in wavelengths 250, 350, and 500 μm for imaging and 194−671 μm for spectroscopy. Both PACS and SPIRE consist of bolometer arrays (2 for PACS and 5 for

SPIRE) that measure the radiation by detecting a small change in the temperature of the sensor caused by the absorption of the radiation from the source. In this work, imaging data between 70 to 250 μm has been used for studying the dust distribution and global properties, and also for identifying and characterizing the embedded stellar population.

To study the gas properties and kinematics of the cloud and clumps, this thesis utilised the molecular line data of CO (J = 1−0) isotopologues from the Purple Mountain Observatory (PMO). The PMO uses a 13.7-m single-dish radio telescope that operates in millimetre wavelength. It consists of a heterodyne receiver system, i.e. a 2SB 9-beam Superconducting Spectroscopic Array Receiver (SSAR) (Shan et al., 2012). A heterodyning is a technique of signal processing in which an incoming frequency signal is shifted to another desired frequency, called an intermediate frequency signal, by mixing it with a reference signal generated by a local oscillator. The SSAR system operates in the frequency range of 85−115 GHz and is capable of tracing molecular clouds by observing multiple lines simultaneously. In this work, the CO data has been used, which is taken as a part of the Milky Way Imaging Scroll Painting (MWISP; Su et al., 2019) survey.

To explore the magnetic field structure around the central clump/hub of G148.24+00.41, we have observed the central region of the cloud for dust emission polarization using the James Clerk Maxwell Telescope (JCMT). The JCMT is a single-dish 15-m radio telescope located near the summit of Mauna Kea, which operates in submillimeter wavelength[1]. It started its operations in 1987 and is now operated by the East Asian Observatory. Unlike optical and infrared telescopes, which collect photons, radio telescopes receive signals as fluctuating voltages at their centre feed horn, which varies at the same frequency as the electromagnetic radio signal from the target. That frequency signal is then transferred to the receiver system for signal processing. We observed the central region of G148.24+00.41 using the Submillimetre Common User Bolometer Array 2 (SCUBA-2), a 10,000-pixel bolometer camera that operates simultaneously at 450 and 850 μm (Holland et al., 2013). The camera has 8 arrays of Transition Edge Sensors (TES), 4 at each wavelength, and each array has $32 \times 40 = 1280$ bolometers, which means a total of 5120 bolometers at each wavelength. To trace the polarization signal, another instrument named POL-2 is used in front of SCUBA-2. The POL-2 is a linear polarimetry instrument module for SCUBA-2 that measures the linear polarization in terms of stokes vectors, I, Q, and U (Friberg et al., 2016). The POL-2 consists of a calibrator grid, a rotating half-wave plate (HWP), and an

[1] https://www.eaobservatory.org/jcmt/about-jcmt/

analyser grid.

To characterize the emerging young cluster in G148.24+00.41, the central clump/hub region of the cloud has also been observed in NIR photometric JHK_s bands using the 3.6-m Devasthal Optical Telescope (DOT). The DOT is located at the Devasthal Observatory, near Nainital, India, and operated by the Aryabhatta Research Institute of Observational Sciences (ARIES), India. It started its operation in 2016 - 2017. For this work, the observations have been taken with the TANSPEC (TIFR-ARIES Near Infrared Spectrometer; Sharma et al., 2022) instrument mounted on DOT, which has a 1024 × 1024 H1RG detector. The typical FWHM of TANSPEC's images is around 0.8 arcsec in NIR bands. The data obtained from the TANSPEC is deep up to K_s ~18.6 mag (signal-to-noise ratio = 5) for the cluster region.

The NIR data from the Spitzer Space Telescope was used for identifying the disk-bearing members of the cluster in G148.24+00.41. The *Spitzer* was launched in 2003 and carried an 85-centimetre infrared telescope to survey the sky in infrared wavelengths (3−180 μm). For this work, data in the 3.6 and 4.5 μm bands have been used, taken with the Infrared Array Camera (IRAC) as part of the Spitzer Warm Mission Exploration Science program. The spatial resolution of the *Spitzer* IRAC images is around 2 arcsec.

To study the properties of young embedded clusters selected for examining the scaling laws, we used NIR photometric data from UKIDSS. The UKIDSS is an astronomical survey conducted by the United Kingdom Infra-Red Telescope (UKIRT) with a Wide Field Camera (WFCAM). The UKIRT[2] is a 3.8-m infrared reflecting telescope located at Mauna Kea, Hawai'i. The WFCAM has 4 Rockwell Hawaii-II 2048 × 2048 HgCdTe detectors with a pixel scale of ~0.4″, and have broadband $ZYJHK$ filters and narrowband $H2$ and $Br\gamma$ filters (Casali et al., 2007). The UKIDSS Galactic Plane Survey (GPS), is mostly used in this work, which has a depth of $K \approx 18.1$ mag (Lawrence et al., 2007).

1.7 Thesis objective

1. To thoroughly characterize the G148.24+00.41 cloud in order to better understand the cluster formation mechanisms in molecular clouds. In particular, to shed light on the

[2] https://about.ifa.hawaii.edu/ukirt/about-us/

question of how an intermediate-to-massive bound cluster may emerge from a cloud. The broad aim is to explore the following points:

i. To estimate the G148.24+00.41 cloud properties, like mass, size, dense gas fraction, and density profile from dust continuum and dust extinction maps and compare them with those of nearby clouds.

ii. To investigate the spatial distribution and evolutionary stages of young protostars in the cloud, and their connection to the possible fragmentation and evolution of the cloud.

iii. To extract structures within the cloud, estimate their various gas properties, and investigate their role in mass assembly processes leading to the formation of dense clumps and subsequent stellar clusters.

iv. Investigate the relative role of different physical factors in the cluster formation process within dense regions of the cloud such as hub or clump. Also, calculate the energy budget, i.e. gravitational potential energy, magnetic energy, and total kinetic energy of the structures in the hub region, to understand their present dynamical status.

v. To characterize the young cluster, FSR 655, located in the hub of the cloud (i.e. its present-day properties like mass, age, extinction, SFR, and SFE) in order to understand its present evolutionary status and likely fate.

2. To explore the connection between SFR and gas mass at the clump scale using a sample of cluster-forming clumps. We employed a similar methodology and approach implemented for the young cluster of G148.24+00.41. Our broad aim with this statistical sample is to explore:

i. What are the SFRs and efficiencies at the clump scale, and do these parameters vary significantly as functions of gas mass or time scales, like free-fall time? And what are the implications of the measured SFR and SFE in the context of early cluster evolution.

ii. Whether the scaling relations obtained by earlier studies at the extragalactic and cloud scales are also followed at the clump scale.

Overall, this thesis aims to contribute to a better understanding of the cluster formation process and the effect of the initial conditions, cloud environment, and different physical factors on it.

1.8 Outline of the thesis

The thesis comprises seven chapters; the brief details of the chapters are given below.

Chapter 1: Introduction

This chapter provides a brief overview of star and star cluster formation and various physical factors involved and also presents the current understanding of the problems and the motivation behind the thesis. The chapter also provides an overview of ground and space-based telescopes and instruments whose data has been used in this thesis.

Chapter 2: Dust properties of G148.24+00.41 and its cluster formation potential

This chapter describes the detailed analysis of cloud properties using the dust emission and dust extinction data. A dust extinction map was made to determine the cloud parameters and compare them with those of nearby molecular clouds, including GMCs like Orion-A. Also, the point sources are used to investigate the clustering structure and to check the presence of mass segregation in the cloud. The chapter also discusses the results in the prospect of massive cluster formation models. The results of this chapter are published in the MNRAS journal (Rawat et al., 2023).

Chapter 3: Gas properties, kinematics, and cluster formation at the nexus of filamentary flows in G148.24+00.41

This chapter deals with the cloud parameters estimated from the CO (J = 1−0) isotopologues molecular line data. The integrated intensity maps, excitation temperature map, optical depth map, and column density maps were made to analyse various parameters. The molecular cube data has been used to investigate the overall gas motion and the role of filamentary flows in cluster formation in the G148.24+00.41 cloud. The chapter presents the extraction and analysis of filamentary structures and sub-structures within the cloud. Also, this chapter gives a detailed study of filamentary accretion flows, and the stability of filaments and clumps. The results of this chapter are published in the MNRAS journal (Rawat et al., 2024b).

Chapter 4: Magnetic fields around the hub region of G148.24+00.41

This chapter presents the analysis done over the central/hub region of G148.24+00.41 to study the magnetic field structure and its relative strength in comparison to gravity and turbulence, using dust emission polarization data from the JCMT. The results discussed here are published in the MNRAS journal (Rawat et al., 2024a).

Chapter 5: FSR 655: A young cluster formed at the heart of G148.24+00.41

This chapter presents the near-infrared study of the young cluster formed at the hub of G148.24+00.41. The chapter describes the methodology and provides a detailed study of cluster properties and their comparison with other nearby young clusters. This chapter forms a base for our statistical work on young clusters. The results of this chapter are accepted for publication in the AJ journal.

Chapter 6: Star formation scaling laws at the clump scale

This chapter presents the statistical analysis of 17 young cluster-forming clumps to first evaluate their individual properties using near and far infrared data sets and then analyse the relation between SFR and gas mass at a small, i.e. clump scale.

Chapter 7: Summary, conclusion, and future prospects

This chapter offers a thorough overview of the entire thesis, discussing the motivation, key results and their implications on a larger perspective. It highlights the key points from each chapter and connects them with the current understanding of the field. The chapter also discusses any caveats of the study and suggests the requirement of better sensitivity observations, improvements in the current work and areas of future research.

This page was intentionally left blank.

Chapter 2

Dust properties of G148.24+00.41 and its cluster formation potential

The general consensus is that giant molecular clouds convert ∼3−10% of their mass into stars before being dispersed (Evans et al., 2009; Lada et al., 2010). In this regard, massive bound clouds with mass $\geq 2 \times 10^5$ $M_\odot$ are the potential formation sites for massive stellar clusters of mass $> 10^4$ $M_\odot$, assuming the star-formation efficiency is as low as 5%. Studies of Galactic disk clouds, suggest that clouds with a relatively high dense gas fraction (i.e. fraction of gas with $n \geq 10^4$ cm^{-3}, or N(H_2) $\geq 6.7 \times 10^{21}$ cm^{-2} with respect to the total gas of the cloud; Lada et al., 2010) are the sites of richer star formation (Lada et al., 2012; Evans et al., 2014), while other studies suggest that the Galactic environment plays a significant role in defining the initial conditions of star-formation in molecular clouds (e.g. Galactic centre clouds, see review by Henshaw et al., 2023). The geometry and structure of molecular clouds also likely play a crucial role in the formation and growth of star clusters (e.g. Burkert & Hartmann, 2004; Heitsch et al., 2008; Pon et al., 2012; Clarke & Whitworth, 2015; Heigl et al., 2022; Hoemann et al., 2023). Therefore, to understand the formation of intermediate-to-massive clusters, studies of dust and gas properties of GMCs that are in the earliest stages of star formation are needed. In this chapter, we discuss the global dust properties of the chosen massive cloud, G148.24+00.41, discussed in Chapter 1.

Despite the presence of only 1% dust in the ISM, it plays a very crucial role in the formation of molecules in the ISM, and hence the molecular clouds. The interaction and coupling of gas and dust in dense molecular clouds enable the use of dust signatures as the indirect tracers of the total gas content of the clouds. Dust causes the extinction of starlight and also emits the absorbed light thermally at longer wavelengths, both of which can be used to study the dust properties of the cloud. Estimating the total mass reservoir of the cloud, as well as that within its various substructures, is a crucial factor that likely determines the total stellar mass that will emerge from the cloud. Most of the nearby GMCs are well characterized with either dust continuum (e.g. Gloud belt survey; André et al., 2010) or dust extinction (e.g. Lada et al., 2010) maps to understand their star and star cluster formation potential. This chapter is based on the characterization of the global dust properties and structure of G148.24+00.41 for the first time using mainly the dust continuum emission and dust extinction data. In addition, weexplored the spatial distribution and clustering structure of newly formed stars in the cloud using infrared point sources to discuss different cluster formation mechanisms.

2.1 Data used

The dust extinction of background stars causes the near-IR excess emission in the light of stars, which can be used to trace the H_2 column density. For this purpose, the near-IR (J, H, and K) photometric catalogues were used from the UKIDSS 10th data release (Lawrence et al., 2007). These catalogues are the data products of the UKIDSS GPS survey (Lucas et al., 2008), done using the observations taken with the UKIRT 3.8-m telescope. The UKIDSS GPS data has saturation limits at J = 13.25, H = 12.75 and K = 12.0 mag (Lucas et al., 2008). For sources brighter than these above limits, 2MASS photometry values were used. The GPS data are ~3 magnitudes deeper than 2MASS data, thus, would give a better assessment of extinction than those measured by Dobashi (2011).

The cold dust emission mostly comes at the far-infrared or submillimetre wavelengths. To trace the cold dust of G148.24+00.41, far-infrared images of Hi-GAL survey (Molinari et al., 2010), taken with the *Herschel* PACS and SPIRE instruments, were used. These images are centred on wavelengths of 70, 160, 250, 350, and 500 μm, with angular resolutions of 8.5, 13.5, 18.2, 24.9, and 36.3 arcsec, respectively (Molinari et al., 2010).

To calculate the distance to the cloud, ^{12}CO (J = 1−0) emission molecular data at 115 GHz was also used, which was observed with the 13.7-m radio telescope as a part of the MWISP survey (Su et al., 2019), as discussed in the previous chapter. The angular resolution of the CO data is ~50″ (or ~0.8 pc at the distance of 3.4 kpc; see Sect. 2.2.1 for distance), while its spectral resolution is ~0.16 km s^{-1}. The details of the CO data are discussed in the next chapter, where a detailed investigation of G148.24+00.41 has been done using CO (J = 1−0) isotopologue tracers. The typical sensitivity per spectral channel is about 0.5 K (for details, see Su et al., 2019). This data brings a factor of ∼10 improvement in the spatial resolution and a factor of 8 in the velocity resolution compared to the previous CO survey data (beam ~8.5′, velocity resolution ∼1.3 km s^{-1}; Dame et al., 2001) used by Miville-Deschênes et al. (2017) to identify the cloud.

2.2 Analyses and results

2.2.1 Distance, physical extent, and large-scale gas morphology of G148.24+00.41

Before one embarks on the properties of the cloud, it is essential to derive its distance, as the distance of the cloud is important to calculate its fundamental properties, such as mass, size, and density. Also, as discussed in section 1.6.1 of Chapter 1, the distance of the cloud is somewhat uncertain (3.2−4.5 kpc). Therefore, it is crucial to better constrain the distance of the G148.24+00.41 cloud. The Galactocentric radius and distance of the clouds can be determined using the Galaxy rotation curve and the radial velocity of gas clouds, which is known as the kinematic distance method. The gas clouds orbit around the galactic centre with some orbital velocity, and their radial velocity component can be estimated from the Doppler shift of the spectral lines. Using the Galaxy rotation curve, this radial velocity can be related to a unique Galactocentric radius and distance if the cloud is in the inner Galaxy region. If the cloud is in the outer Galaxy region, then there will be two distances, near and far, to the same radial velocity (Roman-Duval et al., 2009). In this case, it is required to resolve the distance ambiguity.

The Gaussian profile fit to the CO spectrum of G148.24+00.41 is shown in Figure 2.1. From the fit, the peak systemic velocity (radial velocity) of the cloud with respect to the local standard of rest (V_{LSR}), the 1D velocity dispersion (σ_{1d}), and the associated velocity range were found to be around −34.07 ± 0.02 km s^{-1}, 1.51 ± 0.02 km s^{-1}, and [−37, −30] km s^{-1}, respectively. The estimated line-width ($\Delta V = 2.35\,\sigma_{1d}$) and 3D velocity dispersion ($\sigma_{3d} = \sqrt{3} \times \sigma_{1d}$) associated with the CO profile is ~3.55 and 2.62 km s^{-1}, respectively. From Figure 2.1, it can be seen that the CO emission shows a flattened shape around the peak. However, such a flattened profile is not found in the ^{13}CO spectrum (velocity resolution ~0.14 km s^{-1}) of the source, observed by Urquhart et al. (2008). This suggests that probably due to the high optical depth, self-absorption occurs in the ^{12}CO line, resulting in the flattened top seen in the line profile.

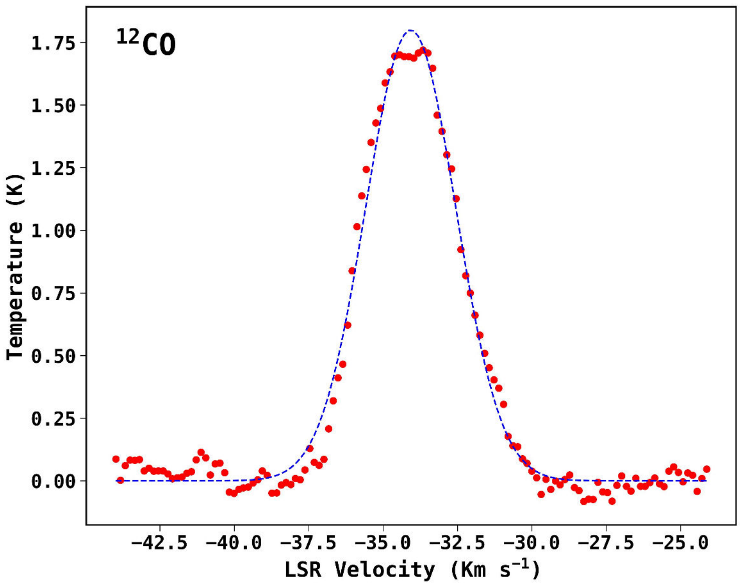

Figure 2.1: The average ^{12}CO spectral profile towards the direction of G148.24+00.41. The dashed blue line represents the fitted Gaussian profile.

After getting the V_{LSR} of the cloud, the distance was calculated using the Monte Carlo-based kinematic distance calculation code[1] (described in Wenger et al., 2018), V_{LSR} value as -34.07 ± 0.02 km s^{-1}, and considering the recent galactic rotation curve model of Reid et al. (2019). The simulation was run 500 times, resulting in a kinematic distance of approximately 3.4 ± 0.3 kpc, which is used in this work. In the case of G148.24+00.41, no near-far kinematic distance ambiguity is present, as the cloud is located in the outer galaxy.

Figure 2.2 shows the DSS2 R-band optical image of the G148.24+00.41 cloud along with

[1] https://github.com/tvwenger/kd

the contours of the ^{12}CO intensity emission, integrated in the velocity range −37 to −30 km s^{-1}.

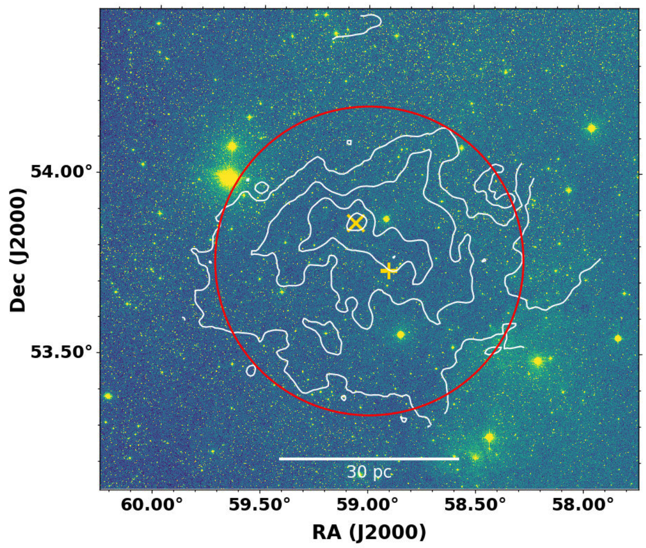

Figure 2.2: DSS2 R-band optical image of the G148.24+00.41 cloud for an area of ~1.9°× 1.3°overlaid with the contours of ^{12}CO (J = 1−0) emission, integrated in the velocity range −37 to −30 km s^{-1}. The contour levels are at 1.5, 10, 20, 30, and 40.0 K km s^{-1}. The red solid circle (centred at: α = 03:55:59.02 and δ = +53:45:48.03) shows the overall extent of the cloud of radius ~26 pc. The plus and cross sign represent the position of TGU 942P7 and IRAS 03523+5343, respectively.

As can be seen from Figure 2.2, the cloud in its central area shows a non-uniform and elongated intensity distribution of CO gas, but overall, it can be approximated to be a nearly circular structure of radius ~26 pc on the plane of the sky. The radius bordering the outer extent of the cloud is marked in the figure by a red circle. From Figure 2.2, it is evident that the cloud is devoid of optically visible star clusters. After inspecting the H_α survey images of the Northern Galactic Plane (Barentsen et al., 2014) and the 6 cm radio continuum images of the Red MSX Source (RMS) survey (Lumsden et al., 2013), it was found that there is no H II region yet formed in the cloud. The non-detection of such sources implies that the cloud is in its early phases of evolution, and strong stellar feedback is yet to commence in the cloud.

2.2.2 Global dust properties and comparison with nearby GMCs

Molecular clouds are characterized by a gas column density corresponding to visual extinction, $A_V \geq$ 1–2 magnitudes. For example, Lada et al. (2010), using near-infrared extinction maps, derived cloud masses of a number of nearby (< 500 pc) molecular clouds, including GMCs like Orion-A, Orion-B, and California, by integrating cloud area above K-band extinction, $A_K \geq$ 0.1 mag. Similarly, for several nearby molecular clouds (< 1 kpc), Heiderman et al. (2010) estimated cloud masses by integrating cloud area above visual extinction, $A_V > 2$ mag. The A_V = 2 magnitude corresponds to A_K ~0.2 mag using the relation, $A_K = 0.112 \times A_V$, from Rieke & Lebofsky (1985).

In nearby molecular clouds, it has been found that young stars that are formed above an extinction threshold of $A_K \geq 0.8$ mag (or equivalent column density $\geq 6.7 \times 10^{21}$ cm^{-2}) are well correlated with the corresponding gas mass (Lada et al., 2010; Heiderman et al., 2010). In fact, Lada et al. (2012) find that above this extinction threshold, a linear relationship between the star-formation rate and the column density is clearly apparent. Lada et al. (2010, 2012) advocated that since above $A_V > 6$ mag, dense gas tracer molecules such as HCN and N_2H^+ have been observed in molecular clouds, thus, a column density above $A_K > 0.8$ (or $A_V > 7$ mag) mag represents the dense gas content of the molecular clouds. Following the same convention, the dense gas properties of the G148.24+00.41 cloud were estimated using this threshold.

The total ($A_K > 0.2$ mag) and dense gas ($A_K > 0.8$ mag) properties of G148.24+00.41 were estimated in two ways: i) using the *Herschel* column density map, and ii) using the UKIDSS-based near-infrared extinction map. The latter is mainly used to compare the global properties of G148.24+00.41 with the properties of the nearby GMCs studied by Lada et al. (2010) and Heiderman et al. (2010).

2.2.2.1 Properties from dust continuum map

Marsh et al. (2017) constructed the dust temperature and molecular hydrogen column density maps of the inner Galaxy using *Herschel* data, collected as a part of the Hi-GAL Survey (Molinari et al., 2010). They constructed maps using the PPMAP technique (see Marsh et al., 2015, for details), resulting in high-resolution (~12″) dust temperature and column density maps. PPMAP technique considers the point spread functions of the telescopes that enable the use of images at their native resolution, and also drops the assumption of uniform dust temperature along the line of sight. Thus, the PPMAP data represents a significant improvement over those obtained with a more conventional spectral energy distribution (SED) fitting technique, in which a pixel-to-pixel modified black-body fit to the *Herschel* images is done after convolving them to the resolution of the 500 μm band. While fitting, the dust temperature is assumed to be uniform everywhere along the line of sight and the dust opacity index is often assumed as 2 (e.g. Battersby et al., 2011; Deharveng et al., 2012; Könyves et al., 2015; Schisano et al., 2020). Owing to better resolution as well as its ability to account for the line-of-sight temperature variation, PPMAP data have been used in the analysis of several molecular clouds (e.g. Marsh & Whitworth, 2019; Spilker et al., 2021).

Figure 2.3a shows the *Herschel* column density map overlaid with the contours of CO emission. As can be seen, the morphology of the column density map correlates well with the overall CO emission, particularly in the central area. Owing to high resolution, the column density map in the central area of the cloud shows more clumpy and filamentary structures. Figure 2.4 shows the N(H_2) versus T_d distribution within the cloud boundary, showing that they are inversely correlated as seen in infrared dark clouds (e.g. Battersby et al., 2011). Within the cloud boundary, wefind that the column density lies in the range 2.0–40.0 × 10^{21} cm^{-2} with a median value of ~3.2 × 10^{21} cm^{-2}, while the dust temperature lies in the range 12.7–21.3 K, with a median value of ~14.5 K.

The global properties of the cloud were estimated by considering all the pixels within the cloud area whose N(H_2) value is greater than 20×10^{20} cm^{-2}. Using the empirical relation, A_V = N(H_2)/9.4× 10^{20} mag, from Bohlin et al. (1978) and the extinction law, $A_K = 0.112 \times A_V$, from Rieke & Lebofsky (1985), A_K can be related to N(H_2) by $A_K = N(H_2) \times 1.2 \times 10^{-22}$ mag. Using this relation, it is found that the opted N(H_2) threshold corresponds to $A_K \approx 0.2$ mag, similar to the value chosen for nearby GMCs for estimating cloud mass. Using the following relation, the integrated column density ($\Sigma N(H_2)$) is converted to mass (M_c):

$$M_c = \mu_{H_2} m_H A_{pixel} \Sigma N(H_2) \quad (2.1)$$

where m_H is the mass of hydrogen, A_{pixel} is the area of the pixel in cm^2, and μ_{H_2} is the mean

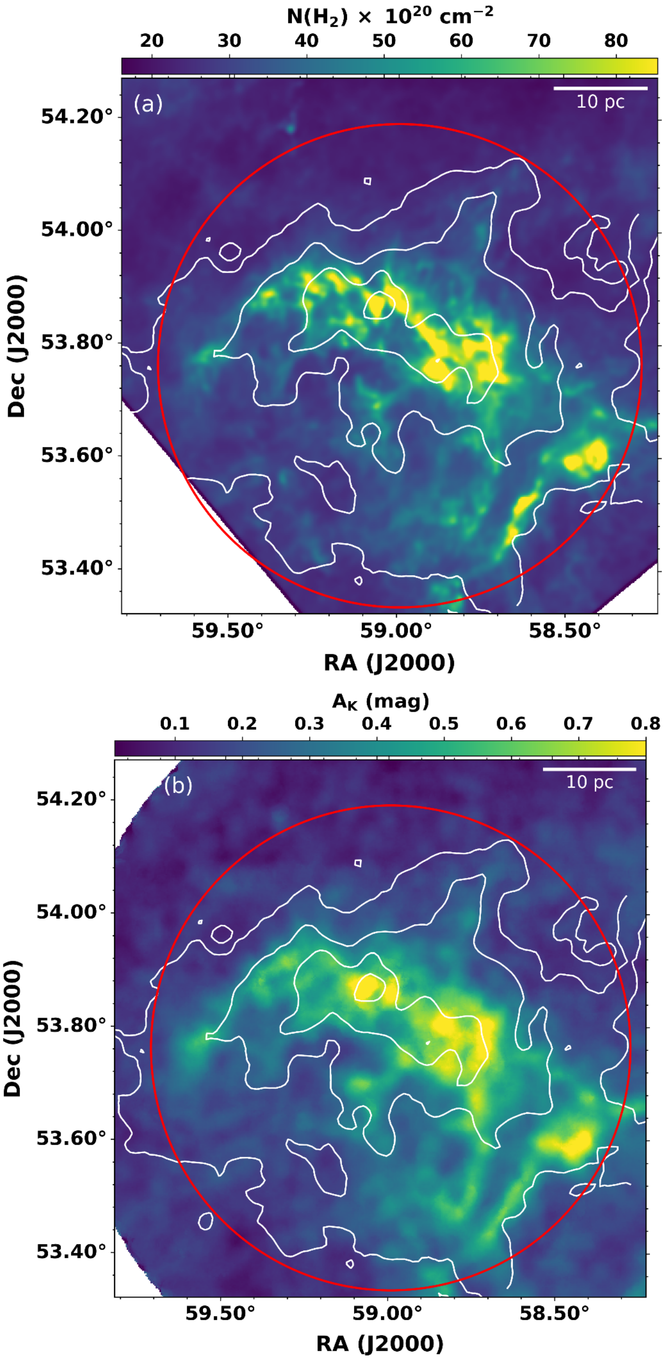

Figure 2.3: (a) *Herschel* column density map (resolution ∼ 12′′) and (b) K-band extinction map (resolution ∼ 24′′), over which the contours of CO integrated emission are shown. The contour levels are the same as in Figure 2.2. The solid red circle denotes the boundary of the cloud.

molecular weight that is assumed to be 2.8 (Kauffmann et al., 2008). Before integrating, a mean background $N(H_2)$ value of 13×10^{20} cm^{-2} was also subtracted from each pixel. This is done to correct for the contribution from the diffuse material along the line of sight. The mean background level was estimated from a relatively dust-free region near the cloud.

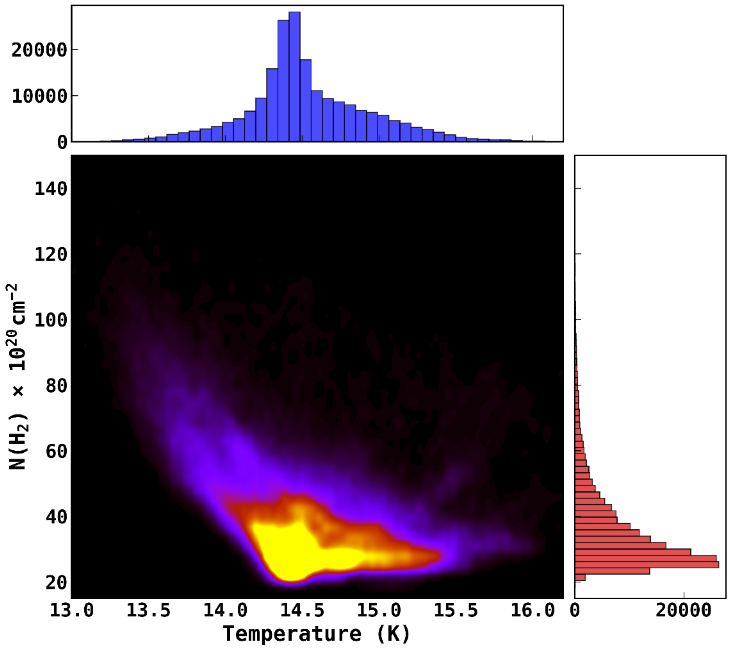

Figure 2.4: Column density versus temperature diagram, showing the distribution of physical conditions of dust in G148.24+00.41.

It is to be noted that though the PPMAP provides a better resolution, the output of the PPMAP technique can vary depending upon the variation in input parameters like opacity index and temperature bin resolution (e.g. PPMAP algorithm considers 12 temperature bins, equally spaced between 8 K and 50 K), which may give rise to uncertainty in column density and the estimated mass. Marsh et al. (2017) show that the global properties of a Hi-GAL field (i.e. a 2°.4 × 2°.4 tile of the Hi-GAL survey that hosts a molecular cloud M16) are not strongly affected due to variations in the input parameters. For example, the variation in mass is up to 20%, and temperature is around ± 1 K, for using β in the range 2.0–1.5 and temperature bins from 12 to 8 K. To check the effects of the PPMAP assumptions on the global properties of G148.24+00.41, wecompared the maps of the PPMAP made by Marsh et al. (2017) with the maps of the Schisano et al. (2020), made with the conventional method as described above. For Galactic plane clouds like G148.24+00.41, both the authors have used the images of the Hi-GAL survey, with the same opacity index (β = 2) and gas-to-dust ratio (R =100). We found that the properties of G148.24+00.41 largely remain the same, i.e. the difference in total mass is ~15%, and in mean temperature is ~2%. Although both methods give similar values of total mass, the true uncertainty of mass can be high, as it depends on the number of properties such as dust opacity, gas-to-dust ratio, dust temperature, and distance.

In the present case, the dust temperature is unlikely the major cause of uncertainty for G148.24+00.41, but assuming an uncertainty of 30% in dust opacity index and 23% in the gas-to-dust ratio (see Sanhueza et al., 2017, and discussion therein) and using a distance uncertainty of ~9%, the likely total uncertainty in our mass estimation is found to be around ~45%[2], although it is prone to large systematic error due to variations in the CO abundance and poorly constrained dust properties. It is to be noted that the estimated mass will increase by a factor of 2.6 if the gas-to-dust ratio value from the prediction of Giannetti et al. (2017) for G148.24+00.41's galactic location is to be considered.

Assuming circular geometry, we calculated the effective radius as r_{eff} = (Area / π)$^{0.5}$, the mean hydrogen volume density as n_{H_2} = 3M_c / $4\pi r^3_{eff}\mu_{H_2}m_H$, and the mean surface density as Σ_{gas} = M_c / πr^2_{eff} of the cloud. The total M_c, r_{eff}, the mean n_{H_2}, and the mean Σ_{gas} for the cloud are found to be (1.1 ± 0.5) × 10^5 $M_\odot$, 26 pc, 22 ± 11 cm^{-3}, and 52 ± 25 $M_\odot$ pc^{-2}, respectively. We find that these properties are consistent with those found in the Milky Way GMCs (Σ_{gas} = 50 $M_\odot$ pc^{-2}, Mass ≥ 10^{5-6} $M_\odot$; Lada & Dame, 2020).

As discussed earlier, we also estimated the dense gas properties of G148.24+00.41 by integrating cloud area above A_K ≥ 0.8 mag. Doing so, we find the total M_c, the r_{eff}, the mean n_{H_2}, and the mean Σ_{gas} to be (2.0 ± 0.9) × 10^4 $M_\odot$, 6 pc, (3.21 ± 1.65) × 10^2 cm^{-3}, and (1.77 ± 0.85) × 10^2 $M_\odot$ pc^{-2}, respectively. These results are also summarised in Table 2.1. It is important to note that without background subtraction, the total mass and dense gas mass are 1.6 and 1.2 times higher than the mass measured with background subtraction. However, in the present work, we have used the measurements estimated with the background subtraction.

2.2.2.2 Properties from near-infrared extinction map

One way to characterize the global properties of a star-forming cloud is to use its extinction map. The advantage of using an extinction map in estimating column density is that it only depends on the extinction properties of the intervening dust, therefore providing an independent measure of cloud properties that can be compared with those obtained from dust continuum measurements. However, the limitation is that in the zone of high column densities where the optical depth in the infrared becomes too high to see background stars, it underestimates the column density values.

[2] It is worth noting that recent evidence shows that the gas-to-dust ratio varies with the Galactocentric radius (Giannetti et al., 2017)

Table 2.1: G148.24+00.41 properties from dust continuum and dust extinction maps.

	Dust continuum map		**Extinction map**		
Parameter	Whole Cloud	Dense Gas	Whole Cloud	Dense Gas	Unit
Mass	$(1.1 \pm 0.5) \times 10^5$	$(2.0 \pm 0.9) \times 10^4$	$(9.1 \pm 2.4) \times 10^4$	$(3.0 \pm 0.8) \times 10^3$	$M_\odot$
Effective Radius	26	6	24	2.4	pc
Average Volume density	22 ± 11	$(3.21 \pm 1.65) \times 10^2$	23 ± 8	$(7.52 \pm 2.75) \times 10^2$	cm^{-3}
Average Surface density	52 ± 25	$(1.77 \pm 0.85) \times 10^2$	50 ± 16	$(1.66 \pm 0.52) \times 10^2$	$M_\odot\ pc^{-2}$

We generate a K-band extinction map using the *UKDISS* point source catalogue, discussed in Section 2.1 and implementing the PNICER algorithm discussed in Meingast et al. (2017). The PNICER algorithm derives an intrinsic feature distribution along the extinction vector using a relatively extinction-free control field. It fits the control field data with Gaussian mixture models (GMMs) to generate the probability density functions that denote intrinsic features, like intrinsic colours. The advantage of PNICER is that it uses all possible combinations of the NIR bands, such that the sources which do not have data in all wavelength bands will not affect the results. The PNICER creates PDFs for all combinations and automatically chooses the optimal extinction measurements for the target field (for details, see Meingast et al., 2017). In the present case, for creating an extinction map of the G148.24+00.41 cloud, we choose a dust-free area close to the cloud area as our control field (i.e. the same area used for finding mean background column density).

Figure 2.3b shows the obtained K-band extinction map along with the CO contours. As can be seen, morphologically, the extinction map correlates well with the overall structure of the CO emission, as well as with the *Herschel* column density map. We find that within the cloud area defined by the CO boundary, the dynamic range of our K-band extinction is in the range of 0.15 to 1.0 mag, with a median of 0.24 mag. The sensitivity limit of the extinction map is close to the sensitivity limit (i.e. $A_{\rm K}$ ~0.2 mag) of the *Herschel* column density map.

Considering that the different approaches and tracers are used to make both maps, the observed small difference at the cloud boundary is quite reasonable. However, it is worth stressing that, unlike the *Herschel* map, the extinction map in this work is insensitive to high column density zones of the cloud, which is the major source of uncertainty in estimating cloud properties, particularly the properties of the dense gas content. In addition, the global properties of the cloud are also affected by systematic error in the adopted extinction law and distance. Here, the gas-to-dust ratio, $\frac{N(\mathrm{H_2})}{A_{\rm V}} = 9.4\times 10^{20}\ \mathrm{cm^{-2}\ mag^{-1}}$, has been taken based on a total-to-selective extinction, $R_V = 3.1$ typical for the diffuse interstellar medium (Bohlin et al., 1978). However, the R_V value can reach up to ~5.5 (Chapman et al., 2009) in molecular clouds, for which the gas-to-dust ratio would change by ~20% (Cambrésy, 1999). For the G148.24+00.41 cloud, due to the combined uncertainties (i.e. due to extinction law and distance), the uncertainty in mass is around ~27%. This may be considered as lower-limit to the true uncertainty for clouds like G148.24 + 00.41 having a high dense gas fraction (discussed in Sect. 2.2.2.3). Nonetheless, taking the estimated uncertainty as face value, we estimated the total M_c, r_{eff}, mean n_{H_2}, and mean Σ_{gas} for the G148.24+00.41 cloud as (9.1 ± 2.4) × 10^4 $M_\odot$, 24 pc, 23 ± 8 cm^{-3}, and 50 ± 16 $M_\odot$ pc^{-2}, respectively. And for dense gas ($A_K \geq 0.8$ mag), the total M_c, r_{eff}, mean n_{H_2}, and mean Σ_{gas} is (3.0 ± 0.8) × 10^3 $M_\odot$, 2.4 pc, (7.52 ± 2.75) × 10^2 cm^{-3}, and (1.66 ± 0.52) × 10^2 $M_\odot$ pc^{-2}, respectively. All these measurements are also tabulated in Table 2.1. As can be seen from the table, the obtained dense gas properties are found to be lower than the values obtained from the column density map, which could be due to the fact that the inner area of the extinction map is not sensitive to the high column density.

It is to be noted that, in general, it has been found that the global properties of the cloud measured from dust and extinction maps differ within a factor of 2–3 as both the techniques involved different sets of assumptions (e.g. Lombardi et al., 2013, 2014; Zari et al., 2016), all of which are difficult to evaluate independently. Regardless of the different limitations of both methods, in the present case, the global properties of the whole cloud measured from both methods are in close agreement with each other. This ensures the fact that the studied cloud is indeed a GMC of mass nearly 10^5 $M_\odot$ enclosed in a radius of ~26 pc.

2.2.2.3 Enclosed mass and dense gas fraction

Figure 2.5 shows the enclosed mass of the G148.24+00.41 cloud obtained from the *Herschel* column density map at different column density thresholds (shown by a solid blue line), and for comparison purposes, the cloud masses of the nearby GMCs as measured by Lada et al. (2010) and Heiderman et al. (2010) at different column density thresholds are also shown. The typical uncertainties associated with the masses of these nearby clouds lie in the range of 20% to 60% (e.g. Heiderman et al., 2010). As can be seen, the total mass of the G148.24+00.41 cloud is comparable to the mass of the GMCs like Orion-A, Orion-B, and California and lies well above the mass of the other nearby molecular clouds. In Figure 2.5, the G148.24+00.41 cloud's mass measured using the extinction map at different thresholds (shown by a solid red line) is also shown. As can be seen from the extinction measurements also, the obtained total mass of G148.24+00.41 is comparable to the nearby GMCs. However, at the high-extinction threshold (e.g., $A_K \geq 0.8$ mag), our measurements fall well below the mass of Orion-A and Orion-B. This is because, unlike nearby GMCs, our extinction map is not sensitive to the high column density zone of the G148.24+00.41 cloud. It is worth noting that the extinction maps used to measure the

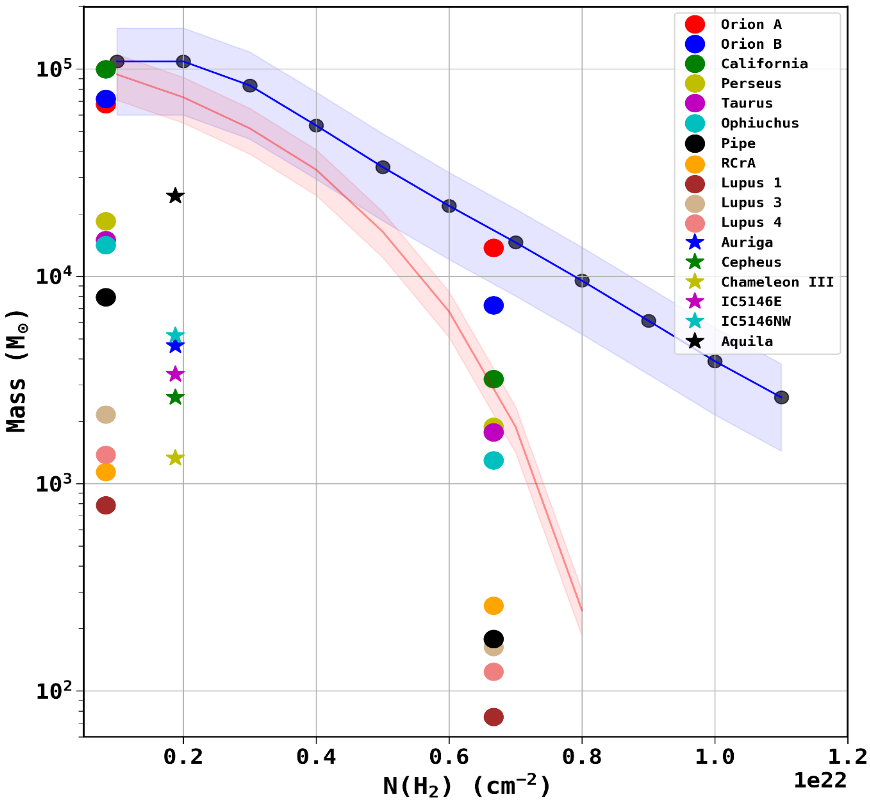

Figure 2.5: Enclosed mass of G148.24+00.41 at various column density thresholds. The blue and red lines show the cloud mass evaluated from the dust continuum and extinction map, respectively, at different column density thresholds. The shaded regions show the error in the estimated cloud mass. The coloured dots and stars show the mass of the nearby MCs taken from Lada et al. (2010) and Heiderman et al. (2010), respectively. Only for putting *Herschel* and extinction based measurements at the same level, in this plot, the blue curve has been extended down to $N(H_2) \sim 0.1 \times 10^{22}$ cm^{-2}, however, since the *Herschel* column density map is not sensitive to column density less than $\sim 0.2 \times 10^{22}$ cm^{-2}, the cloud mass remains flat.

properties of the nearby GMCs are sensitive up to A_K ~5 mag (e.g. see Figure 1 of Lada et al., 2010), while our map is sensitive up to A_K ~1.0 mag. In general, the highest extinction that can be probed with the extinction map is sensitive to the distance of the cloud and the surface density of field stars in its direction.

As mentioned in Sect. 2.2.2 for nearby clouds, a correlation exists between the gas mass measured above the extinction threshold of $A_K > 0.8$ mag and the number of embedded YSOs identified in the infrared (Lada et al., 2010). Similar visual extinction thresholds in the range 7–8 mags are also obtained by Heiderman et al. (2010); Evans et al. (2014) and André et al. (2014)

while analysing nearby GMCs using extinction maps and dust column density maps, respectively. In particular, Lada et al. (2012) found a strong linear scaling relation between star-formation-rate and dense gas fraction (i.e. $f_{\mathrm{den}}=\frac{Mass(A_{\mathrm{K}}>0.8\,mag)}{Mass(A_{\mathrm{K}}>0.1\,mag)}$). Therefore, the characterization of dense gas fraction is an important parameter for understanding the net outcome of star-formation processes, although it may not hold true for environments such as the Galactic centre, where the critical density threshold for star formation is likely elevated due to the more extreme environmental conditions (Henshaw et al., 2023).

From dust analysis of G148.24+00.41, it is found that the gas mass lies above $A_{\mathrm{K}} \geq 0.8$ mag is ~2.0×10^4 $M_\odot$, while the total mass is ~1.1×10^5 $M_\odot$, resulting f_{den} as 18%. Figure 2.6 shows the comparison of dense gas fraction between G148.24+00.41 and the clouds studied by Lada et al. (2010). For nearby GMCs, these authors found the mean value of f_{den} as 0.10 ± 0.06 with a maximum around ≈ 0.20. As can be seen from Figure 2.6, compared to nearby clouds, the f_{den} of G148.24+00.41 is on the higher side and comparable to that of the Orion-A, whose dense gas content is ~1.4×10^4 $M_\odot$ (Lada et al., 2010). Lada et al. (2010) measured the total mass of Orion-A around ~7×10^4 $M_\odot$ within an area of effective radius ~27 pc. In terms of total mass, effective area, and dense gas mass, G148.24+00.41 resembles Orion-A. The above analyses suggest that, like Orion-A, in G148.24+00.41, a significant fraction of mass is still in the form of dense gas.

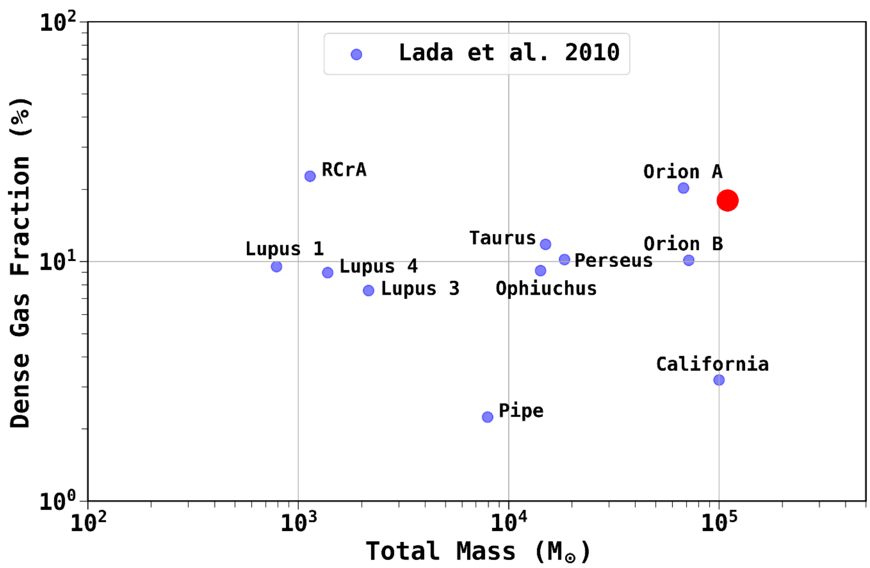

Figure 2.6: Comparison of dense gas fraction of G148.24+00.41 with the nearby MCs given in Lada et al. (2010). The location of G148.24+00.41 is shown by a red circle.

The caveat of this comparison is that it is drawn by comparing measurements between the extinction map and the column density map. However, as discussed above, the extinction maps of nearby clouds are sensitive up to $A_{\rm K}$ ~5 mag, so it seems that the high dense gas fraction that is observed in G148.24+00.41 may hold true (or may not deviate significantly), if a more sensitive extinction map like nearby GMCs were available or if the comparison is made with the *Herschel* based measurements of nearby GMCs. To validate the later hypothesis, we measured the dense gas mass of Orion-A using the available *Herschel* column density map of the Herschel Gould Belt Survey (André et al., 2010), which is limited to the central area of the Orion-A cloud. Doing so, we find the total mass of Orion-A to be $\sim 3\times10^4$ M$_\odot$, while the total dense gas is $\sim 9\times10^3$ M$_\odot$. The area covered by the *Herschel* observations of Orion-A is less by a factor of two compared to the area covered by the extinction map used by (Lada et al., 2010), thus, the estimated total mass from *Herschel* is expected to be lower. However, we find that the dense gas mass obtained for Orion-A using both the aforementioned maps is largely the same. This is because the extinction map of Orion-A covers the entire dense gas area of the *Herschel* map.

2.2.2.4 Structure and density profile

The well-known scaling law, between the cloud size and mass, $M_c = \Sigma_{A_0}\pi R^2$ was first documented by Larson (1981). Heyer et al. (2009) using ^{13}CO observations (beam size ~45″ and spectral resolution ~0.2 km s^{-1}), estimated Σ_{A_0} (mass surface density) value to be ~42 ± 37 M$_\odot$ pc^{-2} for larger and distant GMCs. Lombardi et al. (2010) from their analysis of nearby clouds using extinction maps argued that Σ_{A_0} depends on the parameter A_0, the extinction, defining the outer boundary of the cloud and found that Σ_{A_0} value increases as the extinction threshold increases. They also suggested that all clouds follow a Larson-type relationship and, therefore, very similar projected mass densities at each extinction threshold. However, they find that the mass-radius relation for single clouds does not hold in their sample, indicating that individual clouds are not objects that can be described by constant column density.

In Figure 2.7a, the mass-size relation of G148.24+00.41 measured from the dust column density map is compared with the data of the nearby clouds studied by Lada et al. (2010). The dotted lines show the least square fit of the form $M_c = \Sigma_{A_0}\pi R^\gamma$ with $\gamma \sim 2$ to the measurements of the nearby clouds (Lada et al., 2010; Krumholz et al., 2012) at $A_{\rm K} \geq 0.1$ mag and $A_{\rm K} \geq 0.8$ mag. By doing so, we estimated the Σ_{A_0} value to be 29.1 ± 0.1 M$_\odot$ pc^{-2} and 232.1 ± 0.1 M$_\odot$ pc^{-2} for

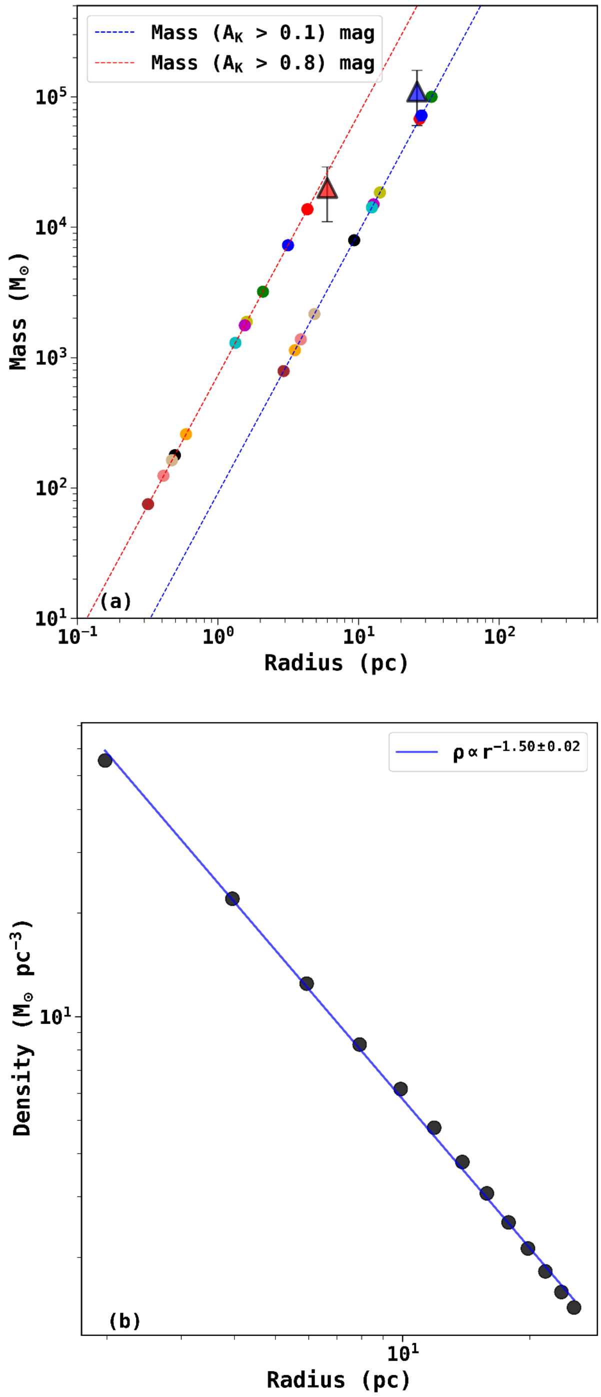

Figure 2.7: (a) Cloud mass of the nearby molecular clouds estimated above extinction thresholds of $A_{\rm K}$ = 0.1 mag and $A_{\rm K}$ = 0.8 mag as a function of their radius. The color codes for the MCs are the same as shown in Figure 2.5, The blue and red dotted lines show the best-fitted mass-radius relation of the form, $M_c = \Sigma_{A_0} \pi R^2$, to the data for $A_{\rm K}$ = 0.1 mag and $A_{\rm K}$ = 0.8 mag, respectively. The location of G148.24+00.41 is represented by triangles with error bars. (b) Density profile of G148.24+00.41 (shown by dots) along with the best-fitted power-law profile (shown by solid line) of index $\sim -1.50 \pm 0.02$.

mass measured above $A_\mathrm{K} \geq 0.1$ mag and $A_\mathrm{K} \geq 0.8$ mag, respectively. Despite different methods being used for mass measurements, as can be seen from Figure 2.7a, the G148.24+00.41 cloud (shown by large triangles) closely follows the mass-size relation of the nearby clouds for different thresholds. For G148.24+00.41, the slightly high Σ_{A_0} corresponding to scaling-law $A_\mathrm{K} \geq 0.1$ mag could be due to the fact that its mass has been measured at a higher extinction threshold. i.e. at $A_\mathrm{K} \geq 0.2$ mag, as our *Herschel* column density map is not sensitive below $A_\mathrm{K} = 0.2$ mag. This figure also shows that the dense gas and total mass of G148.24+00.41 are higher than the ones for the nearby GMCs.

The density profile of a single cloud is also important for theoretical considerations of star formation. For example, it has been suggested that a density profile of the form, $\rho(\mathrm{r}) \propto \mathrm{r}^{-1.5}$, is indicative of a self-gravitating spherical cloud supported by turbulence (e.g. Murray & Chang, 2015), while a profile of the form, $\rho(\mathrm{r}) \propto \mathrm{r}^{-2}$, is indicative of a gravity dominated system (e.g. Donkov & Stefanov, 2018; Li, 2018; Chen et al., 2021). Figure 2.7b shows the density profile of the G148.24+00.41 cloud along with the best-fitted power-law profile (blue solid line). It is found that $\rho(\mathrm{r}) \propto \mathrm{r}^{-1.5}$ best fits the overall large-scale structure of the cloud. It is important to note that this is the overall density profile of the cloud, but individual dense pockets of gas or clumpy structures can have a steeper density profile. As G148.24+00.41 is located at 3.4 kpc, unveiling the profile of such structures would require high-resolution observations. However, it is worth mentioning that steeper density profiles with an average power-law index between −1.8 to −2 have been observed in massive star-forming clumps (e.g. Garay et al., 2007).

2.2.2.5 Boundness status of G148.24+00.41

A large reservoir of bound gas is key for making massive clusters because theories and simulations often invoke gas inflow from large scale (e.g. Gómez & Vázquez-Semadeni, 2014; Padoan et al., 2020). However, it is suggested that on relatively short time-scales (typically a few Myr) since its formation, GMCs can be unbound as colliding flows and stellar feedback regulate the internal velocity dispersion of the gas and so prevent global gravitational forces from becoming dominant (Dobbs et al., 2011). So relatively older clouds can be unbound, although it is also suggested that large-scale unbound clouds can also have bound substructures where star cluster formation can take place (Clark & Bonnell, 2004; Clark et al., 2005).

Whether a cloud is bound or not is usually addressed by calculating the virial parameter,

$\alpha = \frac{M_{vir}}{M_c}$, which compares the virial mass to the actual mass of the cloud (Bertoldi & McKee, 1992). A cloud is bound if $\alpha_{vir} < 2$ and unbound if $\alpha_{vir} > 2$ (Mao et al., 2020). It is in gravitational equilibrium if its actual mass and virial mass are equal. The virial mass of G148.24+00.41 is estimated by assuming it to be a spherical cloud with a density profile, $\rho \propto r^{-\beta}$, and using the equation from MacLaren et al. (1988) in the following rewritten form:

$$M_{\rm vir}(M_\odot) = 126\left(\frac{5-2\beta}{3-\beta}\right)\left(\frac{R}{\rm pc}\right)\left(\frac{\Delta \rm V}{\rm km\ s^{-1}}\right)^2, \tag{2.2}$$

where R is the radius of the cloud and ΔV is the line-width of the gas. Here, β is adopted as 1.50 ± 0.02 and ΔV as 3.55 ± 0.05 km s^{-1}(see Section 2.2.1), with the assumption that ΔV describes the average line width of the whole cloud, including the central region. The derived virial mass turns out to be $\sim (5.50 \pm 0.16) \times 10^4$ M$_\odot$, while the estimated dust mass is $\sim (1.1 \pm 0.5) \times 10^5$ M$_\odot$ (see Section 2.2.2.1), resulting $\alpha \simeq 0.5 \pm 0.2$, and hence the whole cloud is likely bound. This remains true even if we use the lower mass obtained from extinction analysis.

2.2.3 Protostellar content and inference from their distribution

2.2.3.1 *Herschel* point sources and their evolutionary status

The *Herschel* satellite offers a unique opportunity to study the earliest phases of stellar sources. In particular, *Herschel* 70 μm band is very important for identifying deeply embedded class 0/I objects because it has been found that 70 μm is less sensitive to circumstellar extinction and geometry of the disc that significantly affects the 3.6–24 μm band. 70 μm is also less affected by external heating that becomes effective above 100 μm (Dunham et al., 2006).

Figure 2.8a shows the *Herschel* 70 μm image of the G148.24+00.41 cloud. As can be seen, the image displays a significant number of sources distributed roughly in a linear sequence from north-east to south-west, and most of the sources seem to be embedded in high column density material of N(H_2) $> 5.0 \times 10^{21}$ cm^{-2}. Since such high column density regions of a molecular cloud are the sites of recent star formation (e.g. André et al., 2010), these sources are possibly young protostars of the G148.24+00.41 cloud at their early evolutionary stages.

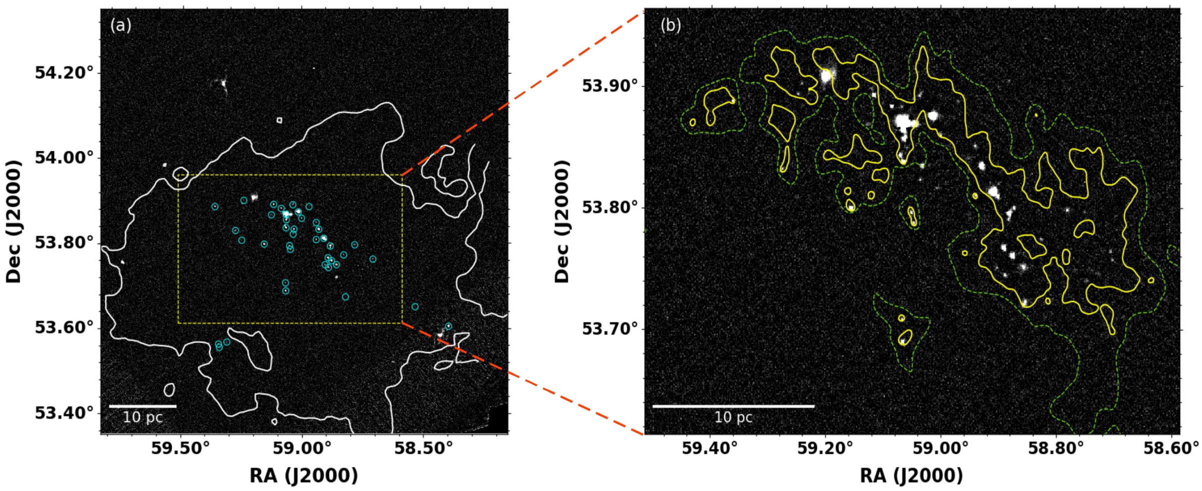

Figure 2.8: (a) Unsharp-masked 70 μm *Herschel* image of G148.24+00.41 over which 70 μm point sources are highlighted in cyan circles. The white contour shows the outermost contours of CO-integrated emission. (b) A zoomed-in view of the central area of the cloud. The green dotted and yellow solid contour corresponds to the column density value of 5.0×10^{21} cm^{-2} ($A_{\rm V}$ ~5 mag) and 6.7×10^{21} cm^{-2} ($A_{\rm V}$ ~7 mag), respectively, enclosing the distribution of most of the 70 μm point sources.

To understand the nature of the sources, the *Herschel* 70 μm point source catalogue (Marton et al., 2017; Herschel Point Source Catalogue Working Group et al., 2020) was downloaded from Vizier (Ochsenbein et al., 2000). In total, 48 point sources were retrieved within the cloud radius having SNR > 3.0. As noted by Herschel Point Source Catalogue Working Group et al. (2020), the detection limit of the *Herschel* point source catalogue is a complex function of the source flux, photometric band, and background complexity. Thus, the reliability of the downloaded point sources was checked by visually inspecting their positions and intensities on the 70 μm image. Doing so, it is found that some sources are too faint to be considered as point sources, and also a few likely bright sources (which appear to be extended on the image) are missing in the catalogue. The former could be the artefact due to the non-uniform background level usually found in *Herschel* images, while the latter could be due to the fact that these sources failed to pass the point source quality flags such as confusion and blending flags, implemented in Herschel Point Source Catalogue Working Group et al. (2020) to be called a point source. To check the reliability of the faint sources, I create different unsharp-masked images by subtracting median-filtered images of different windows from the original one (e.g. Deharveng et al., 2015). Unsharp-masked images are useful to detect faint sources or faint structures that are hidden inside bright backgrounds. We again over-plotted the point sources and found that a few sources are likely false detections, thus, did not use them in this work. After removing likely spurious sources, the total number of point sources is 40, with the faintest being a source of ~96 mJy. In Figure 2.8a, these point sources are marked in cyan circles.

In order to assess the evolutionary status of the point sources, their locations in the 70 μm flux density versus 160 μm to 70 μm flux density ratio diagram were compared with that of the well-known protostars of the Orion complex, shown in Figure 2.9. The Orion protostar sample is taken from the *Herschel* Orion Protostar Survey (HOPS; Furlan et al., 2016). It consists of 330 sources that have 70 μm detection, 319 of which have been classified as class 0, class I, or flat-spectrum protostars based on their mid-IR spectral indices and bolometric temperatures, while 11 sources have been classified as class II objects. As can be seen from Figure 2.9, most

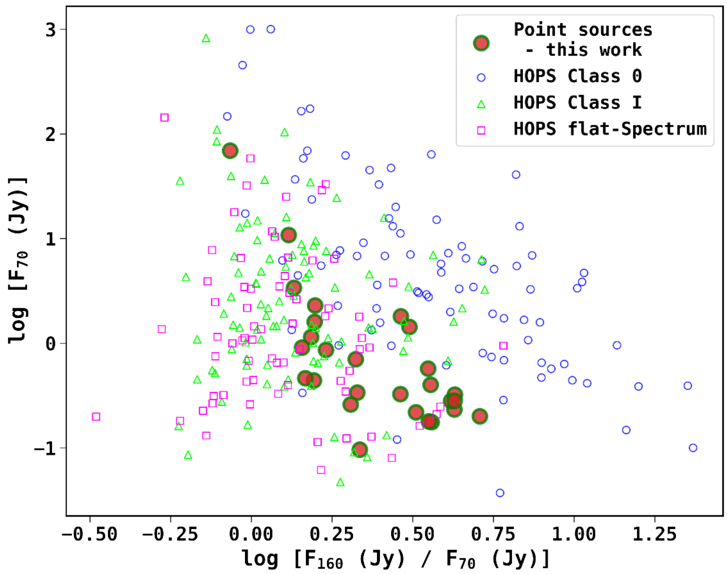

Figure 2.9: Plot of 70 μm flux density against 160 μm to 70 μm flux density ratio for protostars (shown by red solid circles) of the G148.24+00.41 cloud. In the plot, the open circles, triangles, and squares are the class 0, class I, and flat-spectrum sources, respectively, from the *Herschel* Orion Protostar Survey.

of the point sources (red dots) have 160 μm to 70 μm flux density ratio $\geq$ 1.0 like the HOPS protostars. The only source that shows a relatively smaller ratio with respect to the rest of the sources is the most luminous 70 μm source. This source is the most massive YSO in our sample (more discussion in Section 2.2.3.3 and 2.2.3.4). To assess the degree of contamination that might be present in the protostar sample in the form of extragalactic sources or other dusty objects along the line of sight, a similar analysis was done for the point sources present in the control field region. None of the control field sources were found to be located in the zones of the HOPS protostars, implying that contamination is negligible and the majority of the identified 70 μm point sources in G148.24+00.41 are likely true protostars. The identification of these protostars suggests that the central area of the cloud is actively forming protostars compared to the rest of the cloud.

2.2.3.2 Fractal nature of the cloud

For clouds and clumps at their early stage of evolution, the distribution of cores or young protostars carries the imprint of the original gas distribution. We examined the structure of the G148.24+00.41 cloud using *Herschel* identified protostars and implementing the statistical Q-Parameter method (Cartwright & Whitworth, 2004), which is based on the minimum spanning tree (MST) technique. An MST is defined as a unique network of straight lines that can connect a set of points without closed loops, such that the sum of all the lengths of these lines (or edges) is the lowest. The Q-Parameter method has been extensively studied in the literature for understanding the clustering (large-scale radial density gradient or small-scale fractal) structure of the star-forming regions and molecular clouds (e.g. Schmeja & Klessen, 2006; Parker et al., 2014; Sanhueza et al., 2019; Dib & Henning, 2019; Sadaghiani et al., 2020). Q is expressed by the following equation:

$$Q = \frac{\bar{l}_{edge}}{\bar{s}}, \tag{2.3}$$

where the parameter $\bar{l}_{edge}$ is the normalized mean edge length of MST, defined by:

$$\bar{l}_{edge} = \frac{(N-1)}{(AN)^{1/2}} \sum_{i=1}^{N-1} m_i \tag{2.4}$$

where N is the total number of sources, m_i is the length of edge i, and A is the area of the smallest circle that contains all the sources. The value of $\bar{s}$ represents the correlation length, i.e. mean

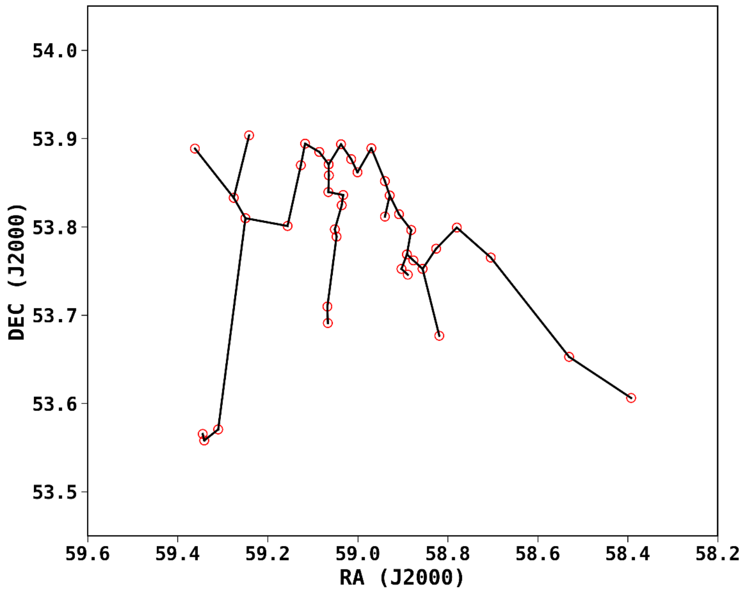

Figure 2.10: Minimum spanning tree distribution of the protostars in our sample. The red circles indicate the positions of the protostars, while the lines denote the spanning edges.

projected separation of the sources normalized by the cluster radius and is given by

$$\bar{s} = \frac{2}{N(N-1)R} \sum_{i=1}^{N-1} \sum_{j=1+i}^{N} |\vec{r}_i - \vec{r}_j| \tag{2.5}$$

where r_i is the vector position of the point i and R is the radius corresponding to area A. The $\bar{s}$ decreases more quickly than $\bar{l}_{edge}$ as the degree of central concentration increases, while $\bar{l}_{edge}$ decreases more quickly than $\bar{s}$ as the degree of subclustering increases (Cartwright & Whitworth, 2004). Therefore, the Q parameter not only quantifies but also differentiates between the radial density gradient and fractal subclustering structure.

Figure 2.10 shows the MST graph of the protostars in our sample. In the present case, the radius is defined as the projected distance from the mean position of all cluster members to the farthest protostar, following Schmeja & Klessen (2006). Doing so, we calculated $\bar{l}_{edge}$ and $\bar{s}$ as 0.27 and 0.41, respectively, which leads to a Q value of $\sim$ 0.66. Including the protostars identified by the Star Formation in the Outer Galaxy (SFOG) survey (Winston et al., 2020), which has used *Spitzer-IRAC*, *WISE*, and *2MASS* data in the wavelength range 1$-$22 μm, though the statistics of the protostars sample improved to 70, the Q-value was found to largely remain the same, i.e. Q $\sim$0.62, a change of only 6%. It is to be noted that the normalization to cluster radius makes the Q parameter scale-free, but a small dependence of the number of stars on the Q parameter is found in simulations (e.g. Parker, 2018). This is also seen in the present work with a change in Q value only by 6%. Apart from the number of stars, the presence of outliers can also significantly affect the Q parameter (Parker & Schoettler, 2022). To check the significance of outliers on the Q value, we removed possible outliers from our sample, which are far away from the main star-forming region (i.e. sources located outside the rectangular box shown in Figure 2.8a; these sources are also located away from the A_V ~5 mag contour, shown in the right panel of Figure 2.8b) and did the MST analysis. Doing so, we found that the Q value changes only by 3%, resulting in a total uncertainty of ~7% (i.e. Q = 0.660 ± 0.046) due to the above factors.

We also looked at how the completeness of the 70 μm catalogue could affect the estimated Q-value. Since most of the protostars are distributed in the central area of the cloud with $A_V > 5$ mag, the completeness limit of the 70 μm catalogue was estimated in the central area, i.e. the area roughly enclosing the boundary of the $A_V > 5$ mag. The completeness limit was estimated by injecting artificial stars on the 70 μm image and performing detection and photometry in the same way as done in the original catalogue (for details, see Marton et al., 2017). By doing so, it is found that the 70 μm point source sample in the central area is ~80% complete at the flux level of around 200 mJy, as shown in Figure 2.11. Recalculating the Q value above the 80% completeness limit, the Q value turns out to be 0.71. The value of Q > 0.8 is interpreted as a smooth and

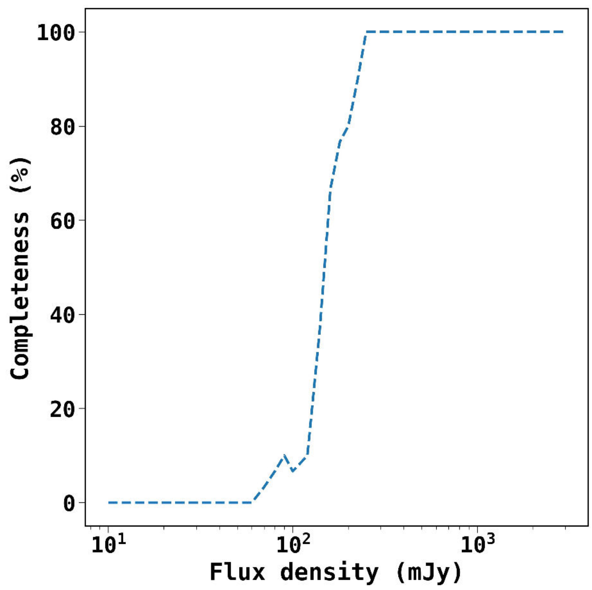

Figure 2.11: Completeness of *Herschel* 70 μm point source catalogue towards the central region of the cloud (see text for details).

centrally concentrated distribution with volume density distribution $\rho(r) \propto r^{\alpha}$, while Q < 0.8 is interpreted as clusters with fractal substructure, and Q $\simeq$ 0.8 implies uniform number density and no subclustering (see Cartwright & Whitworth, 2004, for discussion). Cartwright & Whitworth (2004) drew these inferences by studying the structure of the artificial star clusters, created with a smooth large-scale radial density profile ($\rho(r) \propto r^{\alpha}$) and with substructures having fractal dimension D, and correlating them with the Q-value. The fractal substructures of various fractal dimensions were generated following the box fractal method of Goodwin & Whitworth (2004). Cartwright & Whitworth (2004) found that Q is correlated with the radial density exponent α for Q > 0.8, and for fractal clusters, the Q is related to fractal dimension D such that the Q parameter changes from 0.80 to 0.45 as the D changes from 3.0 (no subclustering) to 1.5 (strong subclustering). The estimated Q value (i.e. $Q = 0.660 \pm 0.046$) in this work, corresponds to a notional fractal dimension, D ~2.2 (see Figure 5 of Cartwright & Whitworth, 2004), which represents a moderately fractal distribution. This analysis suggests that the cloud in its central area is moderately fractal.

2.2.3.3 Luminosity of protostars and their correlation with the gas surface density

Dunham et al. (2006), using radiative transfer models, demonstrated that 70 μm is a crucial wavelength for determining bolometric luminosity (L_{bol}) of embedded protostars, as radiative transfer models are strongly constrained by this wavelength, and it is largely unaffected by the details of the source geometry and external heating. Furthermore, Dunham et al. (2008) and Ragan et al. (2012) find that the 70 μm flux correlates well with the bolometric luminosity of the low and high-mass protostars, respectively (see also discussion in Elia et al., 2017). Thus, in this work, the empirical relation between 70 μm flux and L_{bol} given by Dunham et al. (2008) is used for estimating L_{bol} of the protostars:

$$L_{bol} = 3.3 \times 10^{8} F_{70}^{0.94} \left(\frac{d}{140pc}\right)^{2} L_{\odot}, \tag{2.6}$$

where F_{70} is in erg cm^{-2} s^{-1}, though this way of estimating luminosity is likely accurate within a factor of 2–3 (e.g. Commerçon et al., 2012; Samal et al., 2018). The luminosity of the sources estimated in this way is found to be in the range of ~3–1850 $L_{\odot}$, with a median value

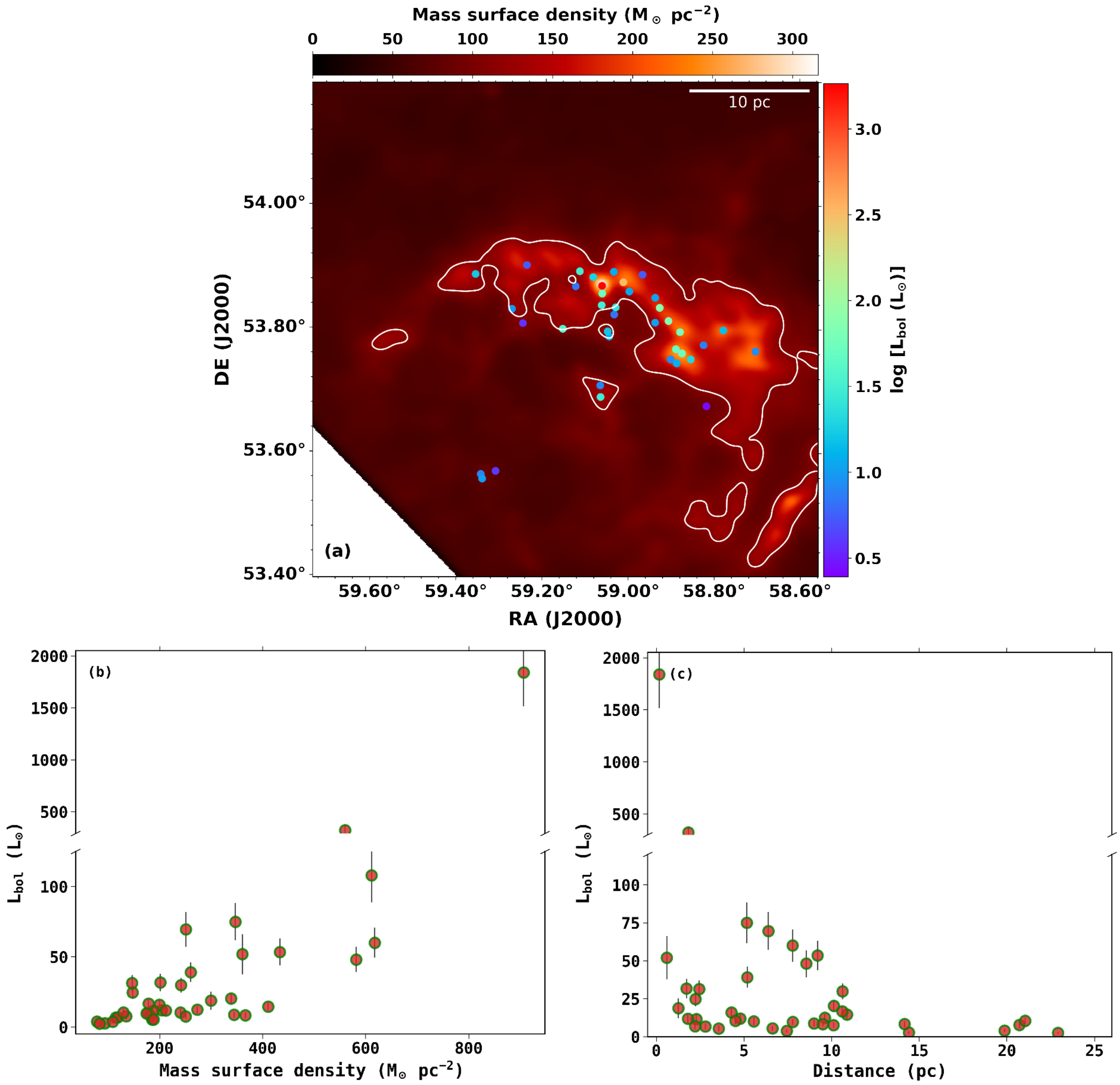

Figure 2.12: (a) Spatial distribution of protostars on the smoothed mass surface density map (beam $\sim 30''$). The overplotted white contour corresponds to the mass surface density of 110 $M_\odot$ pc^{-2} that encloses most of the sources. The right colorbar shows the bolometric luminosity of the protostars on a log-scale. The highest luminosity source ($L_{bol} \approx 1900\ L_\odot$) is shown by a red dot. (b) Plot showing the luminosity of the protostars vs. their corresponding mass surface density. (c) Plot showing the radial distribution of luminosity of the protostars from the likely centre of cloud's potential.

around 12 $L_\odot$.

Figure 2.12a shows the luminosity distribution of the sources on the mass surface density map, made from the column density map. The uncertainty in the luminosity is due to the uncertainty in the distance of the cloud and the flux of the point sources. As can be seen, the most luminous source (the reddest solid dot) is located in the zone of the highest surface density, and most of the sources are confined to surface density > 110 $M_\odot$ pc^{-2}. Figure 2.12b shows the bolometric luminosity versus peak mass surface density corresponding to the source location. From the figure, one can see that sources are distributed in the surface density range 80–900 $M_\odot$ pc^{-2} and show a positive correlation with the mass-surface density, implying that higher luminous sources are found in the higher surface density zones. Figure 2.12c shows the luminosity distribution of the sources from the location of the cloud's likely centre of potential. As discussed in Section 2.2.2.1, the inner region of the cloud is elongated and filamentary, making it difficult to find its centre of gravitational potential. Therefore, the cloud's gravitational centre is considered as the location of the highest surface density area on the smoothed surface density map (shown in Figure 2.12a). We made a smoothed map to understand the structure that dominates the large-scale distribution as a function of scale. The highest surface density area on the smoothed map also corresponds to the location of a hub, seen in the *Herschel* SPIRE images (discussed in Section 2.3.1.3). From Figure 2.12c, a declining trend of luminosity distribution with the distance from the adopted centre can be seen, although many low-luminosity sources are also located close to the centre along with the most luminous source.

Altogether, the above analyses suggest that although protostars are distributed in a range of surface densities, the luminous sources are located in the highest surface density zones and also close to the cloud's centre of potential.

2.2.3.4 Mass segregation

A higher concentration of massive objects near the cloud or cluster centre compared to that of their low-mass siblings is known as mass-segregation. However, it remains unclear whether mass segregation is primordial or dynamical, particularly in young star-forming regions or cluster-forming clumps. Mass segregation is an important constraint on theories of massive stars and associated cluster formation. For example, it is suggested that cores in the dense central regions of cluster-forming clumps can accrete more material than those in the outskirts; therefore, primordial mass segregation would be a natural outcome of massive star formation (Bonnell & Bate, 2006; Girichidis et al., 2012). However, it is also suggested that mass segregation can also occur dynamically. In this scenario, massive stars form elsewhere but sink to the centre of the system potential through dynamical interaction with the other members (e.g. Allison et al., 2010; Parker et al., 2014, 2016; Domínguez et al., 2017).

One way to test the above theories is to look for the distribution of young protostars and cores in young molecular clouds. Because, the velocity dispersion of cores in young star-forming regions is found to be ~0.5 km s^{-1}, while the velocity dispersion of the class II sources in the same regions is found to be higher, at around 1 km s^{-1}(e.g. NGC 1333; Foster et al., 2015). Thus, the class II stars of a star-forming region can travel pc-scale distance in a Myr timescale from their birth locations, while protostars being young (age $\sim 10^5$ yr) and often attached to the host core, nearly represent their birth locations.

To quantify the degree of mass-segregation (Λ_{MSR}) in star-forming regions, Allison et al. (2009a) described a statistical way that uses MST distribution of stars. This method works by comparing the average MST length of the most massive stars of a cluster with the average MST length of a set of the same number of randomly chosen stars and is written as:

$$\Lambda_{MSR}(N) = \frac{< l_{random} >}{l_{massive}} \pm \frac{\sigma_{random}}{l_{massive}}, \tag{2.7}$$

For good statistical results, one needs to take a significant number of random samples (Maschberger & Clarke, 2011). Here, $< l_{random} >$ is the sample mean of average MST lengths of N randomly selected stars, $l_{massive}$ is the average MST length of N most massive stars, and σ_{random} is the standard deviation of the length of these N random stars. The Λ_{MSR} greater than 1 means that the N most massive stars are more concentrated compared to a random sample, and therefore, the cluster shows a signature of mass segregation, while $\Lambda_{MSR} \sim 1$ implies that the distribution of massive stars is comparable to that of the random stars.

In the present work, we have not estimated the mass of the protostars (typical age $\sim 10^5$ yr), however, since luminosity is proportional to the mass (e.g. from the theoretical isochrones of Bressan et al. (2012), we find that $M_* \propto L^4$ for the stars in the mass range 1–10 M$_\odot$ and an age of 10^5 yr), thus, it is considered that any evidence of luminosity segregation is equivalent to mass-segregation. Only the *Herschel* protostars were used to test the mass-segregation effect, as luminosity measurements of only these protostars were available. It is important to acknowledge that in this simple mass-luminosity relation, the role of accretion luminosity on the total luminosity of the protostars has been ignored, but it is expected to be around 25% for the class I sources (e.g. Hillenbrand & White, 2004).

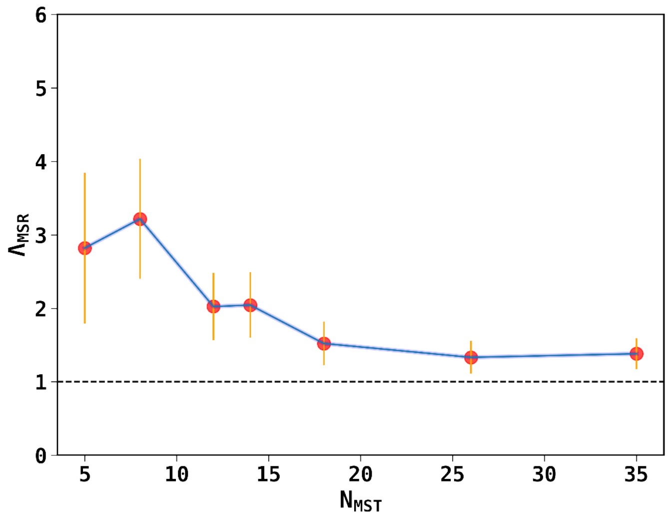

Figure 2.13: Plot showing the evolution of Λ_{MSR} for G148.24+00.41 with different number of most massive sources, $\mathrm{N}_{\mathrm{MST}}$. The dashed line at Λ_{MSR} ~1 shows the boundary at which the distribution of massive stars is comparable to that of the random stars.

We calculated the Λ_{MSR} starting at N (number of most massive stars) = 5 up to the number of protostars in our sample and calculated $< l_{random} >$ by picking 500 random sets of N stars. Figure 2.13 shows the Λ_{MSR} for increasing values of N. As can be seen, the 8 most massive stars show the maximum value of Λ_{MSR} (i.e. ~3.2 ± 0.5) , then Λ_{MSR} progressively decreases and becomes flat beyond 18 most massive stars. The larger σ_{random} is expected for small N due to stochastic effects in choosing the small random sample (Allison et al., 2009a). As done in the Q parameter analysis, we also estimated the effect of 70 μm point source sample completeness on the mass-segregation and found that Λ_{MSR} to be around 2.8, which is though on the lower-side of the Λ_{MSR} measured for the entire cloud but within the error. This analysis tells that the 8 most massive stars of G148.24+00.41 are likely 3 times closer to each other compared to the typical separation of 8 random stars in the region, suggesting that the mass-segregation effect is likely present in G148.24+00.41. These eight most massive stars (L ≥ 50 $L_{\odot}$) of G148.24+00.41 are located within ~9 pc from the adopted centre. The likely cause of the observed mass-segregation is discussed in Section 2.3.1.3. It is worth mentioning that, like here, mass-segregation of cores has been investigated in a few filamentary environments using ALMA observations involving a small number of cores. For example, Plunkett et al. (2018) reported that massive cores of Serpens South are mass segregated with a median $\Lambda_{\rm MSR}$ of $\simeq 4$. Similarly, Sadaghiani et al. (2020) also find evidence of mass segregation in the filaments of NGC 6334 with $\Lambda_{\rm MSR}$ value in the range $\simeq$ 2–3. However, it is to be noted that within the G148.24+00.41 cloud area, the SFOG survey has identified 48 protostars, 31 of which have no counterparts in the 70 μm catalogue. These are likely the low-luminosity sources of the cloud beyond the sensitivity limit of the 70 μm image. Since the SFOG survey has used data in the wavelength range 1–22 μm to identify these protostars, robust estimation of their bolometric luminosity is not possible. Thus these sources were not used in the MST analysis. However, it is worth mentioning that the non-inclusion of these protostars and also any embedded low-luminosity protostars that are not detected in the SFOG survey may bias our results. Future high-sensitivity multi-band long-wavelength observations are needed for a more precise estimation of the mass segregation.

2.3 Discussion

The G148.24+00.41 cloud is massive and bound, yet it is still speculative to say whether it will form a high-mass cluster. In Section 1.5.1 of Chapter 1, various scenarios for intermediate-to-massive cluster formation were discussed, depending on the process of matter accumulation and the driving factors behind it. The different scenarios are *monolithic* (Banerjee & Kroupa, 2015), *global hierarchical collapse* (Vázquez-Semadeni et al., 2019), *conveyor-belt collapse* (Longmore et al., 2014; Walker et al., 2016; Barnes et al., 2019; Krumholz & McKee, 2020), and *inertial inflow model* (Padoan et al., 2020).

The aforementioned models broadly suggest that, while the molecular cloud globally evolves, due to its hierarchical nature, it also simultaneously forms stars at local high-density structures (i.e. within the filaments or dense regions), as their free-fall times are shorter than the free-fall time of the global cloud. And as the evolution of the cloud proceeds, the cold matter in the extended environment and the protostars formed within them can eventually be transported to the remote collapse centre, located at the cloud's centre of potential. This can occur via filaments, anchored by large-scale global collapse (for details, see review articles by Pineda et al., 2022;

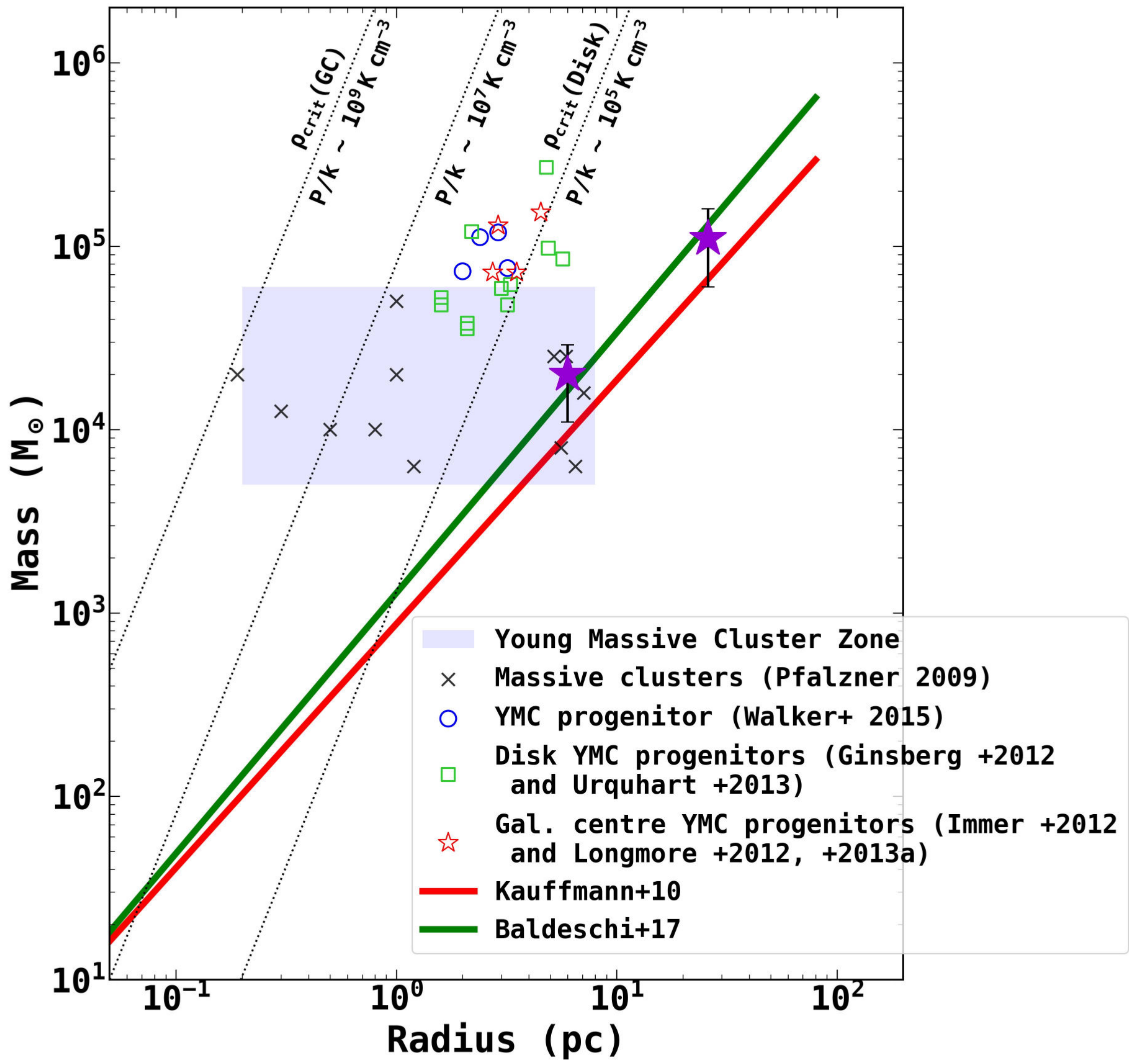

Figure 2.14: Mass - radius relation for massive star formation and YMCs in the Milky Way. The red line is the threshold for massive star formation from Kauffmann & Pillai (2010), while the green line is from Baldeschi et al. (2017) threshold. The hatched rectangle shows the location of Galactic young massive clusters tabulated in Pfalzner (2009). The green squares are YMC progenitor candidates in the disk (Ginsburg et al., 2012; Urquhart et al., 2013), and the blue circles and red stars are the YMC progenitors in the Galactic centre from Walker et al. (2015) and Immer et al. (2012); Longmore et al. (2012, 2013), respectively. Dotted lines show the predicted critical volume density thresholds for the Galactic centre, intermediate region, and the Galactic disk, assuming pressures of P/k $\sim 10^9$, P/k $\sim 10^7$, and P/k $\sim 10^5$ K cm^{-3}, respectively. The locations of G148.24+00.41 are shown in purple star symbols, corresponding to the mass measured at $A_{\rm K}$ = 0.2 mag and 0.8 mag, respectively.

Hacar et al., 2022), where filaments act like conveyor-belts. In these scenarios, star formation would proceed over several crossing times leading to significant age spread in cluster members, the seeds of massive stars are expected to be located near the cloud's centre of potential, and younger stars are expected to form in the end. As a consequence, primordial mass segregation is expected, and also, the cloud's central potential is expected to have more young stars compared to the stars in the extended part of the cloud (e.g., see discussion in Vázquez-Semadeni et al., 2019).

In the following, we discuss the possible scenarios of massive stars and associated cluster formation in G148.24+00.41, and discuss the results in the context of the above cluster formation theories.

2.3.1 Observational evidence of massive cluster formation and processes involved in G148.24+00.41

2.3.1.1 Evidence of high-mass star and associated cluster formation

Observations suggest that the mass of the most massive star of a cluster is proportional to the total mass of the cluster (e.g. Weidner et al., 2010). Therefore, the presence of young massive star(s) in a cloud is an indication of ongoing cluster formation. Another way of finding whether or not a cloud would form a high-mass cluster is to look for mass versus radius diagram as it is suggested that to form a high-mass cluster, a reservoir of cold gas concentrated in a relatively small volume is likely required (e.g. Bressert et al., 2012; Ginsburg et al., 2012; Urquhart et al., 2013).

Based on column density maps derived from dust emission (MAMBO and Bolocam) and extinction (2MASS) data, Kauffmann & Pillai (2010) suggested a criterion for massive star formation. They argued that the clouds known to be forming massive ($M_* \sim 10\ M_\odot$) stars have structural properties described by $m(r) > 870\ M_\odot (r/\mathrm{pc})^{1.33}$, where $m(r)$ is the mass within radius r. Clouds below this criterion are unlikely to form massive stars. A similar conclusion is also given by Baldeschi et al. (2017) for cold structures to form high-mass stars. Figure 2.14 shows these empirical relations along with the location of the G148.24+00.41 cloud corresponding to its total mass and dense gas mass. As can be seen, both the estimates of G148.24+00.41 lies nearly above these relations, suggesting that massive star formation is expected in G148.24+00.41.

However, it is worth noting that simulations suggest that the star formation efficiency, though highly dependent on the initial conditions, is usually low at the very initial stages of cloud evolution and accelerates after a few free-fall time (Zamora-Avilés et al., 2012; Lee et al., 2016; Caldwell & Chang, 2018; Clark & Whitworth, 2021). In addition, models also suggest that compared to low-mass stars, the massive stars form last in a molecular cloud (Vázquez-Semadeni et al., 2009, 2019), which is supported by some observations (e.g. Foster et al., 2014), however, there are also contrasting observational results suggesting that massive stars may form in the early phases of the molecular clouds (e.g. Zhang et al., 2015).

All the above models point to the fact that the non-detection of high-mass stars in a massive cloud does not imply that it would not form high-mass stars. It may simply be due to the fact that the cloud is at the very early stages of its evolution and has not had enough time to form massive stars. Nonetheless, in the present work, the most luminous 70 μm point source of our sample corresponds to a probable massive YSO (MYSO; RA = 03:56:15.36, Dec = +53:52:13.10) listed in the MYSO sample of the Red MSX Source survey (Lumsden et al., 2013). Cooper et al. (2013) confirms the YSO nature of the Red MSX Source using near-infrared spectroscopy observations. Scaling the luminosity of the Red MSX massive YSO tabulated in Cooper et al. (2013) to the distance of G148.24+00.41, its luminosity comes out to be ~4200 $L_\odot$ (= $7300 \times (3.4\ \mathrm{kpc}/4.5\ \mathrm{kpc})^2$), which is two times of the 70 μm flux-based luminosity estimation (see Section 2.2.3.3). The dynamical age of the MYSO based on the extent and the velocity of the outflow lobes, traced with the CO (J = 3–2) transition, is suggestive of a very young age, around $\sim 10^5$ yr (Maud et al., 2015). No UCH ii region has been detected in the 5GHz continuum image of the RMS survey. The typical age of the UCH ii region is around $\sim 10^5$ yr. All these results imply that the MYSO is in its early stages of evolution.

Figure 2.14 also shows the location of YMCs (Mass > 5×10^3 $M_\odot$ and Age < 5 Myr; Pfalzner, 2009) by the shaded area. Also shown are the YMC precursor clouds of the Galactic disk (Ginsburg et al., 2012; Urquhart et al., 2013) and Galactic centre (Immer et al., 2012; Longmore et al., 2012, 2013; Walker et al., 2015). The YMC precursor clouds that have been identified at the Galactic centre are mostly quiescent despite tens of thousands of solar masses of gas and dust within only a few parsecs.

It is believed that massive Galactic centre clouds are favourable places for YMC formation. It hosts the two most massive clusters (mass $\sim 10^4$ $M_\odot$) in the Galaxy, the Arches and Quintuplet, which have formed in the Galactic centre recently, with ages of ~3.5 and 4.8 Myr, respectively (e.g. Walker et al., 2018). As can be seen from Figure 2.14, in terms of mass and compactness, compared to Galactic centre clouds, the dense gas mass of G148.24+00.41 is lower by an order of magnitude while its radius is higher by a factor of 2–3. In G148.24+00.41, star formation is underway, as evident from the detection of YSOs of various classes, therefore, some of the gas has already been consumed in the process. Even then, comparing the current location of G148.24+00.41 with the location of the YMC progenitor clouds in the Galactic disk and centre, it appears that G148.24+00.41 may not form a YMC like the Arches cluster (mass > 10^4 $M_\odot$ and radius ~0.5 pc). By comparing the mass surface density profile of G148.24+00.41 within 2 pc from the hub centre with other Galactic YMC precursor clouds discussed in Walker et al. (2016), it is found that the surface density profile of G148.24+00.41 is substantially below all of the Galactic centre clouds, and the extreme cluster forming regions in the disc. This again points to the fact that although G148.24+00.41 has a significant mass reservoir, it is spread over a larger projected area, hence the lower surface mass density and lower potential for forming a star cluster like the Arches.

The figure also shows the turbulent pressures for the different environments in our Galaxy (for details see Longmore et al., 2014). Assuming that G148.24+00.41 is pressure confined by the turbulent pressure of the Galactic disk, to become unbound, the internal pressure of the cloud has to be of the order of 10^5 K cm^{-3}. The present dynamical status of G148.24+00.41 suggests that it is gravitationally bound. In the following, we explore what kind of cluster G148.24+00.41 may form.

2.3.1.2 Likely age and mass of the total embedded stellar population

In the field of G148.24+00.41, the SFOG survey has identified 175 YSOs, out of which 48 are class 0/I, 120 are class II, and 7 are class III sources. We matched and combined the SFOG YSO catalogue with the protostars identified in this work, which resulted in a total of 187 YSOs, out of which 70 were found to be protostars.

Young stellar objects take different amounts of time to progress through the various evolutionary stages. Protostars (Class 0, Class I, and flat-spectrum sources) represent an earlier stage of young stellar object's evolution than the class II and class III sources, thus, the ratio of protostars to the total number of YSOs (or class II sources) are often used to derive relative ages

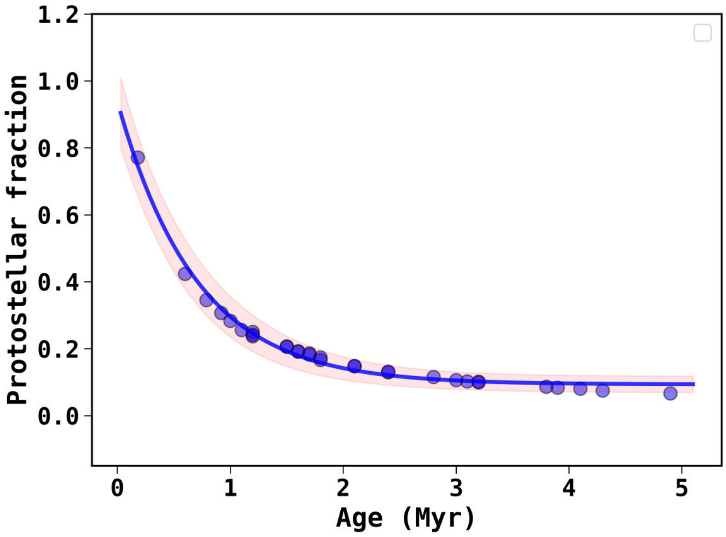

Figure 2.15: Age of stellar sample vs. fraction of protostars. The blue line shows the best-fit exponential decay curve (see text for more details).

of the star-forming regions (e.g. Jørgensen et al., 2006; Gutermuth et al., 2008; Myers, 2012). For deriving an approximate age of G148.24+00.41, its protostellar fraction is compared with that of the well-known star-forming regions. Figure 2.15 shows the protostellar fraction (i.e. the ratio of protostars to the total number of protostars plus class II YSOs) vs. age of the 23 star-forming regions tabulated in Myers (2012). In this figure, class III sources are not considered in the total number of YSOs following Myers (2012), as the authors did not consider class III sources in their analysis, arguing that they are incomplete. As can be seen from Figure 2.15, the protostellar fraction declines with age. Assuming that the protostellar fraction decays exponentially with age, like the disk fraction in young clusters (Ribas et al., 2014), we fitted the observed protostellar fraction as a function of time using an exponential law of the form: $f_{pro} = A\,exp\left(\frac{-t}{\tau}\right) + C$, where t is the age of the sample (in Myr), A is the initial protostellar fraction, τ is the characteristic timescale of decay in protostellar fraction (in Myr), and C is a constant level. The best-fitted value of A, τ, and C are 0.847 ± 0.022, 0.700 ± 0.024, and 0.093 ± 0.005, respectively. The derived relation is an indication of the fact that the protostar's life-time is around ~0.7 Myr. For G148.24+00.41, the protostellar fraction is found to be ~37% with an admittedly high uncertainty, which is difficult to quantify considering the likely completeness limits of various bands used in the SFOG survey for identifying the YSOs and also the sensitivity limits of these bands in detecting disk-bearing stars in the cloud due to its distant nature. Nonetheless, taking the observed protostellar fraction a face value and using the above-derived relation, a crude assessment of the age of G148.24+00.41 was made to be roughly around 1 Myr, which is used in this work.

Measuring the mass of individual embedded YSOs is an extremely challenging task in young star-forming clouds due to the presence of variable extinction within the cloud and also the presence of infrared excess in YSOs. Nonetheless, to get a rough census of the total stellar mass that might be embedded in the cloud, we first estimated the typical detection limit of the YSO sample. This was done by searching for counterparts of the YSOs in UKIDSS NIR bands, adopting 1 Myr as their age, and assuming a minimum foreground A_V of 5 mag (which corresponds to the outer column density boundary of the central area, within which the majority of the YSOs are concentrated) in the direction of the YSOs. With this approach, the typical detection limit is found to be around 0.9 $M_\odot$. In this analysis, a 1 Myr theoretical isochrone from Bressan et al. (2012) was utilized, and corrected for distance and extinction to compare with the observed NIR magnitudes of the YSOs.

The luminosity of the most massive YSO is around $\sim$ 1900 $L_\odot$, which corresponds to a star of 8 $M_\odot$ (see Table 1 of Mottram et al., 2011). Considering that there are 187 point sources embedded in the cloud between 0.9 and 8 $M_\odot$ and using the functional form of Kroupa mass-function (Kroupa, 2001), we estimated the total stellar mass to be $\sim$ 500 $M_\odot$ and extrapolating down to 0.1 $M_\odot$, we find the total mass to be $\sim$1000 $M_\odot$. Thus, an embedded population of total stellar mass around 1000 $M_\odot$ is expected to be present in the cloud. It is important to note that applying a higher foreground extinction would give even a higher mass detection limit for YSOs and, thus, a higher total stellar mass.

2.3.1.3 Hub filamentary system and its implication on cluster formation

Figure 2.16 shows the central area of the cloud at 250 μm. In the image, several large-scale filamentary structures (length $\sim$5–20 pc) were found to be apparent. These structures are sketched in the figure by the dotted curves and meant only to indicate the possible existence of large-scale filament-like structures. These structures were identified by connecting nearly continuous dust emission structures present in the cloud. A thorough identification of the filaments is beyond the scope of the present work. Future high-dense gas tracer molecular data would be highly valuable for identifying the velocity coherent structures, thus the filaments in the cloud and their properties (e.g. Treviño-Morales et al., 2019). However, from the present generic sketch, one can see that the central dense location is located at the nexus of six filamentary structures. It is

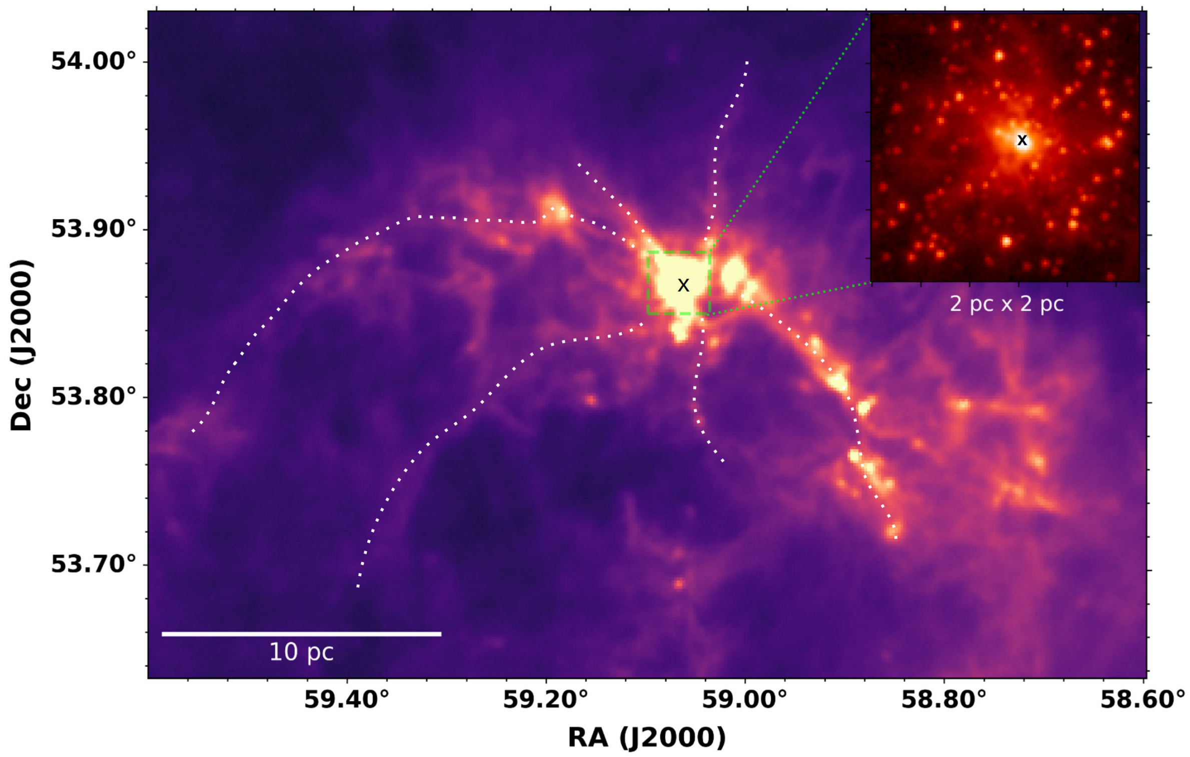

Figure 2.16: *Herschel* 250 μm image of G148.24+00.41, revealing the filamentary structures in its central area. The inset image shows the zoomed-in view of the central region in *Spitzer* 3.6 μm, which is taken from GLIMPSE360 survey (Whitney & GLIMPSE360 Team, 2009). It shows the presence of an embedded cluster in the hub. The cross sign shows the position of the massive YSO.

worth noting that the central area is host to an embedded cluster, as seen in the near-infrared images. The inset image of Figure 2.16 shows the cluster in the *Spitzer* 3.6 μm band, and as can be seen, it contains a rich number of near-infrared point sources with massive YSO at its very centre. Altogether, the whole morphology of Figure 2.16 is consistent with the picture of a hub filamentary system put forward by Myers (2009), where several fan-like filaments are expected to intersect, merge and fuel the clump located at their geometric centre (e.g. see also discussion in Kumar et al., 2022).

As discussed in Section 2.2.3.4, evidence of mass-segregation in the cloud has been observed for luminous sources with luminosity > 50 $L_\odot$ within ~9 pc from the central hub. This observed mass-segregation could be of primordial or dynamical origin. In the case of star clusters, the dynamical origin is primarily driven by the interaction among the stars. In the present case, the total mass of the embedded population is around ~1000 $M_\odot$, which is ~3% of the total gas mass ($N(H_2) > 5\times10^{21}$ cm^{-2}) enclosing these YSOs. This is suggestive of the fact that the gravitational potential in the central area of the cloud is dominated by the gas than the stars; thus, dynamical interaction among the stars might not be so effective at this stage of the cloud's evolution for global mass-segregation to happen. The cold molecular gas and dust are usually thought to impede the process of dynamical interaction.

Filaments are often associated with longitudinal flows (e.g. Peretto et al., 2013; Dutta et al., 2018; Ryabukhina et al., 2018), heading toward the bottom of the potential well of the system (e.g. Treviño-Morales et al., 2019). To understand whether the observed mass-segregation is driven by filamentary flows, we calculated the flow crossing time as: $t_{cr} = \frac{R}{v_{inf}}$, where v_{inf} is the flow velocity, and R is the distance travelled by the gas flow. The typical value of v_{inf} in the range of ~1–1.5 km $s^{-1}pc^{-1}$, observed in the large-scale filaments that are radially attached to the massive star-forming hubs (e.g. Treviño-Morales et al., 2019; Montillaud et al., 2019), was used to calculate the flow travel distance. Doing so, we estimated that in ~0.1–1 Myr of time (i.e. the likely age range of the region; discussed in Sections 2.3.1.1 and 2.3.1.2), the flow would travel a distance in the range of ~0.15 to 1.5 pc. If this flow carries massive prestellar cores or massive protostars along with it, then one would expect that the effect of mass-segregation within 1.5 pc from the centre of the cloud's potential may be of flow origin. However, it is worth stressing that it is very unlikely that the massive prestellar core or protostars would flow along the filaments with the same velocity as gas particles may do. Thus, the aforementioned estimated travel distance would be an upper limit for the protostars.

Since the mass-segregation scale (~9 pc) for the massive stars is larger than the flow travel distance (~0.15–1.5 pc) for the adopted age range of the system, thus the global mass-segregation observed in G148.24+00.41, if confirmed (see possible biases in Section 2.2.3.4), may suggest towards its primordial origin. Deeper photometric observations, along with the velocity measurements of the gas and protostars, would shed more light on this issue.

2.3.1.4 Prospects of cluster formation processes in G148.24+00.41

Simulations suggest that the density profile reflects the physical processes influencing the evolution of a cloud. The overall density profile, $\rho \propto r^{-1.5}$, obtained for G148.24+00.41 is a signature of a self-gravitating turbulent cloud. This is also revealed by the distribution of the protostars. The obtained Q-value around 0.66 from the distribution of protostars, suggests that the central region is moderately fractal with a fractal dimension equivalent to 2.2. This fractal structure could be a consequence of both gravity and turbulence. For example, Dobbs et al. (2005) simulated a turbulent clump of density profile, $\rho \sim r^{-1.5}$ and found that the clump is able to fragment into hundreds of cores that are tied with filamentary structures. Q-value > 0.9 generally represents a steeper density profile of exponent $\beta > 2$. Individual clumps may have a steeper density profile, but the central area as a whole is fractal. In other words, the central area of the cloud is different from the profile that one would expect for a cloud to form a single compact cluster via monolithic collapse. The distribution of protostars across the length of the dense gas over a range of densities (see Section 2.2.3.3) also disfavours a monolithic mode of cluster formation in G148.24+00.41. Walker et al. (2015, 2016) compared the profile of gas density distribution of the YMC precursor clouds with the stellar density distribution of the YMCs. They found that the density profile of the former is flatter compared to the latter, which led them to suggest that the YMC precursors are not consistent with the monolithic formation scenario of star clusters. Doing a similar analysis, the gas surface density profile of the hub area of G148.24+00.41 is found to be flatter than the stellar distribution of YMCs, supporting the above notion that the present cloud is not centrally concentrated enough to form a typical massive cluster in-situ given the present-day mass distribution.

Figure 2.16 shows that the G148.24+00.41 cloud hosts a hub-filamentary system, where cluster formation is happening at the hub of the filaments. The presence of hub-filament systems has also been advocated in flow-driven simulations, including global collapse (Smith et al., 2009; Gómez & Vázquez-Semadeni, 2014; Vázquez-Semadeni et al., 2019). From the evidence of the hub filamentary system, density profile with a power-law index of -1.5, and low Q-value at the central area, it appears that the whole cloud may be self-gravitating globally. However, at smaller scales, star formation can occur in dense structures such as filaments and hubs that are immersed within this large-scale self-gravitating cloud. Moreover, though protostars have formed over a range of densities, the high-luminosity sources (or the high-mass sources) are located around the densest locations of the cloud, suggesting primordial mass-segregation in G148.24+00.41. The low Q-value and the fact that the flow crossing scale is lesser than the mass-segregation scale suggest that mass segregation is likely primordial. In addition, the massive star, which is still at a very young age, of the order of 10^5 yr, is found to be located in the central area of the cloud, while the young class II sources, whose age lies in the range ~1–2 Myr have also been observed in the cloud (Winston et al., 2020).

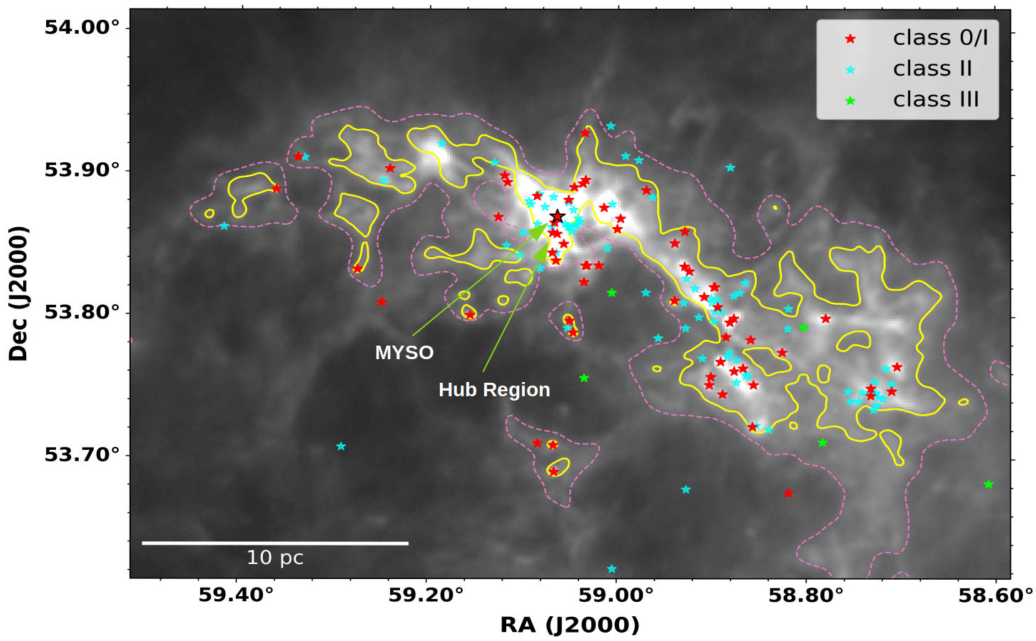

Figure 2.17: The distribution of YSOs from *Herschel* 70 micron point source catalog (Herschel Point Source Catalogue Working Group et al., 2020) and SMOG catalog (Winston et al., 2020) on the *Herschel* 250 micron image. The dotted pink colour contour shows the column density at 5.0×10^{21} cm^{-2} and the yellow solid colour contour shows the dense gas column density at 6.7×10^{21} cm^{-2} (A_K ~0.8 mag). Protostars, class II, and class III YSOs are marked by red, cyan, and green star symbols, respectively.

Figure 2.17 shows the distribution of the YSOs on the *Herschel* 250 μm image. As can be seen, most of the YSOs are located near the hub or associated filaments. It is worth stressing that the detection limit of our identified YSOs is around 1 $M_\odot$. Thus, there may be more faint low-mass YSOs distributed in the extended part or diffuse filaments of the cloud and are not identified here. Also, due to the crowding of stellar sources and bright infrared background, the true YSO number identified inside the hub using *Spitzer* images may be an underestimation. Nonetheless, using the present sample, we calculated the protostellar fraction as a function of distance from the central hub, which is shown in Figure 2.18. As can be seen, the plot signifies that younger sources show the tendency of being located closer to the cloud centre relative to the class II YSOs. All the above evidence points to the flow-driven modes of cluster formation that are discussed in Section 2.3. So, it seems that, if the cloud will ultimately form a high-mass cluster, it has to go through global hierarchical convergence and merger of its both gaseous and stellar content as advocated in conveyor-belt type models (e.g. Longmore et al., 2014; Walker et al., 2016; Vázquez-Semadeni et al., 2019; Barnes et al., 2019). The latter can even occur after no gas is left in the system if the stellar sources are part of a common potential (e.g. Howard et al., 2018; Sills et al., 2018b; Karam & Sills, 2022).

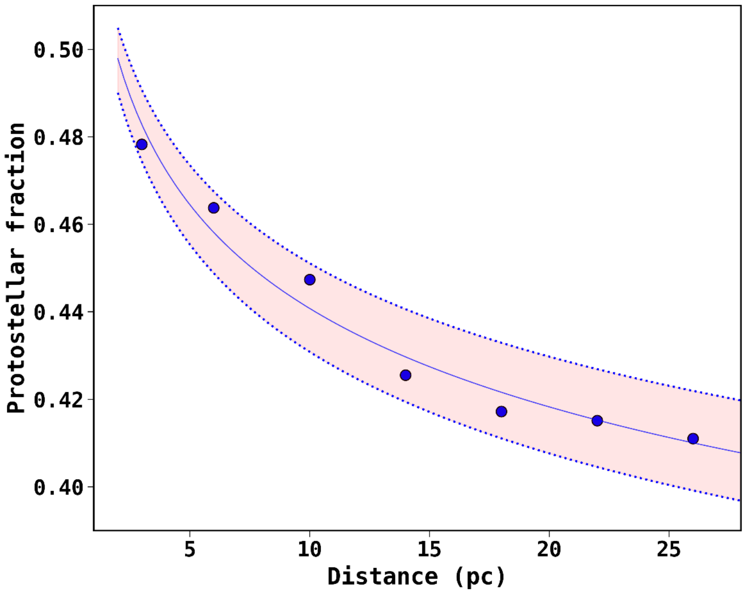

Figure 2.18: Radial distribution of protostellar fraction from the hub location. The blue solid line represents to a power-law profile of index ~-0.08, while the shaded area represents the 1σ uncertainty associated to the power-law fit.

2.3.2 Predictions from models of hierarchical star cluster assembly and merger

Assuming that the cloud will form a high-mass cluster through dynamical processes over an extended period of time (over a few Myr), involving global hierarchical collapse and merger of stars and subgroups, then it is tempting to speculate that what kind of cluster it may form.

Gavagnin et al. (2017) studied the early (up to 2 Myr) dynamical evolution of a turbulent cloud of mass 2.5×10^4 $M_\odot$, radius $\simeq$ 5 pc, and 3D velocity dispersion $\simeq$ 2.5 km s^{-1}. They found that as the cloud collapses, it forms stars in filaments and extended part of the cloud at a slow rate, but a rich high-mass star cluster emerges from the cloud at the end of the simulation that has some features similar to the massive cluster NGC 6303. In terms of mass, radius, and velocity dispersion, the properties of the simulated cloud are nearly the same as the dense gas properties of G148.24+00.41 (see Section 2.2.2.3), implying that G148.24+00.41 has the potential to build a rich cluster.

From an observational point of view, the emergence of a massive star cluster also seems to be feasible for G148.24+00.41, because its embedded stellar mass is ~ 1000 $M_\odot$, while it still has a high reservoir of bound gas to make more stars. Assuming that it is the dense gas that contributes more to star formation, one can make a rough assessment of the total stellar mass that may emerge from the cloud using the relation between star formation rate and dense gas mass of Lada et al. (2012):

$$SFR = 4.6 \times 10^{-8} f_{\rm den} M_{tot}(M_\odot) \;\; M_\odot\, yr^{-1}. \tag{2.8}$$

The M_{tot} and f_{den} are the total mass and dense gas fraction of the cloud, respectively. By taking dense gas fraction ~18%, total gas mass $\sim 1.1 \times 10^5$ $M_\odot$ (see Section 2.2.2.3), and assuming star formation would proceed at a constant rate for another 1 to 2 Myr, find that a stellar system of total mass in the range 1000–2000 $M_\odot$ may emerge from G148.24+00.41. This prediction is also in line with the recent simulation results of Howard et al. (2018). Howard et al. (2018) follow the evolution of massive GMCs (mass in the range 10^4–10^7 $M_\odot$) with feedback on and off. They found that the star clusters emerge from the cloud via a combination of filamentary gas accretion and mergers of less massive clusters, and found a clear relation between the maximum cluster ($M_{\rm max}$) mass and the mass of the host cloud ($M_{\rm GMC}$). Following the prediction of Howard et al. (2018) for "feedback on" and considering the dense gas mass only as the cloud mass, one can say that the dense gas reservoir of G148.24+00.41 has the ability to form a cluster of total stellar mass ~2000 $M_\odot$.

Combining the embedded stellar mass and the expected stellar mass from the present dense gas reservoir, one would expect a total stellar mass in the range 2000–3000 $M_\odot$ to emerge from this cloud. It is worth noting that this is the case, without accreting any additional gas from the extended low-density reservoir beyond the effective radius of the dense gas (i.e. ~6 pc). However, considering the fact that molecular clouds are highly dynamical, if the cluster accretes cold gas from the extended reservoir, then the total stellar mass is likely an underestimation.

It is worth stressing that simulations of cluster-forming clouds have shown that molecular clouds tend to have some degree of fractal structures at their early stages of evolution, as found in G148.24+00.41. But the degree of fractality slowly reduces as the evolution proceeds because gravitational collapse together with stellar dynamical interactions among the stars and the subgroups progressively erase the initial conditions of the cloud and build up a dense and spherical star cluster (e.g. Maschberger et al., 2010; Gavagnin et al., 2017; Howard et al., 2018). If this happens for G148.24+00.41 in future, where most of the stellar sources segregate to a cluster at the bottom of the potential well, a centrally condensed massive cluster with a Q-value > 1 is expected, otherwise, it may evolve into a massive association of stars or groups.

Although, these predictions suggest that the cloud has the potential to form a rich cluster in the range 2000–3000 $M_\odot$, yet further studies of the cloud concerning its gas properties and kinematics are necessary for investigating whether the filaments that appear in the dust continuum images are indeed converging and funnelling the cold matter to the central potential of the cloud. Thus, would facilitate the formation and emergence of a dense cluster like the ones predicted in the above simulations. We discuss this study of filaments and their gas kinematics in the next chapter.

2.4 Summary

This chapter presents a detailed study of global properties and cluster formation potency of the G148.24+00.41 cloud using dust continuum and dust extinction measurements. To estimate the cloud parameters, the *Herschel* dust continuum-based column density map was used, and the extinction map was also made using the *PNICER* technique. From both the dust continuum and dust extinction maps, it is found that the cloud is massive ($M \sim 10^5$ $M_\odot$) and has dust temperature $\sim$14.5 K, radius $\sim$26 pc, and surface mass density $\sim$52 $M_\odot$ pc^{-2}. It follows the power-law density profile with index ~ -1.5 and is gravitationally bound. A comparison of G148.24+00.41 with other Galactic molecular clouds shows that it has a high gas mass content, comparable to GMCs like Orion-A, Orion-B, and California, and higher than other nearby molecular clouds. The mass and effective radius of the cloud follow Larson's relation, which is in agreement with the other nearby MCs.

Based on *Herschel* 70 μm data, 40 protostars were identified, and including the SFOG survey, the total number of protostars reaches to 70. Using MST analysis over these protostars, the clustering structure is found to be moderately fractal or hierarchical with a Q value of ~0.66. The spatial distribution of protostars shows that most of them are located in the central area of the cloud above $N(H_2) > 5 \times 10^{21}$ cm^{-2}. The luminosity distribution shows that the high luminosity sources are relatively closer to the cloud centre and located in high surface density regions compared to low luminosity sources. This indicates the signature of mass segregation in the cloud, and the obtained degree of mass segregation is around 3.2. Using the combined catalogue of 187 YSOs from *Herschel* 70 μm data and SFOG survey of GLIMPSE360 field, the likely total mass of the stellar population embedded in the cloud was estimated to be around 1000 $M_\odot$, and by including the further star formation from dense gas only, it was found that G148.24+00.41 has the potential to form a cluster in the mass range of 2000–3000 $M_\odot$.

The cloud possesses a hub filamentary system, and a young cluster is seen in NIR at the hub location, along with the MYSO of $L = 1900\,L_\odot$. Younger sources were found closer to the cloud's centre of potential than the older ones. From these findings, along with evidence like low Q value, mass segregation, enclosed mass over radius, and density profile, it seems that *monolithic* collapse is not likely a scenario in G148.24+00.41 and the possibility of *conveyor belt* type mode of cluster formation seems more viable.

Chapter 3

Gas properties, kinematics, and cluster formation at the nexus of filamentary flows in G148.24+00.41

" Among the most surprising things in connection with these nebula-filled holes are the vacant lanes that so frequently run from them for great distances. These lanes undoubtedly have had something to do with the formation of the holes and with the nebula in them "

– E. E. Barnard, 1857–1923

In the previous chapter, various properties of G148.24+00.41 were investigated in order to find out its cluster formation potential and mechanism(s) by which an eventual cluster may emerge. Based on *Herschel* observations, it was found that the cloud hosts a massive clump at its centre of potential, which lies at the nexus of several large-scale (5−10 pc) filament-like structures (shown in Figure 3.1). Using *Spitzer* mid-IR images, the presence of an embedded cluster near the geometric central location (shown in Figure 3.1) of the cloud was observed. The cluster is not visible in optical and barely visible in near-infrared 2MASS images, suggesting that the young cluster is still forming. Using various observational metrics of the cloud, it was found that the *monolithic* collapse is not likely a scenario in G148.24+00.41 to form a stellar cluster. Comparing our findings with the prediction of different models of cluster formation, we argued that the cloud has the potential to make an intermediate-to-massive cluster through the hierarchical assembly of both gas and stars, such as those predicated in conveyor-belt type models.

The physical and kinematic structure of gas in GMCs is typically complex due to the interplay of turbulence and gravity. Gas kinematics provides a diagnostic tool for understanding the physical processes involved in the conversion of gas mass into stellar mass. Thus, in this chapter, we explore a 1-square degree area centred around the hub of G148.24+00.41 and present the detailed study of large-scale gas properties and kinematics of the various structures associated with the cloud. The aim is to understand the gas assembly processes from cloud to clump scale and, thus, the role of the gaseous structures in the formation of the stars or star clusters as evidenced in the cloud.

3.1 Filamentary structure of molecular clouds

The quotation given at the start of this chapter by EE Barnard was actually the first reported discussion of filaments in the ISM (Barnard, 1907). In the quotation, it is meant that the dark lanes (filaments) are connected to holes (dense cores) and nebulae (stars). Astronomers have been studying these filaments and their connection with star formation and magnetic fields since 1970 (see the review article by Hacar et al., 2022). However, the observations of *Herschel* space observatory in far-infrared wavelengths revolutionized the study of filaments in the ISM. Its dust continuum images revealed that filaments are ubiquitous in the ISM and present in different environments, from atomic clouds to molecular clouds. Figure 3.2 shows the filamentary structure of the Galactic plane observed from *Herschel* at wavelengths 70, 160, and 350 μm. The regions heated by nearby young stars glow in shorter infrared wavelengths (violet-green regions in Figure 3.2), while the colder regions emit in longer wavelengths (redder regions in Figure 3.2). These filaments appear as dark lanes in near/mid-IR due to dust extinction, while at longer

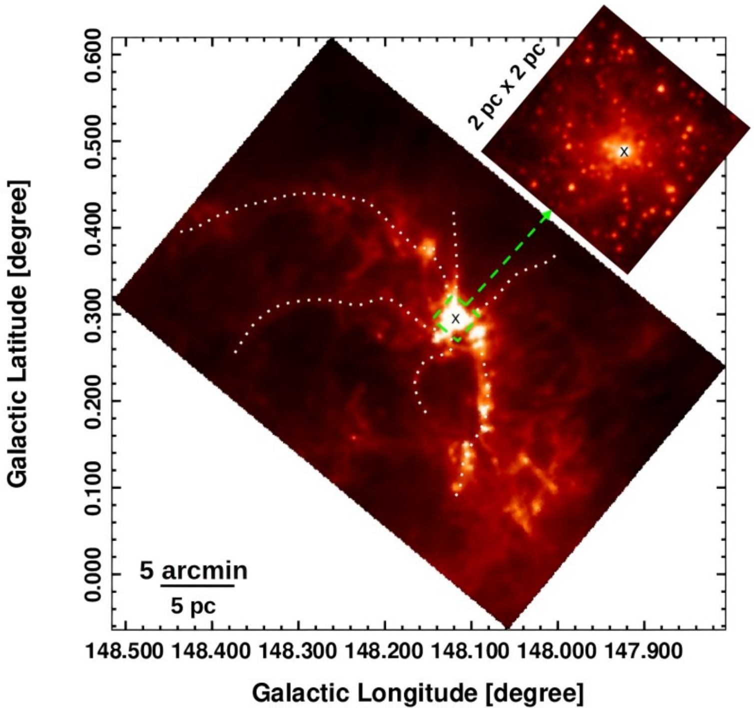

Figure 3.1: Central area of the G148.24+00.41 cloud as seen in *Herschel* 250 μm band, showing the hub-filamentary morphology. The inset image shows the presence of an embedded cluster within the hub region (shown by a green box) at 3.6 μm. The filamentary structures are the same as shown in Figure 2.16. For a better presentation of the molecular data, in this chapter, this figure, as well as the subsequent figures, are presented in the galactic coordinates, whereas figures in Chapter 2 are in the FK5 system.

wavelengths, the filaments appear as emission structures due to cold dust thermal emission.

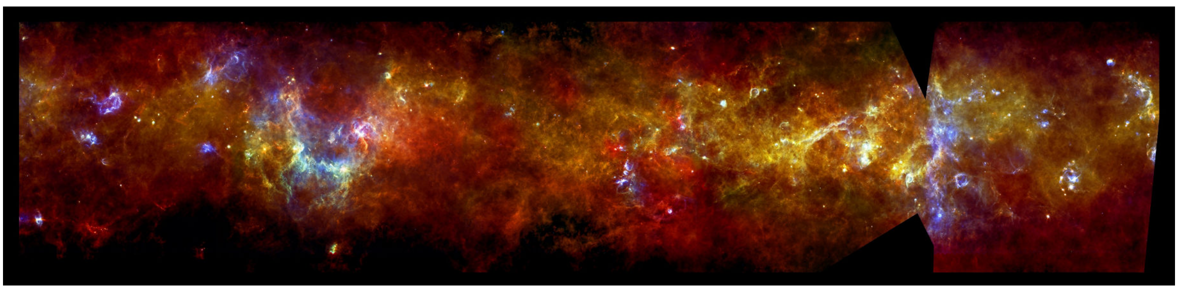

Figure 3.2: The *Herschel* 3-color (blue 70 μm, green 160 μm, and red 350 μm) image of the Galactic plane. *Credit: ESA/PACS & SPIRE Consortium, S. Molinari, Hi-GAL Project.*

Over the last decade, various dust continuum and molecular line observations suggest that the interstellar medium is filamentary, consisting of filamentary structures of different shapes and sizes at all scales (André et al., 2010; Molinari et al., 2010; Schisano et al., 2014; Shimajiri et al., 2019; Liu et al., 2021; Li et al., 2022; Zavagno et al., 2023). These filaments span a huge range of size from sub-parsec in clouds (Hacar et al., 2013) to kpc in spiral arms (Zucker et al., 2015). Depending on densities and scales, they are often called filaments, fibres, and streamers (for details, see review articles by Hacar et al., 2022; Pineda et al., 2022). Many studies from *Herschel*, ALMA, and other molecular line and continuum observations show that the filaments play a very crucial role in the overall star formation process (see Hacar et al., 2022, and references therein). In fact, the filaments are the preferred sites of active star formation (Könyves et al., 2015; André, 2017), with high-mass stars and stellar clusters preferentially forming in the high-density regions of the clouds such as hubs and ridges (Myers, 2009; Motte et al., 2018; Kumar et al., 2020, 2022; Beltrán et al., 2022; Yang et al., 2023; Zhang et al., 2023), where converging flows found to be funnelling the cold matter to the hub through the filamentary networks (e.g. Schneider et al., 2010; Treviño-Morales et al., 2019). Thus, evaluating the physical conditions of the gas in molecular clouds and characterizing structures, such as filaments, ridges, and hubs, and investigating their kinematics using molecular line data, are crucial steps for understanding the evolution of molecular clouds and associated cluster formation.

3.2 Data used

The dust continuum emission data used in the previous chapter are 2D data sets and give the integrated emission of all the dust along the line-of-sight. The advantage of molecular cube data is that it adds an extra dimension, i.e. the velocity information at each pixel, such that each pixel consists of a spectrum. This velocity information is crucial for understanding the gas flow in the cloud. The molecular line data of the G148.24+00.41 complex in ^{12}CO, ^{13}CO, and C^{18}O lines (J = 1–0 transitions) at 115.271, 110.201, and 109.782 GHz, respectively, were observed with the 13.7-m radio telescope as part of the MWISP survey (Su et al., 2019), led by PMO. The MWISP survey mapping covers the Galactic longitude from l = 9°.75 to 230°.25 and the Galactic latitude from b = −5°.25 to 5°.25. The three CO isotopologue line observations were done simultaneously using a 3 × 3 beam sideband-separating Superconducting Spectroscopic Array Receiver system (Shan et al., 2012) and using the position-switch on-the-fly mode, scanning the region at a rate of 50″per second. The calibration was done using the standard chopping wheel method that allows switching between the sky and an ambient temperature load. The calibrated data were then re-gridded to 30″pixels and mosaicked to a FITS cube using the GILDAS software package (Guilloteau & Lucas, 2000). The antenna temperature (T_A) has been converted to the main-beam temperature (T_{MB}) using the relation $T_{MB} = T_A/B_{eff}$, where B_{eff} is the beam efficiency, which is 46% at 115 GHz and 49% at 110 GHz. The spatial resolutions (Half Power Beam Width; HPBW) of the observations are around ∼49″, 52″, and 52″for ^{12}CO, ^{13}CO, and C^{18}O, respectively, which correspond to a spatial resolution of ∼0.8−0.9 pc at the distance of the cloud (∼3.4 kpc). The spectral resolution of ^{12}CO is ∼0.16 km s^{-1} with a typical rms noise level of the spectral channel is about 0.5 K, and of ^{13}CO and C^{18}O is ∼0.17 km s^{-1} with a rms noise level of 0.3 K (for details, see Su et al., 2019).

3.3 Analyses and results

The advantage of using the CO (1–0) isotopologues is that one can use the ^{12}CO emission to trace the enveloping layer (i.e. ∼10^2 cm^{-3}) of the molecular cloud to reveal its large-scale low surface brightness structures and dynamics. On the other hand, the optically thin ^{13}CO and C^{18}O emission (discussed in Section 3.3.1.2) can trace the denser regions (i.e. ∼10^3–10^4 cm^{-3}) such as large-scale filamentary structure and dense clumps within the cloud. By combining the CO isotopologues, the overall properties of the diffuse regions of the cloud, as well as the gas properties and physical conditions of the dense structures within it, can be determined.

3.3.1 Global cloud morphology, properties, and kinematics

3.3.1.1 Gas morphology and kinematics

In the previous chapter, based on ^{12}CO spectrum and comparing the CO gas morphology with the dust continuum images (*Herschel* images at 250, 350 and 500 μm), it was shown that the G148.24+00.41 cloud component mainly lies in the velocity range of −37.0 km s^{-1} to −30.0 km s^{-1} in agreement with the previous studies (e.g. Urquhart et al., 2008; Miville-Deschênes et al., 2017). Figure 3.3 shows the average spectrum of all three isotopologues towards the cloud.

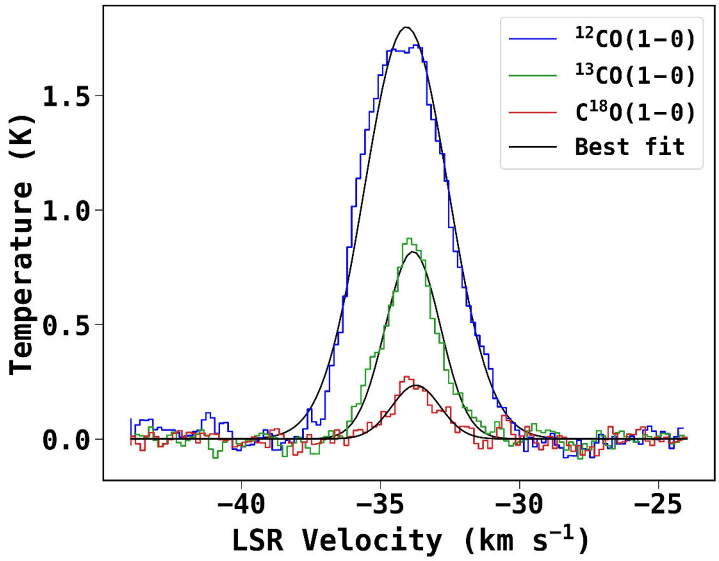

Figure 3.3: The average ^{12}CO, ^{13}CO, and C^{18}O spectral profiles towards the direction of the G148.24+00.41 cloud. The black solid curve shows the Gaussian fit over the spectra.

We fitted a Gaussian function to the line profiles and derived the peak velocity, velocity dispersion (σ_{1d}), and velocity range of each spectrum, which are given in Table 3.1. The estimated line-width ($\Delta V = 2.35\,\sigma_{1d}$) and 3D velocity dispersion ($\sigma_{3d} = \sqrt{3} \times \sigma_{1d}$) associated with the ^{12}CO profile are 3.55 and 2.62 km s^{-1}, for ^{13}CO are 2.30 and 1.70 km s^{-1}, and for C^{18}O are 2.04 and 1.51 km s^{-1}, respectively. We want to point out that the optical thickness of ^{12}CO may affect the velocity centroid and velocity dispersion of the line profile. Therefore, the ^{12}CO data has been used to measure the global properties and distribution of low-density gas, while the kinematics of dense structures or properties of dense clumps have been derived using the ^{13}CO and C^{18}O data.

The integrated intensity (moment-0) maps of ^{12}CO, ^{13}CO, and C^{18}O line emissions, integrated in the velocity range given in Table 3.1, are shown in Figure 3.4. Also shown are the contours above 3σ of the background value, where σ is the standard deviation of the background emission. As discussed earlier, in molecular clouds, the ^{12}CO, traces better the diffuse emission, while ^{13}CO and C^{18}O probe deeper into the cloud and trace higher column density regions. Though the spatial resolution of the data is relatively low, the presence of several filamentary structures can be seen in the ^{13}CO map (details are discussed in section 3.3.2), while C^{18}O emission seems better at tracing the central area and the dense clumpy structures of the cloud. In G148.24+00.41, we find that ^{13}CO covers ~87% of the ^{12}CO emission, while C^{18}O covers only 43%.

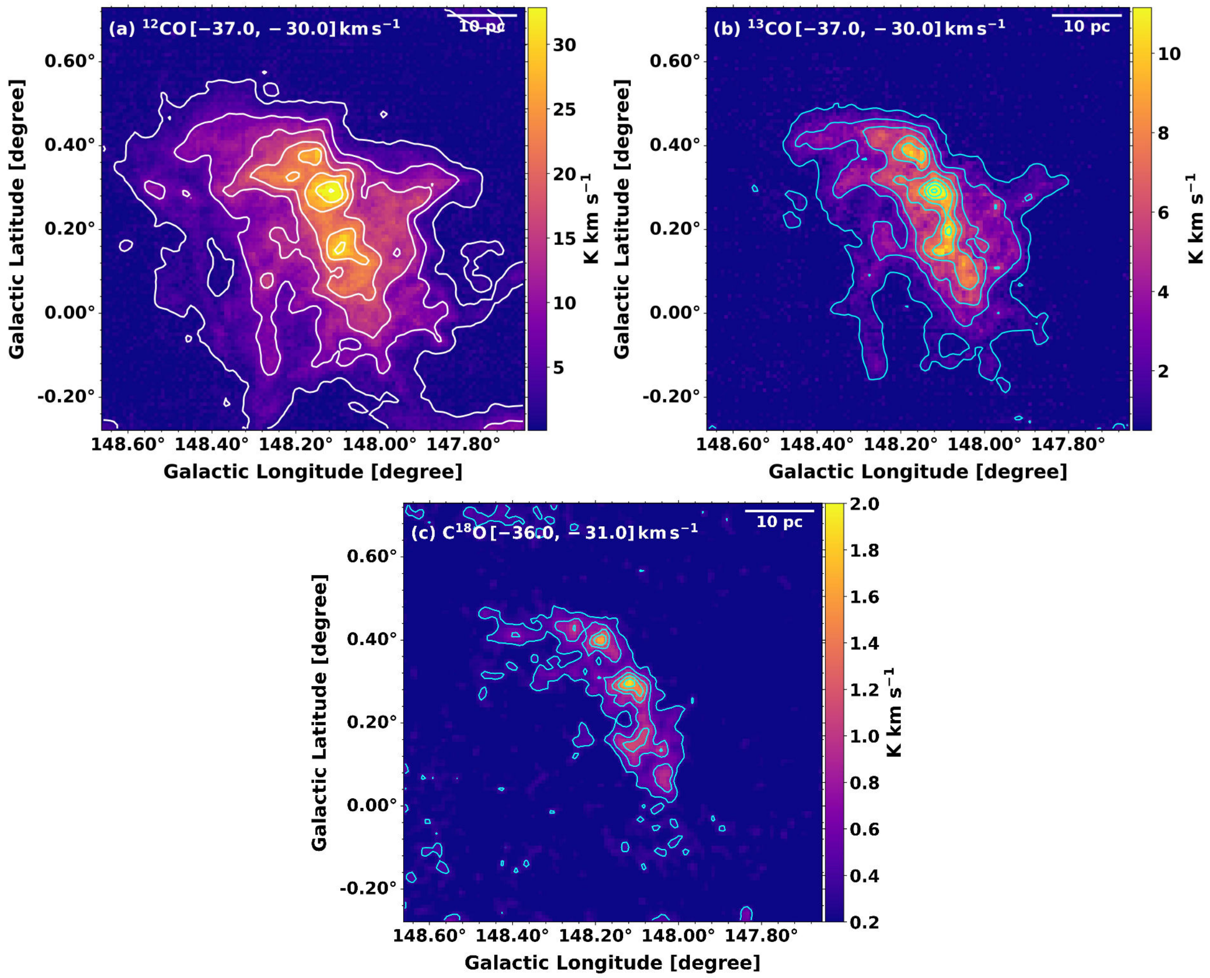

Figure 3.4: (a) ^{12}CO integrated intensity (moment-0) map of the cloud with contour levels at 1.5, 7.08, 12.67, 18.25, 23.83, 29.42, and 35 K km s^{-1}. (b) ^{13}CO integrated intensity map of the cloud with contour levels at 0.9, 2.7, 4.5, 6.3, 8.1, 9.9, 11.7, and 13.5 K km s^{-1}. (c) C^{18}O integrated intensity map of the cloud with contour levels at 0.35, 0.68, 1.01, 1.34, 1.67, and 2.0 K km s^{-1}. The contours are drawn 3σ above the background value of individual maps. The C^{18}O map has been smoothened by 1 pixel to improve the signal.

In order to understand the overall velocity distribution and velocity dispersion of the ^{12}CO and ^{13}CO gas in the cloud, we made intensity-weighted mean velocity (moment-1) and velocity dispersion (moment-2) maps, which are shown in Figures. 3.5a-b and Figures. 3.5c-d, respectively. In general, the velocity distribution maps reveal that the outer extent of the cloud exhibits blue-shifted velocities relative to the systematic one, typically ranging from −36 to −34 km s^{-1}, while the central region displays a red-shifted velocity range, from −34 to −30 km s^{-1}. Since moment analysis represents the mean velocity of the gas along the line of sight, it is insensitive to the kinematics of the multiple velocity structures, if present in the cloud (more discussion in Section 3.3.2.2). Figures. 3.5c-d shows that the velocity dispersion is not uniform across G148.24+00.41, it varies from 0.2 to 2.3 km s^{-1}, with a notable increase in the cloud's central area. The velocity dispersion of ^{12}CO gas may be on the higher side due to the optical depth effect, but this trend also holds true for the relatively optically thin ^{13}CO line. In the central area, a patchy increase in velocity dispersion can be seen at several locations. More discussion on this is given in Section 3.3.3.2. Additionally, the ^{12}CO map reveals high velocity dispersion in the north-eastern side of the cloud, whose exact reason is not known to us. External shock compression can result in such high dispersions. Although a young (~4 Myr) H II region is found to be present in the vicinity of the cloud (Romero & Cappa, 2009). However, the H II region is located in the south-western direction of G148.24+00.41 and is also at a different distance (i.e. ~1 kpc) with respect to it. A detailed investigation covering wider surroundings of G148.24+00.41 is needed to better understand its origin, which is beyond the scope of the present work.

3.3.1.2 Physical conditions and gas column density

Assuming the molecular cloud is in local thermodynamic equilibrium and ^{12}CO is optically thick, the excitation temperature, optical depth, and column density of the G148.24+00.41 cloud can be calculated using the measured brightness of CO isotopologues. Under LTE, the kinetic temperature of the gas is assumed to be equal to the excitation temperature. Using equation 1.1 and assuming beam filling factor to be 1 and T_{bg} = 2.7 K for CMBR, the T_{ex} can be derived and written in a simplified form (Garden et al., 1991; Nishimura et al., 2015; Xu et al., 2018) as :

$$T_{\mathrm{ex}}^{1-0} = \frac{5.53}{\ln\left[1 + \frac{5.53}{T_{\mathrm{MB,peak}}^{12,1-0} + 0.84}\right]}, \tag{3.1}$$

where $T_{\mathrm{MB,peak}}^{12,1-0}$ is the peak brightness temperature of the ^{12}CO emission along the line of sight. Based on the above formalism, the excitation temperature at each pixel of the cloud was derived. Figure 3.6a shows the excitation temperature map, which ranges from 5 K to 21 K with a median around 8 K. The temperature map shows a relatively high temperature in the central region of the cloud with respect to the outer extent. This is likely due to the fact that the central region is heated by the protostellar radiation, where it has been found that protostars are actively forming (see Figure 2.17 in Chapter 2). The obtained average excitation temperature of the cloud is

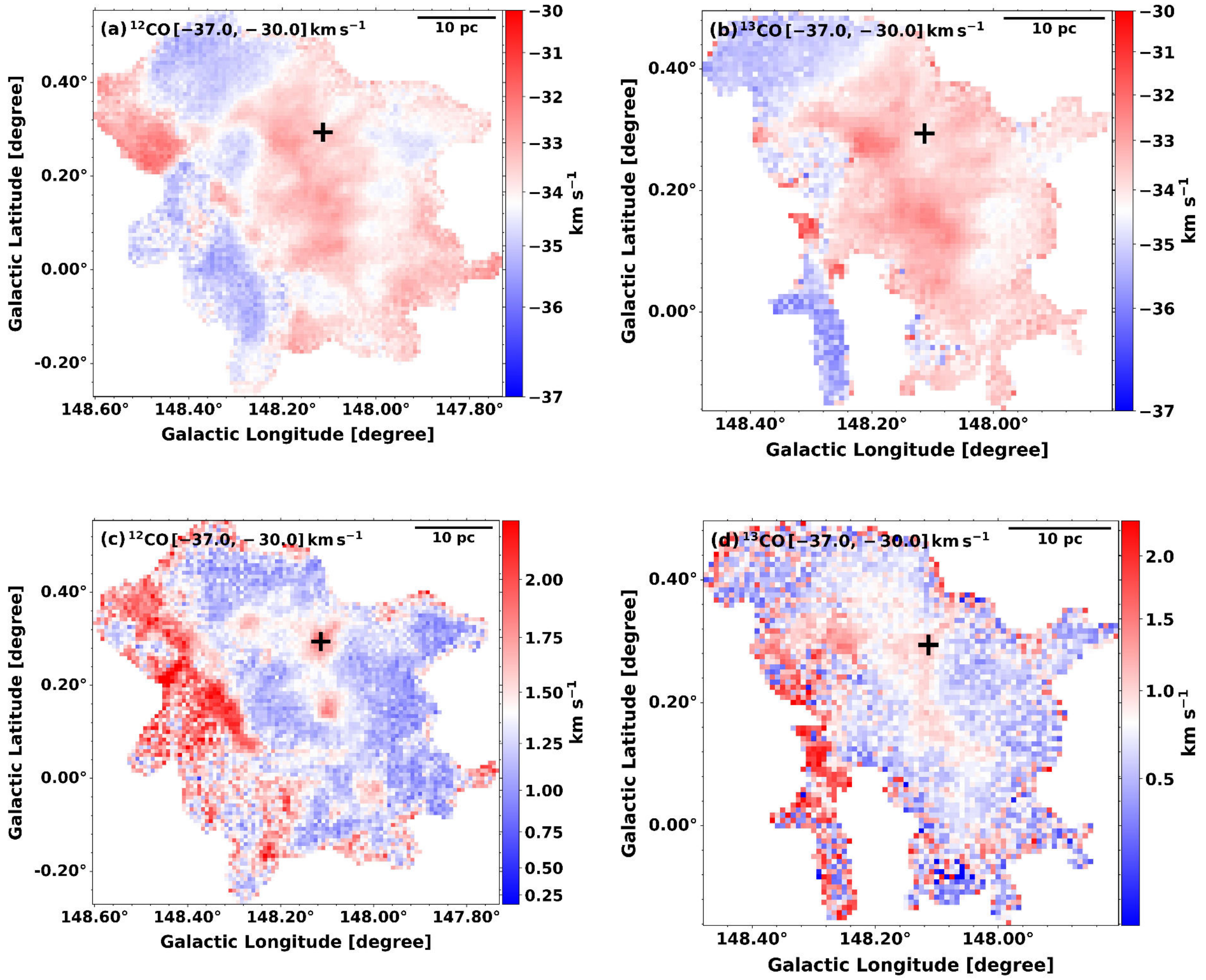

Figure 3.5: (a) ^{12}CO and (b) ^{13}CO velocity maps of G148.24+00.41. (c) ^{12}CO and (d) ^{13}CO velocity dispersion maps of G148.24+00.41. The location of the hub is marked with a plus sign.

found to be similar to the ^{12}CO based excitation temperature of massive GMCs with embedded filamentary dark clouds (e.g. ~7.4 K, Hernandez & Tan, 2015, and references therein) and also similar to other nearby molecular clouds such as Taurus (~7.5 K, Goldsmith et al., 2008) and Perseus (~11 K, Pineda et al., 2008).

Next we derived the optical depth maps of ^{13}CO and C^{18}O gas using the following relations (Garden et al., 1991; Pineda et al., 2010):

$$\tau_{13} = -\ln\left[1 - \frac{T^{13}_{\mathrm{MB,peak}}}{5.29}\left[\frac{1}{\exp(5.29/T_{\mathrm{ex}}) - 1} - 0.164\right]^{-1}\right] \tag{3.2}$$

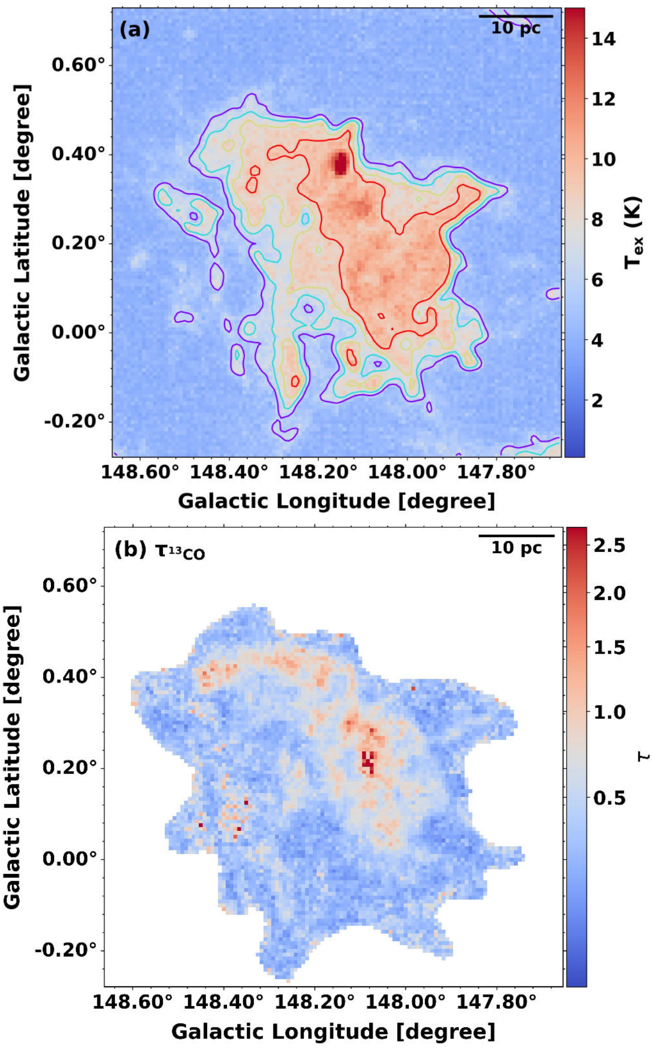

Figure 3.6: (a) Excitation temperature map overplotted with contours at 6, 7, 8, and 9 K. (b) Optical depth map of ^{13}CO .

$$\tau_{18} = -\ln\left[1 - \frac{T^{18}_{\rm MB,peak}}{5.27}\left[\frac{1}{\exp(5.27/T_{\rm ex}) - 1} - 0.166\right]^{-1}\right], \tag{3.3}$$

where $T^{13}_{\rm MB,peak}$ and $T^{18}_{\rm MB,peak}$ is the peak brightness temperature of ^{13}CO and C^{18}O, respectively. The optical depths of ^{13}CO and C^{18}O lines are estimated to be $0.1 < \tau(^{13}\mathrm{CO}) < 3.0$ and $0.05 < \tau(\mathrm{C}^{18}\mathrm{O}) < 0.25$, respectively. Figure 3.6b shows the optical depth map of the ^{13}CO emission. Within the cloud area, it was found that only a 5% fraction of the area is of high ($\tau > 1$) optical depth, implying that most of the observed ^{13}CO emission is optically thin.

We then calculated the column density of ^{13}CO and C^{18}O using the following relations from

Bourke et al. (1997):

$$N(^{13}\mathrm{CO})_{\mathrm{thin}} = 2.42 \times 10^{14} \times \left(\frac{T_{\mathrm{ex}} + 0.88}{1 - \exp(-5.29/T_{\mathrm{ex}})} \right) \times \frac{1}{J(T_{\mathrm{ex}}) - J(T_{\mathrm{bg}})} \int T_{\mathrm{MB}}(^{13}\mathrm{CO})\,dv \quad (3.4)$$

$$N(\mathrm{C}^{18}\mathrm{O})_{\mathrm{thin}} = 2.42 \times 10^{14} \times \left(\frac{T_{\mathrm{ex}} + 0.88}{1 - \exp(-5.27/T_{\mathrm{ex}})} \right) \times \frac{1}{J(T_{\mathrm{ex}}) - J(T_{\mathrm{bg}})} \int T_{\mathrm{MB}}(\mathrm{C}^{18}\mathrm{O})\,dv \quad (3.5)$$

However, the ^{13}CO based column density may underestimate the column density in the central area of the cloud, where ^{13}CO is optically thick. Many studies on the GMCs and Infrared Dark Clouds have accounted for line optical depth while estimating their physical properties (Roman-Duval et al., 2010; Hernandez et al., 2011). I, thus applied the following correction to the $N(^{13}\mathrm{CO})_{\mathrm{thin}}$ following Pineda et al. (2010); Li et al. (2015). Since the observed C^{18}O emission is optically thin, no optical depth correction was made to $N(\mathrm{C}^{18}\mathrm{O})_{\mathrm{thin}}$.

$$N(^{13}\mathrm{CO})_{\mathrm{corrected}} = N(^{13}\mathrm{CO})_{\mathrm{thin}} \times \frac{\tau_{13}}{1 - e^{-\tau_{13}}} \quad (3.6)$$

The ^{13}CO and C^{18}O column densities are then converted to the molecular hydrogen column density using the relation, N(H_2) = 7 × 10^5 N(^{13}CO) (Frerking et al., 1982) and N(H_2) = 7 × 10^6 N(C^{18}O) (Castets & Langer, 1995), respectively. The molecular hydrogen column densities from the ^{13}CO and C^{18}O gas emission are estimated to be around 0.9×10^{21} cm^{-2} < N$(H_2)_{^{13}CO}$ < 2.4×10^{22} cm^{-2} and 1.1×10^{21} cm^{-2} < N$(H_2)_{C^{18}O}$ < 2.0×10^{22} cm^{-2}, respectively. For the common area, the column density of both the maps are in agreement with each other by a factor of 1.5. The observed variation in column density values might be due to the abundance variations of these isotopologues. For example, chemical models and observations suggest that selective photo-dissociation and fractionation can significantly affect the abundance of CO isotopologues (e.g. Shimajiri et al., 2015; Liszt, 2017).

Since ^{13}CO covers a larger area and has a better signal-to-noise ratio compared to C^{18}O,

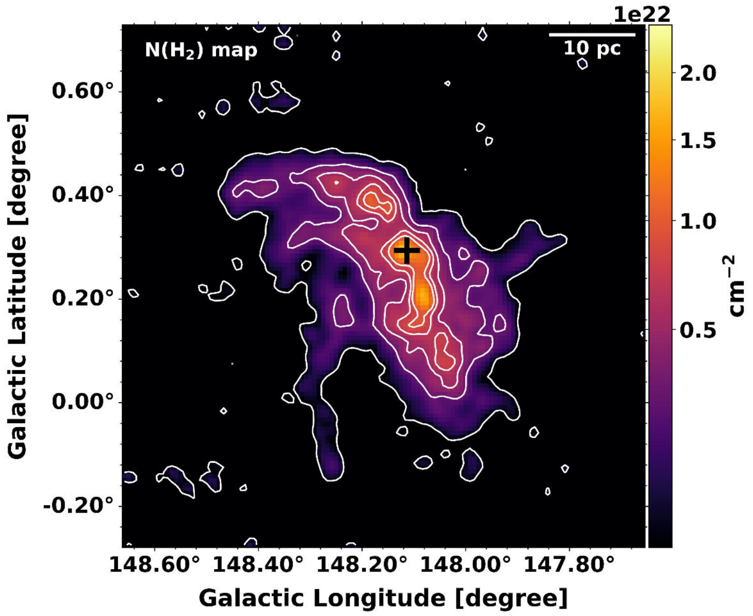

Figure 3.7: Molecular hydrogen column density map based on ^{13}CO . The contour levels are shown above 3σ of the background value, starting from 0.9×10^{21} to 9×10^{21} cm^{-2} . The location of the hub is marked with a plus sign.

thus, we used ^{13}CO based column density map for further analysis, such as in deriving the global properties of the cloud. Figure 3.7 shows the ^{13}CO based N(H$_2$) map, tracing well the central dense location of the cloud. We find the peak value of N(H$_2$) is around 2.4×10^{22} cm^{-2}, which corresponds to the location of the hub.

The ^{12}CO emission in G148.24+00.41 is more extended than ^{13}CO emission; thus, for estimating column density of the cloud area located outside the boundary of ^{13}CO emission, we also estimated the hydrogen column density of each pixel directly from the ^{12}CO intensity, I(^{12}CO), using the relation N(H$_2$) = X$_{\rm CO}$ I(^{12}CO). Here X$_{\rm CO}$ is the CO-to-H$_2$ conversion factor, whose typical value is $\sim 2.0 \times 10^{20}$ cm^{-2} (K km s^{-1})$^{-1}$ (Dame et al., 2001; Bolatto et al., 2013; Lewis et al., 2022) with an uncertainty of around 30% (Bolatto et al., 2013). We also estimated the total ^{12}CO column density from the ^{13}CO optical depth map, using an average value of ^{12}CO / ^{13}CO abundance of ∼60 (Frerking et al., 1982) and equation 3 of Garden et al. (1991). Doing so, we found that the total molecular hydrogen column density of the cloud based on both approaches is within a factor of 1.3.

The ^{12}CO and ^{13}CO column density maps are combined to make a composite molecular hydrogen column density map. For the area lying outside the area of ^{13}CO emission, the column

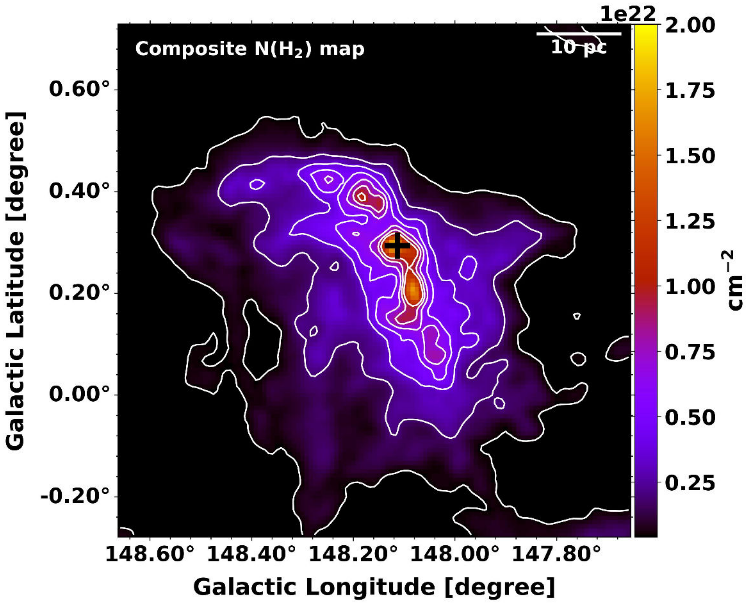

Figure 3.8: Composite N(H$_2$) map based on ^{12}CO and ^{13}CO column density maps. The contour levels are shown above 3σ of the background value, starting from 4.3 × 10^{20} to 1 × 10^{22} cm^{-2} . The location of the hub is marked with a plus sign.

density values from the ^{12}CO emission were taken. Although we used N(H$_2$)$_{^{13}\mathrm{CO}}$ column density values within the ^{13}CO emission area, we observed that some of the pixels in the central area of the ^{13}CO map exhibit lower column density values than the neighbouring pixels. Overall, these outliers do not affect the measured global properties. Nonetheless, in these pixels, if the ratio of N(H$_2$)$_{^{13}\mathrm{CO}}$ to N(H$_2$)$_{^{12}\mathrm{CO}}$ is found to be > 1, the pixel values from the N(H$_2$)$_{^{13}\mathrm{CO}}$ map are considered, otherwise, from the N(H$_2$)$_{^{12}\mathrm{CO}}$ map. The combined composite map made in this way is shown in Figure 3.8. The column density of the composite map lies in the range of 0.2 × 10^{21} cm^{-2} to 2.4 × 10^{22} cm^{-2}. The difference in column density values at the boundary of ^{13}CO emission from both the tracers are within a factor of 1.2, thus reasonably agreeing with each other.

3.3.1.3 Global cloud properties and comparison with Galactic clouds

We obtained the cloud properties like mass, effective radius, surface density, and volume density, following the approach described in Section 2.2.2.1 of Chapter 2. Briefly, we estimated the mass of the cloud using equation 2.1. Then, we defined the outer extent (thus the area) of G148.24+00.41 for different tracers by considering emission within the 3σ contours (see Figure

3.4) and derived its properties within this area. The cloud mass from ^{12}CO, ^{13}CO, and C^{18}O based N(H$_2$) column density map, calculated above the 3σ emission is ~5.8 × 10^4 M$_\odot$, ~5.6 × 10^4 M$_\odot$, and ~3.5 × 10^4 M$_\odot$, respectively. The cloud mass estimated from the composite column density map is found to be ~7.2 × 10^4 M$_\odot$. To check the boundness status of G148.24+00.41, we calculated its virial mass using the relation, $M_{vir} = 126 \times 1.33\, r_{\rm eff} \Delta V^2$, for density index, $\beta = 1.5$ (see equation 2.2). Using $r_{\rm eff}$ and ΔV values of ^{12}CO, ^{13}CO, and C^{18}O (see Table 3.1), the estimated $M_{\rm vir}$ is around ~4 × 10^4 M$_\odot$, 1.5 × 10^4 M$_\odot$, and 8.6 × 10^3 M$_\odot$, respectively. Since the virial mass of G148.24+00.41, as estimated by ^{12}CO, ^{13}CO, and C^{18}O, is less than their respective gas mass, it implies that the cloud is bound in all three CO isotopologues. We acknowledge that the optical thickness of ^{12}CO line can make the line profile broader, as discussed in Section 3.3.1.1, thus, the ^{12}CO based virial mass can be an upper limit. Even then, the aforementioned boundness status of the cloud will remain true.

The typical uncertainty associated with the estimation of gas mass from the ^{12}CO, ^{13}CO, and C^{18}O emissions is in the range 35−44%. Because the uncertainty in the assumed X$_{\rm CO}$ factor and in the isotopic abundance values of CO molecules, used in converting N(CO) to N(H$_2$) is around 30 to 40% (Wilson & Rood, 1994; Savage et al., 2002; Bolatto et al., 2013). The distance uncertainty associated to the cloud is around 9%. In addition, the estimation of N(CO) is also affected by the uncertainty associated with the estimated gas kinematic temperature. In the present case, it was found that the average gas kinetic temperature (8 K) is lower than the average dust temperature of the cloud, 14.5 ± 2 K (see Chapter 2). When gas and dust are well mixed, the gas kinematic temperature better corresponds to the dust temperature, and this occurs when the density is > 10^4 cm^{-3}. For example, Goldsmith (2001) found that dust and gas are better coupled at volume densities above 10^5 cm^{-3}, which are typically not traced by ^{12}CO and ^{13}CO data (n$_{\rm crit}$ < 10^4 cm^{-3}). They find a temperature difference of ~4 K at density ~10^5 cm^{-3}and completely negligible at density ~10^6 cm^{-3}. Moreover, it is also suggested that if the volume density of the gas is lower than the critical density of ^{12}CO, this would lead to a lower excitation temperature (Heyer et al., 2009). Assuming the true average temperature of the gas to be around 14 K, it would change the ^{13}CO column density by a factor of 14%, hence the estimated gas mass would also change by this factor.

In the present work, though we have derived the masses using canonical values of X factor and the CO abundances, however, it is worth mentioning that many studies have suggested that these values increase towards the outer galaxy (Nakanishi & Sofue, 2006; Pineda et al., 2013; Heyer & Dame, 2015; Patra et al., 2022). Since G148.24+00.41 is located in the outer galaxy (i.e. ~11.2 kpc from the Galactic centre), the derived masses are likely underestimations. For example, we find that implementing X_{CO} value from the relation given in Nakanishi & Sofue (2006), would increase the total $N(H_2)_{^{12}CO}$ column density and thus, the mass by a factor of ~2.

The total gas mass estimated for G148.24+00.41 using the composite column density map, within uncertainty, agrees with the dust-based gas mass $\sim(1.1 \pm 0.5) \times 10^5$ $M_\odot$, derived in Chapter 2. The mass, mean column density, effective radius, surface density, and volume density of the cloud are given in Table 3.1. The derived surface mass density from ^{12}CO, ^{13}CO, $C^{18}O$, and composite map is ~52, 59, 72, and 63 $M_\odot$ pc^{-2}, respectively. The surface mass density from ^{12}CO is similar to the value obtained for G148.24+00.41 from the dust continuum and dust extinction-based column density maps for the same area in Chapter 2 (i.e. Σ_{gas} = 52 $M_\odot$ pc^{-2}). Since the isotopologues trace different areas of the cloud, their estimated surface densities are different, with a gradual increase from low-density to high-density tracer.

Comparing the properties of G148.24+00.41 with other Galactic clouds, we find that the ^{12}CO surface density of G148.24+00.41 is significantly higher than the average surface density (~10 $M_\odot$ pc^{-2}) of the outer Galaxy molecular clouds of our own Milkyway (Miville-Deschênes et al., 2017). Miville-Deschênes et al. (2017) studied Galactic plane clouds using ^{12}CO and found that the average mass surface density of clouds is higher in the inner Galaxy, with a mean value of 41.9 $M_\odot$ pc^{-2}, compared to 10.4 $M_\odot$ pc^{-2} in the outer Galaxy. Similarly, we also find that the derived ^{13}CO surface density of G148.24+00.41 is on the higher side of the surface densities of the Milkyway GMCs studied by Heyer et al. (2009). Heyer et al. (2009) found an average surface density value ~42 $M_\odot$ pc^{-2} using ^{13}CO data, assuming LTE conditions and a constant H_2 to ^{13}CO abundance, similar to the approach used in this work. Recently Lewis et al. (2022) investigated nearby star or star-cluster forming GMCs, including Orion-A, using ^{12}CO emission and similar X_{CO} factor used in this work. Comparing the surface densities of these clouds, we find that the surface density of G148.24+00.41 is higher than most of their studied GMCs (average ~37.3 ± 10 $M_\odot$ pc^{-2}) and comparable to the surface density of Orion-A (see Figure 8 of Lewis et al., 2022). All the aforementioned comparisons support the inference drawn in Chapter 2 on G148.24+00.41 based on the dust continuum analysis, i.e. G148.24+00.41 is indeed a massive GMC like Orion-A.

3.3.2 Filamentary structures in G148.24+00.41

As discussed in Chapter 2, based on dust continuum maps, it was suggested that the central cloud region likely consists of six filaments, forming a hub filamentary system (HFS) with the hub being located at the nexus or junction of these filaments. Molecular clouds with HFSs are of particular interest because these are the sites where cluster formation would take place, as advocated in many simulations (e.g. Naranjo-Romero et al., 2012; Gómez & Vázquez-Semadeni, 2014; Gómez et al., 2018; Vázquez-Semadeni et al., 2019). Massive and elongated hub regions are sometimes referred to as "ridges" (e.g. Hennemann et al., 2012; Tigé et al., 2017; Motte et al., 2018).

The LOS velocity gradient, traced by molecular lines, is commonly interpreted as a proxy for the POS gas motion. Recent molecular line observations have revealed the kinematic structures of several HFSs in nearby clouds, and significant velocity gradients are observed along several filaments that are attached to HFSs (e.g. Liu et al., 2012; Friesen et al., 2013; Hacar et al., 2018; Dewangan et al., 2020; Chen et al., 2020; Yang et al., 2023; Liu et al., 2023). These gas motions are thought to represent dynamical gas flows which are fuelling the hub. In the following, we identify and characterize the filamentary structures in the cloud and discuss their role in star and cluster formation observed in the cloud.

3.3.2.1 Identification of global filamentary structures

We used a python-based package - *FilFinder*[1] (Koch & Rosolowsky, 2015) to identify the filamentary structures of the cloud using the ^{13}CO based molecular hydrogen column density map. The *FilFinder* package picks out the structures within a given mask by comparing each pixel to those in the surrounding neighbourhood using adapting thresholding. The algorithm then reduces the filament mask to skeletons using the Medial Axis Transform (MAT) method. Finally, it prunes down the skeleton structure to a filamentary network. *Filfinder* not only extracts bright filaments but also reliably extracts fainter structures such as striations. We set the following

[1] https://github.com/e-koch/FilFinder

Table 3.1: G148.24+00.41 properties from CO emission. The mass of the cloud from ^{12}CO, ^{13}CO, and C^{18}O is calculated above 3σ from the mean background emission. The FWHM is the line-width of the spectra, calculated as $\Delta V = 2.35\sigma_{1D}$.

Emission	Velocity interval (km s^{-1})	V$_{peak}$ (km s^{-1})	FWHM (ΔV) (km s^{-1})	Mean N(H$_2$) ($\times 10^{21}$ cm^{-2})	Mass (M$_\odot$)	n(H$_2$) (cm^{-3})	r$_{eff}$ (pc)	Σ_{gas} (M$_\odot$ pc^{-2})
^{12}CO	(−37.0, −30.0)	−34.07	3.55	2.3	5.8×10^4	30	18.8	52
^{13}CO	(−37.0, −30.0)	−33.83	2.30	2.6	5.6×10^4	37	17.3	59
C^{18}O	(−36.0, −31.0)	−33.72	2.04	3.2	3.5×10^4	63	12.4	72
Composite-map (^{12}CO & ^{13}CO)	(−37.0, −30.0)	—	—	2.8	7.2×10^4	37	19.0	63

optimum values in *Filfinder* for creating mask and applying adapting thresholding, whose output matches better with the elongated structures visually seen in the column density map: i) global threshold, the intensities below this value are cut off from being included in the mask, as two times the background column density value, ii) adaptive threshold, the expected full width of filaments for adaptive thresholding, as 10 pixels (i.e. ∼5 times beam-width), iii) smooth size, used to smoothen the image to minimize the extraneous branches on the skeletons as 2 pixels (i.e. ∼1.0 times beam-width), iv) size threshold, the minimum dimensions expected for a filament as 100 pixels^2 (i.e. ∼20 times beam area). The emission structures were first flattened to 95 percentiles before applying the adapting thresholding to suppress the significantly brighter objects than filamentary structures such as dense cores.

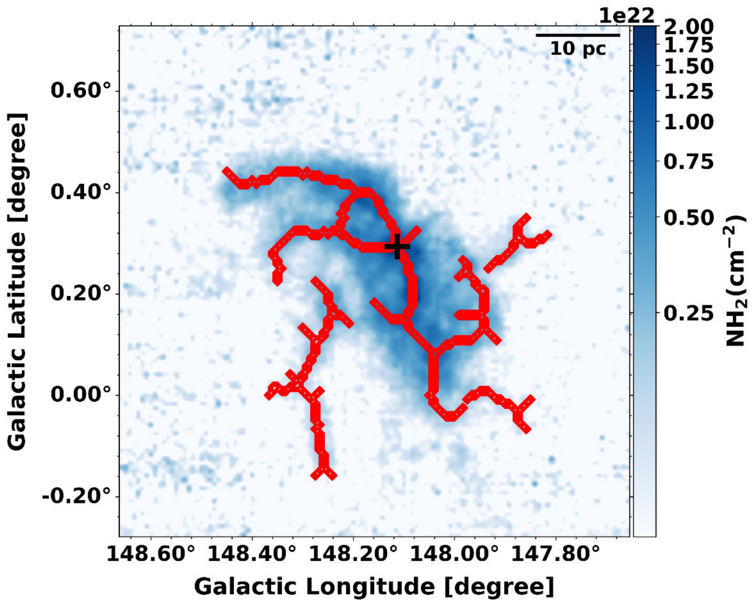

Figure 3.9: Global skeletons of G148.24+00.41 showing the filamentary structures, main ridge, nodes, and central hub location, over the ^{13}CO based N(H_2) map. The location of the hub is marked with a plus sign.

Figure 3.9 shows the extracted skeletons of the G148.24+00.41 cloud. It can be seen that the *Filfinder* algorithm reveals several filamentary structures, including the main central filament that runs from north-east to south-west, and also several nodes where the filaments are intersecting. The column density map is created from the integrated intensity map. So it's important to acknowledge that in the integrated intensity map, multiple individual velocity features may blend together and appear as a single one, as observed in nearby filamentary clouds (e.g. Hacar et al., 2013, 2017) or in distant ridge (e.g. Hu et al., 2021; Cao et al., 2022). Velocity sub-structures of gas in a cloud can be inspected using channel maps, in which the emission integrated over a narrow velocity range is examined. It is then possible to identify individual velocity coherent structures that are very likely to correspond to the physically distinct structures of the cloud.

3.3.2.2 Small-scale gas motion and velocity coherent structures

Figure 3.10 shows the ^{13}CO velocity channel maps with a step of 0.34 km s^{-1}. As can be seen from the channel maps, along with several compact emissions, multiple spatially elongated velocity structures are also present. These elongated structures are marked as St-1, St-2, St-3, St-4, St-5, and St-6 on the map. The location of these structures in the map corresponds to either the maximum intensity feature or has relatively the longest distinct visible structure, or both. These structures have noticeable differences in velocity because they emerge in different velocity channels.

The majority of these structures appear to move towards the hub location, marked by a plus sign on the map. The merger and convergence of these structures form a nearly continuous structure in the central area of the cloud, referred to as the "ridge", where the hub is located. The ridge is marked by a solid green line on the channel map. The ridge also seems to be attached to several small-scale strand-like, nearly perpendicular elongated structures (shown by arrows in Figure 3.10). The kinematic association of such perpendicular structures with the main filament/ridge indicates the possible direct role of the surrounding gas on the formation and growth of the main filament/ridge (e.g. Cox et al., 2016). Besides, one can see that the structure, St-2, is composed of 2-3 small-scale filamentary structures that are seen in the channel maps at around -35.1 to -34.4 km s^{-1}. These structures are indistinguishable in the integrated intensity map shown in Figure 3.4b, emphasizing that some of the elongated filamentary structures that are visible in the integrated intensity map could be the sum of multiple velocity coherent structures.

3.3.2.3 Likely velocity coherent filaments

In molecular clouds, small-scale velocity coherent filaments (VCF) have been identified using position-position-velocity (PPV) maps, where the velocity components are grouped based on how closely they are linked in both position and velocity simultaneously (e.g. Hacar et al.,

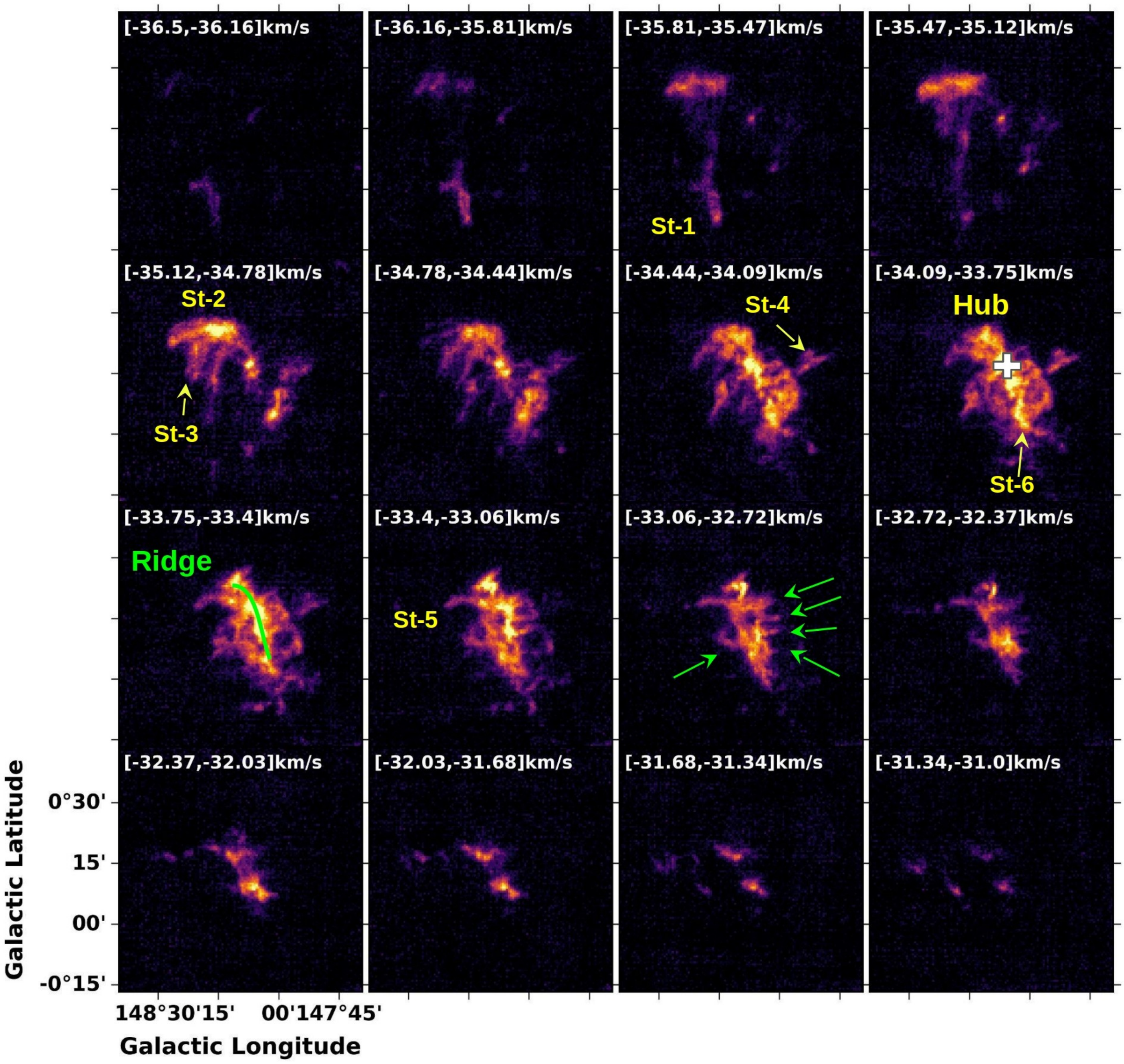

Figure 3.10: Velocity channel maps in units of K km s^{-1}for the ^{13}CO emission. The velocity ranges of the channel maps are indicated at the top left of each panel. The ridge (green curve), strands (green arrows), structures (yellow arrows), and the hub location (plus) are marked in the channel maps.

2013). In the literature, identification of VCFs is primarily done using high-resolution and high-density tracer (e.g. NH_3, N_2H^+, $C^{18}O$) data cubes and preferentially on the nearby clouds, where structures are well resolved (e.g. Hacar et al., 2017, 2018; Shimajiri et al., 2019). However, as witnessed from the channel maps, the gas kinematics of the cloud is quite complicated with overlapping structures. Disentangling and identifying individual velocity coherent structures is challenging with the present data. Nonetheless, to identify the likely VCF of G148.24+00.41, we followed an approach similar to that of the nearby molecular clouds. We visually inspected the

^{13}CO data cube and identified the velocity coherent structures that are continuous in position as well as velocity in the data cube. We then made the integrated intensity map of the structure by integrating the emission in the velocity range that encompasses the majority of its emission. In this way, we identified six likely velocity coherent filamentary structures in G148.24+00.41.

Figure 3.11 shows an example of an intensity map, integrated in the sub-velocity range, [−37.0, −34.0] km s^{-1}, where filament F1, F2, and F3 are identified, while F4, F5 and F6, are identified in the full velocity integrated intensity map (see Figure 3.9). Compared to Figure 3.11, the identification and delineation of F3 filament is confusing and difficult in Figure 3.9, whereas in Figure 3.11, the structure of F3 is better apparent, and seems to connect to F2. Although our approach is subject to the choice of velocity range, it is noted that, except for one, the majority of the identified structures matched well with the structures shown in Figure 3.9, but were separated into different velocity coherent filaments.

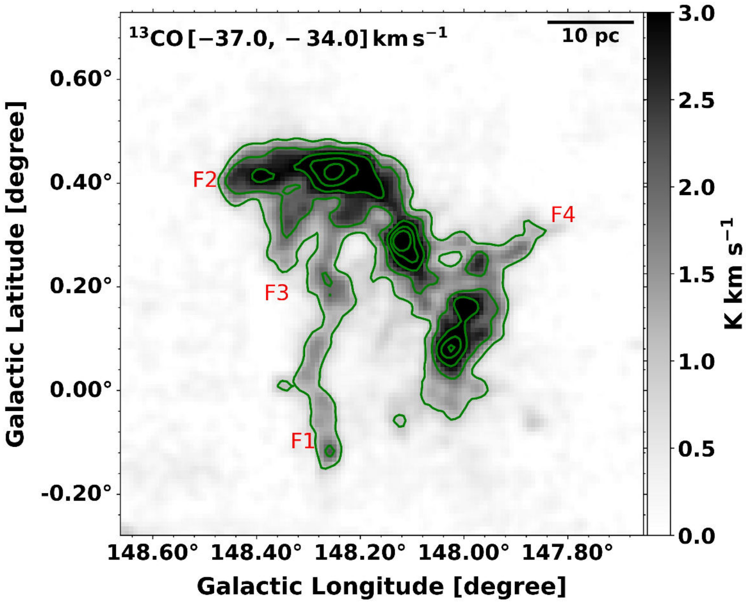

Figure 3.11: ^{13}CO integrated intensity map in the sub-velocity range, −37.0 km s^{-1}to −34.0 km s^{-1}. The filamentary features- F1, F2, and F3 are prominent in this velocity range. Filament-F4 is also visible here.

All the identified structures are marked in Figure 3.12 as F1, F2, F3, F4, F5, and F6. Figure 3.12 also shows the *FilFinder* extracted filament spines over their ^{13}CO integrated intensity emission. Most of these filaments correspond to the structures marked in Figure 3.10. The length of the filaments lies in the range of 15−40 pc. It is important to emphasize that while we have identified six probable filaments within the cloud based on our data, the identification of such structures is also subject to the resolution of the data. Comparing the morphology of the ^{13}CO integrated intensity-based filamentary structures with the dust-based filamentary structures visually identified in Chapter 2, we find that the filaments F2, F5, and F6 reasonably agree with the major filaments identified in Chapter 2, which are also marked in Figure 3.1. While the smaller *Herschel* filaments attached to the hub are not identifiable in our low-resolution data. Future high-resolution observations may resolve the filaments into multiple sub-filaments (e.g. Hu et al., 2021). Nonetheless, due to the lack of high-resolution data sets, we proceed with the presently available data to characterize the identified filamentary structures to get a sense of their role in the cluster formation of the cloud.

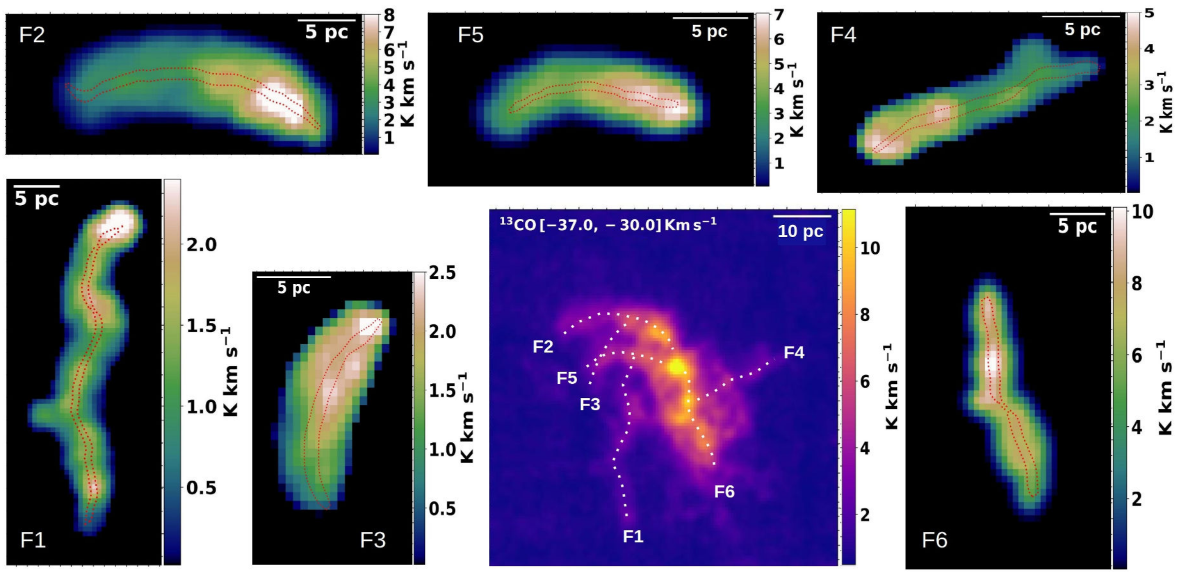

Figure 3.12: ^{13}CO integrated intensity maps of individual filaments. The red-dotted curve in each filament map shows the filament spine extracted from *Filfinder*.

3.3.2.4 Properties of the filaments

We make use of *RadFil* [2] (Zucker & Chen, 2018), a python-based tool to obtain the radial profile and width of the filament. *RadFil* also uses the *FilFinder* to generate the filament spines. It requires two inputs, image data and filament mask, which was provided from the output of *FilFinder* for the individual filament. *RadFil* first smooths the filament spine and then makes perpendicular cuts to the tangent lines sampled evenly across the smoothed filament (see Figure

[2]https://github.com/catherinezucker/radfil

3.13a). Each cut is shifted to the peak intensity along the cut, which is marked by the blue dots in Figure 3.13a. Then, it computes the radial distances from the peak intensity point and the corresponding pixel intensities for each intersecting pixel along a given cut (see Zucker & Chen, 2018). In this way, *RadFil* generates the intensity profile of each cut. Following the procedure, equidistant cuts were made perpendicular to the spine using a sampling frequency of 1 beam size. The radial profile at each cut was extracted, which gives an average profile or master profile of the filament and is shown in Figure 3.13b.

The filament width (FWHM) was identified by fitting a Gaussian function on the entire ensemble of the cuts. Before fitting the profile, a background was subtracted using the background subtraction estimator of *RadFil* (Zucker & Chen, 2018). The background was estimated using the first-order polynomial for all the profiles at a given radial distance from the centre pixel (highest intensity pixel). The radial distance for background estimation is taken in the range where the observed intensity of the radial profile seems to be at a constant level for the filaments. The same procedure is done for all the filaments, and their *RadFil* generated figures are shown in Appendix A. The best-fit parameters are given in Table 3.2.

We obtained the deconvolved FWHM by taking into account the beam size (52″) as: $\mathrm{FWHM_{decon}} = \sqrt{\mathrm{FWHM}^2 - \mathrm{FWHM}^2_{\mathrm{bm}}}$ (Könyves et al., 2015), where $\mathrm{FWHM_{bm}}$ is the beam size. The obtained $\mathrm{FWHM_{decon}}$ for all the filaments are listed in Table 3.2. In our case, the filament widths turn out to be in the range of 2.5−4.2 pc, with a mean ∼3.7 pc. The obtained widths are found to be higher than the typical width of ∼0.1 pc obtained from *Herschel*-based dust emission analysis of nearby clouds (e.g. André et al., 2010, 2014; Arzoumanian et al., 2019). However, it is worth noting that many observations and simulations have also argued that the width of filaments depends on many factors such as the fitted area, used tracer, resolution of the data, distance, evolutionary status of the filaments, and magnetic field (e.g. see Smith et al., 2014; Schisano et al., 2014; Federrath, 2016; Panopoulou et al., 2017; Suri et al., 2019; Panopoulou et al., 2022). For example, Panopoulou et al. (2022) found that the mean filament width for the nearby clouds is different from that of far away clouds. They also found that the mean per cloud filament width scales with the distance approximately as 4−5 times the beam size. Although the debate on the characteristic filament width of 0.1 pc is yet to be settled (see discussion in Panopoulou et al., 2017, 2022), we want to emphasize that the extracted filament widths in this work might be on the higher side because G148.24+00.41 is located at a distance of ∼3.4 kpc

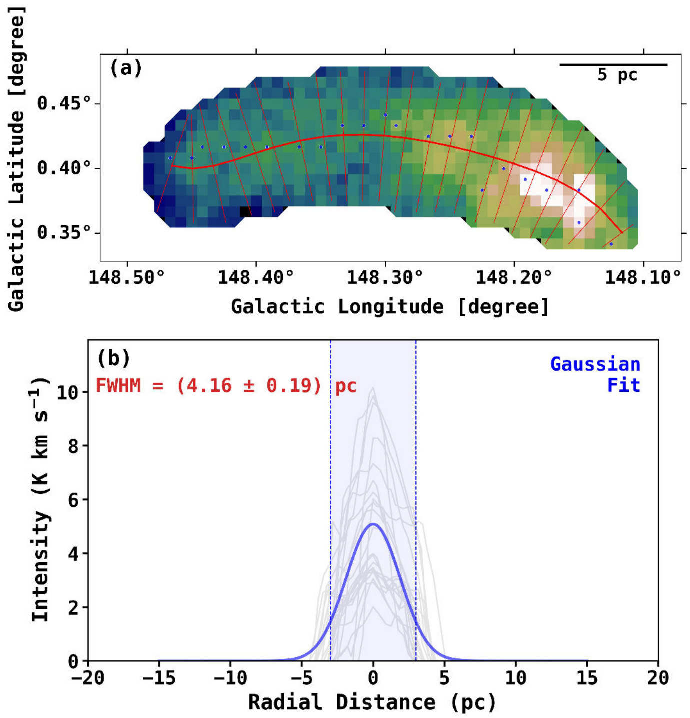

Figure 3.13: (a) The filament spine of F2 (red solid curve) shown over the ^{13}CO integrated intensity emission, integrated in the velocity range, [−37.0, −34.0] km s^{-1}. (b) The radial profile of filament F2, built by sampling radial cuts (red solid lines perpendicular to filament spine shown in panel a) at every 2 pixels (roughly 1 beam size ∼52″or 0.9 pc). The radial distance at a given cut is the projected distance from the peak emission pixel, shown by blue dots in panel a. The grey dots trace the profile of each perpendicular cut, and the blue solid curve shows the Gaussian fit over these filament profiles. The light-blue shaded region shows the range of radial distance taken for the Gaussian fit.

and analyzed with the low-resolution (∼0.9 pc) and low-density tracer CO data. Moreover, some of the filaments (e.g. F2) could be the sum of a series of sub-filaments, whereas the filaments identified in nearby clouds are well resolved. In addition, ^{13}CO is tracing better the enveloping layer of the filaments. Nonetheless, it is worth mentioning that using the PMO ^{13}CO data, Liu et al. (2021) and Guo et al. (2022), found similar mean filament widths of ∼3.8 pc and ∼2.9 pc, respectively, for Galactic plane filamentary clouds located at 2.4 kpc and 4.5 kpc, respectively.

Future, high-resolution molecular data may be able to better characterize the filaments of G148.24+00.41. However, with the available data, we proceed to derive the properties of the filaments, such as mean line mass and column density, as well as the kinematics and dynamics of the filaments along their spines.

We estimated the total mass of the filaments within their widths using the ^{13}CO-based N(H_2) column density, following the same procedure discussed in Section 2.2.2.1. The derived mass was then divided by the lengths of the filaments to obtain their mass per unit length, M_{line}. The properties of the filament, such as total mass, mean N(H_2), aspect ratio (i.e. length/width), and M_{line} are tabulated in Table 3.2. The aspect ratios of the filaments are in the range of 4−10. Generally, a filament is characterized by an elongated structure with an aspect ratio greater than ∼3−5 (André et al., 2014). The M_{line} of the filaments F1, F2, F3, F4, F5, and F6 is found to be ∼92, 171, 93, 138, 233, and 396 $M_\odot$ pc^{-1}, respectively, with a mean around 187 $M_\odot$ pc^{-1}. M_{line} is a critical parameter for assessing the dynamical stability of the filaments, which is discussed in Section 3.4.1.

3.3.2.5 Kinematics of the gas along the filament spine

To examine the kinematics, physical conditions, and dynamics of the gas along the filaments, we used ^{13}CO molecular line data and estimated the parameters within the filament width. In Figure 3.14, the variation of velocity, velocity dispersion, column density, and excitation temperature along the filament spines from their tail to head is shown. The farthest point of the filament spine from the hub is referred to as the tail, while the head is referred to as the tip of the filaments near the hub.

In filamentary clouds, the observed velocity gradient along the long axis of the filaments is referred to as the longitudinal in-fall motion of the gas. To assess the amplitude of the longitudinal flow along the filaments' long axis, we estimate the velocity gradient of each filament by doing the linear fit to the observed velocity profile along their spines. In some filaments (e.g. F6), noticeable fluctuations in the velocity profiles are seen. Similarly, for filaments F1 and F4, a negative gradient towards the tail of the filaments is seen. This could be due to the local gravitational effect of the compact structures and associated star formation activity (e.g. Peretto et al., 2014; Yang et al., 2023). For example, in F1, a noticeable dense compact gas is seen in the tail (see Figure 3.12), which might have reversed the flow of direction due to local gravity. Similar situations have also been seen in other filaments as well, for example, see Filament Fi-NW of the SDC 13 hub filamentary system (Peretto et al., 2014).

From the linear fit, the overall velocity gradient along the filament - F1, F2, F3, F4, F5, and F6 are found to be 0.04, 0.06, 0.02, 0.06, 0.06, and 0.03 km s^{-1}pc^{-1}, respectively. The

Table 3.2: Filament properties determined from ^{13}CO . The filament F1, F2, and F3 are extracted in the velocity range, [−37.0, −34.0] km s^{-1}, while the filament F4, F5, and F6 are extracted in the velocity range, [−37.0, −30.0] km s^{-1}.

Filament	Length (pc)	Width (pc)	Mass ($\times 10^3$ M$_\odot$)	Mass$_{line}$ (M$_\odot$ pc^{-1})	Mass$_{crit}$ (M$_\odot$ pc^{-1})	Mean N(H$_2$) ($\times 10^{21}$ cm^{-2})	$\frac{\sigma_{nt}}{c_s}$
F1	38.0	3.61	3.5	92	90	1.1	2.4
F2	25.7	4.16	4.4	171	94	3.0	2.4
F3	14.0	3.53	1.3	93	90	1.5	2.4
F4	18.1	3.28	2.5	138	215	2.3	3.7
F5	14.6	2.69	3.4	233	495	4.4	5.8
F6	17.4	2.49	6.9	396	283	9.0	4.0

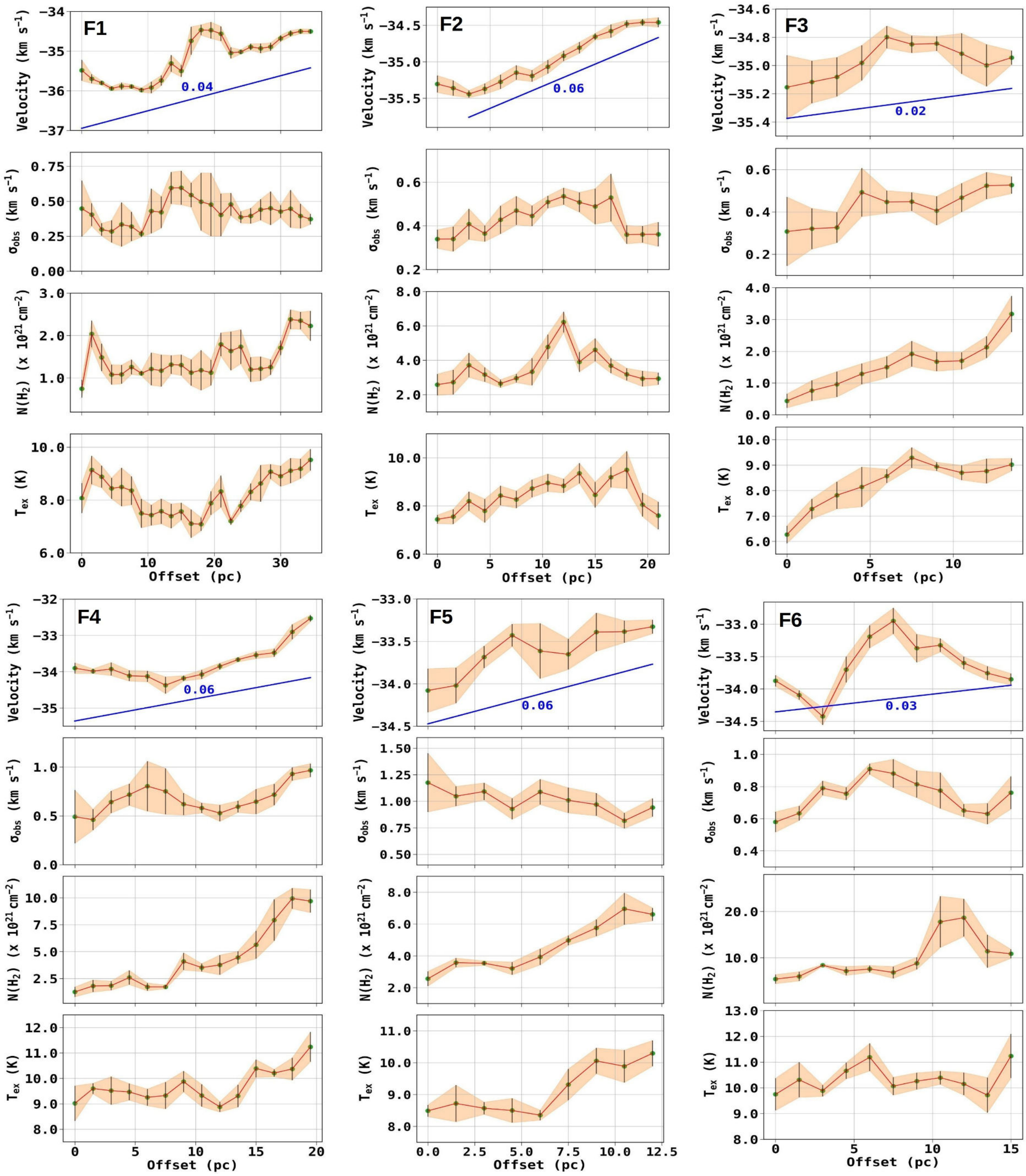

Figure 3.14: The average velocity, velocity dispersion, column density, and excitation temperature as a function of distance from the filament tail to the head, determined using ^{13}CO. The offset 0 pc is at the filament tail. The error bars show the statistical standard deviation at each point. The blue solid line in the top panel of each filament plot shows the linear fit to the data points, whose slope (marked in the plot) gives the velocity gradient along the filament.

observed velocities are line-of-sight projected velocities, and thus, small velocity gradients in some filaments could be due to the filament orientation close to the plane-of-sky. Filaments with low inclination angles would make any identification of gas flows along the filaments very difficult. Nonetheless, the observed velocity gradient for most of the filaments is close to the velocity gradient observed in large-scale giant molecular filaments (GMFs), i.e. filaments with lengths > 10 pc. (e.g. Ragan et al., 2014; Wang et al., 2015; Zhang et al., 2019). For example, Ragan et al. (2014) found 0.06 km $s^{-1}pc^{-1}$, as an average of the 7 filaments in their sample. Similarly, Wang et al. (2015) find velocity gradient in the range 0.07−0.16 km $s^{-1}pc^{-1}$ in their sample of GMFs. Similar gradients have also been seen in some large-scale individual filaments (e.g. Hernandez & Tan, 2015; Zernickel, 2015; Wang et al., 2016). Higher velocity gradients have been observed in filaments at parsec and sub-parsec scales with high-resolution data, particularly in those filaments/elongated structures that are close to the hub or massive clumps (e.g. Liu et al., 2012; Chen et al., 2020; Zhou et al., 2022, 2023). The general finding is that the velocity differences (δV) between the filaments and central clump/hub become larger as they approach the central clump (i.e. $\delta V \propto \delta R^{-1}$, where δR is the distance to the clump; e.g. see Hacar et al., 2022). This is also observed in G148.24+00.41 as in the proximity of hub (i.e. within the distance of 3 pc), it was found that the associated filaments F2 and F6 show higher velocity gradients, ~0.2 km $s^{-1}pc^{-1}$, towards their respective heads, which can be seen from Figure 3.15. Figure 3.15a shows the Position-Velocity (PV) diagram of the central filamentary area covering (see Figure 3.9) spines of the filaments F2 and F6 (marked in Figure 3.12). The figure also shows the positions of the clumps identified in Section 3.3.3. Figure 3.15b shows the gas velocity variation along the arrows marked in Figure 3.15a. The gas profile shows a dip in the PV diagram, like the V-shaped structure found in other filaments, which is considered as a signature of gas inflow along the filaments towards a hub/clump (e.g. Zhou et al., 2022).

To understand the level of turbulence in the filaments, we also calculated the non-thermal velocity dispersion ($\sigma_{\rm nt}$) and Mach number ($M = \sigma_{\rm nt}/c_{\rm s}$) from the total observed velocity dispersion ($\sigma_{\rm obs}$) using the relation,

$$\sigma_{\rm nt} = \sqrt{\sigma^2_{\rm obs} - \sigma^2_{\rm th}}, \tag{3.7}$$

where $\sigma_{\rm th} = \sqrt{k_{\rm B}T_{\rm K}/\mu_{\rm i}m_{\rm H}}$ is the thermal velocity dispersion. $T_{\rm K}$ is the gas kinetic temperature, $k_{\rm B}$ is the Boltzmann constant, and $\mu_{\rm i}$ is the mean molecular weight of the observed tracer (e.g.

$\mu(^{13}CO) = 29$ and $\mu(C^{18}O) = 30$). The mean σ_{obs} is obtained from the velocity dispersion (moment-II) map within the filament region. Using the average T_{ex} of the filaments as T_{kin}, we calculated the σ_{th} and σ_{nt} of the filaments. Using σ_{nt} and thermal sound speed, $c_s = \sqrt{k_B T_K/\mu m_H}$ with mean molecular weight per free particle, $\mu = 2.37$ (Kauffmann et al., 2008), we calculated the total effective velocity dispersion

$$\sigma_{eff} = \sqrt{\sigma_{nt}^2 + c_s^2}, \tag{3.8}$$

The Mach number for the filaments is tabulated in Table 3.2. The gas in the individual molecular filaments of G148.24+00.41 is found to be supersonic with sonic Mach number ∼2–6[3]. This is in agreement with the results of Wang et al. (2015) and Mattern et al. (2018) toward a sample of large-scale filaments measured with the low-resolution (30−46″) ^{13}CO data using Galactic Ring Survey and SEDIGISM survey data (for details, see Table. 1 of Schuller et al., 2021). However, we want to stress that the derived properties are from the medium-density tracers such as ^{13}CO, but the high-density tracers that would trace very central regions of the filament may give different results. For example, Pineda et al. (2010) comparing high-density and low-density tracers suggested that the sub-sonic turbulence is surrounded by supersonic turbulence in the filaments of the Perseus cloud. Results from high-resolution observations also show that the velocity dispersions of resolved nearby filaments and fibres are close to the sonic or sub-sonic speed (e.g. Hacar et al., 2013; Friesen et al., 2016; Hacar et al., 2017; Saha et al., 2022). All these results tend to suggest that the level of turbulence is scale-dependent, and subsonic velocity coherent filaments possibly condense out of the more turbulent ambient cloud/filament.

From Figure 3.14, it was also noticed that the majority of filaments exhibit an increasing velocity dispersion as they approach the hub or ridge. The figure also shows that in the majority of the filaments, the increase in velocity dispersion is proportional to the column density of the gas moving from the tail to the head of the filaments, which is also evident in the integrated intensity maps shown in Figure 3.12. In filaments, strong velocity gradients due to rotation have also been observed, but primarily at smaller scales, such as close to the dense clump or along the

[3]The velocity dispersion may be overestimated if the molecular lines are optically thick (Goldsmith & Langer, 1999; Hacar et al., 2016). Along the spine, the optical depth of the ^{13}CO emission for most of the filaments is close to 1. Following the suggestion made by Hacar et al. (2016), this would increase the line width only by 15%, suggesting that even after applying the optical depth correction to the line width, the filaments would remain supersonic.

minor axis of the filaments. In the present case, the velocity gradients along the long-axis of the filaments over large scale (> 5 pc), as well as the increase in velocity dispersion and column density as they approach the bottom of the potential well of the cloud, suggest for longitudinal flow of gas along the filaments toward the hub/ridge as found in numerical simulations (e.g. Heitsch et al., 2008; Carroll-Nellenback et al., 2014; Vázquez-Semadeni et al., 2019).

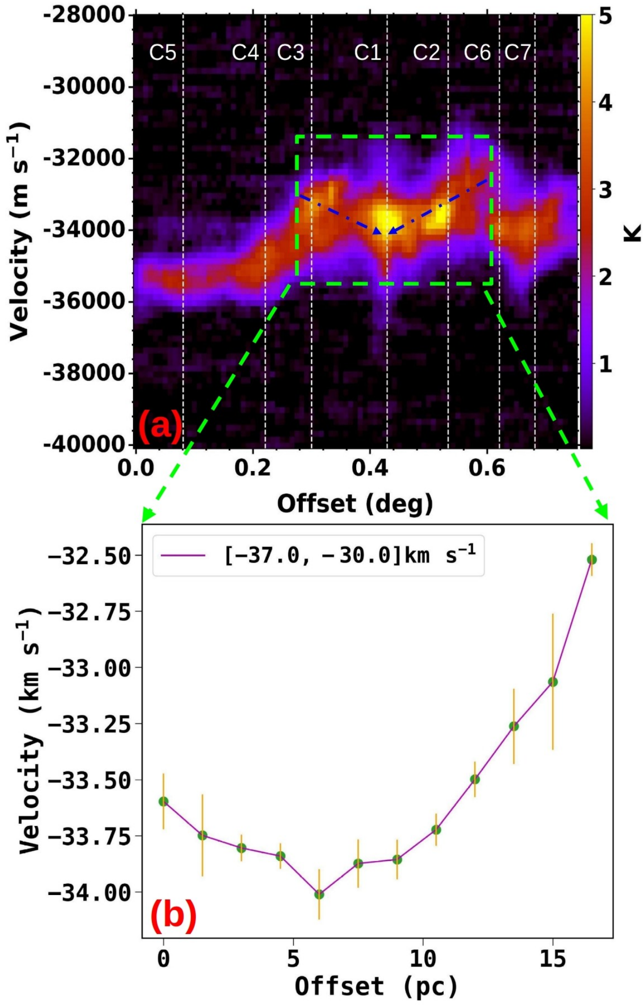

Figure 3.15: (a) The position-velocity (PV) diagram of the full ridge based on ^{13}CO, which is shown in Figure 3.10. The green-dashed box shows the region that is used to see the gas flow structure along the blue dashed-dotted arrows, toward the central hub/clump. The vertical dashed lines show the location of identified clumps, marked with their names (see Section 3.3.3). (b) The variation of average velocity with distance along the arrows (shown in panel a), which shows the velocity gradient towards the central hub/clump.

3.3.3 Dense clumps

Figure 3.4 suggests that the cloud has fragmented into several clumpy structures. These are the clumps of the cloud where star formation could take place. In order to understand the properties and dynamics of these clumps, we utilized $C^{18}O$ data, as it is a better tracer of denser gas and was found to be optically thin in G148.24+00.41.

3.3.3.1 Identification of clumps

For identifying clumps of G148.24+00.41, we implemented the dendrogram (Rosolowsky et al., 2008) method using ASTRODENDRO python package[4]. The dendrogram is a structure-finding algorithm that identifies hierarchical structures in the input two- or three-dimensional array. The output of the dendrogram depends on three parameters: the *minimum value* that defines the background threshold, the *minimum delta or difference* that defines the separation between two substructures, and the *minimum pixels* that defines the minimum number of pixels or size needed for the structure to be called an independent entity. We ran the dendrogram over the $C^{18}O$ integrated intensity map to find the clumps. We carefully investigate and set the following optimum extraction parameters to detect parsec scale clumpy structures while avoiding faint noisy structures. We set the minimum value to be 3σ above the mean background emission, the minimum delta to be 1σ, and the minimum size to be 12 pixels. Doing so, we identified seven clumps in the cloud, which are marked in Figure 3.16a as C1 to C7. The ID, size, and position angle of the clumps are tabulated in Table 3.3.

3.3.3.2 Properties of the clumps

We estimated the mass of the clumps using the integrated intensity emission within the clump boundary, the average excitation temperature from the excitation temperature map shown in Figure 3.6a, and equations 3.5 and 2.1. The clumps are found to be massive with masses in the range 260−2100 $M_\odot$, with the most massive being the central clump, C1, associated with the hub of the cloud. The second most massive clump (C2) is of mass $\sim$1800 $M_\odot$. The mass of C2 is likely an upper limit, as the clump is possibly tracing the part of the filament that connects C1

[4] http://www.dendrograms.org/

Table 3.3: Clump properties. The mass, line-width ($\Delta V = 2.35\sigma_{\rm obs}$), virial parameter ($\alpha$), and the ratio of non-thermal velocity dispersion ($\sigma_{\rm nt}$) to thermal sound speed ($c_{\rm s}$) are calculated using the $C^{18}O$ molecular line data.

Clump	Major axis (pc)	Minor axis (pc)	Position angle (deg)	Mean N(H_2) ($\times 10^{21}$ cm^{-2})	Mass ($M_\odot$)	T_{ex} (K)	ΔV (km s^{-1})	α	$\frac{\sigma_{\rm nt}}{c_{\rm s}}$
C1	2.2	1.4	219.16	11.0	2100	11.3	1.36	0.2	3.0
C2	2.5	1.5	104.45	7.0	1800	10.5	2.02	0.6	4.5
C3	1.9	1.4	200.56	8.1	1600	11.5	1.67	0.4	3.5
C4	2.0	1.0	220.56	5.6	820	8.8	1.08	0.3	2.6
C5	1.4	0.7	218.06	4.2	260	8.0	0.49	0.1	1.2
C6	1.1	0.5	108.68	7.3	280	10.4	1.18	0.5	2.6
C7	1.6	1.0	142.86	6.7	730	10.0	1.46	0.5	3.3

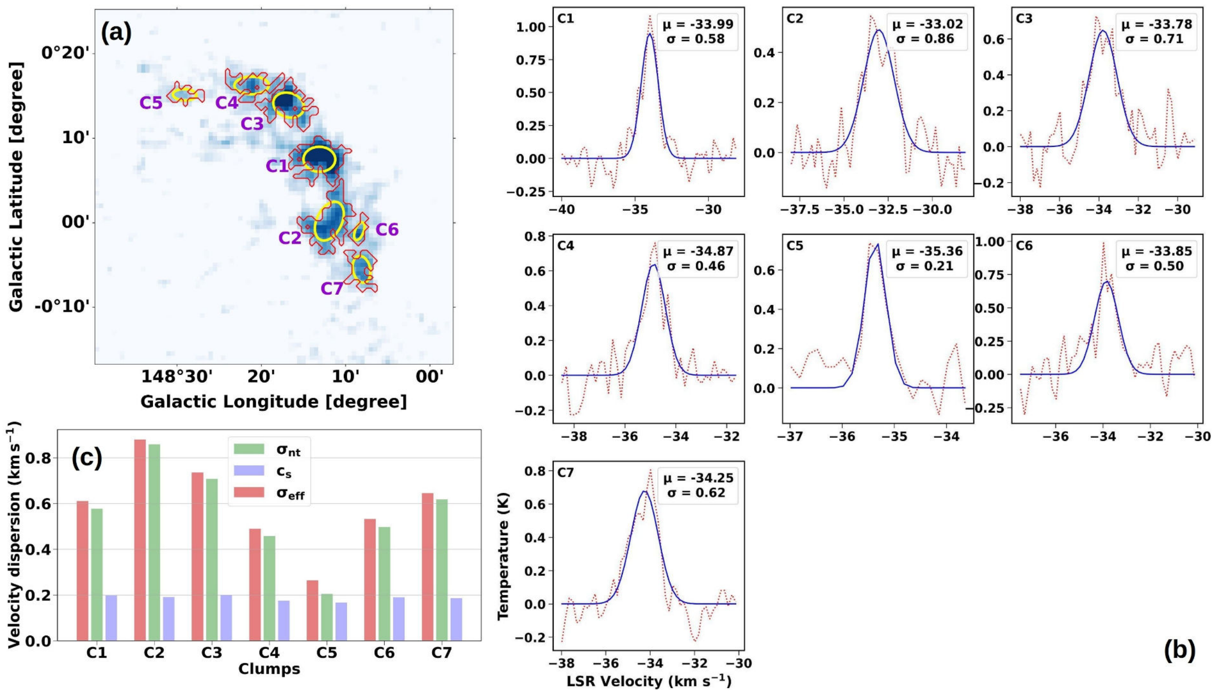

Figure 3.16: (a) The location of the clumps identified using ASTRODENDRO over $C^{18}O$ intensity map. The red contours show the leaf structures identified using dendrograms, and the ellipses show the clump within them. (b) The average $C^{18}O$ spectral profile of the clumps over which the solid blue curve denotes the best-fit Gaussian profile, and their respective mean and standard deviation are given in each panel. (c) The histogram plot of non-thermal (σ_{nt}), thermal sound speed (c_s), and the total effective (σ_{eff}) velocity dispersion of the clumps.

and C2. The effective radius of the clump is calculated as $\sqrt{ab}$, where a and b are the semi-major and semi-minor axes of the clump (given in Table 3.3). The r_{eff} of the clumps are found to be in the range 0.8−1.9 pc, with a mean value of ∼1.4 pc.

Velocity dispersion can reflect the level of turbulence in clumps, and the mean line-width, ΔV of the clump is related to the velocity dispersion as $2.35\sigma_{obs}$. We get the observed velocity dispersion by fitting a Gaussian profile over the $C^{18}O$ spectrum of the clumps. Figure 3.16b shows the average spectral profile of all the clumps. The velocity dispersion of the clumps is in the range of 0.21 to 0.86 km s^{-1}, with a mean value of 0.56 km s^{-1}. As determined for the whole cloud, one can also infer whether the clumps are bound or not by calculating the virial parameter, $\alpha = \frac{M_{vir}}{M_c}$, where M_{vir} and M_c are the virial mass and gas mass of the clumps, respectively. We calculated M_{vir} using density index, $\beta = 2$, by assuming a spherical density profile for the clumps. The r_{eff}, mean T_{ex}, ΔV, M_c, and α values of the clumps are tabulated in Table 3.3. The α value of all the clumps is found to be less than 2, suggesting that they are gravitationally bound and, thus, would form or are in the process of forming stars. This will also remain true even if we take β =1.5.

To determine the contribution of non-thermal (turbulent) support against gravity in the clumps, we calculate the non-thermal velocity dispersion and total effective velocity dispersion from the total observed velocity dispersion, using the same procedures outlined in Section 3.3.2.5. Figure 3.16c shows the $\sigma_{\rm nt}$, $c_{\rm s}$, and $\sigma_{\rm eff}$ values of the clumps based on $C^{18}O$ data. From the figure, it can be seen that for all the clumps, the non-thermal velocity dispersion or the turbulence contribution is more dominant than the thermal component. Using the ratio $\sigma_{\rm nt}/c_{\rm s}$, we calculated the Mach number, which is given in Table 3.3. The Mach number lies in the range of 1.2 to 4.5, with a mean of around 3. Thus, the clumps have supersonic non-thermal motions. The non-thermal motions could be either due to small-scale gas motions within the clump or protostellar feedback due to local star formation activity or a combination of both processes. For example, as discussed in Chapter 2, the hub is also associated with a massive YSO with an outflow. Thus, its radiation and feedback might have also impacted the dynamics of the surrounding gas.

3.4 Discussion

3.4.1 Stability of the filaments

The stability of the filament can be evaluated by comparing its observed line mass, $M_{\rm line}$, with the critical line mass, $M_{\rm crit}$. Assuming filaments are in cylindrical hydrostatic equilibrium, $M_{\rm crit}$, is expressed as (Fiege & Pudritz, 2000):

$$M_{\rm crit} = \frac{2\sigma_{\rm eff}^2}{G} \sim 464\,\sigma_{\rm eff}^2\,(M_\odot\,pc^{-1}), \tag{3.9}$$

where $\sigma_{\rm eff}$ is the effective velocity dispersion in km s^{-1}and G is the gravitational constant. The filament is unstable to axisymmetric perturbation if its line mass exceeds its critical line mass

(Inutsuka & Miyama, 1992). In the case of isothermal filament, $\sigma_{\rm eff}$ = c_s, where c_s is the sound speed of the medium (e.g. Ostriker, 1964). In this scenario, the critical line mass only depends on the gas temperature. The average temperature ($T_{\rm ex}$) of the filaments estimated within their widths lies in the range 8−10 K, which corresponds to $M_{\rm crit}$ ∼13−17 $M_\odot$ pc^{-1}. The estimated line masses of the filaments are significantly higher than their critical thermal line masses. This suggests that either the filaments are collapsing radially or they are supported by additional mechanisms such as non-thermal turbulent motions. These turbulent motions can be generated either due to already-formed stars within the filaments or by the radial accretion/infall of the surrounding gas onto the filaments (Hennebelle & André, 2013; Clarke et al., 2016). The presence of non-thermal motions would increase the effective sound speed, thereby would increase the effective velocity dispersion ($\sigma_{\rm eff} = \sqrt{c_s^2 + \sigma_{\rm nt}^2}$) of the filament, and thus, the critical line mass. At present, the observed velocity dispersion along the filament is higher than that one would expect for a cloud with a temperature in the range 10−15 K. Therefore, to understand the present dynamical status of the filaments, we computed the $M_{\rm crit}$ for the filaments assuming that they are supported by thermal as well as non-thermal motions. Using the mean effective velocity dispersion of the filaments (0.44, 0.45, 0.44, 0.68, 1.03, and 0.78 km s^{-1}), we calculated the $M_{\rm crit}$ values as 90, 94, 90, 215, 496, and 283 $M_\odot$ pc^{-1} for F1, F2, F3, F4, F5, and F6, respectively, with a mean value around ∼211 $M_\odot$ pc^{-1}.

Arzoumanian et al. (2019) based on *Herschel* analysis and considering thermal line mass as the critical mass, categorised the filaments of the nearby clouds as supercritical filaments ($M_{\rm line}$ ≥ 2 $M_{\rm crit}$,), transcritical filaments (0.5 $M_{\rm crit} \leq M_{\rm line} \leq 2\ M_{\rm crit}$), and subcritical filaments ($M_{\rm line}$ ≤ 0.5 $M_{\rm crit}$). They suggested that thermally subcritical filaments are gravitationally unbound entities, while transcritical and supercritical filaments are the preferable sites for gravitational collapse and core formation. Based on the thermal line mass, all of our filaments are super-critical, thus, might have undergone collapse and sub-sequence fragmentation to form cores. This fact is evident from the distribution of protostars on the filaments, shown in Figure 3.17. The figure shows that most of the protostars have been formed in the ridge/F6 of the G148.24+00.41 cloud, and a few protostars seem to be formed at the head of the filaments F1, F2, and F5. Taking the contribution of non-thermal motion, we find that the line mass of F1, F2, F3, and F6 is larger than their $M_{\rm crit}$ values, suggesting that they are still gravitationally unstable, whereas for F4 and F5, the $M_{\rm line}$ is smaller than the $M_{\rm crit}$ value, suggesting that they are possibly stable against collapse. However, we note that the line masses are estimated with canonical values of ^{12}C to ^{13}C isotope ratio and can be higher by a factor of 1.3, if isotopic ratio at the galactocentric distance of the cloud is considered (e.g. Pineda et al., 2013).

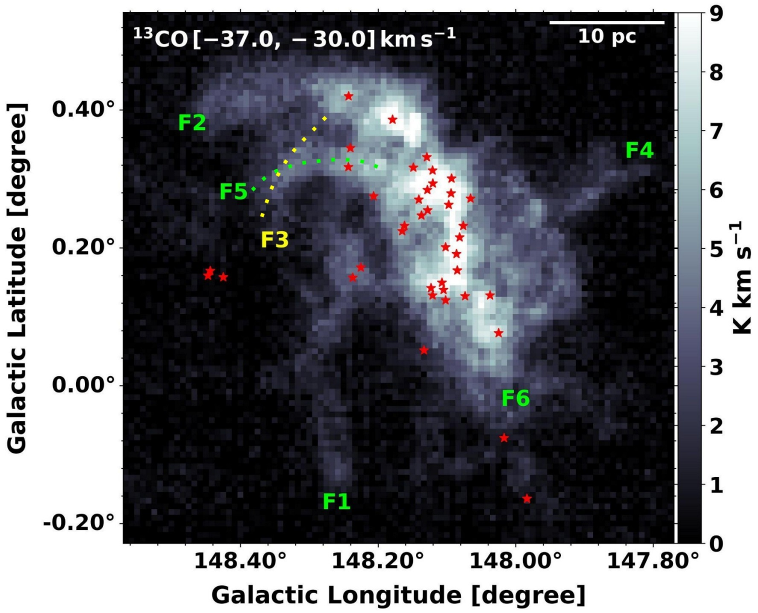

Figure 3.17: The distribution of protostars from *Herschel* 70 micron point source catalogue (Herschel Point Source Catalogue Working Group et al., 2020) on the ^{13}CO integrated intensity map.

In the above discussion, we have investigated the dynamical status of the filaments, however, it is worth mentioning that, in the dynamical scenario of cloud formation and evolution, filaments are very likely to deviate from true equilibrium structures. Because in the dynamical scenario of cloud collapse, filaments are described as dynamical structures that continuously accrete from the ambient gas while feeding dense cores within them. Moreover, it has also been found that due to the gravitational focusing effect, finite filaments are more prone to collapse at the ends of their long axis (Burkert & Hartmann, 2004; Pon et al., 2011), even when such filaments are subcritical. Thus, though the average properties of some of the filaments are sub-critical, they have a higher concentration of column density at their heads due to longitudinal flow along their axis, where filaments can transit from sub-critical to super-critical.

3.4.2 Mass flow rate along the filament axis

Assuming that the observed velocity gradient in filaments is due to gas accretion flow, we estimate the mass accretion rate, $\dot{M}_{||}$ along the filaments using a simple cylindrical model and relation given in Kirk et al. (2013),

$$\dot{M}_{||} = V_{||} \times \rho(\pi r^2) \quad = \quad V_{||}\left(\frac{M}{L}\right), \tag{3.10}$$

where $V_{||}$ is the velocity along the filament, which is multiplied by the density, $\rho = \left(\frac{M}{\pi r^2 L}\right)$, and the perpendicular area (πr^2) of the flow. The r, M, and L are the radius, mass content, and length of the cylinder, respectively. By taking the plane of sky projection with an inclination angle, α, the observed parameters of the cylinder are: $L_{\rm obs} = Lcos(\alpha)$, $V_{||,\rm obs} = V_{||}sin(\alpha)$, and $V_{||,\rm obs} = \Delta V_{||,\rm obs} L_{\rm obs}$. After simplification, the $\dot{M}_{||}$ expression reduces to

$$\dot{M}_{||} = \frac{\Delta V_{||,\rm obs} M}{tan(\alpha)}, \tag{3.11}$$

where, $\Delta V_{||,\rm obs}$ is the observed velocity gradient along the filament. Taking the obtained mass and velocity gradient of the filaments (see Table 3.2), and $\alpha = 45^\circ$ (Kirk et al., 2013), the estimated mass accretion rate for filament F1, F2, F3, F4, F5, and F6 is around ~140, 264, 26, 150, 204, and 207 $M_\odot$ Myr^{-1}, respectively. Among which, the filaments F2, F5, and F6 are directly tied to the hub (see Figure 3.12), whose combined accretion rate is around ~675 $M_\odot$ Myr^{-1}. We note that the combined mass-accretion rate to the hub is an upper limit as the F6 filament will not transfer its mass entirely to the central hub due to the presence of an additional clump competing with it in the filament. However, we have not accounted for the contribution of small-scale filaments attached to the hub, as seen in the *Herschel* dust continuum image (see Figure 2.16), which would conversely add to the combined accretion rate.

Taking the above-measured accretion rate as a face value, we find that it is either comparable or higher than some of the well-known cluster-forming hubs found in the literature, such as Mon R2 (400−700 $M_\odot$ Myr^{-1}, Treviño-Morales et al., 2019), Serpens (100−300 $M_\odot$ Myr^{-1}, Kirk et al., 2013), Orion (385 $M_\odot$ Myr^{-1}, Rodriguez-Franco et al., 1992; Hacar et al., 2017), the DR 21 ridge (1000 $M_\odot$ Myr^{-1}, Schneider et al., 2010), G326.27-0.49 (970 $M_\odot$ Myr^{-1}, Mookerjea et al., 2023), and G310.142+0.758 (700 $M_\odot$ Myr^{-1}, Yang et al., 2023). This comparison, however, should be treated with caution because all these measurements have been done with different tracers having different resolutions that cover different scales around the hubs. Measuring the accretion rate for massive clouds that have hub filamentary systems, such as those mentioned above, in a uniform way, would give more valuable insight into the accretion rate and the mass assembly time scales of such systems.

3.4.3 Overview of cluster formation processes in G148.24+00.41

Vázquez-Semadeni et al. (2019) suggested that due to non-homologous collapse in molecular clouds, a classical signature of spherical collapse is not expected over a larger scale. However, at the clump scale, a global velocity offset between peripheral ^{12}CO and internal ^{13}CO, as found by Barnes et al. (2018), is a signature of collapse. According to Barnes et al. (2019), if the average ^{12}CO profile is red-shifted with respect to the average ^{13}CO profile, the motion of the enveloping ^{12}CO gas is inwards, while if it is blue-shifted, then the motion is outwards. Figure 3.18b shows the line profiles of the CO-molecules within the 3 pc area (marked by the red rectangle in Figure 3.18a) around the hub. The figure shows that the ^{12}CO profile is redshifted with respect to ^{13}CO profile, inferring the net inward motion of ^{12}CO envelope (Barnes et al., 2018). However, to get the conclusive signature of infall motion at the clump scale, a gas kinematics study with high-density tracer data would be highly beneficial (Yuan et al., 2018; Liu et al., 2020; Yang et al., 2023).

In G148.24+00.41, there are six filaments with converging flows heading towards the hub of the cloud. For the filaments having aspect ratio, $\mathrm{A}_0 = \mathrm{Z}_0/\mathrm{R}_0 \gtrsim 2$, one can calculate the longitudinal collapse timescale using a single equation, $t_{\mathrm{COL}} \sim (0.49 + 0.26A_0)(G\rho_0)^{-1/2}$ (Clarke & Whitworth, 2015), where Z_0, R_0, and $\rho_0 = M_{\mathrm{line}}/\pi \mathrm{R}_0^2$ is the half-length, radius, and density of the filament, respectively. In the present case, the aspect ratio of all the filaments is greater than 2. Using the aforementioned formalism, we find that the longitudinal collapse timescale of these filaments is in the range of 5−15 Myr, while the free-fall time of the central clump ($t_{ff} = \sqrt{3\pi/32G\rho_c}$, where ρ_c is the density of the clump) is found to be ∼1 Myr. Since in dynamical hierarchical collapse, each scale accretes from a larger scale, implying that the filaments may continue to fuel the clump for a longer time, provided that they remain bound.

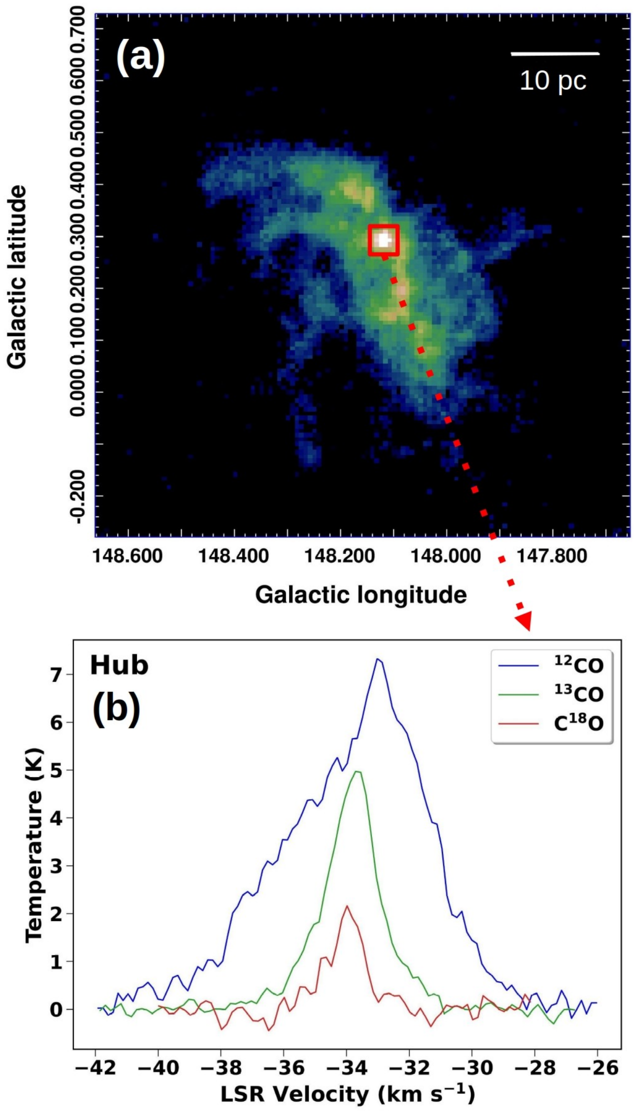

Figure 3.18: (a) The ^{13}CO integrated intensity map showing the location of the hub by a red box, having size ~3.5 × 3.0 pc. (b) The average ^{12}CO, ^{13}CO, and C^{18}O spectral profile of the hub region (shown in panel a).

Taking the upper limit of combined inflow rate to the C1-clump as ~675 M$_\odot$ Myr^{-1}, we estimate that to assemble the current mass of the clump, i.e. ~2100 M$_\odot$, a minimum time of ~3 Myr would be needed, while the age of the cloud based on formed young stellar objects is around 0.5−1 Myr (for details, see Chapter 2). This implies that while the mass assembly is ongoing towards the clump, the star formation in the cloud might have initiated around 0.5−1 Myr ago. However, it is important to acknowledge that the estimated mass assembly time scale to the C1-clump in this work may be an upper limit due to the following reasons: i) the accretion rate was higher during the early phase of cloud evolution, ii) overestimation of the clump mass due to low-resolution data, iii) missing the contribution of other small-scale filaments such as those seen in *Herschel* images, or a combination of all. Future high-resolution observations focusing on the clump area would shed more light on the latter two hypotheses. Nonetheless, the derived accretion rate is close to those found in some of the well-known cluster-forming hub-filamentary systems (discussed in Section 3.4.2) and also to the prediction of massive cluster-forming simulations (e.g. Vázquez-Semadeni et al., 2009; Howard et al., 2018). For example, Vázquez-Semadeni et al. (2009) using numerical simulations, suggest that the formation of massive stars or clusters is associated with large-scale collapse involving thousands of solar masses and accretion rates of $\sim 10^{-3}$ $M_{\odot}$ yr^{-1}.

The G148.24+00.41 cloud has fragmented into seven massive clumps in the range of 260−2100 $M_{\odot}$, and the majority of them have the potential to form an independent group of stars or cluster (e.g. to form a massive star and associated cluster, a minimum mass ≥ 300 $M_{\odot}$ is needed; see Appendix A in Sanhueza et al., 2019). However, our search for the presence of embedded sources within the clumps using mid-IR data (i.e. using 3.6 μm *Spitzer* images) resulted that the massive clumps are associated with stellar sources, and the hub (i.e. the clump C1) hosts the most compact and richer stellar group. In Chapter 2, it was also found that the most luminous ($\sim$1900 $L_{\odot}$) protostar of the complex is located within the hub. Thus, we hypothesize that in the G148.24+00.41 cloud, the cluster formation predominantly in the C1 clump is facilitated by filamentary accretion flows, which can either be gravity-driven (GHC; Gómez & Vázquez-Semadeni, 2014; Vázquez-Semadeni et al., 2019) or turbulence-driven (I2; Padoan et al., 2020). The cluster in the hub has the potential to grow into a richer cluster by gradually accumulating additional cold gas. In Chapter 2, based on the spatial and temporal distribution and fractal subclustering of the stellar sources in G148.24+00.41, it was suggested that GHC might be the dominant mechanism responsible for the formation of the stellar cluster in this cloud. Based on the low-resolution CO data, used in this work, it is difficult to distinguish between the aforementioned two models. Future shock tracer observational data would be helpful in this regard, as the I2 model suggests the formation of filaments due to shocks, while in GHC, the filaments form due to large-scale gravity flow (Yang et al., 2023). Regardless of the origin of the flow, it is certain that there is a merger or coalescence of converging flows at the location of the hub. Figure 3.19 illustrates the potential structure and overall gas kinematics of the cloud, forming clusters at the nodes of the filamentary flows, with the richest cluster being located at the bottom of the cloud's potential.

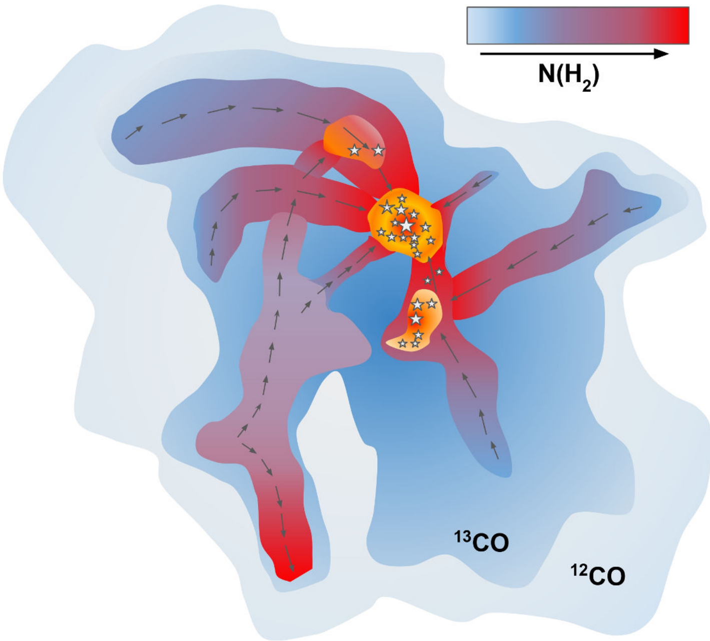

Figure 3.19: Cartoon illustrating the observed structures in G148.24+00.41. The black arrows represent the directions of the overall gas flow. The background colour displays the local density of ^{12}CO and ^{13}CO.

3.5 Summary

In this chapter, the gas properties and kinematics of G148.24+00.41, along with the filamentary structures and clumps within it, were studied. Using CO isotopologues molecular line data, we made the excitation temperature and optical depth maps and, from them, made CO-based molecular hydrogen column density maps. Using these column density maps, it is confirmed that the cloud is massive ($\sim10^5$ M$_\odot$), bound, and hosts a massive clump of mass $\sim$2100 M$_\odot$ nearly at its geometric centre. Based on the low-resolution ^{13}CO data, we identified six likely velocity coherent, large-scale (length > 10 pc and aspect ratio > 4) filamentary structures in the cloud. Out of which, three filaments (namely F2, F5, and F6) are directly tied to the clump located in the hub. We could not identify and characterize three relatively small-scale filaments that are attached to the hub as seen in the *Herschel* images, thus, their role and properties are not investigated in this chapter.

The filaments have undergone fragmentation as several protostars (age $\leq 5 \times 10^5$ yr) that are identified using 70 μm and 160 μm images in the chapter 2 are found to be associated with the filaments. Particularly, the filament F6 has a high line mass, thus associated with a chain of protostars along its spine. In the case of the other filaments, the protostars are located close to their respective head, where strong density enhancement is seen in their respective integrated intensity map. These density enhancements could be due to the filamentary accretion flows along their long axis towards the hub location. In fact, the velocity profile of the filaments suggests that each filament is possibly undergoing longitudinal collapse, as the majority of them tend to show a velocity gradient in the range 0.03−0.06 km $s^{-1}pc^{-1}$. The increase in velocity along the filaments is also correlated with the increase in column density and velocity dispersion. We have also found higher velocity gradients near the hub location, implying the acceleration of gas motion towards the hub. We estimated that each filament has the potential to fuel the cold gaseous matter at a rate ranging from 26 to 264 $M_\odot$ Myr^{-1} to the centre of the cloud. Though the kinematic features are suggestive of large-scale flows toward the hub, but due to the presence of other clumps in the ridge, the kinematics of the filaments are found to be complicated. Future high-resolution observations will be essential to better understand the kinematics and dynamics of the gas in the filaments and the hub, and unveil the multi-scale process of massive cluster formation.

The cloud has fragmented into seven massive clumps having mass in the range 260−2100 $M_\odot$. The clump located at the hub of the cloud is the most massive one and is associated with a massive YSO and a stellar cluster. All these pieces of evidence suggest that within the cloud, the hub is the dominant place where a prominent cluster is in the process of emerging. Overall, our results are consistent with the flow-driven gas assembly, leading to the formation of a dense clump in the hub and the subsequent emergence of a stellar cluster.

Chapter 4

Magnetic fields around the hub region of G148.24+00.41

In the previous two chapters, we presented the global dust and gas properties, as well as the gas kinematics of the whole G148.24+00.41 cloud and the substructures within it, in order to understand its cluster formation potential and mechanism. In the previous chapter, the longitudinal filamentary flows towards the hub region where the most massive clump (C1) is located were discussed. As discussed in the previous chapters, it is an active region of star formation and a dominant place for a stellar cluster to form. This chapter focuses on the C1 clump of G148.24+00.41, looking at the present role of the magnetic field in comparison to gravity and turbulence in the overall star-formation process of the C1 clump/hub region.

The molecular clouds inherit a very weak seed magnetic field from the ISM during their formation, and that magnetic field sustains due to small ionization caused by UV photons and cosmic rays, and it becomes stronger with the evolution of the cloud (McKee & Ostriker, 1977). Especially cosmic rays are the main source of ionization in the densest regions of molecular clouds where UV photons can not penetrate. The molecular clouds are coupled with the Galactic scale magnetic field, but their magnetic field morphology can be significantly affected by turbulent and gravitational flows and stellar feedback, like protostellar outflows and expanding H II regions. Thus, molecular clouds are the dense regions of magnetized turbulent ISM where stars form in gravitationally unstable regions. The low galactic star formation rate and star formation efficiency in molecular clouds are generally due to the support against gravitational collapse provided by both magnetic fields and turbulence, along with the role of stellar feedback. The importance of the magnetic field in the formation of clouds, filaments, and stars within them and its role in cloud dynamics have been discussed in detail in Chapter 1.

The magnetohydrodynamic simulations suggest that the filamentary converging flows would impact the magnetic field morphology of the star-forming regions (Gómez et al., 2018). In G148.24+00.41, converging gas flows were found along the filaments towards the hub. So, it is interesting to investigate the influence of gas flows on the B-field morphology in the hub of the cloud. Since it is suggested that magnetic field morphology and strength dynamically evolve in molecular clouds, thus, it is equally important to examine the role of the magnetic field in the stability of such hub systems, as it is expected that gravity would play a dominant role in the onset of star formation within such systems.

This chapter presents the work that has been done to investigate the morphology and strength of the magnetic field of the C1 clump based on dust polarization measurements. Also, the chapter discusses the relative importance of the magnetic field in comparison to gravity and turbulence in the overall star formation process of the clump.

4.1 Dust polarization of starlight

As discussed in Section 1.1.2 of Chapter 1, the light from the background stars gets polarized by a small fraction through the intervening dust present in the ISM or cloud (Hall, 1949; Hiltner, 1949). This polarization signal can be used to study the details of dust and magnetic fields in those regions. The correlation between polarization fraction and the amount of dust present in the region shows that the asymmetric dust grains are the cause of interstellar polarization (e.g. Serkowski et al., 1975).

Dust polarization observation is a key tool for tracing the POS magnetic field geometry in star-forming regions. The polarization is caused by elongated dust grains that are asymmetric in size, with their shorter axis preferentially aligned along the magnetic field direction (Lazarian, 2007; Hoang & Lazarian, 2008). Due to this alignment of dust grains, the light gets slightly more blocked along their longer axis in comparison to their shorter axis (i.e. dichroic extinction), which results in the polarization of light. The scattering polarization caused by the scattering of background starlight through the dust comes in optical and near-infrared wavelengths and has polarization vectors parallel to the POS magnetic field. Whereas the dust emission polarization mostly comes in far-infrared and sub-mm wavelengths and has polarization vectors perpendicular to the POS magnetic field. Figure 4.1 shows a schematic diagram of aligned dust grains and the scattering and emission polarization caused by them. The optical or NIR polarizations are limited to the diffused and low-density cloud regions for tracing the magnetic field, whereas the emission polarization is better for tracing magnetic fields in dense regions of clouds, like clumps and dense cores.

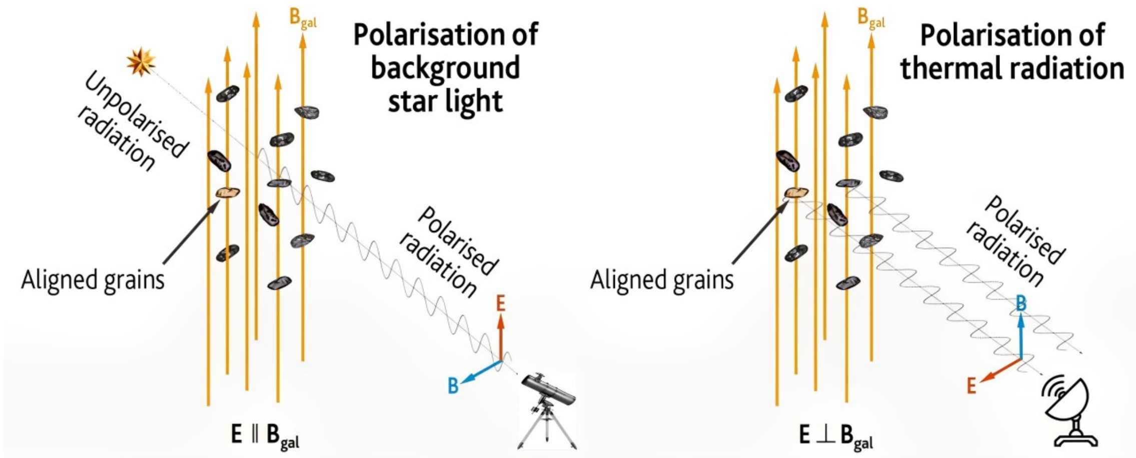

Figure 4.1: A schematic image of dust scattering and emission polarization. *Credit: EU Research Summer 2020, Blazon Publishing and Media Ltd.*

There are different mechanisms for dust grain alignment (see the review article by Andersson et al., 2015), but the most widely accepted one being is the radiative alignment torque (RAT) mechanism (Lazarian, 2007; Hoang & Lazarian, 2014; Andersson et al., 2015). In the RAT mechanism, the asymmetric and irregular dust grains offer a differential extinction cross-section to the radiation coming from the stars, and due to this, a torque is produced that rotates the dust grains. The rotating paramagnetic dust grains become magnetized and acquire a magnetic moment due to the *Barnett effect*. Now, this magnetic moment of dust grains interacts with the external magnetic field and starts to precess around the magnetic field direction, known as *larmor precision*. With the radiation coming from the stars continuously providing the torque to the dust grains, the grain's spin axis (shorter axis) aligns with the magnetic field direction (for more details, see Andersson et al., 2015). In this work, we used emission polarization-based measurements at 850 μm to study the magnetic field morphology and its role in the hub of the cloud.

4.2 Observations and data sets

4.2.1 Dust continuum polarization observations using JCMT SCUBA-2/POL-2

The C1 clump/hub region of G148.24+00.41 was observed with SCUBA-2/POL-2 instrument mounted on the JCMT, a single-dish sub-millimetre telescope in Mauna Kea, Hawaii, USA. The POL-2 instrument is a linear polarimetry module (Friberg et al., 2016) for the SCUBA-2, a 10,000 bolometer camera on the JCMT (Holland et al., 2013). The data was acquired between 2022 November 25 and 2023 January 03 (project code: M22BP055; PI: Vineet Rawat) in the band 2 weather conditions under an atmospheric optical depth at 225 GHz (τ_{225}) of 0.04 to 0.06. The observations were taken in 10 sets with an integration time of 30 minutes each, resulting in a total integration time of around 5.5 hr. The POL-2 DAISY scan mode (Holland et al., 2013; Friberg et al., 2016) was adopted, which generates a map of high signal-to-noise ratio (SNR) within a central region spanning a diameter of 3′, and the noise level gradually increases towards the edges of the map. The region is observed in both the 450 and 850 μm continuum polarizations simultaneously, with a resolution of $9\farcs6$ and $14\farcs1$, respectively. Due to the low sensitivity of the 450 μm data, this paper presents the analyses and results based on only 850 μm dust polarization data.

The data reduction was carried out using the *pol2map*[1] script in the SMURF package (Chapin et al., 2013) of Starlink (Currie et al., 2014). The POL-2 is characterized by linear

[1] http://starlink.eao.hawaii.edu/docs/sc22.htx/sc22.html

polarization that produces Stokes I, Q, and U vector maps. The *Skyloop* mode was utilised to minimise the uncertainty associated with map creation, while the MAPVARS mode was enabled to asses the total uncertainty from the standard deviation among individual observations. The details of the data reduction process of POL-2 can be found in Pattle et al. (2017) and Wang et al. (2019). Finally, the I, Q, and U maps, along with their variance maps, are used to create a debiased polarization vector catalogue. The catalogue consists of total intensity (I), stokes vectors (Q and U), polarization intensity (PI), polarization fraction (P), polarization angle (θ_P), and their associated uncertainties (δI, δQ, δU, δPI, δP, and $\delta\theta_P$, respectively).

The I, Q, and U maps are produced with 4″pixel size, while the polarization catalogue is binned to 12″, for better sensitivity. A flux calibration factor of 668.25 Jy beam^{-1} pW^{-1} is used for 850 μm Stokes I, Q, and U map to convert them from pW to mJy/beam and to account for the flux-loss due to POL-2 insertion into the telescope. This calibration factor comprises 495 Jy/beam/pW for reductions using 4″pixels of SCUBA-2, multiplied by the standard 1.35 factor for POL-2 losses (Mairs et al., 2021).

The polarised intensity is defined to be positive, so the uncertainties of the Q and U Stokes vector would bias the polarised intensities towards larger values (Vaillancourt, 2006; Kwon et al., 2018). The debiased polarization intensity and its uncertainty are calculated as

$$PI = \sqrt{Q^2 + U^2 - 0.5(\delta Q^2 + \delta U^2)} \tag{4.1}$$

and

$$\delta PI = \sqrt{\frac{(Q^2 \delta Q^2 + U^2 \delta U^2)}{(Q^2 + U^2)}},$$

respectively. The debiased polarization fraction and its uncertainty are then calculated as

$$P = \frac{PI}{I} \tag{4.2}$$

and

$$\delta P = \sqrt{\frac{\delta PI^2}{I^2} + \frac{\delta I^2 (Q^2 + U^2)}{I^4}},$$

respectively. The polarization angle and its uncertainty are calculated as

$$\theta_P = \frac{1}{2}\tan^{-1}\left(\frac{U}{Q}\right) \tag{4.3}$$

and

$$\delta_{\theta_P} = \frac{1}{2}\sqrt{\frac{(U^2\delta Q^2 + Q^2\delta U^2)}{(Q^2+U^2)^2}},$$

respectively. The polarization angle increases from the north toward the east, following the IAU convention. The mean rms noises in the Stokes I, Q, U, and PI measurements with 12″ bin size are 1.4, 1.1, 1.1, and 1.1 mJy beam^{-1}, respectively. Following the standard convention, for magnetic field, hereafter, B-field orientations, the polarization angles are rotated by 90 degrees.

4.3 Analyses and results

Figure 4.2a shows the ^{13}CO intensity map of G148.24+00.41, integrated in the velocity range of -37.0 km s^{-1} to -30.0 km s^{-1}, where one can see a bright spot in the centre of the map. This location corresponds to the C1 clump, whose mass and effective size based on C^{18}O data are ~2100 M$_\odot$ and ~1.8 pc, respectively. The filamentary features attached to the C1 clump can also be seen in *Herschel* 250 μm image, shown in Figure 4.2b. Such hub filamentary systems with the clump being located at the nexus or junction of the filaments are of particular interest because these are the sites where cluster formation would take place, as advocated in simulations and observations (e.g. Naranjo-Romero et al., 2012; Gómez & Vázquez-Semadeni, 2014; Gómez et al., 2018; Vázquez-Semadeni et al., 2019; Kumar et al., 2020).

Figure 4.2c shows the Stokes I map of the region, where the location of the C1 clump is also shown. From the figure, it can be seen that the 850 μm JCMT data (beam size ~14″) has resolved multiple sub-structures in the central region of the cloud. We found sub-structures like a central clump, a clump located on the western side, and a prominent elongated structure on the northeastern side of the central clump. In addition to these prominent sub-structures, a few compact structures are also visible in the image.

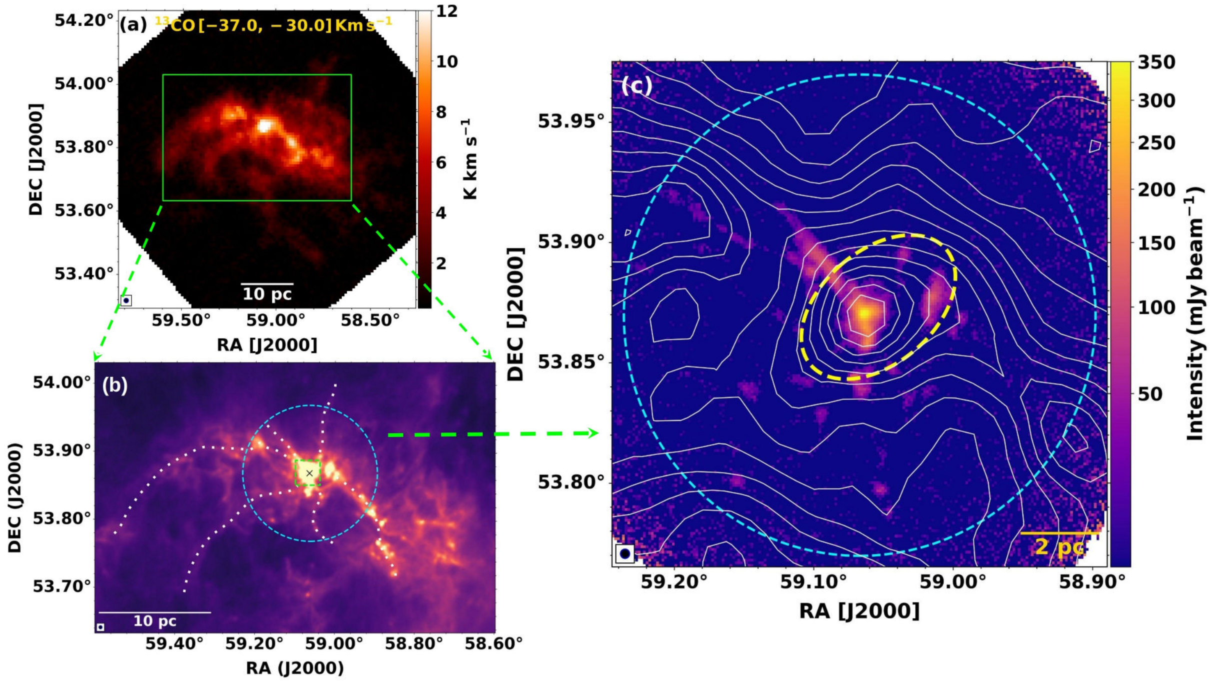

Figure 4.2: (a) ^{13}CO (J = 1−0) intensity map of G148.24+00.41, integrated in the velocity range −37.0 km s^{-1}to −30.0 km s^{-1}. (b) The central region (encompassed by the solid green box in panel-a) of G148.24+00.41 as seen in *Herschel* 250 μm band, showing the hub-filamentary morphology of the cloud. The figure is the same as Figure 2.16 in which the blue circle shows the JCMT scanned region of diameter ∼12′(∼12 pc). The green dashed box marks the central area of the hub, where an infrared cluster is seen, and the cross sign indicates the position of a massive young stellar object. (c) The 850 μm Stokes I intensity map of the central region of G148.24+00.41 mapped by JCMT SCUBA-2/POL-2, along with the contours of ^{13}CO integrated intensity emission, drawn from 1.5 to 15 K km s^{-1}with a step size of ∼0.96 K km s^{-1}. The rms noise of the 4″pixel-size Stokes I map is around ∼5 mJy beam^{-1}. In panel-c, the yellow ellipse shows the position of the C1 clump, identified using C^{18}O data (spatial resolution ∼52″). The beam sizes of the ^{13}CO integrated intensity map, *Herschel* 250 μm map, and JCMT 850 μm map are ∼52″, 18″, and 14″, respectively, shown as a framed-blue dot at the bottom left of each panel.

4.3.1 B-field morphology

In order to select the significant polarization detections, we set the following criteria for selecting data: I/δI > 10, P/δP > 2, and P < 30%. By doing this, we got 69 polarization measurements in our target region. The P values range from ∼2 % to ∼29 % with a mean and standard deviation around ∼11 ± 8 %. The B-field orientations are widely distributed, ranging from ∼6° to 180° with a mean and standard deviation around ∼91°± 48°, suggesting a complex B-field morphology in the region. The mean uncertainties in polarization fraction and polarization angle are ∼3.5% and ∼9°, respectively. Figure 4.3a and b show the distribution of polarization vectors and B-field orientations, respectively, over the 850 μm Stokes I dust continuum emission map of the region. The contour levels in the map are shown above 3σ from the background, where σ is the mean rms noise (5 mJy beam^{-1}) of the Stokes I map.

In this work, based on 850 μm Stokes I intensity and magnetic field orientations, we defined the central clump, clump located on the western side, and northeastern elongated structure as CC, WC, and NES, respectively, as marked in Figure 4.3b. The approximate extents of these regions are defined by considering the outermost closed contours of the 850 μm Stokes I map. From Figure 4.3b, it can be seen that the B-field orientations in the CC are mostly oriented along the east-west direction (PA ∼90°), while some of them are at smaller position angles. There exist mixed B-field orientations in the NES region, some in the low-density area are nearly perpendicular to the major axis of the NES, while some closer to the CC are parallel to it. In the WC, most of the B-fields are converging towards the centre, aligned along the southeast direction, which may be influenced by gravity (see Section 4.3.3.2 and 4.4.1). Overall, the B-field morphology around the central region of G148.24+00.41 is complex, which is probably due to hierarchical fragmentation and a network of filamentary flows towards the hub, as found in the cloud.

Figure 4.4a shows the histogram of the B-field orientations in the central region of G148.24+00.41, which is broadly distributed. The CC is showing mixed morphology, having two peaks, one at ∼38° (i.e. with position angles close to northeast), and the second is at ∼80° (i.e. with position angles parallel to east). The NES shows a flat distribution over a broad range, but a slightly higher distribution at a position angle around ∼180°. The WC, though, has a small number of segments, shows a peak around ∼125°, i.e. mostly in the southeast direction. All these orientations are also clearly evident in Figure 4.4b, which shows the distribution of B-field position angles. From Figure 4.4b, it can be seen that the B-field angles change roughly from ∼180° to ∼70° while going from the elongated structure towards the central clump.

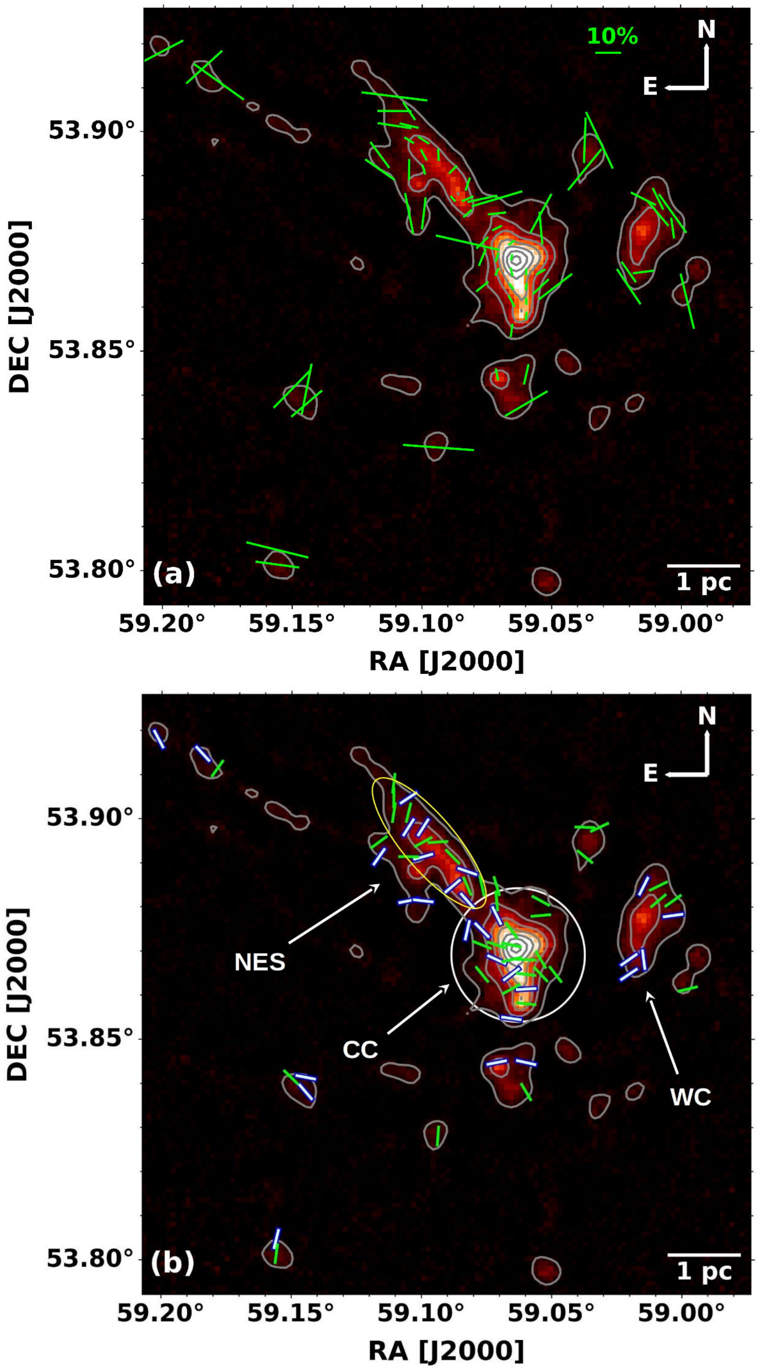

Figure 4.3: (a) Polarization vector map with lengths proportional to polarization fraction, and (b) magnetic field orientation map with fixed lengths. The background is the Stokes I image at 850 μm, and the contour levels are drawn at 3σ above the rms noise level of 5 mJy beam^{-1}, starting from 15 mJy beam^{-1}to 300 mJy beam^{-1}. The segments shown are binned to a 12″pixel grid and correspond to polarization data with I/δI > 10 and P/δP > 2. The lightcyan and green vectors in panel-b show the measurements with 2 < P/δP < 3 and P/δP > 3, respectively. The regions used for B-field calculation are also shown in panel-b by a white circle and yellow ellipse for the CC and NES, respectively.

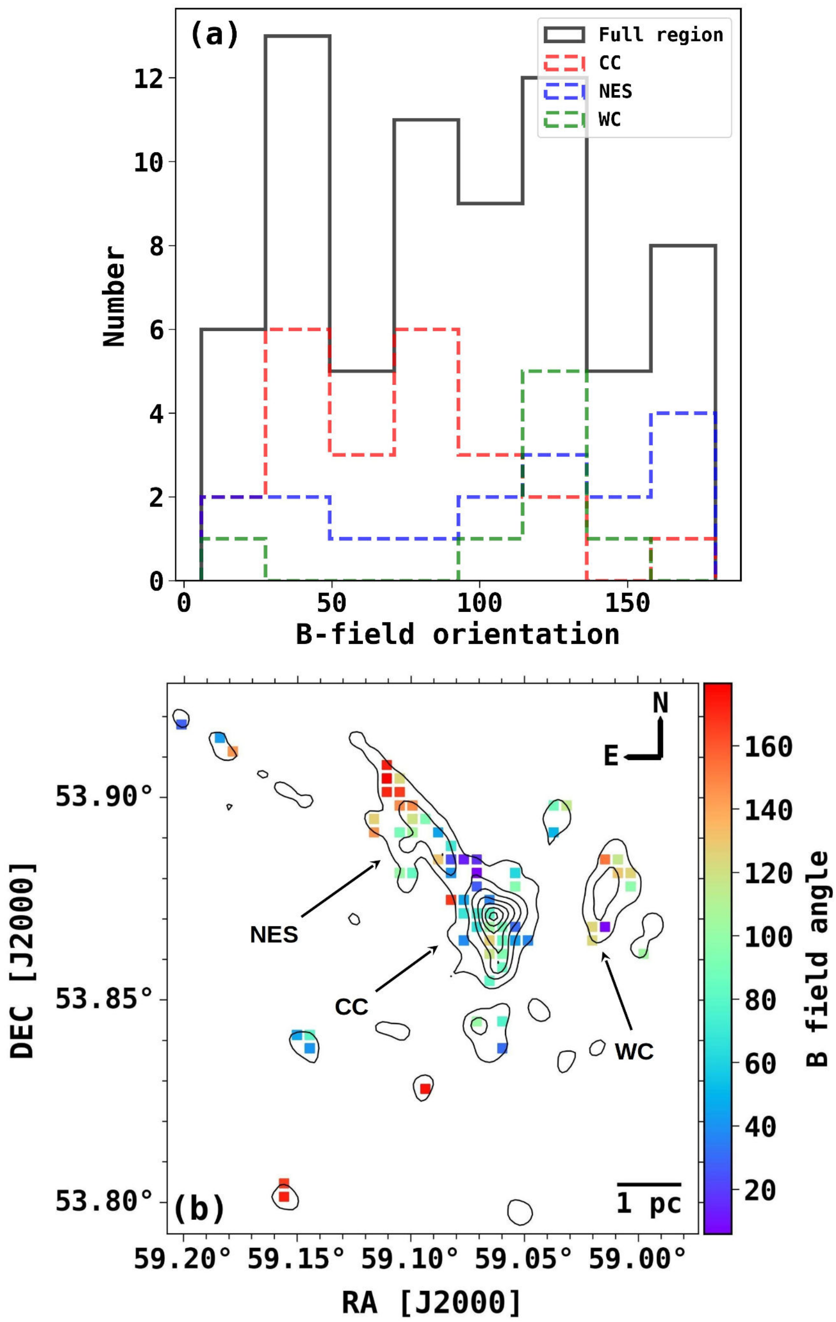

Figure 4.4: (a) Histogram of B-field position angles for the whole region, CC, NES, and WC. (b) Distribution of B-field position angles over the contours of 850 μm Stokes I map. The contour levels are the same as in Figure 4.3.

4.3.2 Variation of polarization fraction: depolarization effect

Figure 4.5 shows the distribution of polarization fraction over the contours of Stokes I emission. From the figure, it can be seen that the polarization fraction is lower in the high-intensity regions compared to the low-intensity regions, which shows the decreasing trend of polarization fraction with the total intensity, known as depolarization. The depolarization effect has been reported in several studies (Girart et al., 2006; Tang et al., 2013; Sadavoy et al., 2018; Soam et al., 2018; Liu et al., 2019, 2020), and is mainly explained by the inefficient radiative alignment of dust grains in high-density regions or integration effect across complex magnetic fields. In high-density regions, the radiative alignment torques decrease due to the attenuation of interstellar radiation that results in poor grain alignment, and hence a decrease in polarization fraction. However, the grain characteristics like size, shape, composition, and grain growth can also affect the dust grain alignment. The turbulent nature of the B-field and unresolved complex and tangled B-fields within the JCMT beam, being averaged across the beam, can also give low dust polarization (Planck Collaboration et al., 2016, 2020). We want to point out that in the hub/C1 clump of G148.24+00.41, supersonic non-thermal motions have been found (sonic Mach number ≈ 3, see Table 3.3 in Chapter 3). Therefore, the turbulent nature of the B-field can also be the cause of depolarization in our target.

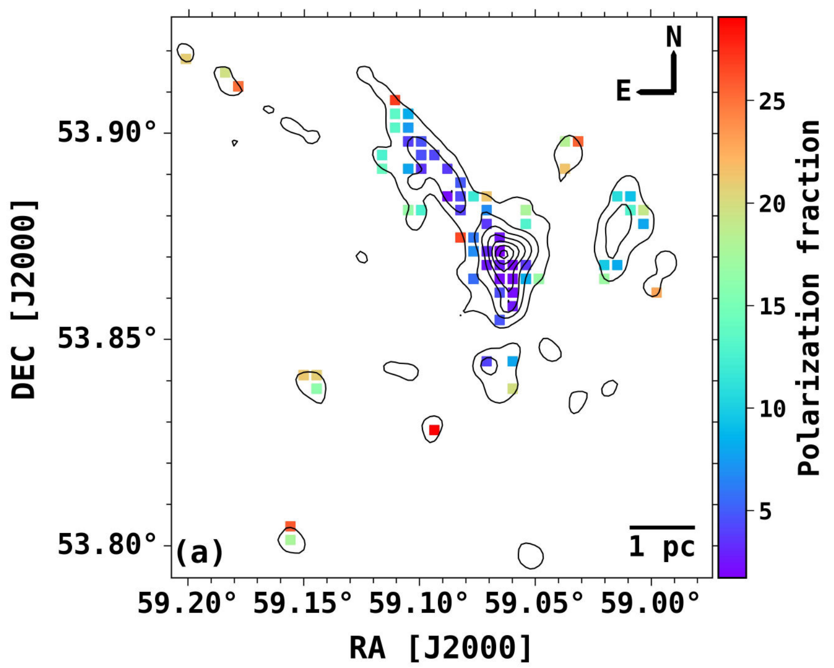

Figure 4.5: Distribution of dust polarization fraction (P in %) over the contours of 850 μm Stokes I map. The contour levels are the same as in Figure 4.3.

The relation between polarization fraction and intensity is expected to follow a power-law, $P \propto I^{-\alpha}$ (Whittet et al., 2008). A range of α values has been found in molecular clouds from ~0.5 to 1 (Chung et al., 2023, and references therein). The α value is often used as an indicator of the dust grain alignment efficiency. When α = 0, it implies a constant grain alignment efficiency, α = 0.5 implies that the alignment decreases linearly with the increasing optical depth, while α = 1 implies an alignment limited to the outer regions of the cloud, and at higher density, there is no preferred alignment of grains relative to the magnetic field (Whittet et al., 2008). We fit the P-I relation with a single power-law (weighted-fit) and found an index, α = 0.95 ± 0.04, which shows that the dust grain alignment efficiency is decreasing in the central dense region of G148.24+00.41. However, Pattle et al. (2019) shows that the conventional approach of fitting a single power-law over the polarization measurements debiased with Gaussian noise is only applicable above a high SNR cut. But in low polarized intensity regions, a high SNR would discard more data, and therefore, the α index will be overestimated (Pattle et al., 2019; Chung et al., 2023; Lin et al., 2023). Wang et al. (2019) also found that the value of α depends upon the cut of SNR and tends to −1 if we put a constraint on P/δP. Hence, to obtain the true value of the α index, it is recommended to use the non-debiased polarization measurements, including both the low and high SNR data, and should not put constraints on P/δP (Pattle et al., 2019; Wang et al., 2019).

We followed the Bayesian method of Wang et al. (2019) to determine the true value of α by using the non-debiased polarization data, which follows well the Rice distribution (see Pattle et al., 2019; Wang et al., 2019, and references therein)

$$F(P|P_0) = \frac{P}{\sigma_P^2} \exp\left[-\frac{P^2 + P_0^2}{2\sigma_P^2}\right] I_0\left(\frac{PP_0}{\sigma_P^2}\right), \tag{4.4}$$

where P and P_0 are the observed and true polarization fraction, respectively, σ_P is the uncertainty in the polarization fraction, and I_0 is the zeroth-order modified Bessel function. We used non-debiased data with an SNR of 2 (i.e. I/δI > 2) to include most of the data points and used the power-law model, $P_0 = \beta I^{-\alpha}$, with uncertainty $\sigma_P = \sigma_{\rm QU}/I$, where $\sigma_{\rm QU}$ represents the rms noise in Q and U measurements, I is the total observed intensity, and α, β, and $\sigma_{\rm QU}$ are the free model parameters. We employed the Markov Chain Monte Carlo method and used a python package PyMC3 (Salvatier et al., 2016) to fit the Rician model to the data. We set the uniform priors on all three model parameters: $0 < \alpha < 2$, $0 < \beta < 100$, and $0 < \sigma_{\rm QU} < 5$, and otherwise a value of 0 for all the parameters. The details of the methodology are given in Wang et al. (2019). Figure 4.6 shows the derived posterior of each model parameter, along with their 95% highest density interval (HDI), depicting the uncertainty in each parameter. The mean values of α, β, and σ_{QU} are ~0.6, 37, and 1.7, respectively. The α value derived from the non-debiased polarization data is smaller than the α value derived from the conventional approach (i.e. ~0.95).

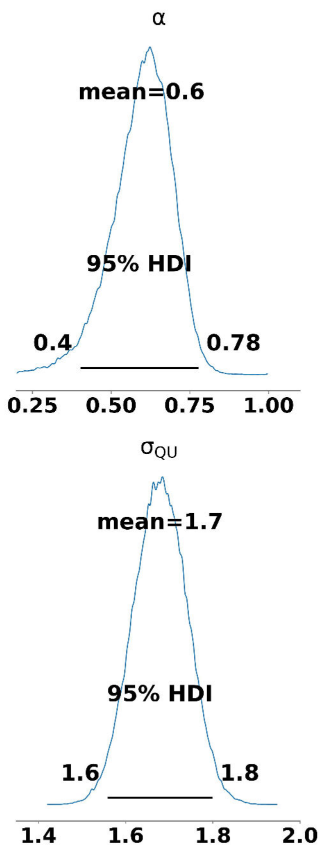

Figure 4.6: The probability distribution function of the fitted model parameters derived using the Bayesian method over the non-debiased polarization data. The mean values of the parameters are shown along with the 95% HDI intervals to represent the uncertainties. The 95% confidence intervals are marked as horizontal bars.

Figure 4.7 shows the non-debiased polarization fraction versus total intensity plot with 50%, 68%, and 95% confidence intervals. The derived α value suggests that the grain alignment is still persisting in the hub of G148.24+00.41, but with decreasing efficiency in the dense regions.

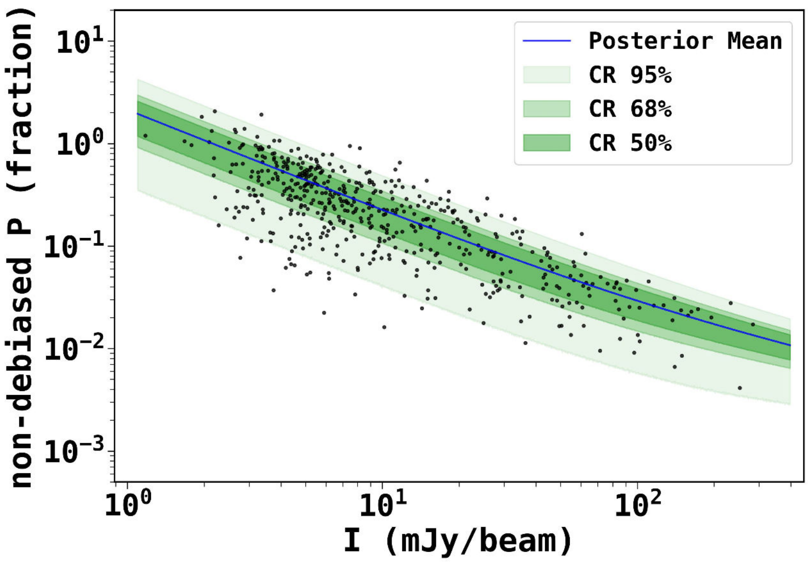

Figure 4.7: Non-debiased polarization fraction versus total intensity. The blue line shows the mean, and the coloured regions show the 95%, 68%, and 50% confidence limits, as predicted by the posteriors of α = 0.6, β = 37, and σ_{QU} = 1.7.

4.3.3 Relative orientations of magnetic fields, intensity gradients, and local gravity

In star-forming regions, various forces interact, like gravity, magnetic field, and turbulence, which shape the geometry of these regions and drive the star-formation process (Ballesteros-Paredes et al., 2007; Koch et al., 2012a; Pattle et al., 2022). Along with the overall strength of these individual factors for an entire region (discussed in Section 4.4.2), it is also important to investigate their localised relative orientations in the map, as it would give insight into the localised effect of these factors (Koch et al., 2012a,b, 2013; Tang et al., 2019; Liu et al., 2020; Wang et al., 2020b). Koch et al. (2012a) developed a technique, "the polarization-intensity gradient-local gravity," using Magnetohydrodynamics (MHD) force equations to measure the local magnetic field strengths. Following the approach of Koch et al. (2012a,b), we find out the angular difference between magnetic field, intensity gradient, and local gravity, and discuss their relative importance at different positions.

4.3.3.1 Intensity gradient versus magnetic field

We used the 850 μm dust continuum intensities of all pixels in the map to determine the directions of intensity gradients. All the pixels that have values above a certain threshold (i.e. 3σ above the mean rms noise in the Stokes I map) are considered for computing the direction of gradients, except those that exist at the edges. For a pixel at position (α_i, δ_j), the position angle (θ'_{IG}) of the intensity gradient is calculated as

$$\theta'_{IG} = (180/\pi) \times \arctan \left[\frac{\Delta I_{\delta_j}}{\Delta I_{\alpha_i}} \right], \tag{4.5}$$

where $\Delta I_{\delta_j} = I_{\delta_{j+1}} - I_{\delta_{j-1}}$ and $\Delta I_{\alpha_i} = I_{\alpha_{i+1}} - I_{\alpha_{i-1}}$.

The θ'_{IG} values are then converted to gradient directions (θ_{IG}) by doing the quadrant corrections, i.e. arranging the angles between 0° and 360° (for details, see Eswaraiah et al., 2020). In order to plot the gradient orientations instead of directions, we folded the θ_{IG} between 0° and 180°. For comparison of the gradient orientations (θ_{IG}) with the B-field orientations (θ_B), we took the average of all the θ_{IG} values within a diameter of $\sim$14″(corresponds to the beam size of JCMT at 850 μm) around each B-field position. We calculated the circular mean to get the average of intensity gradients. In this approach, the angles are treated as unit vectors, which is adequate for broad distributions and ambiguity in angles (Tang et al., 2019). Figure 4.8a shows the orientations of intensity gradients relative to B-field orientations over the 850 μm Stokes I map. We find that the local differences between these orientations are overall widely distributed. However, it can be seen that the intensity gradients are mostly aligned with the B-fields in the CC and WC regions, while the differences in orientations are relatively higher in the NES region. In the observed central region of G148.24+00.41, we found a moderate correlation between θ_B and θ_{IG}, in the CC and WC (see Figures. 4.8a, b). Figure 4.8b shows the distribution of $\Delta\theta_{B,IG} = |(\theta_B - \theta_{IG})|$ over the contours of 850 μm Stokes I map. The $\Delta\theta_{B,IG}$ values lie between 0° and 90° after considering them to be the acute angle. A stronger correlation between θ_B and θ_{IG} tells that the material is following the B-field lines (Koch et al., 2013; Tang et al., 2019, more discussion in Section 4.4.1).

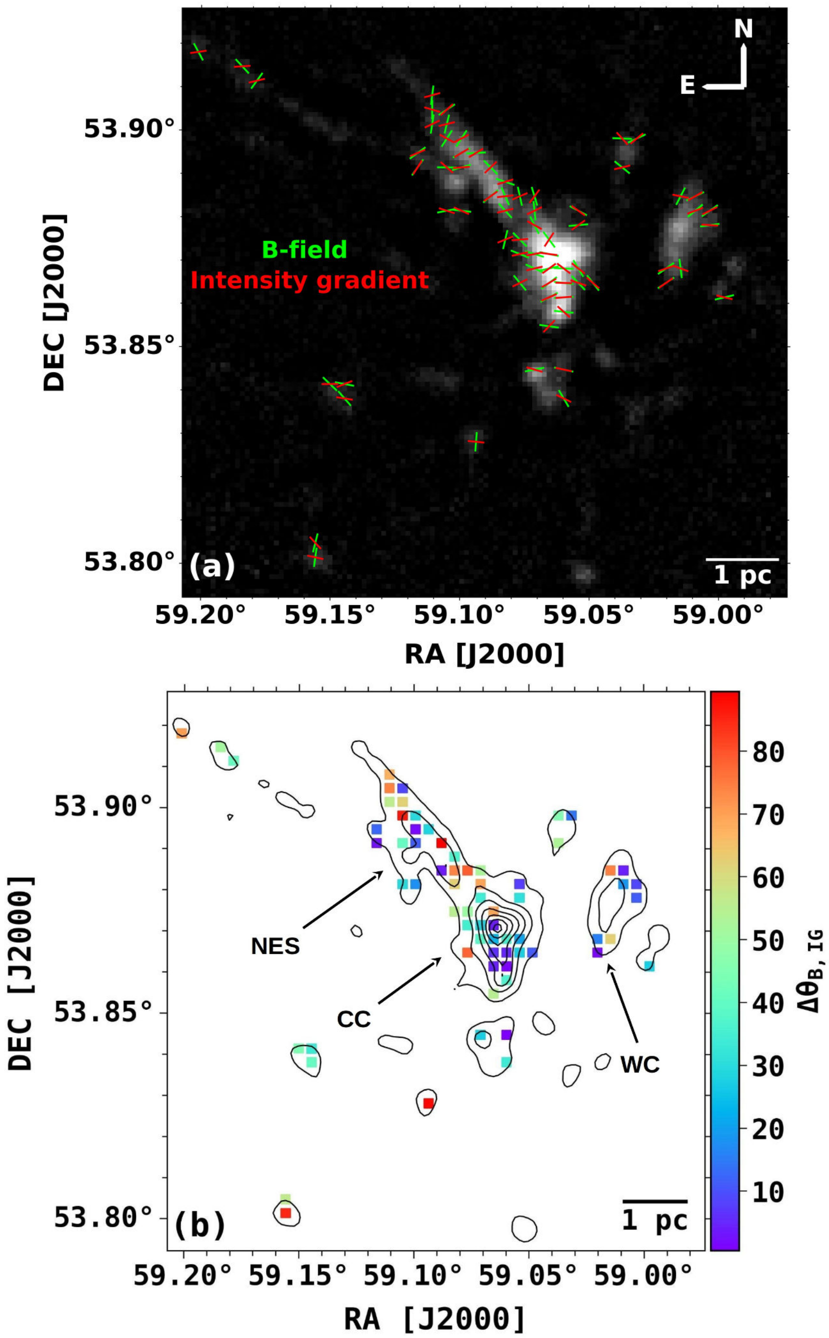

Figure 4.8: (a) The orientations of the B-fields (green segments) and intensity gradients (red segments) are overlaid on the 850 μm Stokes I map. (b) The distribution of the offset between the position angles of the B-fields and intensity gradients, i.e., $\Delta\theta_{B,IG} = |(\theta_B - \theta_{IG})|$ over the contours of 850 μm Stokes I map. The contour levels are the same as in Figure 4.3.

4.3.3.2 Local gravitational field versus magnetic field

In order to investigate the localised effect of gravity on the B-field morphology of the structures, we used the 850 μm dust continuum map to compute the projected gravitational field vectors. The gravitational force at any pixel ($F_{G,i}$) is the vector sum of the forces from all the surrounding pixels and is expressed as (Wang et al., 2020b).

$$F_{G,i} = kI_i \sum_{j=1}^{N} \frac{I_j}{r^2{}_{ij}} \hat{r}, \tag{4.6}$$

where I_i and I_j are the intensity of the pixel at position i and j, respectively, and k is the term that takes care of the conversion of emission to total column density and also includes the gravitational constant. N is the total number of pixels within the selected area, r_{ij} is the projected distance between the pixels i and j, and $\hat{r}$ is the unit vector. Considering only the directions of the local gravitational forces, we take k to be 1 in the above equation by assuming that the spatial distribution of dust will be analogous to the spatial distribution of mass. Similar to the intensity gradient map, we selected those pixels that have intensity values above the threshold, and obtained the local gravity vectors (θ_{LG}) at each B-field position, by taking an average of all vectors within the 14″beam size. Figure 4.9a shows the orientations of local gravity vectors relative to B-field orientations over the 850 μm Stokes I map. From the figure, it can be seen that similar to intensity gradients, the local gravity vectors are also mostly aligned with the B-fields in the CC and WC region, whereas they deviate from the B-fields in the NES region. Figure 4.9b shows the distribution of $\Delta\theta_{B,LG} = |(\theta_B - \theta_{LG})|$ values over the contours of 850 μm Stokes I emission, which are treated to be acute angles.

4.3.3.3 Intensity gradients versus Local gravitational field

Figure 4.10a shows the relative orientations of intensity gradient and local gravity, and Figure 4.10b shows the distribution of the angular difference between their orientations, i.e. $\Delta\theta_{IG,LG}$. Similar to $\Delta\theta_{B,IG}$ and $\Delta\theta_{B,LG}$, the correlation between the angles (θ_{IG} and θ_{LG}) is better in the CC and WC regions in comparison to NES region.

Figures 4.11a-c shows the histogram distribution of the relative position angle differences of

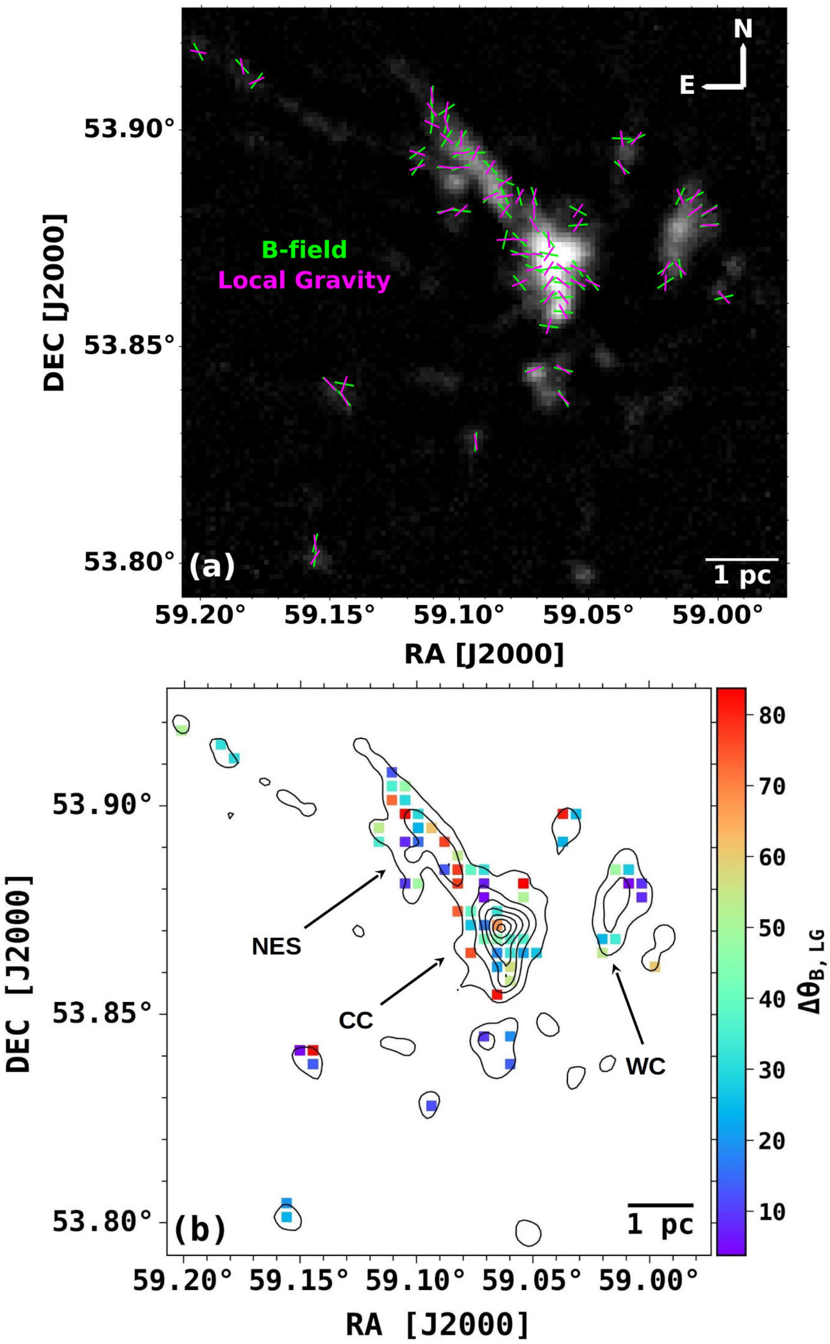

Figure 4.9: (a) The orientations of the B-fields (green segments) and local gravity (magenta vectors) are overlaid on the 850 μm Stokes I map. (b) The distribution of the offset between the position angles of the B-fields and local gravity, i.e., $\Delta\theta_{B,LG} = |(\theta_B - \theta_{LG})|$ over the 850 μm Stokes I map. The contour levels are the same as in Figure 4.3.

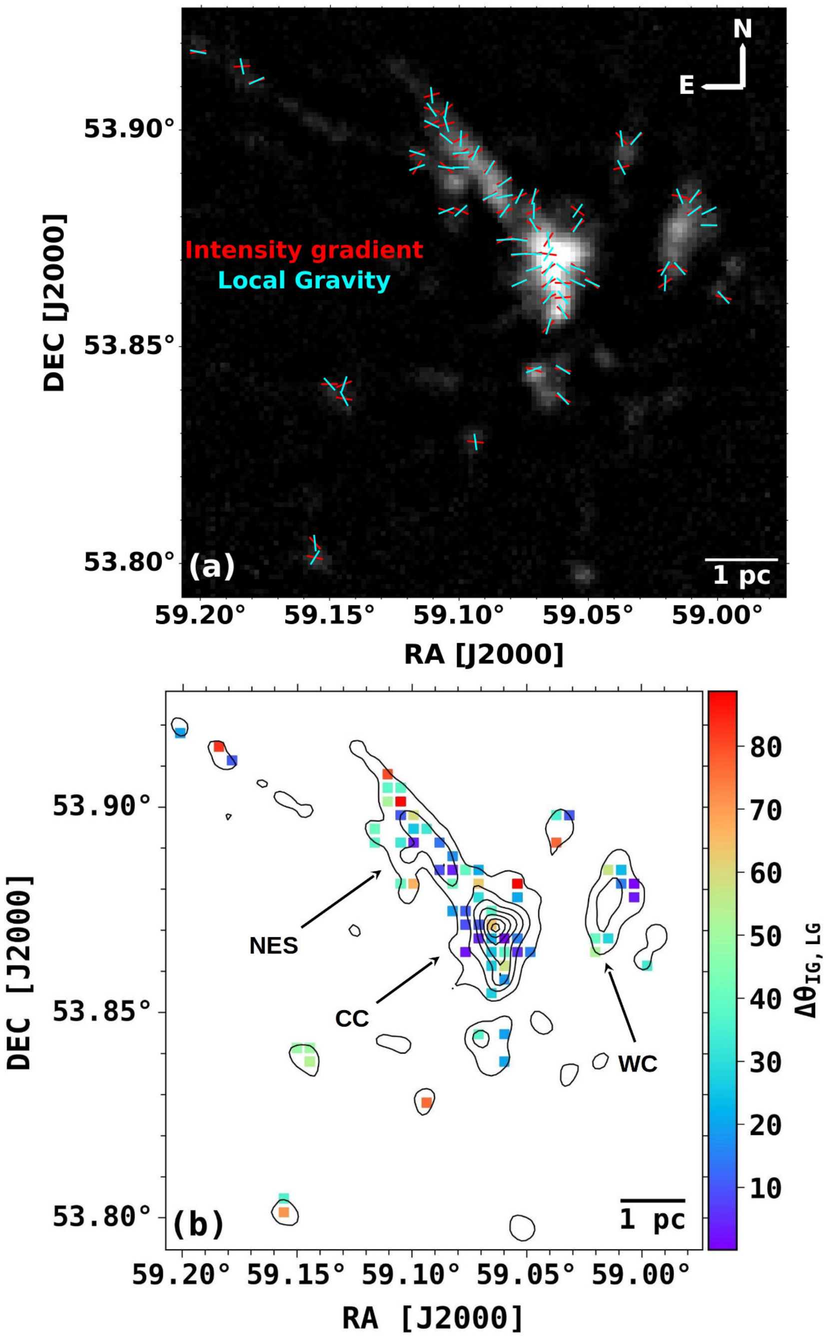

Figure 4.10: (a) The orientations of the intensity gradients (red segments) and local gravity (cyan vectors) are overlaid on the 850 μm Stokes I map. (b) The distribution of the offset between the position angles of the intensity gradients and local gravity, i.e., $\Delta\theta_{IG,LG} = |(\theta_{IG} - \theta_{LG})|$ over the contours of 850 μm Stokes I map. The contour levels are the same as in Figure 4.3.

B-field, intensity gradients, and local gravity, i.e. $\Delta\theta_{B,IG} = |(\theta_B - \theta_{IG})|$, $\Delta\theta_{B,LG} = |(\theta_B - \theta_{LG})|$, and $\Delta\theta_{IG,LG} = |(\theta_{IG} - \theta_{LG})|$. From the figure, it can be seen that the differences in the offset angles are mostly distributed towards the smaller angles. The median of $\Delta\theta_{B,IG}$, $\Delta\theta_{B,LG}$, and $\Delta\theta_{IG,LG}$ is 34°, 32°, and 30° with median absolute deviation of 22°, 18°, and 15°, respectively. The higher angular deviations in the histograms are primarily due to position angles in the elongated structures on the northeastern side, as well as from some structures located south of the CC.

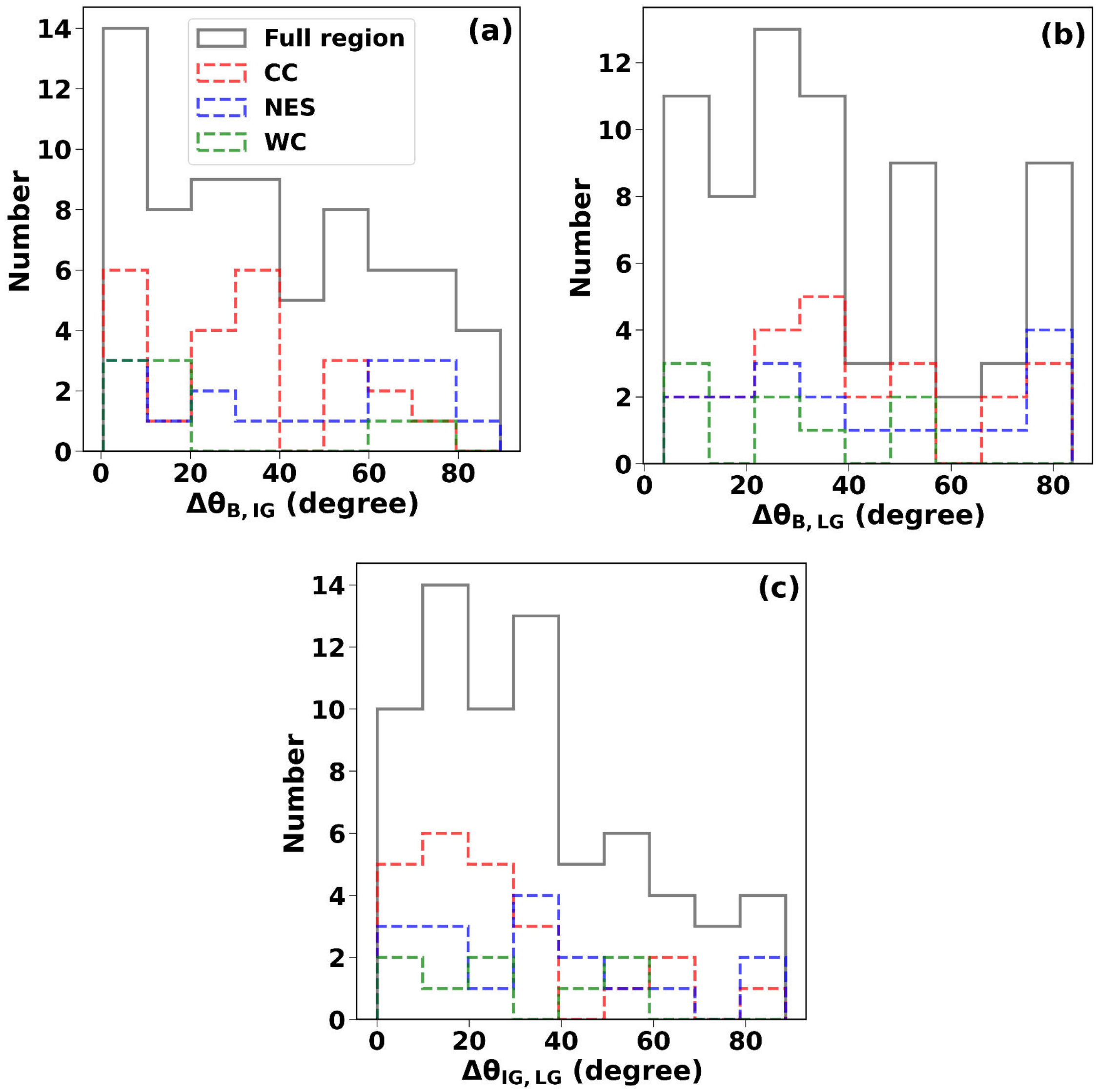

Figure 4.11: Distribution of difference in position angles of (a) magnetic field (θ_B) and intensity gradient (θ_{IG}), (b) magnetic field (θ_B) and local gravity (θ_{LG}), and (c) intensity gradient (θ_{IG}) and local gravity (θ_{LG}). The red, blue, and green histograms show the difference in position angles within the CC, NES, and WC regions, respectively.

As discussed previously, Koch et al. (2012a,b) developed a "polarization-intensity gradient method" that can estimate the local field-to-gravity force ratio Σ_B. This method is based on the assumption that the emission intensity gradients reflect the direction of matter flow due to the combined influences of magnetic pressure force and gravitational force. Using the MHD force equations and geometrically solving them by incorporating the angle between the magnetic field and intensity gradient ($\Delta\theta_{B,IG}$), and between intensity gradient and local gravity ($\Delta\theta_{IG,LG}$), the magnetic field (F_B)-to-gravity force (F_G) ratio can be obtained as

$$\Sigma_B = \frac{sin(\Delta\theta_{IG,LG})}{sin(90 - \Delta\theta_{B,IG})} = \frac{F_B}{|F_G|}. \tag{4.7}$$

In the above equation, the hydrostatic gas pressure is assumed to be negligible. Figure 4.12 shows the Σ_B distribution plot over the Stokes 850 μm intensity map. From the figure, it can be seen that Σ_B is mostly ≤ 1, with a median around ~0.6, which shows that the magnetic field is not solely enough to balance the gravitational force (Koch et al., 2012a). This implies that gravity dominates over the magnetic field to govern the gas motion towards the centre. However, we note that the POL-2 images generally filter out large-scale structures, and so here, the intensity gradient only traces the local structure on a 4″pixel-scale. Therefore, to check the effect of large-scale structures on the intensity gradient and local gravity, we generated similar maps from *Herschel* 250 μm image of G148.24+00.41 and found that the maps are comparable with the JCMT maps. The use of 250 μm map is an optimal choice because compared to *Herschel′s* longer wavelength (i.e. 350 and 500 μm) bands, its resolution (∼18″) is comparable to the resolution of the JCMT 850 μm (14″) map and also it is a better tracer of cold dust compared to *Herschel′s* shorter wavelength (i.e. 70 and 160 μm) bands.

Due to the relatively low number of B-field segments in the WC region, we focused our further analysis, like the study of structure, dust properties, and B-field strength calculation, towards the CC and NES regions.

4.3.4 Column and number densities

Considering the high resolution of the 850 μm data compared to *Herschel* longer wavelength data sets, we calculate the molecular hydrogen column density using the 850 μm dust continuum

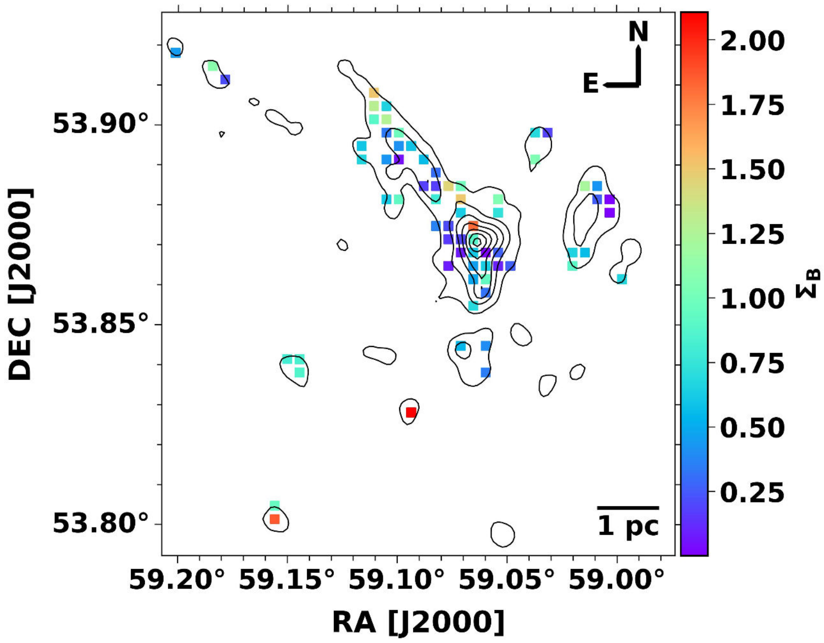

Figure 4.12: Σ_B distribution over the contours of 850 μm Stokes I map. The contour levels are same as in Figure 4.3.

emission. Assuming the dust emission to be optically thin, the column density can be calculated using the relation (Kauffmann et al., 2008),

$$N(H_2) = 2.02\times10^{20}\text{cm}^{-2}\left(e^{1.439\left(\frac{\lambda}{\text{mm}}\right)^{-1}\left(\frac{T_D}{10K}\right)^{-1}}-1\right)$$
$$\times\left(\frac{\kappa_\nu}{0.01\text{cm}^2\text{g}^{-1}}\right)^{-1}\left(\frac{S_\nu}{\text{mJy beam}^{-1}}\right)\left(\frac{\theta_{HPBW}}{10''}\right)^{-2}\left(\frac{\lambda}{\text{mm}}\right)^{3}, \quad (4.8)$$

where S_ν is the flux density in Jy at frequency ν and dust opacity $\kappa_\nu = 0.1(\nu/1\ \text{THz})^\beta = 0.0125$ cm^{2}g^{-1} for $\nu = 0.353$ THz and dust opacity index, $\beta = 2$ (Battersby et al., 2011; Deharveng et al., 2012), and θ_{HPBW} is the beam size (14″at 850 μm). Within the boundaries of CC and NES, the mean T_D is around ∼16.8 K and 13.0 K, respectively (from the dust temperature map of Schisano et al., 2020). The total column density, $\sum N(H_2)$, for CC and NES, are found to be $(3.4 \pm 1.3) \times 10^{24}$ cm^{-2} and $(1.9 \pm 0.7) \times 10^{24}$ cm^{-2}, respectively. Then, assuming the spherical geometry for CC, its number density can be estimated using the relation

$$n_{H_2} = \frac{M}{V\mu m_H} = \frac{\sum N(H_2)\times A_{pixel}}{\frac{4}{3}\pi R_{eff}^3}, \quad (4.9)$$

where M and V are the mass and volume of the region, respectively. The r_{eff} for CC is calculated as $(Area/\pi)^{0.5}$, and is around ~0.9 ± 0.1 pc. Though NES is assumed as an elliptical structure with a semi-minor axis, r_1 = 0.35 ± 0.03 pc and a semi-major axis, r_2 = 1.10 ± 0.09 pc (see Figure 4.3a), in 3-dimension, this elongated structure could be better described by a cylindrical geometry. Therefore, to calculate the number density of NES, its radius (r) and length (L) were adopted to be r_1 and $2r_2$, respectively. Under this approximation, we estimated the n_{H_2} for NES by using $V = \pi r^2 L$ in equation 4.9. The gas mass within the regions is estimated from the total integrated molecular hydrogen column density, using equation 2.1 given in Chapter 2. The total column density, n_{H_2}, and the mass of the regions are given in Table 4.1. The uncertainties in the estimated cloud parameters are mainly due to uncertainty in the gas-to-dust ratio (23%), the dust opacity index (30%), and the distance of the cloud (9%) (for details, see Chapter 2).

4.3.5 Velocity dispersion

We used $C^{18}O$ (J = 1−0) molecular line data, which was taken as a part of the MWISP survey using PMO (discussed in Chapter 3), for finding the velocity dispersion of the CC and NES regions. In Chapter 3, we discussed that in comparison to ^{12}CO and ^{13}CO , $C^{18}O$ emission is optically thin in the G148.24+00.41 cloud. Figure 4.13 shows the $C^{18}O$ spectra averaged within the boundary of the two regions, CC and NES. The Gaussian fitting over the spectra gives the mean velocity as − 34.15 ± 0.04 km s^{-1}and − 33.80 ± 0.04 km s^{-1}, and velocity dispersion (σ_{obs}) as 0.69 ± 0.05 km s^{-1}and 0.41 ± 0.03 km s^{-1}, for CC and NES, respectively. The non-thermal velocity dispersion can be calculated using the relation, $\sigma_{nt} = \sqrt{\sigma_{obs}^2 - \sigma_{th}^2}$, as discussed in Section 3.3.2.5 of Chapter 3. We have used the excitation temperature map of G148.24+00.41 (see Section 3.3.1.2 and Figure 3.6 in Chapter 3) to get the approximate values of the kinetic temperature, as 11.4 K and 10.3 K for CC and NES, respectively. The estimated σ_{th} for the regions is ~ 0.06 km s^{-1}and 0.05 km s^{-1}, respectively, and hence negligible, leading σ_{nt} ~ σ_{obs}. This is an indication of the presence of turbulence in CC and NES, which has already been found for the whole C1 clump in Chapter 3 (sonic Mach number ≈ 3).

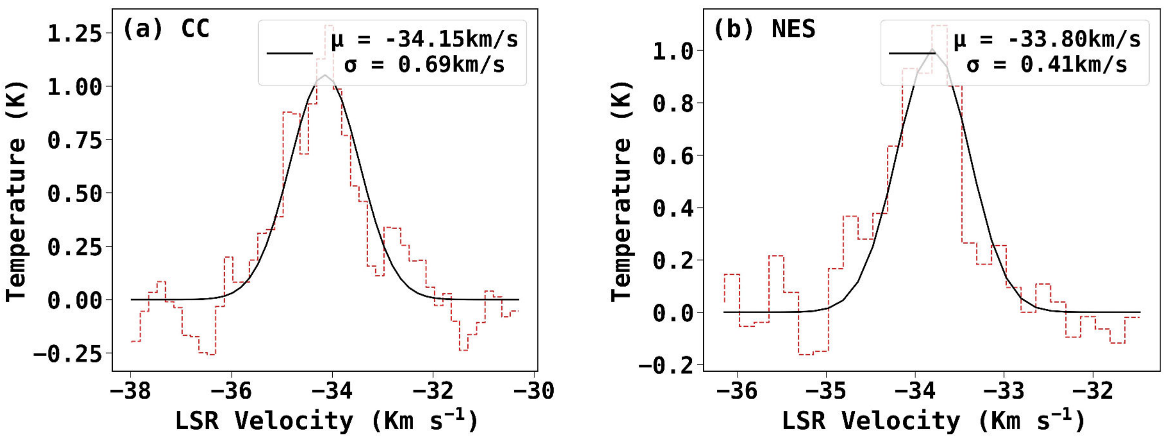

Figure 4.13: $C^{18}O$ average spectral profile for (a) CC and (b) NES.

Table 4.1: Parameters estimated for CC and NES.

No	Parameter	Unit	CC	NES
1	Effective radius (r_{eff})	pc	0.9 ± 0.1	semi-minor axis (r_1) = 0.35 ± 0.03, semi-major axis (r_2) = 1.10 ± 0.09
2	Mean column density $(N(H_2))$	cm^{-2}	$(5.8 \pm 2.2) \times 10^{21}$	$(7.1 \pm 2.7) \times 10^{21}$
3	Number density (n_{H_2})	cm^{-3}	1560 ± 780	3290 ± 1645
4	Mass (M)	$M_\odot$	330 ± 148	188 ± 85
5	Mean dust temperature (T_D)	K	16.8	13.0
6	Observed velocity dispersion (σ_{obs})	km s^{-1}	0.69 ± 0.05	0.41 ± 0.03
7	Thermal velocity dispersion (σ_{th})	km s^{-1}	0.06	0.05
8	Non-thermal velocity dispersion (σ_{nt})	km s^{-1}	0.69 ± 0.05	0.41 ± 0.03
	Structure function analysis			
1	Turbulent-to-ordered magnetic field ratio $\left(\frac{\langle \delta B^2 \rangle^{1/2}}{B_0}\right)$		0.43 ± 0.01	0.46 ± 0.04
2	Angular dispersion (σ_θ)	degrees	22.7 ± 0.6	23.9 ± 1.5
3	Plane-of-sky magnetic field strength (B_{pos})	μG	24.0 ± 6.0	20.0 ± 5.0
4	Mass-to-flux ratio (λ_B)		1.8 ± 0.8	2.7 ± 1.2
5	Alfvén velocity (V_A)	km s^{-1}	1.0 ± 0.4	0.6 ± 0.2
6	Alfvén mach number $(\mathcal{M}_A)$		1.2 ± 0.4	1.2 ± 0.4
7	Magnetic pressure (P_B)	dyne cm^{-2}	$(3.7 \pm 1.9) \times 10^{-11}$	$(2.6 \pm 1.3) \times 10^{-11}$

Table 4.1 – continued from previous page

No	Parameter	Unit	CC	NES
8	Turbulent pressure (P_{turb})	dyne cm^{-2}	$(5.2 \pm 2.7) \times 10^{-11}$	$(2.5 \pm 1.3) \times 10^{-11}$
	Virial balance			
1	Kinetic energy (E_K)	J	$(4.7 \pm 2.2) \times 10^{38}$	$(6.3 \pm 3.0) \times 10^{37}$
2	Magnetic energy (E_B)	J	$(3.3 \pm 3.0) \times 10^{38}$	$(7.0 \pm 5.0) \times 10^{37}$
3	Gravitational energy (E_G)	J	$(10.4 \pm 9.0) \times 10^{38}$	$(14 \pm 12) \times 10^{37}$
4	Kinetic virial parameter ($\alpha_{vir,k}$)		0.9 ± 0.4	0.9 ± 0.4
5	Total virial parameter ($\alpha_{vir,tot}$)		1.2 ± 0.6	1.4 ± 0.7

4.3.6 Magnetic field strength

Davis (1951) and Chandrasekhar & Fermi (1953) proposed a method to estimate the POS component of the magnetic field (B_{pos}), known as the Davis-Chandrasekhar-Fermi (DCF) method, which is based on the assumption that the turbulence-induced Alfvén waves perturb the ordered B-field structure. Therefore, there will be a distorted component of the B-field that would appear as an irregular scatter in polarization angles in comparison to those that are produced by large-scale ordered B-field. Thus, the DCF method implies that the ratio of turbulent (δB) to ordered B-field (B_0) is proportional to the ratio of non-thermal velocity dispersion to Alfvén velocity ($V_A = B_0/\sqrt{4\pi\rho}$, ρ is the gas mass density), i.e. $\frac{\delta B}{B_0} = \frac{\sigma_{nt}}{V_A}$. Also, the dispersion in the B-field position angles (σ_θ) about the large-scale ordered B-field is assumed as $\sigma_\theta = \frac{\delta B}{B_0}$. Using these relations, the POS component of the magnetic field, B_{pos}, can be estimated as

$$B_{pos} = Q\sqrt{4\pi\rho}\,\frac{\sigma_{nt}}{\sigma_\theta}, \tag{4.10}$$

where Q is the correction factor for the line-of-sight and beam-integration effects (Ostriker et al., 2001). The studies show that the beam-integration effect can lead to an underestimation of angular dispersion in polarization angles, resulting in an overestimation of the magnetic field strength (Ostriker et al., 2001; Padoan et al., 2001; Houde et al., 2009). To determine the angular dispersion, there are different statistical methods (see Hildebrand et al., 2009; Houde et al., 2009; Pattle et al., 2017; Liu et al., 2022), which are used in the literature. In this work, we use the structure-function (SF; Hildebrand et al., 2009) method, which gives the $\frac{\delta B}{B_0}$ ratio by accounting for the spatial variation of position angles.

4.3.6.1 Structure function analysis

In the SF method, the magnetic field is assumed to be composed of a large-scale structured field and a turbulent field that are statistically independent. The distinctive behaviour of the two components enables them to distinguish and extract the turbulent component, facilitating the computation of σ_θ. The SF method computes the difference in position angles, $\Delta\phi(l) \equiv \phi(\mathbf{x}) - \phi(\mathbf{x}+\boldsymbol{l})$, between the $N(l)$ pairs of pixels separated by $l = |\boldsymbol{l}|$, using the following function:

$$\langle \Delta\phi^2(l) \rangle^{1/2} \equiv \left(\frac{1}{N(l)} \sum_{i=1}^{N(l)} [\phi(\mathbf{x}) - \phi(\mathbf{x}+\mathbf{l})]^2 \right)^{1/2}. \tag{4.11}$$

This function is referred to as the "angular dispersion function". We want to point out that the polarization position angles are used here for the dispersion function. The angular dispersions, $\Delta\phi$, are kept $\leq 90°$, to avoid the effect of the $\pm$ 180° ambiguity of the magnetic field lines. Under the limit, $\delta < l << d$, the square of the angular dispersion function, known as the "structure function" is characterised by (Hildebrand et al., 2009)

$$\langle \Delta\phi^2(l) \rangle_{tot} - \sigma_M^2(l) \simeq b^2 + m^2 l^2, \tag{4.12}$$

where δ is the correlation length of the turbulent component, and d is the typical length for variation in large-scale B-field. The quadratically added terms in the dispersion function, $m^2 l^2$ and b^2, are the contribution from the B_0 and δB, respectively. The B_0 is expected to increase almost linearly with slope m for $l << d$, and b is a constant turbulent contribution for $l > \delta$ (for details, see Hildebrand et al., 2009). The $\sigma_M^2(l)$ is the contribution from the measured uncertainty in the position angles. The turbulent to large-scale magnetic field strength is given by (Hildebrand et al., 2009)

$$\frac{\langle \delta B^2 \rangle^{1/2}}{B_0} = \frac{b}{\sqrt{2 - b^2}}, \tag{4.13}$$

and B_0 can be estimated by using the modified DCF relation:

$$B_0 \simeq \sqrt{(2 - b^2) 4\pi \mu m_H n_{H_2}} \frac{\sigma_{nt}}{b}. \tag{4.14}$$

Using the Q correction factor, we can determine the POS magnetic field strength:

$$B_{pos} = Q B_0, \tag{4.15}$$

where Q is taken to be 0.5 (Heitsch et al., 2001; Ostriker et al., 2001).

We calculated the dispersion function corrected by measurement uncertainty, i.e. $\langle\Delta\phi^2(l)\rangle_{tot} - \sigma_M^2(l)$ with a bin size of $12''$. We used various bin sizes and found that the fit is converged, and fitting errors are the least for $12''$. Figure 4.14 shows the dispersion in position angles as a function of the length scale for CC and NES. We fitted the dispersion function with the model defined in equation 4.12 using least square fit, over the first few data points to ensure the limit, $l << d$. The best-fits turbulent component, b, for CC and NES are $32^\circ.1 \pm 0^\circ.9$ and $33^\circ.8 \pm 2^\circ.1$, respectively. The dispersion in position angles can be obtained as $\sigma_\theta = b/\sqrt{2}$, which is around $\sim 22^\circ.7 \pm 0^\circ.6$ and $23^\circ.9 \pm 1^\circ.5$ for CC and NES, respectively. These values are close to the maximum value at which the DCF methods would give reliable results ($\sigma_\theta \leq 25^\circ$; Ostriker et al., 2001) if a correction factor of 0.5 is applied. Using equation 4.13, 4.14, and 4.15, we calculated the $\frac{\delta B}{B_0}$ ratio to be around $\sim 0.43 \pm 0.01$ and 0.46 ± 0.04, and B_{pos} to be around $\sim 24.0 \pm 6.0$ μG and 20.0 ± 5.0 μG, for CC and NES, respectively. All the estimated parameters are given in Table 4.1.

4.4 Discussion

The POS magnetic field strength for the CC and NES regions is around ~ 24 μG and 20 μG, respectively. Given the uncertainty of at least a factor of 2 associated with the B-field estimation by the DCF method (Crutcher, 2012), the estimated B-field strengths are within the range of $\sim 10-100$ μG observed in star-forming regions (Chapman et al., 2011; Crutcher, 2012; Pattle et al., 2022). The values are also consistent (i.e. within a factor of 1.5) with the upper limits of the B-field values from Crutcher et al. (2010) relation for the respective density of the regions.

4.4.1 Correlation between magnetic fields, intensity gradients, and local gravity

Due to the low statistics in the polarization data, it is difficult to conclusively comment on the overall morphology of the B-field, intensity gradients, and local gravity. However, through this comparison, some inferences can be drawn over their relative spatial variance. Figure 4.8 and 4.9 shows a correlation between the B-field, intensity gradients, and local gravity in the CC and WC

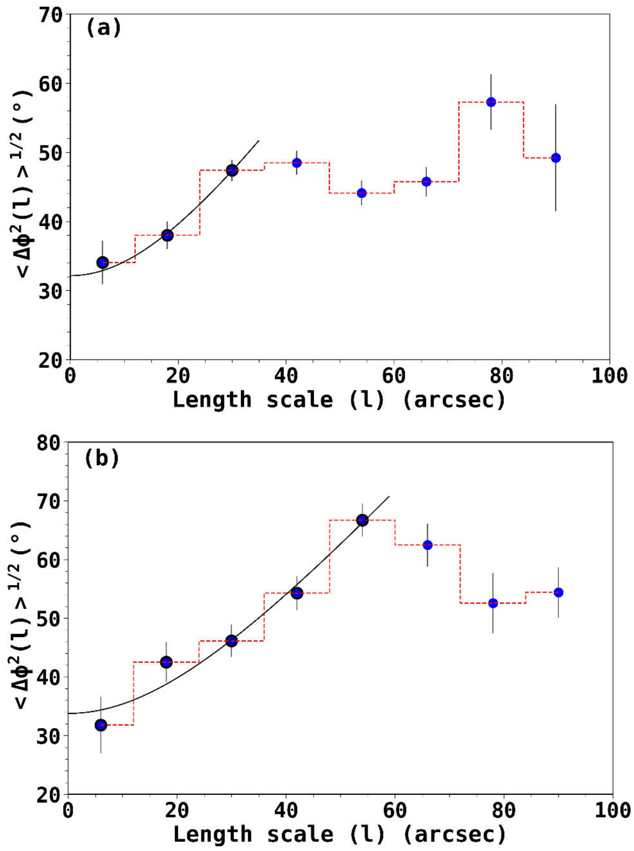

Figure 4.14: The angular dispersion function for (a) CC and (b) NES. The solid curve represents the best-fit model to the data, and the points used for fitting are shown in black encircled circles. The intercept of the best-fit model (l = 0) gives the turbulent contribution to the total angular dispersion. The error bars denote the statistical uncertainties after binning and propagating the individual measurement uncertainties.

regions, whereas the differences in their position angles are relatively higher in the NES region. This correlation can be due to the collapse of the clumps where gravity has pulled in and aligned B-field lines with the intensity gradients, in the CC and WC regions (Koch et al., 2013; Wang et al., 2019). However, in the outer diffused regions, like the elongated structures, the field lines are not yet that much affected by the local gravity.

Some simulations of the global collapse of magnetized clouds have found that the gravitational flows from large scale to small scale, i.e. from filaments to clumps/cores, can drag the magnetic field lines along the flow, causing a “U" shaped geometry of the field lines across the filament spine (Gómez et al., 2018; Vázquez-Semadeni et al., 2019). An evidence of “U" shaped geometry of B-field lines is also found in this work, at the bottom of the elongated part of the central clump. Figure 4.15 shows the zoomed-in view of the central clump region, in which the "U" shaped geometry is sketched from the observed B-field orientations and is shown by magenta curves. High-resolution and sensitivity observations would be required to ascertain the observed morphology. A similar effect of gravity over the B-field morphology has also been found in other observational works (Tang et al., 2019; Wang et al., 2020a,b; Beuther et al., 2020; Busquet, 2020; Pillai et al., 2020).

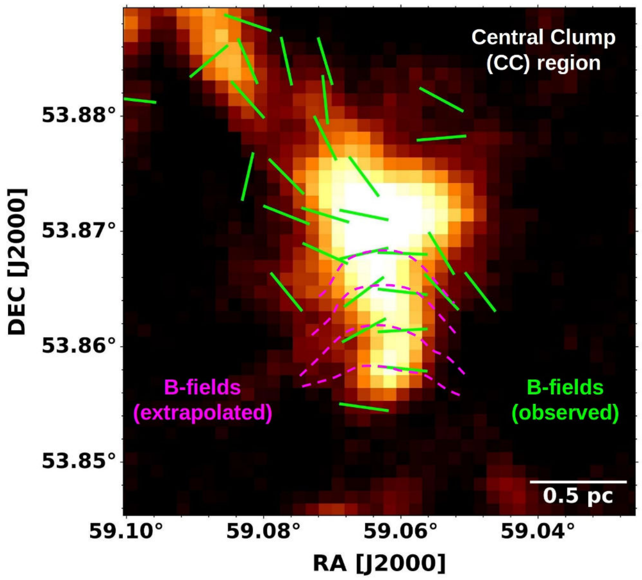

Figure 4.15: Stokes I map of the Central clump region of G148.24+00.41, over which the observed B-field segments are shown (green segments). The B-field segments show a "U" shaped geometry, sketched with observed segments and shown by magenta dashed curves, which may be caused by the drag of gravitational converging flows towards the centre of the cloud.

In Chapter 3, using MWISP CO data, filamentary gas flows were identified in G148.24+00.41 exhibiting noticeable velocity gradients as they move towards the hub. It was found that the velocity gradient increases towards the hub, with a measured value of ~0.2 km $s^{-1}pc^{-1}$ in the proximity of the hub. The aforementioned findings give evidence of accreting gas flows along the filaments towards the cloud's centre, which can affect the B-field morphology by dragging them along the flow. Future high-resolution dust continuum and polarimetric observations might be able to reveal a significant number of polarization vectors at the clump/core scale to better resolve the substructures and the B-field morphology around the hub of G148.24+00.41.

4.4.2 Gravitational stability

4.4.2.1 Mass-to-flux ratio

In order to investigate whether the magnetic field can provide stability to the regions against gravitational collapse, we determine the mass-to-flux ratio (Crutcher et al., 2004). It is generally calculated as a dimensionless critical stability parameter, λ_B, which is basically the comparison of the mass to magnetic flux ratio with the critical ratio (Crutcher et al., 2004):

$$\lambda_B = \frac{(M/\phi)_{obs}}{(M/\phi)_{crit}} = 7.6 \times 10^{-21} \ \frac{N(H_2)(\mathrm{cm}^{-2})}{B_{pos}(\mu G)}, \tag{4.16}$$

where $N(H_2)$ is the mean column density of the region. A clump or dense core is magnetically supercritical ($\lambda_B > 1$) if the magnetic field is not strong enough to support the system against gravitational collapse, whereas a strong magnetic field would make the system magnetically subcritical ($\lambda_B < 1$), i.e. stable against collapse. Using the mean $N(H_2)$ ~$(5.8 \pm 2.2) \times 10^{21}$ cm^{-2} and $(7.1 \pm 2.7) \times 10^{21}$ cm^{-2} , we calculated the critical parameter to be around ~1.8 ± 0.8 and 2.7 ± 1.2 for CC and NES, respectively. The critical parameter shows that both regions are magnetically supercritical. In general, a statistical correction factor is applied to λ_B to account for bias due to geometric effects (Crutcher et al., 2004). Different correction factors are suggested for different geometry of clumps with respect to magnetic field, e.g., $\pi/4$ for spherical clump and $1/3$ for oblate spheroid with major-axis perpendicular to the mean B-field (Crutcher et al., 2004), and $3/4$ for prolate spheroid with major-axis parallel to the mean B-field (Planck Collaboration et al., 2016). Using these correction factors, the mass-to-flux ratios become subcritical to transcritical/supercritical in the range of 0.6 to 1.4 for CC with mean ~ 1.1, and 0.9 to 2.1 for NES with mean ~ 1.7. However, considering the overestimation of B_{pos} in the DCF method itself, the estimated mass-to-flux ratios in this work could also be lower limits. It is important to acknowledge that the estimated B-field strengths and mass-to-flux ratios represent only the average values over the selected regions. The regions can still be super-critical inside but sub-critical in the outer part, as also shown in a recent simulation by Gómez et al. (2021).

4.4.2.2 Turbulence versus magnetic field

Simulations suggest that turbulence plays a dual role in the clouds and their substructures by providing turbulent support against the gravitational collapse at a large scale while producing compressions and shocks at small scales, that create density enhancements and trigger the star formation process (Mac Low & Klessen, 2004; Ballesteros-Paredes et al., 2007; Hennebelle & Falgarone, 2012; Klessen & Glover, 2016). Also, whether it is turbulence (weak B-field models) or magnetic field (strong B-field models) or both, is a subject of investigation regarding their respective roles in the formation of clumps, cores, and subsequent star formation within these structures. In order to investigate their impact, one needs to find out the relative strength of turbulence in comparison to the magnetic field.

The Alfvén Mach number ($\mathcal{M}_A$) infers the relative importance of turbulence and magnetic field in molecular clouds and is defined as $\mathcal{M}_A = \sqrt{3}\sigma_{nt}/V_A$. The Alfvén velocity is calculated as, $V_A = B_{tot}/\sqrt{4\pi\rho}$. The total B-field strength (B_{tot}) of the regions can be determined by using a statistical relation, $B_{tot} = (4/\pi)B_{pos}$ (Crutcher et al., 2004). For CC and NES, the B_{tot} is found to be around 31 ± 8 μG and 26 ± 6 μG, respectively. Using the mass density estimated within the dimensions of two regions (given in Table 4.1) and corresponding B_{tot} values, the V_A for CC and NES are found to be ~1.0 ± 0.4 km s^{-1}and 0.6 ± 0.2 km s^{-1}, respectively. Then, using the corresponding σ_{nt} values, the $\mathcal{M}_A$ is calculated to be around ~1.2 ± 0.4 for both the two regions. A star-forming region is super-Alfvénic if $\mathcal{M}_A > 1$, which means that the turbulent pressure is higher than the magnetic pressure. Conversely, it will be sub-Alfvénic if $\mathcal{M}_A < 1$, which means that the magnetic pressure is higher than the turbulent pressure. In the present case, both the regions are trans Alfvénic.

We also calculated the magnetic and turbulent pressures using the relations:

$$P_B = \frac{B_{tot}^2}{8\pi} \quad \text{and} \quad P_t = \frac{3}{2}\rho\sigma_{nt}^2 \text{ (Spherical)}, \tag{4.17}$$

$$= \rho\sigma_{nt}^2 \quad \text{(Cylindrical)},$$

here, a factor of 3/2 is included to estimate the total turbulent pressure by assuming the non-thermal velocity dispersion to be isotropic in spherical geometry. For the CC region, the magnetic and turbulent pressure is found to be ~$(3.7 \pm 1.9) \times 10^{-11}$ dyne cm^{-2} and ~$(5.2 \pm 2.7) \times 10^{-11}$ dyne cm^{-2}, respectively. For the NES region, P_B and P_t are ~$(2.6 \pm 1.3) \times 10^{-11}$ dyne cm^{-2} and $(2.5 \pm 1.3) \times 10^{-11}$ dyne cm^{-2}, respectively. In the CC region, the turbulent pressure is higher than the magnetic pressure by a factor of ~1.4, while in NES, the pressure values are similar. Also, the thermal pressure ($\sim\rho\sigma_{th}^2$) in both regions, is much smaller than the turbulent and magnetic pressure, which shows that the thermal energy plays a negligible role in energy balance. So, from the Alfvén Mach number and pressure estimation, it seems that the turbulence is slightly more dominant in comparison to the magnetic field in CC, i.e. in the centremost part of G148.24+00.41, while it is similar in the NES.

4.4.2.3 Virial analysis

The virial theorem is a principle that relates the average kinetic energy (E_K) and magnetic field energy (E_B) of a system to its average gravitational potential energy (E_G), which provides insights into the stability and energy distribution of the system. The Virial theorem is written as:

$$\frac{1}{2}\frac{d^2\mathcal{I}}{dt^2} = 2E_K + E_B + E_G, \tag{4.18}$$

where $\mathcal{I}$ is the moment of inertia. The surface energy terms here are neglected. The kinetic energy term is given by (Fiege & Pudritz, 2000)

$$E_K^{sph} = \frac{3}{2}M\sigma_{obs}^2 \quad \text{(Spherical)}, \tag{4.19}$$

$$E_K^{cyl} = M\sigma_{obs}^2 \qquad \text{(Cylindrical)},$$

where M is the mass and $\sigma_{obs}^2 = \sigma_{th}^2 + \sigma_{nt}^2$. The magnetic field energy is given by

$$E_B = \frac{1}{2}MV_A^2 \tag{4.20}$$

and the gravitational potential energy is given by

$$E_G^{sph} = -\frac{(3-a)}{(5-2a)}\frac{GM^2}{R} \quad \text{(Spherical)}, \tag{4.21}$$

$$E_G^{cyl} = -\frac{GM^2}{L} \quad \text{(Cylindrical)},$$

where G is the gravitational constant, R, is the effective radius of the sphere, and L is the length of the cylinder. Here a is the density profile index of the sphere ($\rho \propto r^{-a}$). The energy values for the two regions are listed in Table 4.1. We found that for CC, $|E_G| > E_K > E_B$ (i.e. 10.4:4.7:3.3), while for NES, $|E_G| > E_K \simeq E_B$ (i.e. 14:6.3:7.0), which restates the results of Alfvén Mach number and mass-to-flux ratio calculation, i.e. turbulence is slightly more dominant than the magnetic field in CC, while it is similar in NES, but overall the gravity is the dominant factor in both the regions. Nevertheless, the calculation of individual energy terms is an important exercise, enabling the direct comparison of various forces that govern the evolution of clumps/structures, expressed in the same units.

For a non-magnetized system ($E_B = 0$), the stability criteria is given by $2E_K + E_G < 0$, and based on this condition, the kinetic virial parameter is defined as (Bertoldi & McKee, 1992)

$$\alpha_{vir,k} = \frac{2E_K}{|E_G|} = \frac{3(5-2a)}{(3-a)}\frac{R\sigma_{obs}^2}{GM} \quad \text{(Spherical)}, \tag{4.22}$$

$$= \frac{2L}{GM}\sigma_{obs}^2 \quad \text{(Cylindrical)}.$$

Using the M, R, L, and σ_{obs} values of the regions (given in Table 4.1) in equation 4.22, and adopting $a = 2$ for spherical case, we calculate the $\alpha_{vir,k}$ to be around 0.9 ± 0.4 and 0.9 ± 0.4, respectively for CC and NES. The derived $\alpha_{vir,k} < 2$ means that in the case of a non-magnetized sphere ($E_B = 0$), the thermal plus turbulent contribution is not enough to provide stability to the regions against the gravitational collapse (Kauffmann et al., 2013; Mao et al., 2020). Including the magnetic energy term in the stability criteria, i.e. $2E_K + E_B + E_G < 0$, the total virial parameter is calculated using the modified relation (Bertoldi & McKee, 1992; Pillai et al., 2011;

Sanhueza et al., 2017).

$$\alpha_{vir_{tot}} = \frac{2E_K + E_B}{|E_G|} = \frac{3(5-2a)}{(3-a)} \frac{R}{GM} \left(\sigma_{obs}^2 + \frac{V_A^2}{6} \right) \quad \text{(Spherical)}, \tag{4.23}$$

$$= \frac{2L}{GM} \left(\sigma_{obs}^2 + \frac{V_A^2}{4} \right) \quad \text{(Cylindrical)}.$$

With the magnetic support, the $\alpha_{vir,tot}$ value is estimated to be around $\sim$1.2 ± 0.6 and 1.4 ± 0.7 for CC and NES, respectively. The $\alpha_{vir,tot}$ values for the regions are < 2, which shows that the two regions are bound by gravity and thus can collapse to form stars. The virial analysis shows that the total kinetic energy (E_K, i.e. thermal plus turbulent) in both regions is not sufficient to support them against the gravitational collapse. While magnetic energy, combined with kinetic energy, is found to be comparable to gravitational potential energy.

In the present work, we have estimated magnetic field strengths and derived various parameters for the CC and NES regions. However, we want to stress that these results must be taken with caution as the measurements are uncertain within a factor two due to the inherent large uncertainty in the mass and density of the studied regions. Moreover, the modified DCF methods can be uncertain up to a factor of two or more (Crutcher, 2012), and also, the B-field strength in the studied regions can be biased due to the limited number of B-field segments traced by our observations. Due to all these uncertainties, the mass-to-flux ratio and virial status of the regions should be considered as qualitative indicators of the stability of the region. In the present case, we have used the generally accepted Q value of 0.5 (Crutcher, 2012) in our estimations, however, if we use Q = 0.4, suggested for parsec scale clumps (Padoan et al., 2001), similar to our studied regions, the B-field strengths will reduce by a factor of $\sim$1.2. As a consequence, the CC and NES regions would become more magnetically supercritical. Future high-resolution and more sensitive observations would better constrain the magnetic field and turbulence properties of the hub. However, taking the measured mass-to-flux ratio and virial parameters at face value, it can be argued that, at present, gravity has overall an upper hand over magnetic and kinetic energies in CC and NES, which is consistent with the formation of a young cluster noticed in the hub.

4.4.3 The criticality of magnetic fields in hub-filamentary clumps

Like the CC of G148.24+00.41, the clumps located at the junction of the hub-filamentary systems are known to be potential sites of cluster formation (e.g. Kumar et al., 2020), because such clumps are attached to converging filamentary structures that fuel them with cold gaseous matter (e.g. Myers, 2009; Li et al., 2014a; Treviño-Morales et al., 2019; Kumar et al., 2022). Although physical processes that govern the star formation are scale-dependent, it is worthwhile to compare the global properties of the parsec or sub-parsec scale hub filamentary clumps studied with similar resolution. In the literature, a few such clumps have been studied with JCMT/POL2, these are: IC 5146 E-hub (Wang et al., 2019), G33.92+0.11 (Wang et al., 2020b), Mon R2 (Hwang et al., 2022), IC 5146 W-hub (Chung et al., 2022), and SDC13 (Wang et al., 2022). In the majority of these hub filamentary clumps, except Mon R2, the mass-to-flux ratio and/or virial analysis suggest the dominance or edge of gravitational energy over the magnetic and kinetic energies, similar to the CC region of G148.24+00.41. We found that all the aforementioned clumps are associated with either protostars or an embedded cluster (e.g. Harvey et al., 2008; Gutermuth et al., 2009; Peretto et al., 2014; Liu et al., 2015). Thus, it seems that, at least for those parsec scale hubs that are in the early stages of cluster formation, like the CC of G148.24+00.41, gravity has an upper hand on the energy budget of the system.

4.5 Summary

This chapter specifically focused on the C1 clump, located at the central/hub region of G148.24+00.41, to study the relative role of the magnetic field in comparison to gravity and turbulence in the star and star cluster formation process of the clump. The dust polarization observations of the central part of the G148.24+00.41 cloud were performed to investigate the B-field morphology and its strength relative to gravity and turbulence, using JCMT SCUBA-2/POL-2 at 850 μm. The 850 μm Stokes I intensity map reveals the presence of a central clump, northeastern elongated structure, and western clump around the hub of G148.24+00.41. The B-field segments of CC and NES regions show mixed morphology, while the WC region shows converging B-field segments, mostly aligned along the southeast direction. We found evidence of the depolarization effect, and from the Bayesian analysis over the non-debiased polarization data, found a power-law index, α = 0.6. Although this shows a decreasing level of dust grain alignment, but they can still be aligned with the magnetic field in the central high-density region of the cloud.

We compared the relative orientations of B-fields, intensity gradients, and local gravity over the full map. In the CC and WC regions, the three factors are mostly correlated, while the difference in orientations is higher in the NES region. This suggests that gravity is dragging the intensity gradients and aligning them with the B-fields in the CC and WC clump, while the effect of gravity in NES is comparatively less significant. We constructed the Σ_B map to see the localised B-field strength in comparison to local gravity and found that for most of the parts, Σ_B < 1, i.e. gravitational force is dominant over the magnetic field force.

We determined the B-field strength, B_{pos} for CC and NES to be around 24.0 ± 6.0 μG and 20.0 ± 5.0 μG, respectively. We found that both the CC and NES regions are magnetically transcritical/supercritical and trans-Alfvénic. The turbulent pressure was found to be higher than the magnetic pressure in CC, while they are similar in NES. The virial analysis shows that for CC, the $|E_G| > E_K > E_B$, while for NES, $|E_G| > E_K \simeq E_B$. The magnetic field and turbulence individually are not strong enough to provide stability to the regions against gravity. Both regions were found to be bound by gravity.

Overall, we find that currently, gravitational energy has an edge over the other energy terms of the hub region of G148.24+00.41, thereby will continue to facilitate the growth of the young cluster in the hub. However, it is important to acknowledge that given the large uncertainties associated with our estimates, a conclusive answer would require further precise measurements of magnetic field and cloud properties.

Chapter 5

FSR 655: A young cluster formed at the heart of G148.24+00.41

In the previous chapter, the hub region of G148.24+00.41 was explored to investigate the magnetic field morphology and its relative role in comparison to gravity and turbulence. Our study shows that, at present, gravitational energy has the upper hand over magnetic and kinetic energies, which will continue to facilitate the growth of the young cluster, FSR 655, observed in the hub of G148.24+00.41 from *Spitzer* images. Since the clump is fed by the filamentary converging flows, it is interesting to explore the present-day properties of the cluster and its likely evolution. With this aim, we continue our investigation on the hub region of G148.24+00.41 using deep near-infrared observations.

This chapter provides a detailed characterization of the FSR 655 cluster using near-infrared data obtained with the newly installed 3.6-m Devasthal Optical Telescope, complemented by catalogues from the *Spitzer* observations. We aim to improve the understanding of the current status of the cluster in terms of its evolutionary stage, mass distribution, star formation rate and efficiency, and likely fate in the context of massive cluster formation.

5.1 Observations and data sets

5.1.1 Near-infrared observations

With the aim to obtain the deep near-infrared data, we observed the cluster in J (1.250 μm), H (1.635 μm), and K_s (2.150 μm) bands on 2022 November 27 and 29 with the 3.6-m DOT telescope (Sagar et al., 2019, 2020), Nainital, India. The observations were taken using the TANSPEC instrument, mounted at the f/9 Cassegrain focus of the telescope (Sharma et al., 2022). TANSPEC is equipped with a 1k × 1k HgCdTe imaging array with a pixel scale of 0.245 arcsec, and the image quality is optimized for 1 arcmin × 1 arcmin field of view (FOV).

With TANPSEC, the cluster was observed in four pointings, covering ~2 arcmin × 2 arcmin FOV around the central area of the hub. For each pointing, the seven-point dithered pattern in J, H, and K_s bands was employed. In each dithered position, 8 frames were taken, with an exposure of 20 seconds per frame. The total integration time of the observation per pointing was about 19 minutes in the J, H, and K_s bands.

The standard processing tasks of dark correction, flat-fielding, sky subtraction, and bad-pixel masking were performed. For astrometry, we used WCS tools and SExtractor[1], and finally obtained the calibrated, stacked, and mosaicked science images in three bands (for details see Ojha et al., 2004; Neichel et al., 2015; Sharma et al., 2023). The FWHM values of the images were in the range of 0.8−1.0 arcsec.

The photometry was done using the packages available in IRAF (Tody, 1986, 1993). Using the DAOFIND task of IRAF, the list of point sources in the K_s band with signal 5σ above the background was obtained. We performed point spread function photometry of the sources using the ALLSTAR routine of IRAF. For absolute photometric calibration, we used moderately bright and relatively isolated sources from the 2MASS point sources catalogue (Skrutskie et al., 2006) with the quality flag 'AAA' and photometric error less than 0.1 mag. We obtained the following transformation equations between 2MASS and TANSPEC for the selected sources, which are

[1] https://www.astromatic.net/software/sextractor/

illustrated in Figure 5.1.

$$(J-H) = (0.894 \pm 0.069) \times (j-h) - 0.238 \pm 0.131 \tag{5.1}$$

$$(H-K_s) = (0.950 \pm 0.097) \times (h-k_s) + 0.918 \pm 0.039 \tag{5.2}$$

$$(J-K_s) = (0.907 \pm 0.036) \times (j-k_s) + 0.696 \pm 0.056 \tag{5.3}$$

$$(J-j) = (-0.126 \pm 0.040) \times (j-h) - 9.510 \pm 0.055 \tag{5.4}$$

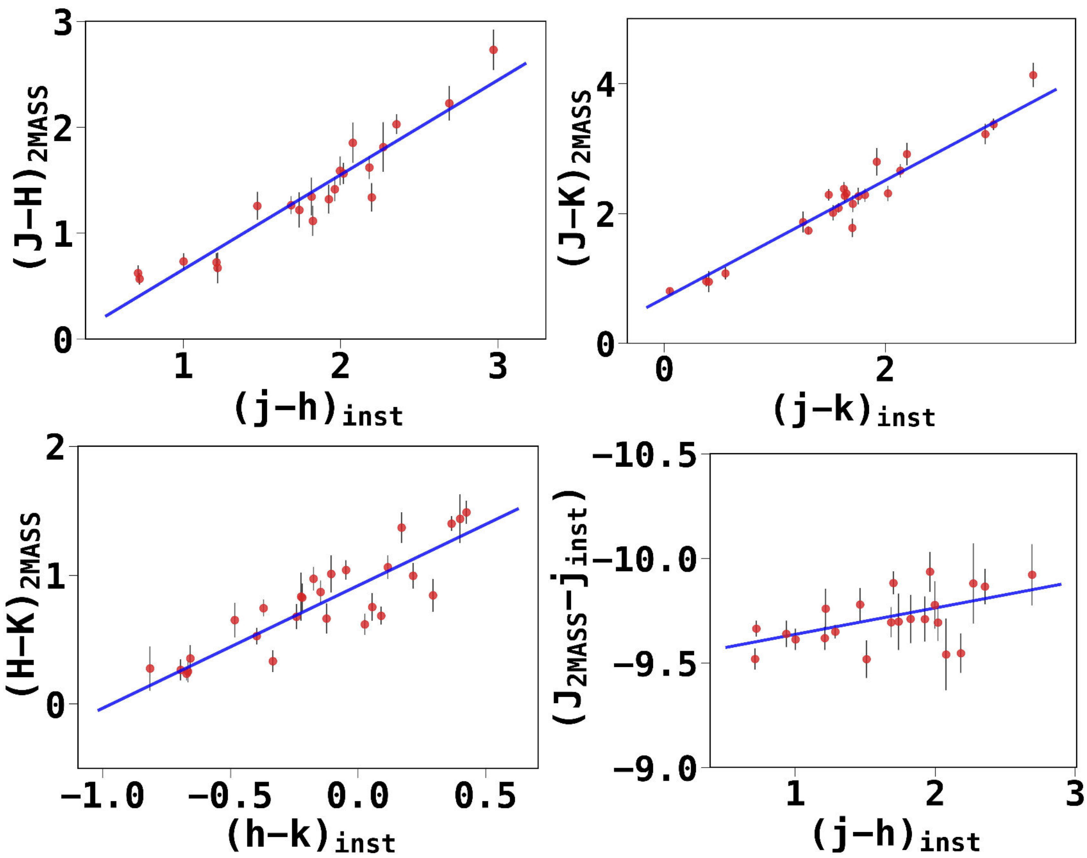

Figure 5.1: Color-color plots of 2MASS magnitudes versus TANSPEC instrumental magnitudes in J, H, and K_s bands.

In the above equations, J, H, and K_s are the standard magnitudes of the stars taken from 2MASS, whereas j, h, and k_s are the instrumental magnitudes from TANSPEC observations. We applied these transformation equations to all the detected sources in the target field. For sources detected in a single band, we simply applied constant shifts to the instrumental magnitudes to get the calibrated magnitudes. These constant shifts were determined in each band as the median difference between the instrumental magnitude and the 2MASS magnitudes for the common sources. In the present work, sources with errors less than 0.2 mag were considered for the analysis. This 5σ sensitivity of the TANSPEC images at J, H, and K_s bands are found to be 20.5, 20.1, and 18.6 mag, respectively. We find that the TANSPEC images are nearly ~1 mag deeper than the existing UKDISS GPS survey near-infrared images of the region.

5.1.2 Galactic population synthesis simulation data

A separate control field could not be observed for FSR 655 due to observational constraints. Therefore, in order to assess the likely contamination of the field population to the cluster population along the line of sight, the Galactic population in the direction of the cluster was obtained using the Besançon population synthesis model[2] (Robin et al., 2004). To obtain the model field population, the Besançon model was simulated for an area equivalent to the observed area of the cluster by adopting the 2MASS photometric system and utilizing the atmosphere models grid of Allard & Freytag (2010). In the simulations, the photometric errors in 2MASS bands were constrained by taking the error as an exponentially increasing function of magnitude, as found in our TANSPEC observations for the cluster. The values of the error function parameters fed to the simulations are obtained by fitting the exponential function over the TANSPEC data. For line-of-sight extinction, we used the commonly adopted Galactic extinction value of 1.2 mag/kpc (Gontcharov, 2012). The Besançon model output data contains distance, visual extinction, J, H, and K_s magnitudes, and the spectral type of each synthetic star. This modelled field population was used to remove the likely contamination present along the line of sight of the cluster (discussed in Sect. 5.2.2.2).

[2] https://model.obs-besancon.fr/

5.1.3 Completeness of the photometric data

In order to access the overall completeness limits of the photometric catalogues, we use the histogram turnover method (e.g. Ohlendorf et al., 2013; Samal et al., 2015; Jose et al., 2017; Damian et al., 2021). In this approach, the magnitude at which the histogram deviates from the linear distribution is, in general, considered as 90% complete. Figure 5.2 shows the Kernel Density Estimation (KDE) histograms of the sources detected in various bands. In comparison to discrete histograms, KDE gives a smooth and continuous distribution, such that it is easier to visualize the deviation in the distribution. Density means the fraction of total data lying in a range, similar to the number of data points in a bin in histograms. The KDE distribution was done using a multivariate normal kernel, with isotropic bandwidth = 1.2 mag. This value was chosen as it was found to be a good compromise between over-smoothing and under-smoothing density fluctuations. With this approach, our photometry is likely complete down to J ~18.6 mag, H ~18 mag, K_s ~17.7 mag. The *Spitzer* 4.5-micron catalogue from the GLIMPSE360 survey (Whitney et al., 2008; GLIMPSE Team, 2020) was also used to access the YSOs of the studied region. The completeness limit of the 4.5-micron catalogue is 14.9 mag and is also shown in Figure 5.2. The observations were taken as part of the Spitzer Warm Mission Exploration Science program and performed using the two short-wavelength IRAC bands at 3.6 and 4.5 μm.

5.2 Results and discussion

5.2.1 Overview of the G148.24+00.41 in CO

Figure 5.3a shows the distribution of the ^{13}CO integrated emissions of G148.24+00.41 as observed with the PMO 13.7-m telescope (beam ~52″). Details of the CO observations and the intensity map can be found in Chapter 3. The ^{13}CO emission represents the relatively dense inner area of the cloud with effective radius ~17 pc (at d ~3.4 kpc). From Figure 5.3a, it can be seen that there is a bright spot at the heart of the cloud (i.e., near the geometric centre). Based on C^{18}O observations, as discussed in Chapter 3, it was observed that this bright spot corresponds

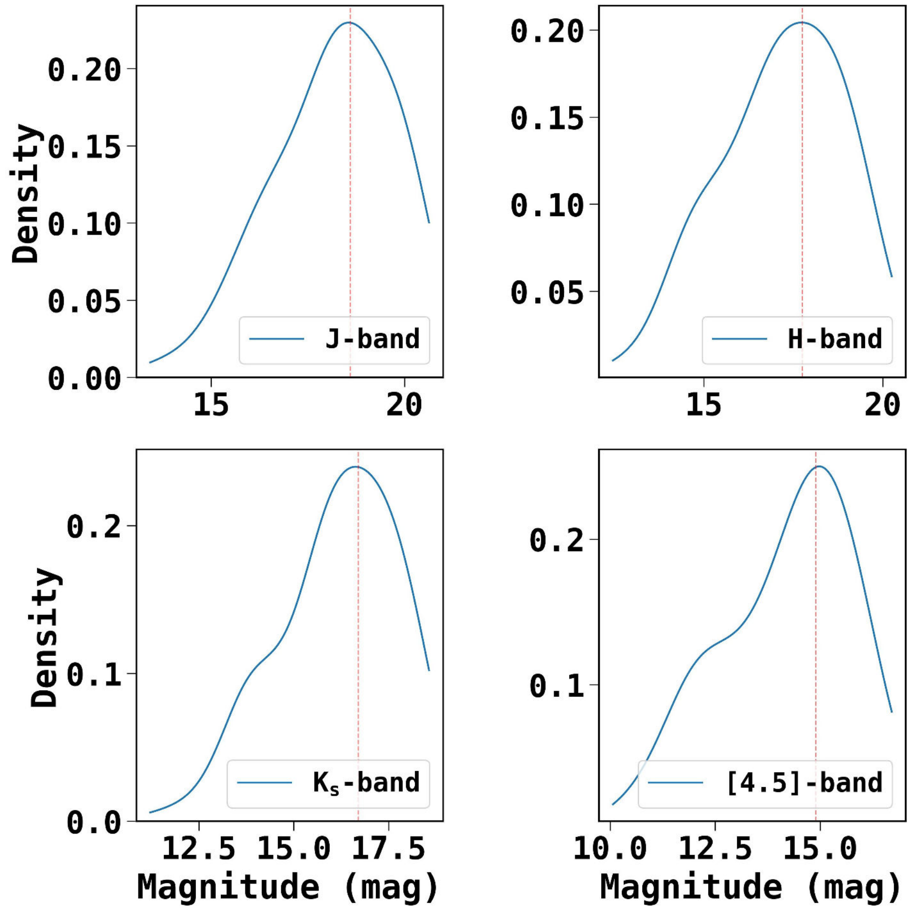

Figure 5.2: Density plots of photometric data of the cluster region in J, H, and K_s bands from TANSPEC and 4.5 μm band from *Spitzer*. The dashed lines in all the panels show the completeness limiting magnitude of 18.6 mag, 18 mag, 17.7 mag, and 14.9 mag in J, H, K_s, and [4.5] μm bands, respectively.

to the location of the most massive clump of the cloud, onto which several large-scale filaments are funnelling cold gaseous matter. The small-scale filamentary structures attached to the centre of the hub, as found in Chapter 3, are shown in Figure 5.3b, mimicking the hub filament system morphology as found in other star-forming regions (e.g. Myers, 2009; Kumar et al., 2018).

5.2.2 Stellar content and cluster properties

Figure 5.3c shows the NIR image of the hub as seen in the TANSPEC bands. Comparing the optical and NIR images of the cluster region, it was found that the clump lacks point sources in the optical bands (e.g., in Digitized Sky Survey's images), while in NIR images, clustering of

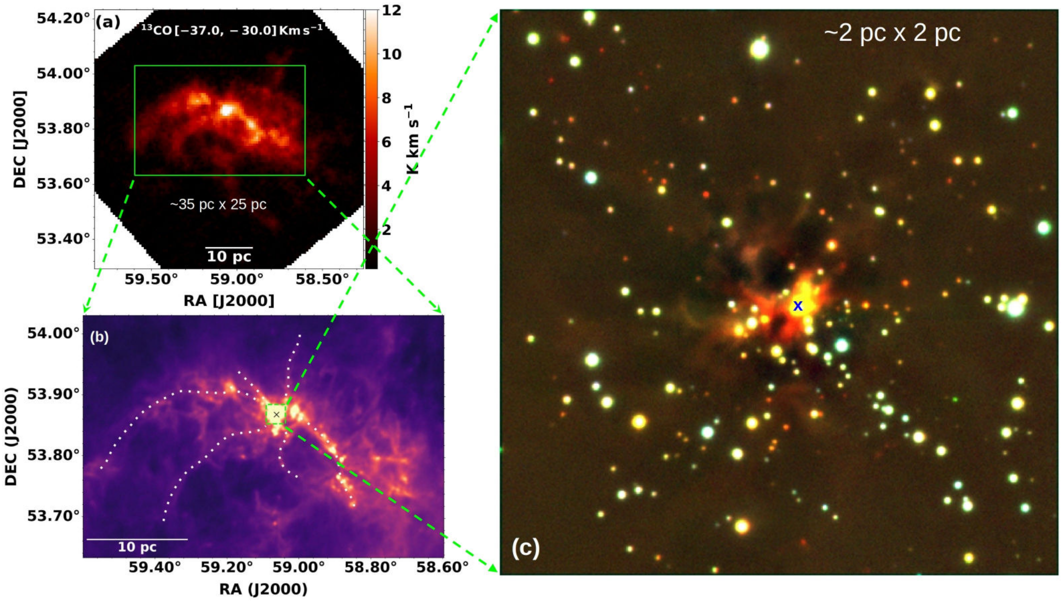

Figure 5.3: (a) ^{13}CO molecular gas distribution of G148.24+00.41. The green solid box here shows the inner cloud region zoomed in panel-b. (b) *Herschel* 250 μm image of the inner cloud region of size ~35 pc × 25 pc (marked by a green solid box in panel-a), along with small-scale filamentary structures as discussed in Chapter 2. The green dashed box shows the hub region of size ~2 pc × 2 pc, which is observed with TANSPEC. (c) NIR color-composite image (Red: K_s band; Green: H band, and Blue: J band) of FSR 655 as seen by TANSPEC. The location of the massive YSO (see text) is shown by a cross symbol.

point sources along with infrared nebulosity can be seen. Figure 5.4a shows the 2D density map of the point sources in the studied area. The stellar density is shown by shaded colors from the peak density to the 10% level. Figure 5.4b shows the cumulative distribution of stars from the centre of the density distribution, and as can be seen, stars are spread within ~90″ radius from the cluster centre, with 50% lying within 38″ and 90% within 63″. Beyond 63″, the distribution deviates from the linear shape and becomes flatter, implying that the improvement in the cluster density is insignificant beyond 63″. Thus considered 63″ as the conservative radius of the cluster, which is around 1 pc at the distance of G148.24+00.41 (i.e., ~3.4 kpc).

The cluster is embedded in a cloud of visual extinction as high as 20 to 30 mag (see Chapter 2), therefore, the contamination due to background stars to the cluster members is expected to be low. Below, we estimate the likely contamination of the field stars and derive properties of the cluster such as extinction, K_s band luminosity function, age, mass function, and star-formation efficiency and rate.

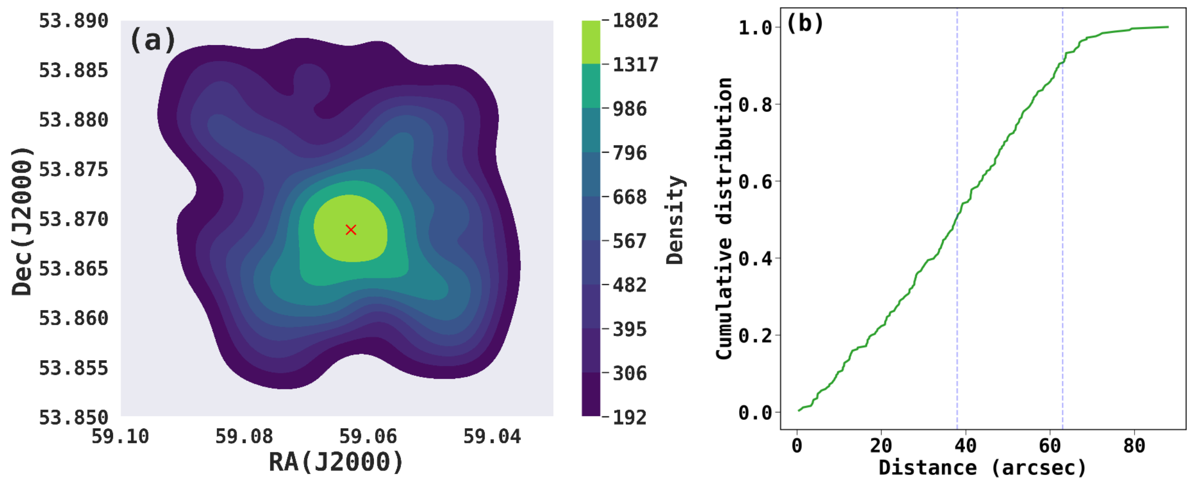

Figure 5.4: (a) The smoothened 2D density map of the sources, shown from the peak density up to the 10% level of stellar density. (b) The cumulative distribution of all the sources as a function of distance from the cluster centre (marked by a cross in panel-a). The dashed lines show the distances from the cluster centre within which 50% and 90% of the sources are lying.

5.2.2.1 Extinction

Extinction plays an important role in deriving cluster properties. The line-of-sight extinction to an individual star can be directly determined from knowledge of its color excess and the extinction law. We estimated the extinction of all the stars observed towards the cluster direction within its radius ($\sim 1'$) using the relation

$$A_V = c \times [(i-j) - (i-j)_0], \tag{5.5}$$

where $(i-j)$ is the apparent and $(i-j)_0$ is the intrinsic colors of the point sources in i^{th} and j^{th} filter. Here, c is the constant based on the extinction law of Rieke & Lebofsky (1985), which is 9.34 and 15.98 for $J-H$ and $H-K_s$ color excess, respectively. In general, $H-K_s$ colors are preferred for deriving extinction of star-forming regions (e.g. Gutermuth et al., 2009) because, in such environments, the majority of the sources can be highly embedded in the dust to be detected in J band. However, excess emission due to circumstellar disk from young sources (see Appendix B.1 for the discussion on the identification of IR-excess sources) can significantly impact $H-K_s$ colors, causing them to appear redder than their intrinsic photospheric colors, resulting in higher A_V values. This can be significant in young clusters, where a significant fraction of the stars can have a circumstellar disk. We thus used both $J-H$ and $H-K_s$ colors to determine the $A_{\rm V}$ of the observed sources by assuming that the majority of the sources within the cluster boundary are cluster members. A combined $A_{\rm V}$ catalogue was then made, where priority was given to the $A_{\rm V}$ values obtained from $J-H$ colors of the common sources, else $A_{\rm V}$ values from $H-K_s$ colors were considered. For estimating $A_{\rm V}$, we use the median intrinsic $J-H$ and $H-K_s$ colors of the GKM dwarfs[3] as 0.39 mag and 0.14 mag from Pecaut & Mamajek (2013) as the typical intrinsic color of the point sources. The $A_{\rm V}$ distribution, with a peak around 11 mag, is shown in Figure 5.5. Although some sources show high $A_{\rm V}$ value, but $A_{\rm V}$ < 22 mag encompasses the majority (~90%) of the sources. For sources within $A_{\rm V}$ < 22 mag, the resultant median visual extinction is 11 ± 4 mag, whose corresponding extinction at K_s band ($A_{\rm K}$) is ~1.23 ± 0.40 mag, following the extinction law ($A_{\rm K} = 0.112 \times A_{\rm V}$) of Rieke & Lebofsky (1985).

The median $A_{\rm V}$ for the common sources detected in the H and K_s bands are higher by ~1.3 magnitude compared to the sources detected in the J and H bands. Assuming that the inner disk emission dominates in the K_s band and has minimal contribution in the H band, this excess extinction could be due to the emission from the circumstellar disk of the disk-bearing cluster members. This excess extinction is equivalent to $\Delta A_{\rm K}$ ~0.15 mag, in K_s band.

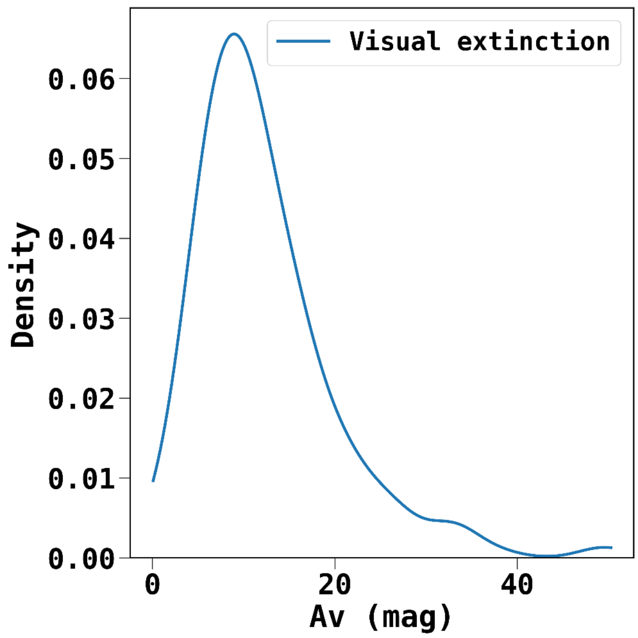

Figure 5.5: The density plot of all the observed sources in the cluster as a function of their visual extinction ($A_{\rm V}$, see Section 5.2.2.1).

[3] Stellar Color/Teff Table

We acknowledge the fact that although the individual A_V values are derived using the extinction law of Rieke & Lebofsky (1985), they only accurately reflect the true visual extinctions as long as the assumed reddening law is appropriate for this cloud. The extinction law given by Rieke & Lebofsky (1985) has a negative power law dependency on the wavelength with a power law slope, alpha ~1.6. Grain growth in cold clouds can alter the extinction law. Some studies show higher alpha values, 1.6–2.6, with a median around 1.9 in molecular clouds (see Wang & Jiang, 2014; Maíz Apellániz, 2024, and references therein). If the extinction law corresponding to the slope of 1.9 (Messineo et al., 2005) is used, it is found that the median A_V of the cluster changes by only ~0.3 mag (or A_K = 0.03 mag).

In the preceding paragraphs, we determined the median A_V of the cluster by assuming that all the observed sources within the cluster boundary are cluster members. However, if the field population is significant towards the cluster direction, it may affect the true median extinction value of the cluster. To further validate the robustness of the derived extinction value, we use the NIR excess emission sources, identified using the JHK_s and $HK_s[4.5]$ color-color (CC) diagrams (discussed in Appendix B.1) for deriving the median extinction of the cluster. Using only these excess sources (i.e., disk-bearing cluster members) and following the same approach illustrated in the previous paragraphs, the median visual extinction turns out to be around 11 mag, in agreement with the earlier estimation.

5.2.2.2 Likely field population

Figure 5.6 shows the $H-K_s$ color distribution of the field sources obtained from the population synthesis model (see Section 5.1.2), as well as of the total observed sources in the cluster direction. As can be seen, the field population shows a narrow $H-K_s$ color distribution peaking at 0.3 mag (i.e., corresponds to A_V ~3 mag, using equation 5.5), with the majority lying below 0.4 mag (i.e., corresponds to A_V ~4 mag) while the $H-K_s$ color of the cluster field shows a wide distribution having a peak around 1 mag, with the majority lying below 2.5 mag. It implies that the majority of the sources with $H-K_s$ color below 0.4–0.5 mag are likely the field population along the direction of the cluster. From the population synthesis model, we find that the majority of the model population is located at a distance of less than 3.4 kpc and, thus, is likely the foreground population in the direction of the cluster. There may be some background field stars among the observed sources towards the cluster direction, but we assume their contribution to be small, given the sensitivity of our observations and the high column of matter present in the clump.

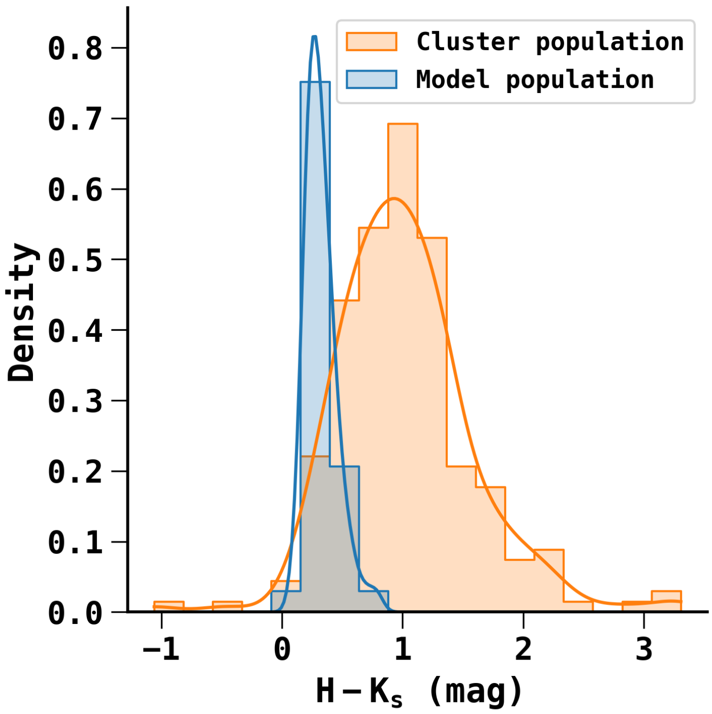

Figure 5.6: The distribution of all the sources observed towards the cluster and the Besançon model generated sources, shown as a function of their $(H - K_s)$ colors. The blue and orange curves show the corresponding density plots of the cluster and model population, respectively.

To illustrate this, in Figure 5.7, the K_s vs $H - K_s$ diagram of the population synthesis field sources is shown along with the main-sequence locus reddened by A_V = 0, 4, 11, and 22 mag. As can be seen, most of the relatively bright stars (e.g., K_s < 15.5 mag) and the majority of the faint stars are located within the A_V = 4 mag locus, suggesting 4 mag is likely the foreground extinction in the direction of the cluster. The red stars represent the background sources (i.e., sources with d > 3.4 kpc) reddened by A_V = 11 mag and A_V = 22 mag. As can be seen, if background sources are located behind A_V = 22 mag, most of them would be beyond our sensitivity limit of the K-band, while only a few sources would contaminate our cluster sample if they are located behind the cluster and lie in the range of A_V ∼11−22 mag.

If we assume that most of the sources within the cluster radius with color $H - K_s$ > 0.5 mag are likely the cluster members, the expected percentage of background contamination to our sample will be around ∼10%. More on this point is discussed further in Section 5.2.2.4. This contamination fraction would be further less if we consider sources above 0.5 to 1 $M_\odot$. For

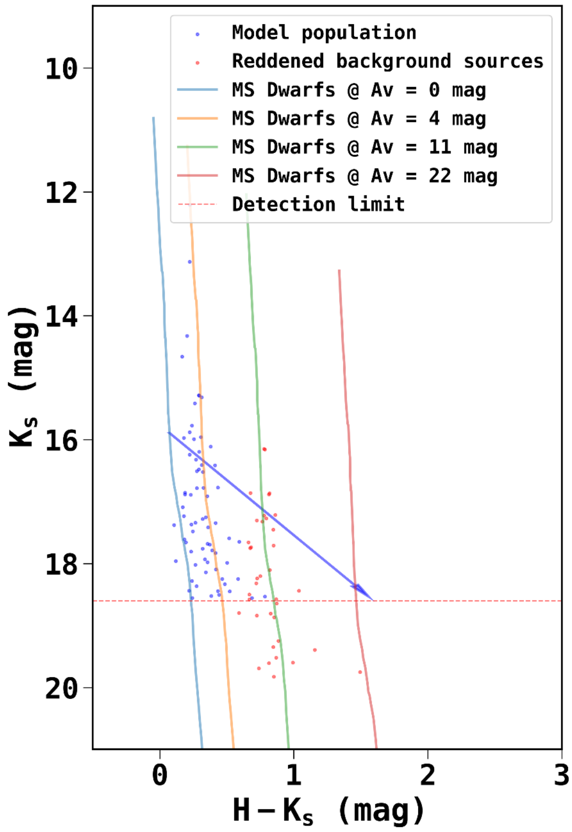

Figure 5.7: K_s vs. $H - K_s$ diagram of the model population. The red dots show the background sources (d > 3.4 kpc) reddened by A_V = 11 mag (average extinction towards the cluster). The colored curves show the main-sequence dwarfs locus reddened by A_V = 0, 4, 11, and 22 mag. The blue arrow shows the reddening vector drawn from the 1 $M_\odot$ limit.

example, the blue arrow in Figure 5.7 shows the reddening vector from the base of 1 $M_\odot$ dwarf locus, which reveals that the background contamination above 1 $M_\odot$ is negligible.

5.2.2.3 K_s band luminosity function and likely age

K_s band Luminosity Function (KLF) of different ages are known to have different peak magnitudes and slopes. Thus, a comparison of the observed KLF with the model KLFs can constrain the age of a cluster (Lada & Lada, 1995; Megeath et al., 1996; Muench et al., 2000; Ojha et al., 2004, 2011; Jose et al., 2012; Kumar et al., 2014). KLF is expressed by the following equation:

$$\frac{dN}{dm_k} = \frac{dN}{dM_*} \times \frac{dM_*}{dm_k}, \tag{5.6}$$

where m_k is the K_s band luminosity and M_* is the stellar mass (e.g., Lada & Lada, 2003). In the equation, the left-hand term represents the number of stars for a given K_s band magnitude bin, while the first term on the right-hand side is the underlying stellar mass function, and the second term is the mass-luminosity relation (MLR). To derive the KLF of the cluster, one first needs to correct for field contamination. To do so, we used the model star counts predicted by the Besançon model discussed in Section 5.1.2. The advantage of using the Besançon model is that the background stars (d > 3.4 kpc) can be separated from the foreground stars (d < 3.4 kpc). While all the stars in the field suffer a general interstellar extinction, only the background stars suffer an additional extinction due to the molecular cloud. Besançon model gives extinction of individual stars ($A_{\rm Vi}$) along the line of sight. The median extinction of the cluster is $A_{\rm V}$ =11 mag. We, therefore, reddened the background stars by applying an extra extinction of $\Delta A_{\rm Vi}$ (= $A_{\rm V}$ − $A_{\rm Vi}$) to put them behind a cloud of visual extinction 11 mag. Both the foreground and reddened background stars are then combined to make a whole set of contaminating field stars. Then, cluster counts were corrected by subtracting the contaminating field star counts from the cluster star counts. The field-corrected cluster KLF, "KLF-01", is shown in Figure 5.8a. The figure also shows the KLF of the reddened field and cluster before the field decontamination. We also made another field-corrected KLF, "KLF-02". The KLF-02 is obtained by simply reddening all the model sources by $A_{\rm V}$ = 8 mag ($A_{\rm V}$ = 11 − 3), thereby bringing both the cluster and field sources to the same median $A_{\rm V}$ value of 11 mag, and then subtracting the field counts from the cluster counts. The 3 mag is the average extinction of the field sources based on their average $H - K_s$ colors (see Section 5.2.2.2). The second method is also often adopted in the literature when distance information of the field sources is not available (e.g. Jose et al., 2011).

We then generate synthetic clusters for the age range between 0.1 to 3 Myr at an interval of 0.5 Myr, using the Stellar Population Interface for Stellar Evolution and Atmospheres (SPISEA) python code (Hosek et al., 2020). We choose the following procedure in the SPISEA code: (1) assume that the distribution of stars in the cluster follows Kroupa (2001) mass-function, (2) use the mass-luminosity relation for the aforementioned ages from the MIST isochrone models of solar metallicity (Choi et al., 2016), and (3) adopted Rieke-Lebofsky extinction laws (Rieke & Lebofsky, 1985) and 2MASS filter pass-bands (for more details, see Hosek et al., 2020). Next, we convert the absolute K_s band magnitude of the cluster stars to the apparent magnitude using the distance modulus and average extinction of $A_{\rm K}$ ~1.2 mag ($A_{\rm V}$ ~ 11 mag) of the cluster. Then, we constructed the KLFs using apparent K_s band magnitudes and subsequently smoothed the

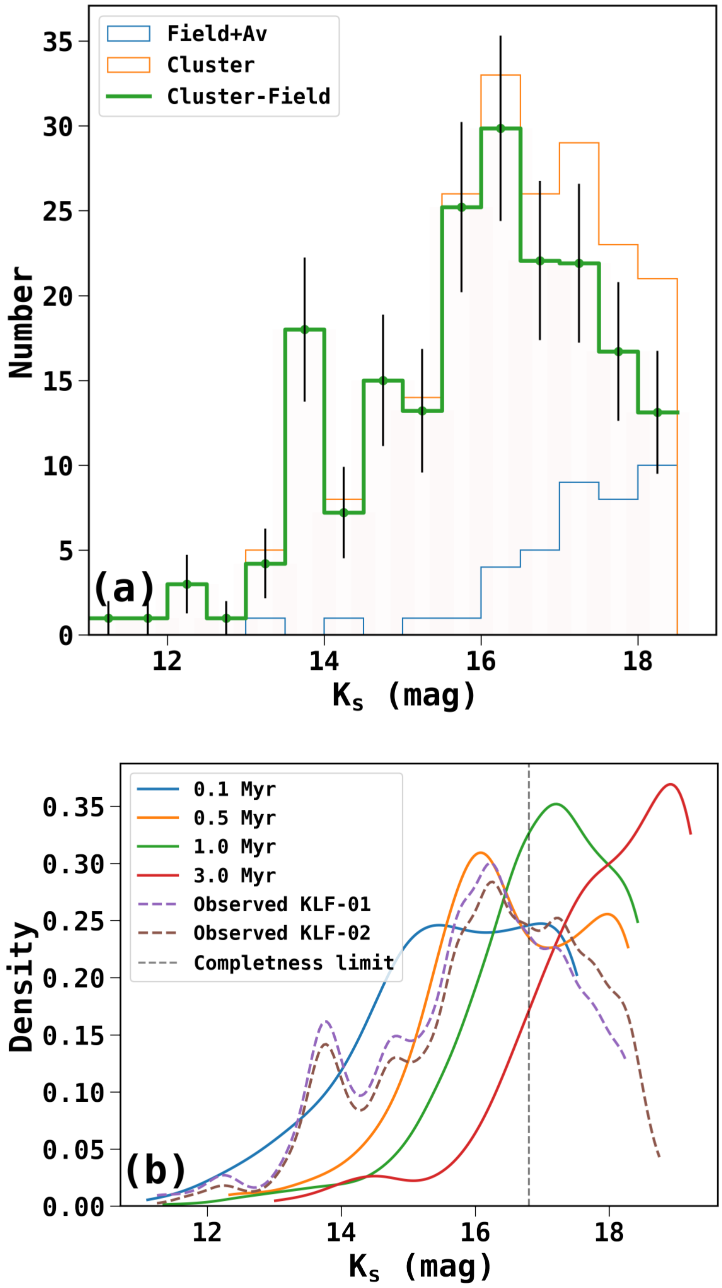

Figure 5.8: (a) K_s band luminosity function of the cluster, reddened model control field, and control field subtracted cluster shown by orange, blue, and green histograms, respectively. The error bars represent the Poisson error. (b) K_s band density plots of synthetic clusters of age 0.1, 0.5, 1.0, and 3.0 Myr, shown by solid curves. The dashed curves show the K_s band density plots of the reddened control field subtracted cluster.

KLFs with Gaussian KDE bandwidth of K_s = 1 mag, to account for various uncertainties present in the observed cluster. These uncertainties include the uncertainty of ~0.4 mag in the mean extinction of the cluster and a likely uncertainty of ~0.15 mag due to excess extinction (see

Section 5.2.2.1) in the K_s band. The last step is done to compare model KLFs with the KLF of the observed cluster. Since SPISEA randomly generates sources for a cluster, we ran the simulation 200 times for each synthetic cluster age. Then obtained the median KLF for each synthetic cluster. Figure 5.8b shows the model KLFs of different ages along with the observed field star-subtracted cluster KLFs (KLF-01 and KLF-02) derived in two ways discussed above. As can be seen, barring the bump around K_s ~13.8 mag, the model KLFs with ages in the range of 0.1−1 Myr appear to be reasonably matching with the observed KLFs, while the overall shape of the observed KLF is in better agreement with the model KLF of age = 0.5 Myr. Also, from the disk fraction of FSR 655 (discussed in Appendix B.2), the age of the cluster seems to be less than a Myr. Therefore, ~0.5 Myr appears to be a reasonable assumption as the age of the cluster. The reason for the bump in the KLF around K_s ~13.8 mag is unclear to us, but we believe that given the small area investigated in this work, the origin of the bump is more of a statistical nature. Wider and deeper observations of the cluster field, as well as a nearby control field, would be able to shed more light on this issue.

In molecular clouds, gas is either consumed in the star formation processes or dissipated by various feedback effects due to forming stellar members. It has been found that molecular clouds with age greater than ~5 Myr are seldom associated with molecular gas (Leisawitz et al., 1989). So, the lack of molecular gas and dust is a proxy indication of the cloud's evolution. In Figure 5.9, the median visual extinctions associated with some of the compact (radius < 3 pc) nearby young clusters (< 4 kpc) of age less than 5 Myr are shown that are associated with a few O-type to early B-type stars. We restrict our sample to the aforementioned type clusters in order to be able to compare with the cluster investigated in this work. As one can see from the figure, the visual extinction is decreasing with the age of the cluster, as expected. Seeing the nature of the plot, we fitted the data points with an exponential decay function of the form, A_V = $a \times \exp(-b\tau)$, where τ is the age of the cluster. Before fitting, the extinction values are first corrected for foreground extinction, as found in the literature. The best-fit value of a and b are ~26.30 ± 3.33 and ~1.26 ± 0.05, respectively. We note that though this oversimplified approach suggests the decrease in column density exponentially with time, the real scenario might be more complex as it strongly depends upon the strength of feedback from the stars present in the clump and the rate of star formation. A better sample with nearly similar cluster mass may provide better results, nonetheless, the obtained result provides a proxy way of seeing how the column density might have evolved in the clumps that are host to low to intermediate mass clusters, like

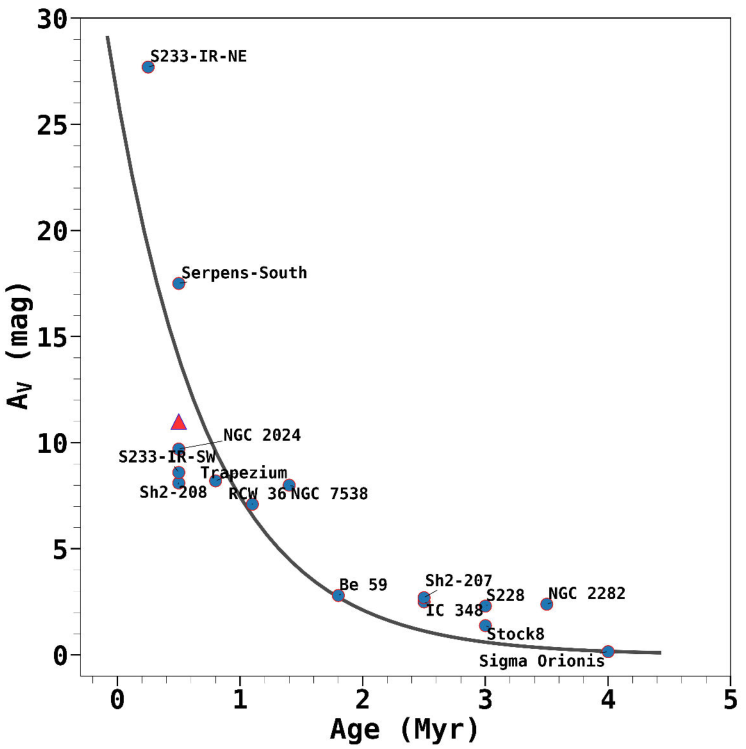

Figure 5.9: Visual extinction versus age plot of different nearby clusters (d $\lesssim$ 4 kpc), given in Table 5.1. The black curve shows the best-fit exponential function (see text for details) with fitted parameters, $a \approx 26.30 \pm 3.33$ and $b \approx 1.26 \pm 0.05$. The red triangle shows the position of FSR 655. Here, the extinction values are corrected for foreground extinction, as found in the literature.

the one investigated in the present work. As it can be observed from the figure, the median A_V of FSR 655 is certainly higher than clusters of age older than 2 Myr (e.g., Stock 8, IC 348, and S228) and comparable to the extinction of the clusters in the range 0.5−1 Myr (e.g., NGC 2024, Sh 2-208, and S233-IR-SW). This again points to the fact that the studied cluster is unlikely to be older than a Myr. The disk fraction of the cluster was also found to be compatible with other nearby clusters of age less than a Myr (for details, see Appendix B.2).

5.2.2.4 Mass-extinction limited sample

As often adopted in young star-forming regions (Andersen et al., 2011; Luhman et al., 2016), a mass-extinction limited sample of stars was defined to derive further properties of the cluster. The mass-extinction limited sample represents all stars in a given area above a certain mass limit after accounting for the effects of extinction and completeness. The primary challenge in obtaining such a sample in young clusters lies in determining the mass limit down to which our

Table 5.1: Parameters of nearby clusters.

No	Name	A_V (mag)	Age (Myr)	Distance (kpc)	Reference
1	Stock8	2.0	3.0	2.3	Jose et al. (2017); Damian et al. (2021)
2	Be 59	4.0	1.8	1.0	Panwar et al. (2018)
3	S228	3.3	3.0	3.2	Yadav et al. (2022)
4	IC 348	3.5	2.5	0.32	Muench et al. (2007)
5	Trapezium	9.2	0.8	0.4	Muench et al. (2002)
6	Sh2-208	10.1	0.5	4.0	Yasui et al. (2016b)
7	Sh2-207	2.7	2.5	4.0	Yasui et al. (2016a)
8	S233-IR-SW	9.8	0.5	1.8	Yan et al. (2010)
9	S233-IR-NE	28.9	0.25	1.8	Yan et al. (2010)
10	NGC 2282	4	3.5	1.65	Dutta et al. (2015)
11	NGC 7538	11	1.4	2.7	Sharma et al. (2017)
12	RCW 36	8.1	1.1	0.7	Baba et al. (2004); Ellerbroek et al. (2013)
13	NGC 2024	10.7	0.5	0.42	Levine et al. (2006)
14	Serpens South	19.5	0.5	0.44	Jose et al. (2020)
15	Sigma Orionis	0.155	4.0	0.4	Walter et al. (2008)

The mean extinction values of the clouds are taken from the quoted references. For the age of the regions, wherever the range was given, we have taken the mid values.

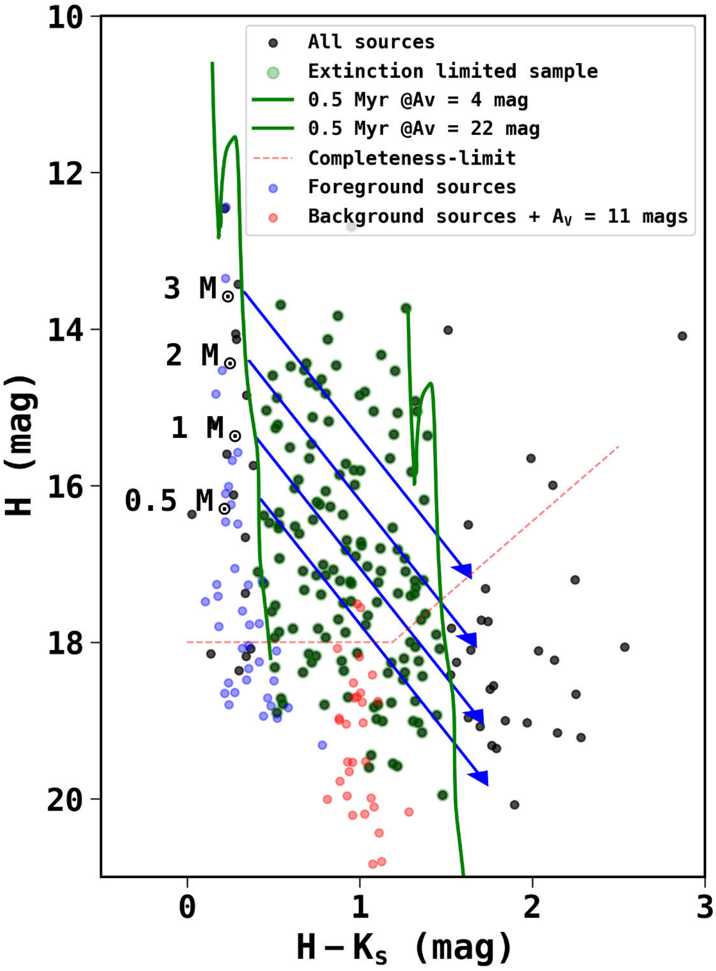

Figure 5.10: The H vs $H-K_s$ color-magnitude diagram of sources in the cluster and control field. The black dots show all the sources observed in the cluster region. The green dots show the sample within A_V = 4 to 22 mag. The blue dots show the foreground control field sources, and the red dots show the background control field sources, which are reddened to match the median visual extinction of the cluster region, i.e., A_V = 11 mag. The MIST isochrones of 0.5 Myr (Choi et al., 2016) are reddened by A_V = 4 and 22 mag and are shown in green curves. The blue arrows represent the reddening vectors, and the completeness limits of the data are marked by red dashed lines.

data is complete. This determination depends on the age of the cluster and the level of extinction, both of which can be uncertain in young clusters. Unlike open clusters (e.g. Sagar et al., 2001; Sharma et al., 2006; Kumar et al., 2008), young clusters show variable extinction, which makes it difficult to assign a unique mass to a given source. In order to derive the mass-extinction limited sample, we use H vs. $H-K_s$ color-magnitude diagram. Figure 5.10 shows the H vs $H-K_s$

color-magnitude diagram of all the sources. Assuming that the approximate age of the cluster is around 0.5 Myr, a 0.5 Myr MIST isochrone (Choi et al., 2016) reddened by $A_V = 4$ and 22 mag is also shown in Figure 5.10. In the figure, the completeness limit is also shown by the dashed line, while the reddening vectors originating at masses of 3 $M_\odot$, 2 $M_\odot$, 1 $M_\odot$, and 0.5 $M_\odot$ are shown by blue arrows. To obtain the mass-extinction limited sample, we choose the visual extinction in the range of 4−22 mag, because most of the sources below $A_V = 4$ mag are likely the foreground sources of the field, while only 10% of the sources lie above $A_V = 22$ mag. Applying a high extinction threshold would guarantee a complete sample above a certain mass limit, but it would result in a high minimum mass limit above completeness. The $A_V = 22$ mag is a reasonable choice to have a statistically significant number of stars while still reaching fairly low masses above the completeness limit. With $A_V = 22$ mag limit, the sample used in this work is found to be better complete above 1 $M_\odot$ and considerably complete down to 0.5 $M_\odot$.

Field star contamination generally dominates in the low-mass ends of the stellar population. The background and foreground contamination levels in our mass-extinction limited cluster sample are expected to be minimal. In Figure 5.10, the foreground (blue dots) and background (red dots) population from the Besançon model are also shown. The background populations are reddened to match the median visual extinction of the cluster, i.e., $A_V = 11$ mag. Even with this minimum extinction, almost no background population above 0.5 $M_\odot$ was seen.

5.2.2.5 Mass function

The stellar initial mass function describes the mass distribution of the stars at birth in a stellar system and is fundamental to several astrophysical concepts. Most of the observational studies focusing on the high-mass end (mass > 0.5 $M_\odot$) have found no gross variation of IMF across the Milky Way disc as well as in the local solar neighbourhood (Sagar, 2002; Bastian et al., 2010; Hopkins, 2018), and are in agreement with Salpeter (Salpeter, 1955) or Kroupa (Kroupa, 2001) type mass function distribution. At the high-mass end (mass > 0.5 $M_\odot$), the mass-function power-law exponent "Γ" is found to be close to 2.3 in the linear form (i.e., $\frac{dN}{dM} \propto M^{-\Gamma}$) or 1.3 in the logarithm form (i.e. $\frac{dN}{dlogM} \propto M^{-\alpha}$; Kroupa, 2001), where $\alpha = \Gamma - 1$.

Studying young clusters, like the one investigated in this work, has the advantage that the dynamical effect of mass segregation will have minimal effect on the shape of the IMF (e.g. Pandey et al., 1992; Allison et al., 2009b). In the following, we tried to estimate the IMF of FSR

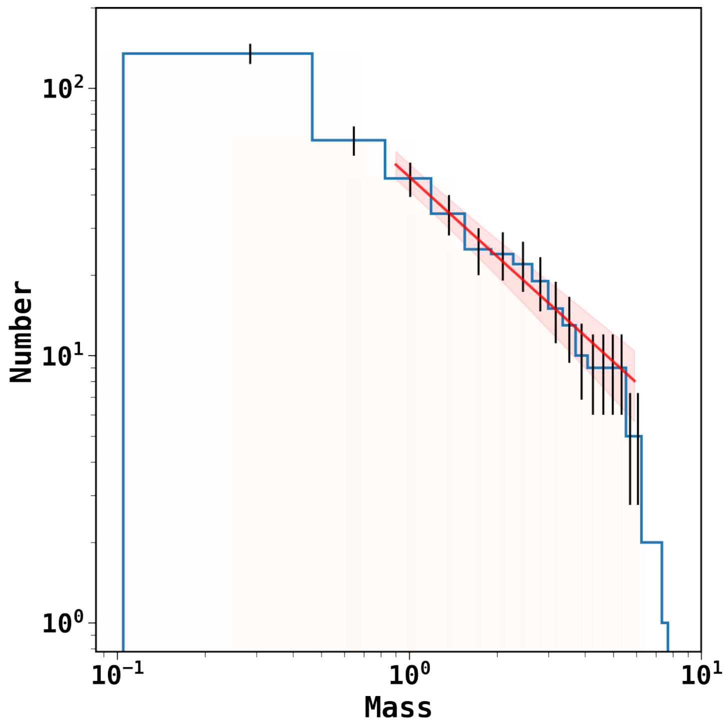

Figure 5.11: Cumulative initial mass function of the cluster. The red line shows the best-fit power-law mass function with index, α = 1.00 ± 0.15 for the mass range of 1 to 4 $M_\odot$.

655. There are several factors that can affect the IMF shape while dealing with the embedded clusters (e.g. Damian et al., 2021). The principal factors are the effect of NIR−excess and variable extinction in estimating the mass of the stars, low statistics of member stars due to high extinction in getting robust α value, and contamination at the low-mass end. Since our J band is least sensitive to the detection of the point sources, to mitigate the effect of NIR excess sources, we used the H band luminosity as it is less affected by circumstellar matter compared to other longer wavelengths. To partially mitigate the effect of low statistics, we use cumulative mass-function (e.g. Rodón et al., 2012) of the form:

$$N(>M) \propto kM^{-\alpha} \tag{5.7}$$

Figure 5.11 shows the cumulative mass function, $N(>M)$ of the cluster, where N is the number of sources with mass larger than M and the error bars represent the Poisson noise of $\sqrt{N}$. Using weighted least-square fit, we find $\alpha = 0.95 \pm 0.12$ for the mass range of 0.5 to 4 $M_\odot$. By excluding the points lower than 1 $M_\odot$ in the fitting, to avoid any possible bias that may be introduced by the completeness correction and/or in-proper account of field star contamination at the fainter mass end, we find $\alpha = 1.00 \pm 0.15$ for the mass range of 1 to 4 $M_\odot$. The obtained slopes are, though flatter, but in agreement with the Kroupa IMF (Kroupa, 2001) within 3σ uncertainty, where σ is the error in our measurements. We exclude sources above 4 $M_\odot$ in fitting as the M-L relation at younger ages (e.g. as found with 0.5 Myr MIST isochrone) is non-linear in the range 4−12 $M_\odot$, thus, a star can not have a unique mass around this mass range. We note that, though our results show a flatter IMF for FSR 655, but should be treated with caution due to various uncertainties involved.

Future more sensitive photometric and spectroscopic observations would improve the robustness of our results with better estimation of extinction, contamination, and contribution from infrared excess. Nevertheless, the characterization of young compact clusters, like the one investigated in this work, is a useful exercise for assessing the mass distribution at the very initial stages of cluster formation.

5.2.2.6 Star formation efficiency and rate

The emergence of a bound cluster also depends on the efficiency with which gas is converted into stars, i.e., SFE (ϵ). The total gaseous mass ($M_{\rm gas}$) present in the cluster within its radius was estimated using the *Herschel* molecular hydrogen column density map (Marsh et al., 2017). We determined the total integrated column density over the cluster area and converted it into mass using equation 2.1. The gas mass of the cluster region is found to be ~750 ± 337 $M_\odot$. The uncertainty in the gas mass is around 45%, which includes the uncertainty in the distance of the cloud, gas-to-dust ratio, and dust opacity index (details are given in Chapter 2). In order to calculate the mass of the cluster (M_*), we integrated the IMF of the cluster with Kroupa IMF index, $\Gamma = 2.3$ (Kroupa, 2001), within the mass limits of 0.5 to 15 $M_\odot$. Then, extrapolated down to 0.08 $M_\odot$ to determine the mass at the lower-mass end, i.e., from 0.5 to 0.08 $M_\odot$, by assuming $\Gamma = 1.3$ (Kroupa, 2001). The total stellar mass of the cluster is found to be ~180 ± 13 $M_\odot$. Using $M_{\rm gas}$ and M_*, we calculated the $\epsilon = M_* \,/\, (M_{\rm gas} + M_{\rm cluster})$ to be around 0.19 ± 0.07 in the cluster region.

The star formation rate describes the rate at which the gas in a cloud is converting into stars. The SFR can be estimated as, SFR = $M_*/t_{\rm clust}$, where $t_{\rm clust}$ is the star formation timescale of the cluster. Assuming $t_{\rm clust}$ as 0.5 Myr, we obtained the SFR in the cluster region to be around 360 ±

26 $M_\odot$ Myr^{-1}. The projected area of the cluster region, over which the cloud mass was estimated, is calculated as $\pi r_{\rm eff}^2$ and is found to be ~3.14 ± 0.57 pc^2. Here, $r_{\rm eff}$ = 1 pc is the radius of the cluster region. Normalizing the derived SFR by the cloud area, the SFR per unit surface area, $\Sigma_{\rm SFR}$ is determined to be ~114.6 ± 22.2 $M_\odot$ Myr^{-1} pc^{-2}, and the gas mass surface density, $\Sigma_{\rm gas}$ is determined to be ~240 ± 115 $M_\odot$ pc^{-2}.

Krumholz et al. (2012) argued that since different clouds can be at different evolutionary stages, therefore normalizing the $\Sigma_{\rm gas}$ with the free-fall timescale would give a better correlation with the $\Sigma_{\rm SFR}$. A better correlation of $\Sigma_{\rm SFR}$ with $\Sigma_{\rm gas}/t_{\rm ff}$ has been found in some studies (Krumholz et al., 2012; Lee et al., 2016; Pokhrel et al., 2021) and the general form of the relation is expressed as follows (Krumholz et al., 2012)

$$\Sigma_{\rm SFR} = \epsilon_{\rm ff}\frac{\Sigma_{\rm gas}}{t_{\rm ff}}, \tag{5.8}$$

where $\epsilon_{\rm ff}$ is the star formation rate per freefall time, which is defined as $\epsilon_{\rm ff} = \epsilon \times t_{\rm ff}/t_{\rm clust}$ (Lee et al., 2016). To test this star-formation relation, we estimate the free-fall timescale of the cluster using the following relation,

$$t_{\rm ff} = \left(\frac{3\,\pi}{32\,G\mu m_{\rm H} n_{\rm H_2}}\right)^{1/2}. \tag{5.9}$$

The $n_{\rm H_2}$ is calculated as $M_{\rm gas}/(4/3)\pi r^3 \mu m_{\rm H}$, which is around 2637 ± 1318 cm^{-3}. Using equation 5.9, we calculate $t_{\rm ff}$ to be around ~0.60 ± 0.15 Myr. Using $t_{\rm ff}$, $t_{\rm clust}$ = 0.5 Myr, and ϵ = 0.19 of the cluster region, we determined $\epsilon_{\rm ff}$ to be around 0.23 ± 0.10.

5.2.2.7 Possibility of FSR 655 emerging as a massive cluster

From the stellar population and gas content of the FSR 655 region, the SFE and SFR of the cluster were estimated to be around 19% and 360 $M_\odot$ Myr^{-1}, respectively. As discussed in Chapter 3, the cluster is located in a massive clump, which is situated at the filamentary hub of the cloud, and the filaments are inflowing cold gaseous matter at a rate of ~675 $M_\odot$ Myr^{-1} towards the hub. Moreover, it was found that in the central region of the clump, the virial analysis suggests that, at present, the magnetic field and turbulence are not sufficient enough to prevent the collapse of the central clump region (see Chapter 4). So, we hypothesize that if the star formation continues in the clump with the current rate for another 2 Myr along with the continuous mass supply through the filaments, then a cluster of total stellar mass ~1000 $M_\odot$ is expected to emerge at the hub of G148.24+00.41.

5.3 Summary

In this chapter, we have studied a young cluster, FSR 655 located at the hub of the G148.24+00.41 cloud, in order to better understand the formation of star clusters in GMCs. To study the cluster properties, the cluster region (~2′× 2′) is observed with the TANSPEC NIR camera mounted on the 3.6-m DOT. The reduced photometric data is sensitive down to 5σ limiting magnitude of 20.5, 20.1, and 18.6 mag in J, H, and K_s bands, respectively.

The cluster shows differential extinction with a mean visual extinction of ~ 11 mag, whereas the foreground visual extinction in the direction of the cluster is around 4 mag. The age of the cluster derived by matching the KLF of the cluster members with the KLFs of the synthetic clusters is found to be around 0.5 Myr. Using the JHK_s and HK_s[4.5] CC diagrams, we find the disk fraction to be around 38 ± 6% and 57 ± 8%, respectively. Using the Kroupa initial mass function, the present-day total stellar mass of the FSR 655 cluster was determined to be ~ 180 ± 13 $M_\odot$. The gas mass of the cluster is around 750 ± 337 $M_\odot$, which gives the SFE of ~ 19 ± 7% and SFR as ~ 360 ± 26 $M_\odot$ Myr^{-1}.

Taking these results at face value and assuming a constant SFR for a time span of 2 Myr, the cluster has the potential to grow further to become a 1000 $M_\odot$ cluster. Given the fact that the cluster is located near the geometric centre of the cloud, whose mass is ~10^5 $M_\odot$, evidence of gas in-fall onto the region at a high rate via large-scale filamentary flows have been observed, it is not unreasonable to think that the cluster will increase in mass in the future and may emerge as a massive cluster. Moreover, simulation suggests an accelerated pace of star formation in molecular clouds with SFR $\propto t^2$ due to global hierarchical and runway collapse of molecular gas up to a few Myr since the beginning of the star formation (e.g. Caldwell & Chang, 2018; Vázquez-Semadeni et al., 2019). So, the possibility of FSR 655 becoming a more massive and richer cluster seems to be viable.

Chapter 6

Star formation scaling laws at the clump scale

Stars are born in groups, deeply embedded within dense clumps of molecular gas. The fate of a nascent stellar system, whether to become an expanding association or to remain a bound cluster, is determined by how rapidly and effectively it disperses the gas material of the clump/cloud. This process is controlled primarily by two parameters: the efficiency of star formation and the timescale on which the remaining gas is disrupted. If the gas removal is rapid relative to the free-fall time, then more than half the mass must be in stars for the cluster to remain bound (Hills, 1980). On the other hand, a sufficiently slow mass loss allows a virialized stellar system to expand adiabatically and remain bound. The stellar feedback, rapid gas expulsions, violent dynamical interactions, and tidal disruptions are the possible reasons for a cluster to become unbound over time and dissolve (Krumholz et al., 2019). The massive stellar clusters in the universe or in our own Milky Way, which are still bound by gravity even after multiple free-fall times, must be unique in terms of their star formation histories and initial conditions. By star formation history, we mean the star formation efficiency and the timescale in which the gas is converted into stars, which is still not well understood. Some theories suggest that the disruption effect of stellar feedback becomes less significant in high surface density clouds or in massive clusters (see the review article by Krumholz et al., 2019). As discussed in chapter 1, the SFE within the cluster-forming region can impact the emergence of a rich and bound cluster. In addition, it is also suggested that the primordial structure and density profile of the gas also plays a decisive role in massive stars and associated cluster formation (e.g. Bonnell & Bate, 2006; Parker et al., 2014; Chen et al., 2021). Thus, the prerequisite condition to improve our understanding of the formation of intermediate to massive star clusters is to investigate a sample of young clusters of different ages and masses that have recently formed in massive clouds. In this regard, it is important to analyze the stellar properties, i.e. SFR and SFE, of a sample of cluster-forming clumps. Young clusters, which are at the early stages of star formation, tell about the local environment of their parental clump. Also, studying a sample of young clusters would help us delineate the relation between stars and the star-forming material at the clump scale in order to better understand the cluster formation process. Moreover, as discussed in Chapter 1, a high-mass gas assembly with a high SFE is also a possible way of forming an intermediate-to-massive stellar cluster. The SFE generally found in molecular clouds is very low (2−6%; Evans et al., 2009; Lada et al., 2010; Heiderman et al., 2010; Evans et al., 2014), but it can be high in clumps due to their high density.

Star formation is important for the evolution of the galaxy; therefore, it is crucial to understand what governs and regulates the star formation process. The relation between star formation rate surface density and gas mass surface density, i.e. the “scaling law," is very well defined at the extragalactic scale by the Kennicutt-Schmidt relation (Kennicutt, 1998b):

$$\Sigma_{\mathrm{SFR}}(\mathrm{M_\odot\,yr^{-1}kpc^{-2}}) = (2.5 \pm 0.7) \times 10^{-4} \left(\frac{\Sigma_{\mathrm{gas}}}{1\mathrm{M_\odot\,pc^{-2}}} \right)^{1.4 \pm 0.15} . \quad (6.1)$$

Although large-scale studies offer crucial insights into the correlation between the overall properties of galaxies and the formation of stars, the conversion of gas into stars occurs at a more localized level, i.e. in molecular clouds.

Studying the scaling laws in the molecular clouds of our own Milky Way Galaxy offers the advantage of having the highest resolution than any other extragalactic clouds. Therefore, the clouds and the sub-structures within them, along with the stars, can be better resolved and studied at various scales. The earlier studies on scaling laws at the cloud scale show higher slopes than KS relation, broad distribution, and weaker correlation between Σ_{SFR} and Σ_{gas} (Evans et al., 2009; Lada et al., 2010; Heiderman et al., 2010; Kennicutt & Evans, 2012; Lada et al., 2013; Evans et al., 2014; Vutisalchavakul et al., 2016; Heyer et al., 2016). Evans et al. (2014) also shows that the inclusion of the free-fall timescale does not reduce the scatter in scaling relation. The reasons like observational biases and the impact of physical factors for the weaker correlation and large scatter in the scaling laws at the molecular cloud scale are discussed in detail in Section 1.5.3 of Chapter 1. However, recent studies by Pokhrel et al. (2020, 2021) re-investigated the scaling laws in 12 nearby molecular clouds and within single clouds and found a good correlation between Σ_{SFR} and Σ_{gas}. The authors also showed that the correlation becomes even better by including the free-fall time scale in the relation. Pokhrel et al. (2020, 2021) reduced the observational biases by considering various uncertainties in parameters like total stellar mass and gas mass, and better sampling the protostars from the SESNA catalogue (Gutermuth et al., 2019).

In molecular clouds, the clumps are the actual sites where clusters form; therefore, it is crucial to examine the behaviour of scaling laws at the clump scale for a deeper understanding of the key processes that govern and regulate the formation of stars. In addition, understanding the SFR−gas mass scaling relations over different spatial scales is important for the evolution of molecular clouds. So far, mostly different relations have been found for different data sets depending upon the data quality, scale size, sample size, and observational constraints, but the local gas environment is also believed to play a substantial role. In this work, we extend the studies on star formation scaling relations to clump scale by investigating a sample of active cluster-forming clumps. We aim to estimate the gas properties of the clumps and star formation properties of the clusters formed within them, and then explore their correlations. To do so, we used near-infrared data from the UKIDSS and followed a similar methodology as adopted for the FSR 655 cluster in Chapter 5.

6.1 Data used

6.1.1 Near-infrared data

To determine the cluster properties, NIR photometric data (J, H, and K) from the UKIDSS's Galactic Plane Survey (GPS; Lucas et al., 2008) and the Galactic Cluster Survey (GCS; Casewell & Hambly, 2013) from DR10 plus were used in this work. The survey area of the GPS includes 1868 square degrees of the northern and equatorial Galactic plane at Galactic latitudes $-5° < \mathrm{b} < 5°$ and ~200 square degrees area of the Taurus-Auriga-Perseus molecular cloud complex in the J, H, and K filters (Lucas et al., 2008). The GPS survey has a resolution of around 1 arcsec. The GCS survey covers an area of 1067 square degrees that includes 10 open clusters and stellar associations (Lawrence et al., 2007). The depth of the GPS in J, H, and K bands is 19.8, 19.0, and 18.1 mags, respectively, while for GCS, the depth is 19.6, 18.8, and 18.2 mags, respectively.

In this analysis, only those point sources were used which have an error of less than 0.1 mag in all three bands. In order to include brighter sources, the 2MASS NIR data is also used (Cutri et al., 2003).

6.2 Methodology

The identification and counting of YSOs and using the information of their average mass and lifetimes is a direct way to quantify the SFR, which is known as the star-count method. However, in previous studies that are based on *Spitzer* data, the star-count method was mostly employed for nearby clouds (< 1 kpc) (Evans et al., 2009; Heiderman et al., 2010; Lada et al., 2010) due to the low sensitivity of the *Spitzer* data at larger distances. In distant star-forming regions, the indirect tracers of SFR are used like Hα emission, UV continuum, infrared luminosities, and radio continuum emission (see the review article by Kennicutt, 1998a; Kennicutt & Evans, 2012). In this study, the UKIDSS NIR data is used to reach a fairly low mass limit for each cluster. To determine the total stellar mass and age of the clusters, we have followed the same method and steps as discussed in Chapter 5.

6.3 Sample

To get a statistical sample, compact clusters up to a distance of 2.5 kpc were selected. At a larger distance limit, it is difficult to count each star in the cluster because of the sensitivity limits of the observations, as the stars become fainter due to higher interstellar extinction at larger distances. The clusters were further shortlisted based on the presence of significant cold dust emission at far-infrared (FIR) wavelengths, identified through inspection of *Herschel* and *AKARI* images using the ALADIN software (Baumann et al., 2022). Those clumps were removed from the sample, which are part of a highly structured environment, such that their centre and extent, as well as their associated gas properties, were critical to define. Most of the clusters in our sample are very young, such that they are either barely visible or invisible in optical images such as DSS-2 and Pan-STARRS. Based on the above selection, 17 clusters are included in the sample, as listed in Table 6.1.

6.4 Analyses and results

Here, we present the analysis steps applied for all the clusters in our sample and present the results by giving an example of the IRAS 06063+2040 cluster and its corresponding plots. Figure 6.1a-b shows the 3-color RGB image of IRAS 06063+2040 in JHK bands from UKIDSS and 2MASS. Figure 6.1c shows the *Herschel* 500 μm image of IRAS 06063+2040, showing the presence of cold dust in the cluster region.

6.4.1 Completeness of the NIR photometric data

Firstly, the completeness of the UKIDSS NIR data was checked using the histogram turnover method. As discussed in Chapter 5, this method gives a proxy determination of completeness limits. The 90% completeness limit for most of the clusters was found to be in the range 17.8−18.3, 17.2−17.5, and 16.8−17.0 mag in J, H, and K bands, respectively.

Table 6.1: Sample of clusters.

No	Name	GLON (degree)	GLAT (degree)	D (kpc)	Reference
1	IRAS 06063+2040	189.859	0.502	2.1	1
2	IRAS 06055+2039	189.769	0.336	2.1	1
3	IRAS 06068+2030	190.053	0.538	2.0	2
4	IRAS 22134+5834	103.875	1.856	1.5	3
5	IRAS 06056+2131	189.030	0.784	2.0	4
6	Sh2-255	192.601	-0.047	2.0	5
7	[IBP2002] CC14	173.503	-0.060	1.8	1
8	IRAS 06058+2138	188.949	0.888	2.0	4
9	IRAS 06065+2124	189.232	0.895	2.0	6
10	NGC 2282	211.239	-0.421	1.7	7
11	IRAS 05490+2658	182.416	0.247	2.2	1
12	BFS 56	217.373	-0.080	2.4	8
13	[BDS2003] 89	217.634	-0.177	1.4	9
14	Sh2-88	61.472	0.095	2.1	5
15	IRAS 06104+1524	194.926	-1.194	2.0	3
16	IRAS 06117+1901	191.916	0.822	1.4	1
17	IRAS 05480+2545	183.348	-0.5765	2.1	10

References: [1] Elia et al. (2017), [2] Valdettaro et al. (2001), [3] Maud et al. (2015), [4] Carpenter et al. (1993), [5] Méndez-Delgado et al. (2022), [6] Dutra & Bica (2001), [7] Dutta et al. (2015), [8] Mège et al. (2021), [9] Bica et al. (2003), and [10] Henning et al. (1992).

6.4.2 Extent of the cluster

In comparison to open clusters, defining the centre of young clusters is much more difficult due to low statistics, high dust extinction, nebulosity, and complex shapes. Taking the cluster centre at the geometrical centre depends upon the region of the target adopted for the study and hence can be biased. Therefore, for young clusters in the sample, the highest stellar density point was chosen as the centre of the clusters. First, to assess the shape and size of the cluster, we selected

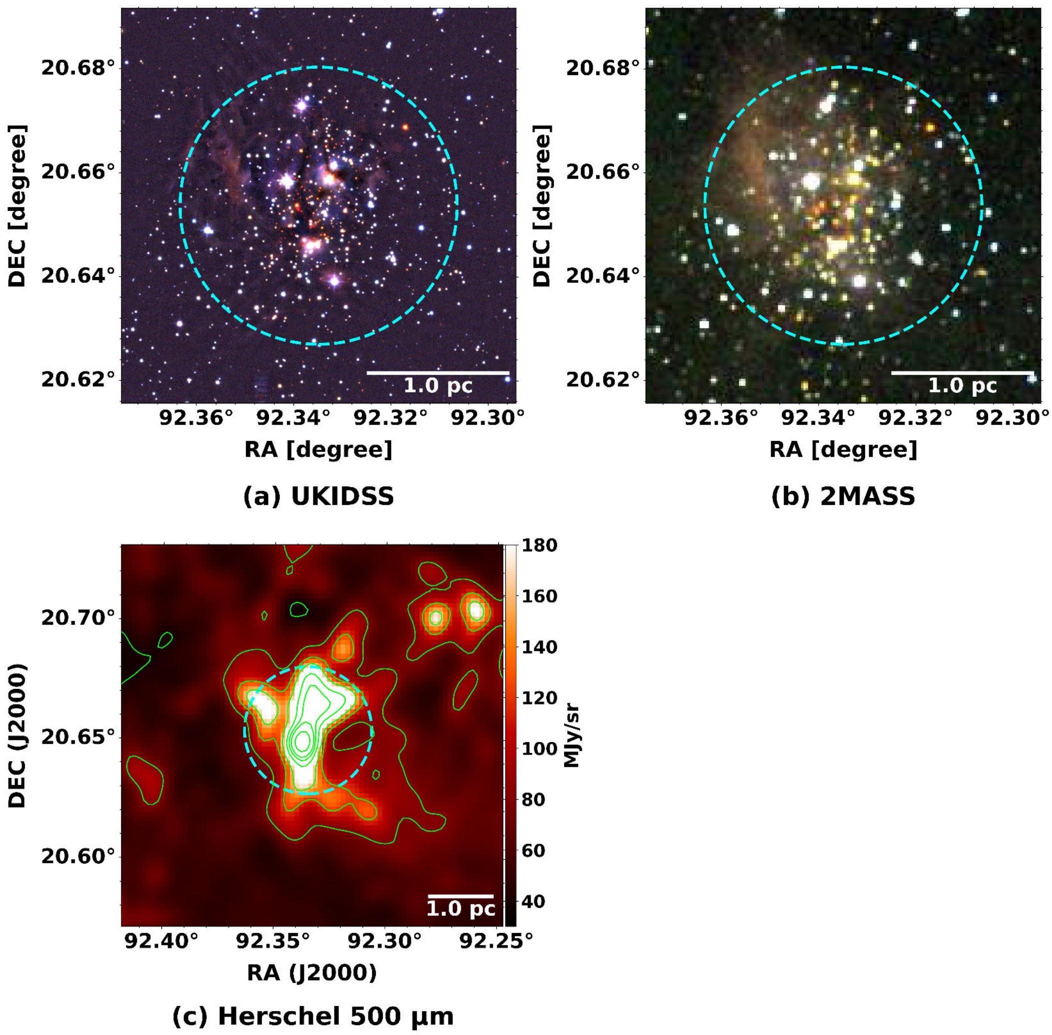

Figure 6.1: (a) UKIDSS and (b) 2MASS NIR color-composite (Red: K or K_s band for 2MASS; Green: H band, and Blue: J band) image of IRAS 06063+2040. The cyan dashed circle shows the extent of the cluster (see Section 6.4.2). (c) The *Herschel* 500 μm image of IRAS 06063+2040 along with contour levels at 20, 40, 80, 120, 160, 240, 320, 400, and 600 MJy/sr.

data for a larger region around the geometric centre of the cluster and plotted a 2-dimensional KDE map with a bin width of 0.5 to 0.7. The region for making the KDE map is selected in such a way that there should be an ample number of stars to make a smoothened KDE map of the cluster. The optimum bin width was chosen to have a good compromise between over- and under-smoothing density fluctuations, depending upon the data statistics in the cluster region. Then, we find the peak density point using Gaussian KDE and choose these coordinates as the approximate centre of the cluster. Figure 6.2a shows the 2D density plot of a cluster with its peak density point marked with a cross sign.

To determine the radius of the cluster ($R_{\rm clust}$), we constructed a radial density profile (RDP) of the cluster. To do this, we first divided the cluster into different annular rings with optimum binning of the distance from the centre. Then, we counted the stars in each radial bin and calculated the stellar density in each annulus by dividing the total counts with the area of the annulus. Figure 6.2b shows the plot of stellar density as a function of radius for IRAS 06063+2040. In order to obtain the radius of the cluster, we fitted the RDP with the empirical King's profile (King, 1962) of the form

$$\rho(r) \propto b_0 + \frac{\rho_0}{\left[1 + \left(\frac{r}{r_c}\right)^2\right]}, \tag{6.2}$$

where b_0, ρ_0, and $r_{\rm c}$ are the background stellar density, peak stellar density, and core radius of the cluster, respectively. The King's profile fit to the stellar density of IRAS 06063+2040 is shown in Figure 6.2b with 3σ uncertainty, and the background stellar density is shown by a solid blue line along with 5σ uncertainty. The radius of the cluster is defined as the radial distance at which the modelled stellar density lies 5σ above the background stellar density. The radius of all the clusters is given in Table 6.2. As can be seen from the table, all the clusters are parsec to sub-parsec in size.

For some clusters, we found that King's profile does not completely becomes flatten at the background stellar density either due to low statistics or confusion with other nearby stellar groups/clusters. In such cases, apart from taking the radius at 5σ above the background stellar density, we also rechecked and confirmed the size of the clusters from the stellar density contours in the 2-D KDE maps of the clusters and by visually inspecting the UKIDSS NIR images.

6.4.3 Field contamination and extinction

The field star population in the cluster region along the line-of-sight can significantly contaminate the cluster population and, hence, the derived cluster properties. In the case of embedded clusters, the background contamination is not that significant, as the background stars are highly extincted by the dust in the cloud itself, such that their extincted magnitudes will lie beyond the sensitivity limits of the observations. Whereas foreground contamination can be very significant and,

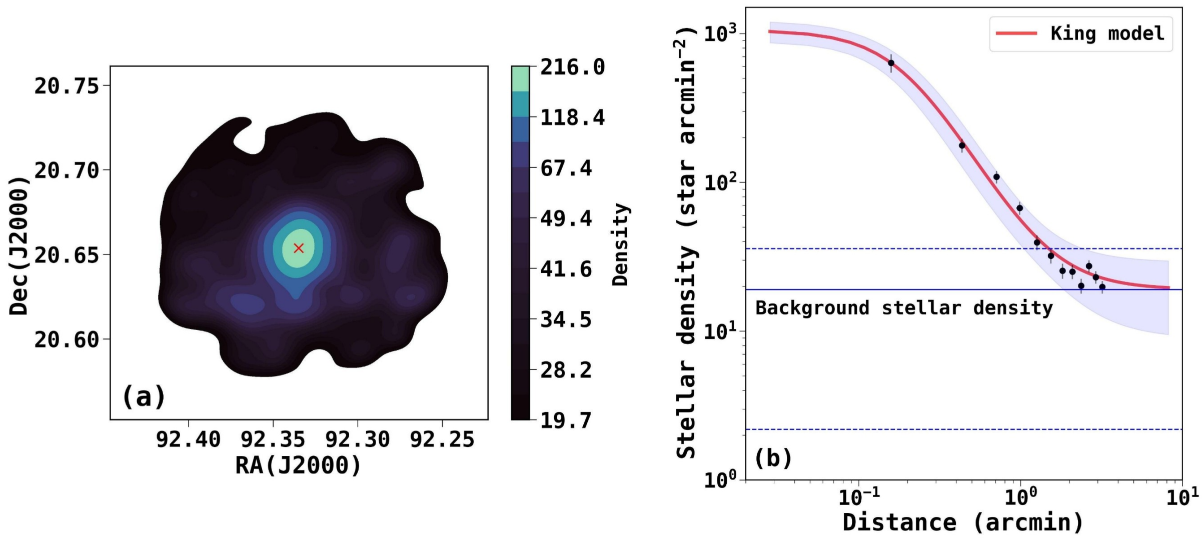

Figure 6.2: (a) A 2-D density plot of the stellar distribution observed in the direction of the IRAS 06063+2040 cluster, with the cross symbol indicating the cluster centre taken at the peak density point. (b) The observed stellar surface density of IRAS 06063+2040 as a function of distance from the centre (cross symbol in panel-a). The red curve shows the best fit King's profile along with 3σ uncertainty as blue shaded region. The error bars at each point represent the Poisson uncertainties. The solid blue line shows the best-fit background stellar density with 5σ uncertainty as blue dashed lines.

therefore, is a factor that needs to be removed. For that, a control field region near the cluster location that is relatively dust-free was selected, and the photometric data was selected in the same way as done for clusters. Large control fields with a radius of around 5−7 arcmin were used to get better statistics of the field population. To estimate the visual extinction (A_V) of the observed stars along the direction and within the region of the cluster, the $J-H$ and $H-K$ colors of the control field sources are assumed to be intrinsic and subtracted from the corresponding colors of the observed stars, as shown in equation 5.5. Figure 6.3 shows the density plot of A_V values for IRAS 06063+2040 with a median around 6.0 ± 3.1 mag. The median A_V for the cluster sample is found to be in the range of 2 to 11 mag and is given in Table 6.3.

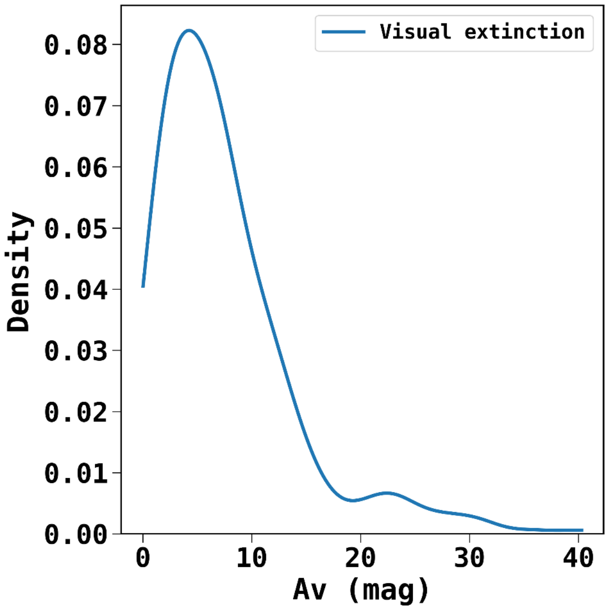

Figure 6.3: Density plot of visual extinction, A_V of all the sources observed towards the direction of IRAS 06063+2040.

6.4.4 *K*-band luminosity function and age estimation

As discussed in Section 5.2.2.3 of Chapter 5, the KLF can be used to estimate the proxy age of a cluster. In order to do that, firstly the contamination of the field stars was removed by subtracting the KLF of the field population from that of the target population. The KLF of the control field is obtained by reddening all the field stars by the median A_V of the cluster region. Figure 6.4a shows the KLF of the cluster before field subtraction and the KLF of the reddened control field with the same bin size. Since the size of the control field region is larger than the size of the cluster region, the field sources are first normalized to the cluster size at each bin and then subtracted from the cluster KLF to obtain the field-subtracted cluster KLF, which is also shown in Figure 6.4a.

To estimate the age (t_{clust}) of the cluster, we compared the field-subtracted cluster KLF with the modelled KLFs of synthetic clusters at different ages. We used the SPISEA code (Hosek et al., 2020) to generate the synthetic clusters with an age range of 0.1 to 3.0 Myr. The details of the steps are given in Section 5.2.2.3 of Chapter 5. Figure 6.4b shows the KLFs of the synthetic clusters and the field subtracted KLF of IRAS 06063+2040. From the figure, it can be seen that the KLF of IRAS 06063+2040 is close to the synthetic KLFs of age between 0.5 to 1.0 Myr.

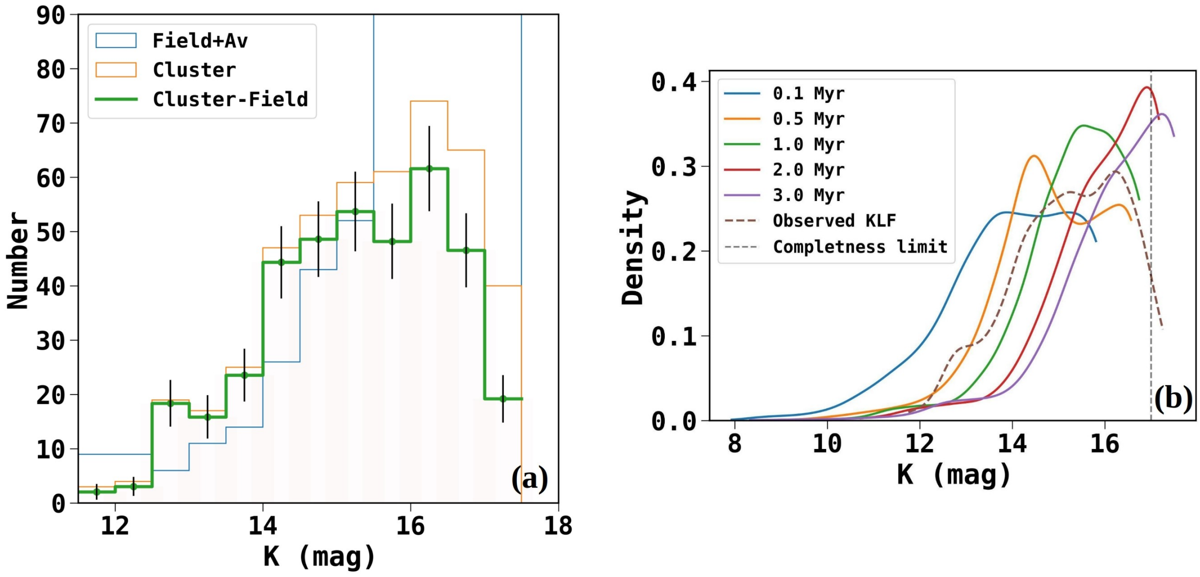

Figure 6.4: (a) K-band luminosity function of the IRAS 06063+2040 cluster (orange), reddened control field (blue), and control field subtracted cluster (green). (b) K-band density plots of synthetic clusters of age 0.1, 0.5, 1.0, 2.0, and 3.0 Myr, shown by solid curves. The dashed curve shows the control field subtracted K-band density plot of IRAS 06063+2040.

Therefore, the mid value of 0.75 Myr was taken as the approximate age of IRAS 06063+2040. Similarly, we have done this for all the clusters in the sample and the age of all the clusters is listed in Table 6.3.

6.4.5 Gas properties of the clusters

One important term in the scaling laws is the gas mass of the star-forming regions. To estimate the gas mass, we utilized the *Herschel* column density maps from Marsh et al. (2017), which are constructed by the PPMAP technique (Marsh et al., 2015; Marsh & Whitworth, 2019) using Hi-GAL data (Molinari et al., 2010) and are available for the entire Galactic plane within a strip of around 2 degrees in the latitude. The gas mass of a clump is calculated by estimating the gas mass within the radius of the cluster embedded in the clump and using equation 2.1. The gas masses of the clumps are given in Table 6.2. The uncertainty associated with the gas mass of the clusters is around 38% (for details, see Chapter 2). The gas mass surface density, number density, and free-fall time of the clumps are estimated by using the equations discussed in Section 2.2.2.1 of Chapter 2. All the physical parameters of the clumps are listed in Table 6.2. We want to point out that for some regions (e.g. IRAS 05480+2545) in which the PPMAP shows saturation at high-density regions, the Hi-GAL column density maps from Schisano et al. (2020) were used.

Table 6.2: Clump physical properties.

No	Name	$r_{\rm eff}$ (pc)	$M_{\rm gas}$ ($M_\odot$)	$\Sigma_{\rm gas}$ ($M_\odot$ pc^{-2})	n_{H_2} (cm^{-3})	$t_{\rm ff}$ (Myr)
1	IRAS 06063+2040	0.97	460	155	1732	0.74
2	IRAS 06055+2039	0.79	810	410	5628	0.41
3	IRAS 06068+2030	0.87	300	126	1564	0.78
4	IRAS 22134+5834	0.48	120	167	3796	0.50
5	IRAS 06056+2131	0.58	520	485	9032	0.32
6	Sh2-255	1.00	1400	398	4151	0.48
7	[IBP2002] CC14	0.57	210	206	3914	0.49
8	IRAS 06058+2138	0.70	750	487	7573	0.35
9	IRAS 06065+2124	0.64	150	114	1954	0.70
10	NGC 2282	0.84	170	77	996	0.98
11	IRAS 05490+2658	1.02	930	284	3036	0.56
12	BFS 56	0.98	640	215	2400	0.63
13	[BDS2003] 89	0.41	68	129	3422	0.53
14	Sh2-88	0.52	550	653	13663	0.26
15	IRAS 06104+1524	0.46	170	258	6095	0.39
16	IRAS 06117+1901	1.02	260	80	856	1.0
17	IRAS 05480+2545	0.81	1100	551	7432	0.36

6.4.6 Cluster mass, star formation rate, and efficiency

As discussed in the last section, we determined the age of individual clusters using their K-band luminosity functions. The theoretical mass-luminosity (dM_*/dm_K) relation corresponding to the determined age of a cluster can be matched with its field-subtracted KLF (K-band magnitude distribution), to obtain the stellar mass distribution of the cluster. Then, the total stellar mass of the cluster can be estimated by integrating its mass distribution function (details are given in Chapter 5) within certain mass limits. We used the mass-luminosity relations from the MIST stellar evolutionary models of solar metallicity (Choi et al., 2016), and used Rieke & Lebofsky (1985) extinction laws to convert the model absolute K-band magnitudes to apparent magnitudes. Then, we fitted the mass distribution of clusters with the following logarithmic form as discussed in Chapter 5.

$$\frac{d\log N(\log M)}{d\log M} \propto M^{-\alpha}. \tag{6.3}$$

The data was fit within the mass limit of 0.4 $M_{\odot}$ to 5−7 $M_{\odot}$, as applicable for each cluster. The α values of all the clusters are found to be within 3σ error of the canonical value of α, i.e. −1.3 (Kroupa, 2001) for the mass range of 0.4 $M_{\odot}$ < M < 10 $M_{\odot}$. The α value of −1.3 corresponds to the Kroupa index, Γ = 2.3 in the linear form of Kroupa IMF (Kroupa, 2001). For example, the mass distribution plot for IRAS 06063 + 2040 is shown in Figure 6.5, which is fitted with a power-law of best-fit index, $\alpha \sim -1.11 \pm 0.18$. The large uncertainties in the best-fit index values are because of low statistics of member stars in clusters. Since the best-fitted IMF slopes are within the uncertainty of the Kroupa slope, so, we used the Kroupa broken power-law to calculate the total stellar mass of all the clusters (for details, see discussion in Chapter 5). Briefly, we integrated the IMFs of the clusters with the Kroupa Γ index of − 2.3 in the linear form within the mass limits of 0.5 to 15 $M_{\odot}$ and extrapolated down to 0.1 $M_{\odot}$ using Γ = − 1.3 for the mass limits of 0.5 to 0.1 $M_{\odot}$. The stellar masses of the clusters are given in Table 6.3. We have also estimated the stellar mass by integrating the IMF directly up to the lower mass limit of 0.1−0.2 $M_{\odot}$ (without extrapolating) for those clusters that have data complete down to these limits. By doing so, we found that the total stellar mass in both the approaches only differs by 5−10%.

From $M_{\rm gas}$, M_*, and $t_{\rm clust}$, the star formation rate and efficiency of the clusters can be estimated, as discussed in Chapter 5. The SFR varies from clump to clump depending upon the stellar mass and age of the cluster within them, and the value lies in the range of 29 to 500 $M_{\odot}$ Myr^{-1} with a median around 107 $M_{\odot}$ Myr^{-1}. The SFEs of the clusters range from 0.07 to 0.62, with a mean and median around 0.27 and 0.22, respectively. However, for clusters in the sample with ages less than 2 Myr, the mean SFE turns out to be around 0.23. The spread in the SFEs may be because of the different evolutionary stages of the clusters. The SFE of a

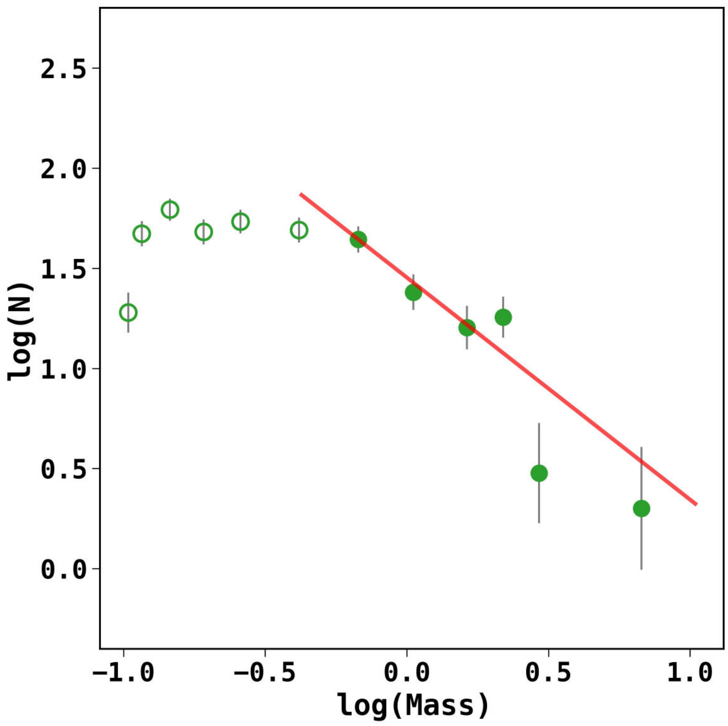

Figure 6.5: The cluster mass distribution function of IRAS 06063 + 2040 in which the error bars represent the $\pm\sqrt{N}$ errors. The solid circles show the data points used for the least squares fit with a power-law function, and the best-fit index, α, is $\sim -1.11 \pm 0.18$.

region initially rises with time as a result of star formation and then later increases due to the decrease in the cluster's gas mass caused by the conversion of gas into stars and/or the dispersal of gas from feedback mechanisms. Hence, the instantaneous SFE initially underestimates and later overestimates the total fraction of gas converted into stars over the lifetime of a star-forming region (Megeath et al., 2022). Therefore, the instantaneous SFE is only reliable for young star-forming regions, which are at the early stages and have significant gas mass left to form stars. The star formation efficiency per free-fall time, as defined in Section 5.2.2.6 of Chapter 5, is better to compare the star formation efficiencies of the clusters in one free-fall time. The $\epsilon_{\rm ff}$ of the clusters ranges from 0.03 to 0.3, with a mean and median around 0.15 and 0.13, respectively. The variation of SFE and $\epsilon_{\rm ff}$ of the clusters is shown in Figure 6.6 with their $\Sigma_{\rm gas}$. Sh2-255 cluster has the maximum SFR (i.e. $\sim$500 $M_\odot$ Myr^{-1}), while IRAS 06065+2124 has the minimum SFR (i.e. $\sim$29 $M_\odot$ Myr^{-1}).

Table 6.3: Cluster properties.

No	Name	A_V (mag)	t_{clust} (Myr)	M_* ($M_\odot$)	Σ_{gas} ($M_\odot$ pc^{-2})	SFE	SFR ($M_\odot$ Myr^{-1})	Σ_{SFR} ($M_\odot$ Myr^{-1} pc^{-2})	Σ_{gas}/t_{ff} ($M_\odot$ Myr^{-1} pc^{-2})
1	IRAS 06063+2040	6.0	0.75	223	155	0.33	297	101	210
2	IRAS 06055+2039	8.6	0.5	134	410	0.14	268	137	1000
3	IRAS 06068+2030	5.1	0.5	83	126	0.22	166	70	162
4	IRAS 22134+5834	7.5	1.5	125	167	0.51	83	115	334
5	IRAS 06056+2131	8.5	0.5	126	485	0.20	252	238	1497
6	Sh2-255	10	1.0	500	398	0.26	500	159	833
7	[IBP2002] CC14	6.6	0.75	47	206	0.18	63	61	418
8	IRAS 06058+2138	10.1	0.5	132	487	0.15	264	172	1376
9	IRAS 06065+2124	5.0	1.5	43	113	0.22	29	22	160
10	NGC 2282	2.3	2.0	89	77	0.34	44	20	79
11	IRAS 05490+2658	10.7	0.5	220	284	0.19	440	135	508
12	BFS 56	8.4	0.75	80	213	0.11	107	35	336
13	[BDS2003] 89	6.8	3.0	110	128	0.62	37	69	242
14	Sh2-88	8.5	0.5	185	653	0.25	370	436	2479
15	IRAS 06104+1524	7.3	1.0	83	258	0.33	83	125	654
16	IRAS 06117+1901	3.1	4.5	270	80	0.51	60	18	76
17	IRAS 05480+2545	6.4	0.75	79	551	0.07	105	51	1542

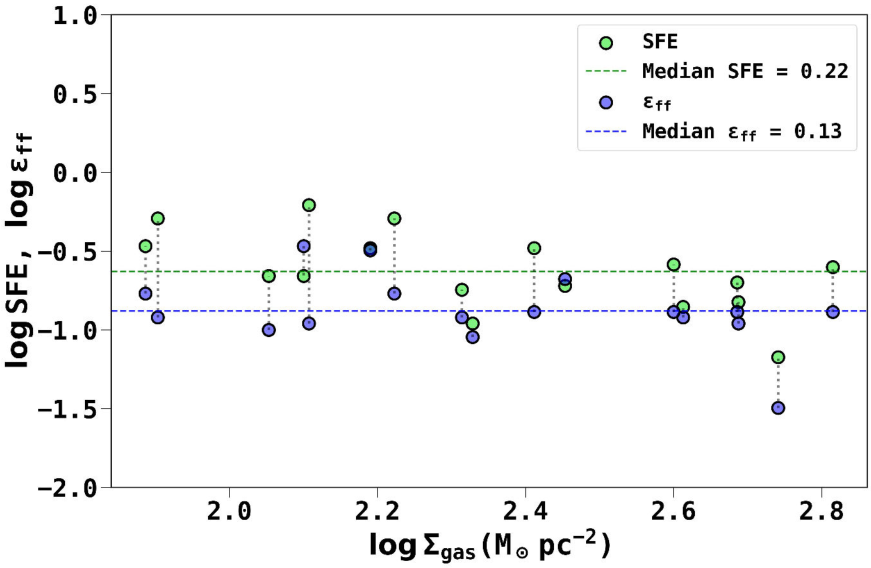

Figure 6.6: The SFE and $\epsilon_{\rm ff}$ of the clusters plotted with their gas mass surface densities.

6.4.7 Scaling laws at clump scale

The observational studies show that the number of young stars is correlated with the gas density, which means that most of the YSOs form in the higher-density structures of the cloud (Heiderman et al., 2010; Lada et al., 2012; Lada et al., 2013; Evans et al., 2014). However, once the feedback effect from massive stars becomes dominant, it disperses the natal gas material. In order to inspect that, we determined $\Sigma_{\rm SFR}$ and $\Sigma_{\rm gas}$ by dividing the SFR and gas mass from the projected area ($A_{\rm clust} = \pi r_{\rm eff}^2$) of the clumps on the plane of the sky. The $\Sigma_{\rm SFR}$ and $\Sigma_{\rm gas}$ values are given in Table 6.3. The mean and median $\Sigma_{\rm SFR}$ of the clusters in our sample are ∼116 and ∼101 $M_\odot$ Myr^{-1} pc^{-2}, respectively, while the mean and median $\Sigma_{\rm gas}$ are ∼282 and ∼213 $M_\odot$ pc^{-2}, respectively. To see the variation of SFR with gas mass, the variation of $\Sigma_{\rm SFR}$ with $\Sigma_{\rm gas}$ is plotted in Figure 6.7, which shows a positive correlation. The Pearson correlation coefficient in the log-log scale is around 0.78. Baring the outlier, IRAS 05480+2545 (yellow dot in Figure 6.7), we find that the Pearson correlation coefficient comes around 0.89. As discussed earlier, scaling laws follow a power-law relation ($\Sigma_{\rm SFR} = A\Sigma_{\rm gas}^N$), which in the logarithmic form can be expressed as

$$\log \Sigma_{\rm SFR} = \log A + N \log \Sigma_{\rm gas}. \tag{6.4}$$

To consider the errors in both axes, we adopted the Orthogonal Distance Regression (ODR) method (Boggs et al., 1988) to fit the data points. With ODR, the best-fit N and $\log A$ values were found to be ~1.60 ± 0.29 and − 1.83 ± 0.65, respectively.

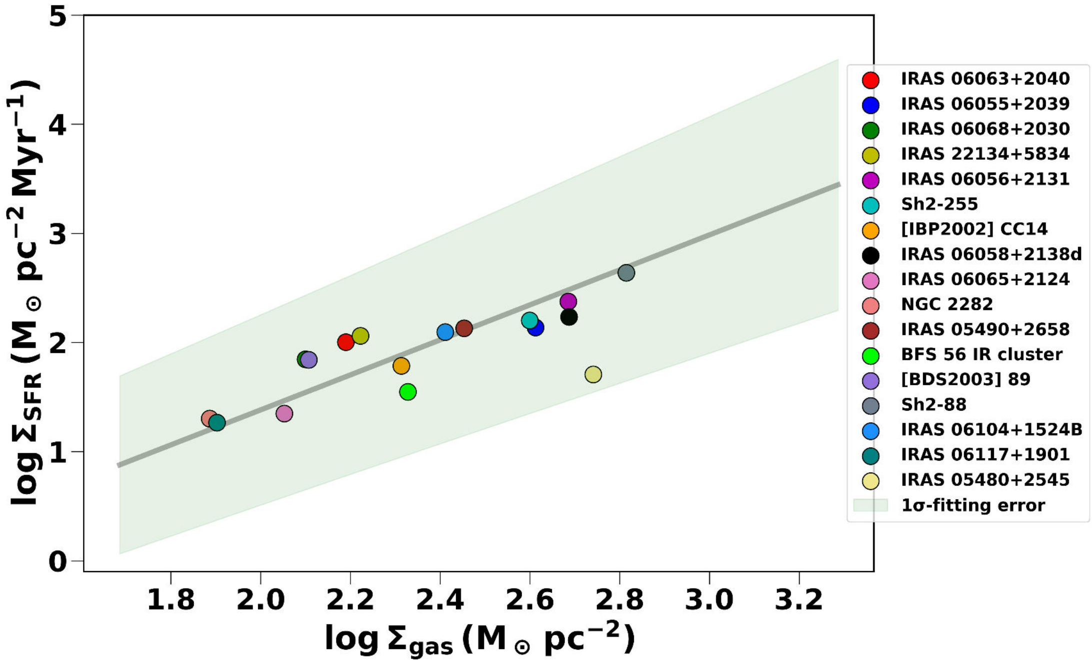

Figure 6.7: Variation of $\log \Sigma_{\rm SFR}$ with $\log \Sigma_{\rm gas}$. The black line shows the ODR fit along with 1σ uncertainty shown as green shaded region.

The theoretical models (Krumholz & McKee, 2005; Krumholz et al., 2019) predict the dependence of star formation rate on the free-fall time of the clouds, which has also been found observationally that the inclusion of free-fall time reduces the scatter in the SFR−gas mass relation (Krumholz et al., 2012; Pokhrel et al., 2021). This relation is known as the volumetric star formation relation and is defined as

$$\log \Sigma_{\rm SFR} = \log A' + N' \log \Sigma_{\rm gas}/t_{\rm ff}, \tag{6.5}$$

where $t_{\rm ff}$ depends only on the volume density of the region. We also explored the volumetric star formation relation for the sample of clumps studied in this work. The $\Sigma_{\rm gas}/t_{\rm ff}$ of the clusters lies in the range of ~76 to 2480 $M_\odot$ Myr^{-1} pc^{-2} with a mean and median around 700 and 418 $M_\odot$ Myr^{-1} pc^{-2}, respectively. Figure 6.8 shows the $\Sigma_{\rm SFR}$ vs $\Sigma_{\rm gas}/t_{\rm ff}$ plot, which shows a relatively less scatter in comparison to $\Sigma_{\rm SFR}$ vs $\Sigma_{\rm gas}$ plot and a positive correlation with Pearson's coefficient of ∼0.81. Again, baring IRAS 05480+2545 cluster in the plot, we find that Pearson's correlation coefficient changes to ∼0.90. We fitted the relation with equation 6.5 using the ODR method and found the best-fit values of N' and $\log A'$ to be ∼1.00 ± 0.16 and − 0.66 ± 0.39, respectively. The index value obtained here for clumps matches well with the mean and median index value of Pokhrel et al. (2021) (i.e. ∼0.94 and ∼0.99, respectively) for volumetric star formation relation at the cloud scale, as they have also used the ODR method for fitting.

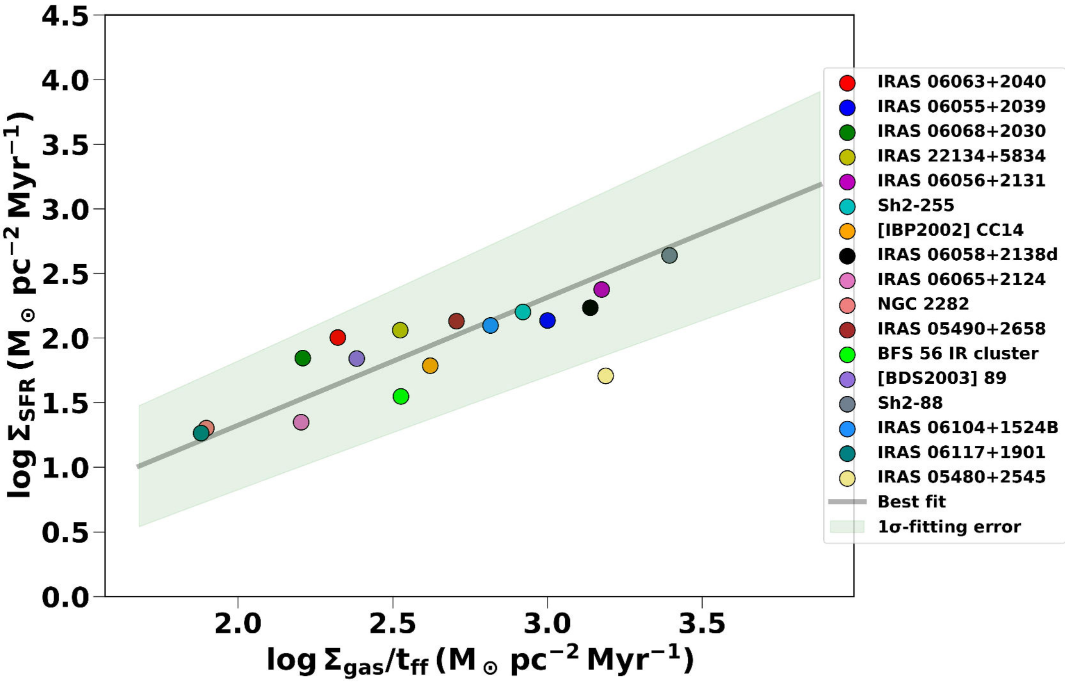

Figure 6.8: Variation of $\log \Sigma_{\rm SFR}$ with $\log \Sigma_{\rm gas}/t_{\rm ff}$. The black line shows the ODR fit along with 1σ uncertainty shown as green shaded region.

6.5 Discussion

6.5.1 Comparison with existing star formation scaling laws

As already discussed, there are previous studies to investigate the scaling laws at cloud scale or within single clouds (Evans et al., 2009; Lada et al., 2010; Heiderman et al., 2010; Gutermuth et al., 2011; Krumholz et al., 2012; Evans et al., 2014; Pokhrel et al., 2021). These studies are done over the nearby clouds (< 1 kpc) and are based on the star count method to determine the SFR. The aforementioned studies tested scaling relations in various forms and found different power-law indexes, which, up to some extent, can be attributed to the differences in methodology, like data resolution, SFR tracers, fitting methods, gas tracers, and completeness of the YSO sample. Moreover, some of the studies found that there is relatively large scatteredness and loose correlation in the SFR−gas mass relation between clouds in comparison to within single clouds (e.g. Lada et al., 2013; Evans et al., 2014).

In Figure 6.9, a comparison of the results of this work with the existing scaling laws at the extragalactic and cloud/clump scale are shown. From the figure, it can be seen that although the index value obtained here (∼1.6) is similar to the KS power law index (∼1.4; Kennicutt, 1998b), the data points from our sample lie much above the KS relation. Similarly, data points of this work also show much higher $\Sigma_{\rm SFR}$ values than predicted by the linear $\Sigma_{\rm SFR} - \Sigma_{\rm gas}$ relation of Bigiel et al. (2008), which is shown by a solid blue line and extrapolated by a blue dotted line towards higher gas densities in the plot. The higher trend of scaling relations than the extragalactic ones has also been found at the cloud scale by other observational studies (Evans et al., 2009; Lada et al., 2010; Heiderman et al., 2010).

In comparison to nearby clouds from c2d and GB survey (Evans et al., 2009; Heiderman et al., 2010; Evans et al., 2014) and from Lada et al. (2010), our sample of cluster forming clumps lies above in the $\Sigma_{\rm SFR} - \Sigma_{\rm gas}$ plot (see Figure 6.9). Heiderman et al. (2010) also examined the scaling relation for the youngest YSOs (e.g. Class I) and found that their $\Sigma_{\rm SFR}$ is higher than the values obtained by including all the YSOs in the clouds, which is also shown in Figure 6.9. From the figure, it can be seen that though the Class I YSO sample of Heiderman et al. (2010) is closest to our sample, but still the clumps within our sample exhibit higher values of $\Sigma_{\rm SFR}$ compared to their Class I YSO sample. Recently, Pokhrel et al. (2021) studied 12 nearby molecular clouds and obtained the $\Sigma_{\rm SFR} - \Sigma_{\rm gas}$ relation within individual clouds, with a mean and median power-law index of ∼2.00 and ∼2.08, respectively, and a spread of ∼0.3 in $\Sigma_{\rm SFR}$ at logarithmic scale. The obtained power law index in this work is shallower, but still consistent within 2σ uncertainty. However, as can be seen from Figure 6.9, our cluster sample lies above the Pokhrel et al. (2021) scaling relation. Taking a mean $\Sigma_{\rm gas}$ of the clumps to be ∼282 $\rm M_\odot\ pc^{-2}$, the predicted value of $\Sigma_{\rm SFR}$ from the scaling relation of Pokhrel et al. (2020, 2021) comes around 6.2 $\rm M_\odot\ pc^{-2}\ Myr^{-1}$, which is around 20 times lower than the corresponding value from the obtained scaling relation in this work.

At the clump scale, Heiderman et al. (2010) investigated the SFR−gas mass relation in massive dense clumps from Wu et al. (2010) that are traced by HCN(1−0) molecular line data. The authors calculated the gas mass from HCN and SFR from infrared luminosities (8−1000 μm) and obtained a linear dependence of $\Sigma_{\rm SFR}$ on $\Sigma_{\rm HCN}$, which is also shown in Figure 6.9. From the figure, it can be seen that our cluster sample lies above their relation by a factor of ~25. The massive clumps from the study of Heyer et al. (2016) are also shown in the figure, and it can be seen that few of them lie close to our cluster sample. Heyer et al. (2016) studied star formation scaling laws in massive clumps of the Milky Way by selecting the clumps from APEX Telescope Large Area Survey of the Galaxy (ATLASGAL) data and linking them to the YSOs from the catalogue of *Spitzer* 24 μm MIPSGAL survey. The authors calculated the total gas mass from the 870 μm flux and evaluated the total stellar mass by sampling the IMF. However, due to the low sensitivity of the MIPSGAL 24 μm data, the mass sensitivity limit of the Heyer et al. (2016)'s YSO sample is only down to 2 $M_\odot$. In most of the clumps, they detected only one or a few protostars in 24 μm, which might have added uncertainty in estimating the total stellar mass of the clumps in their study. The UKIDSS data that has been used in this work is deep down up to 0.5 $M_\odot$ limit, and for most of the clusters, data is sensitive down to 0.1−0.2 $M_\odot$ limit. However, it is to be noted that the sample in Heyer et al. (2016) represents very early stages of cluster-forming clumps, whereas the cluster sample studied in this work is relatively more evolved, with a cluster visibly emerging from the clump in NIR.

The $\Sigma_{\rm SFR} - \Sigma_{\rm gas}$ relation for our cluster-forming clumps shows better correlation and less scatteredness in comparison to those found in some of the earlier studies at cloud/clump scale (Heiderman et al., 2010; Lada et al., 2013; Evans et al., 2014; Vutisalchavakul et al., 2016; Heyer et al., 2016; Retes-Romero et al., 2017). Nevertheless, this scatteredness in our sample of clusters can be attributed to the different evolutionary stages of the clusters. The clusters which are at the initial stages of star formation are gas-rich, while the relatively older clusters tend to deplete gas due to ongoing star formation and associated feedback, as also highlighted by Megeath et al. (2022).

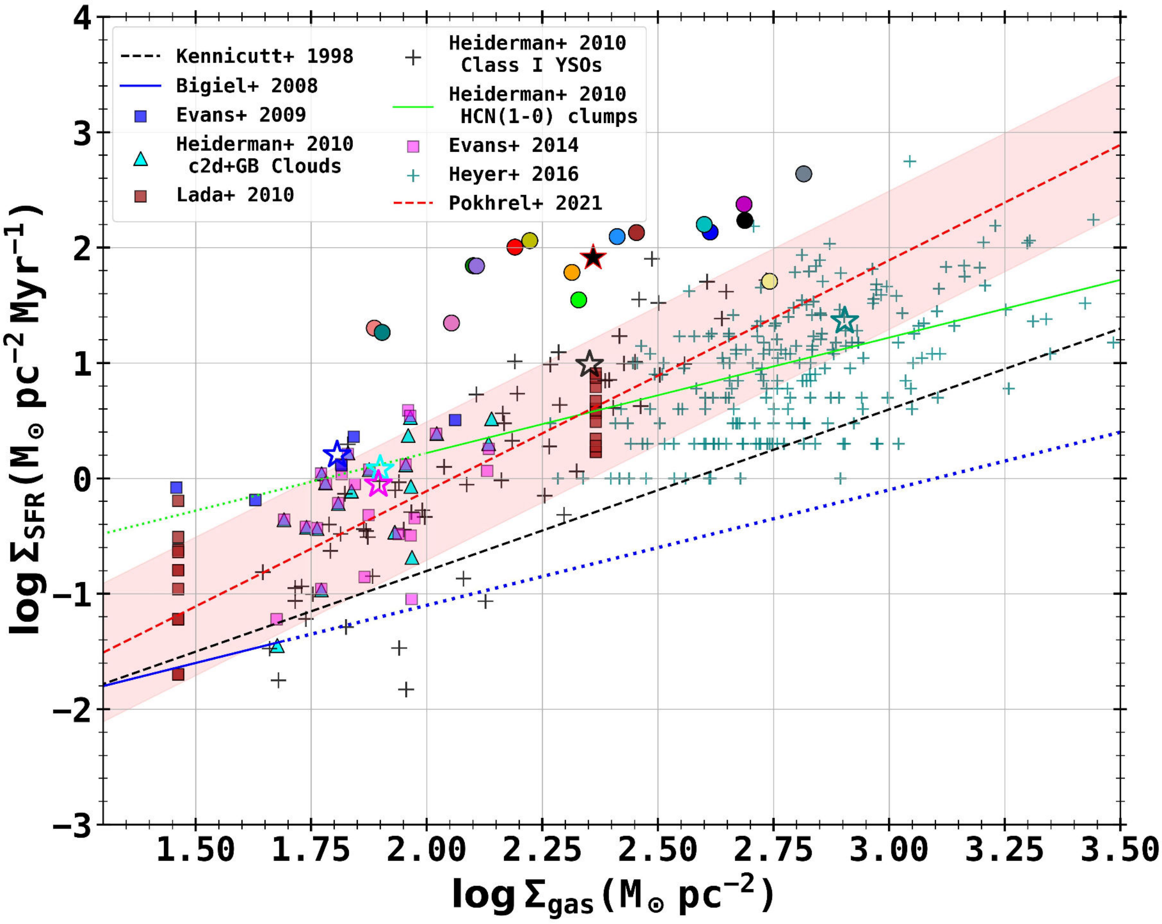

Figure 6.9: Comparison of $\Sigma_{SFR} - \Sigma_{gas}$ relation obtained in this work with the existing relations in the literature. The solid coloured dots denote the clusters in our sample, as shown in Figure 6.7. The galactic scale relations of Kennicutt (1998b) and Bigiel et al. (2008) are shown by black dashed and blue solid lines, respectively. The Bigiel et al. (2008)'s relation is extrapolated by a blue dotted line towards higher surface density. The nearby clouds from Evans et al. (2009) (blue squares), Heiderman et al. (2010) (cyan triangles), Lada et al. (2010) (brown squares), and Evans et al. (2014) (pink squares) are shown. The black pluses show the $\Sigma_{SFR} - \Sigma_{gas}$ values obtained for only Class I YSOs in the nearby clouds by Heiderman et al. (2010). The green solid line shows the relation obtained for HCN(1−0) massive dense clumps by Heiderman et al. (2010), which is extrapolated by a green dotted line towards lower gas mass surface density. The teal pluses show the massive clumps from Heyer et al. (2016). The red dashed line shows the $\Sigma_{SFR} - \Sigma_{gas}$ relation obtained by Pokhrel et al. (2021) with a spread shown as a red shaded area (see text for details). The mean $\Sigma_{SFR} - \Sigma_{gas}$ in our sample is shown by a black solid star, and for other samples, the mean values are shown by open stars of same colours as of their corresponding sample.

Figure 6.10 shows the comparison of the volumetric star formation relation obtained for cluster sample in this work with those observed in some of the previous studies at the cloud scale. Similar to $\Sigma_{SFR} - \Sigma_{gas}$ plot, it is clearly evident from $\Sigma_{SFR} - \Sigma_{gas}/t_{ff}$ plot that our cluster sample lies above the nearby clouds of previous studies (Heiderman et al., 2010; Lada et al., 2010; Evans et al., 2014), and also show less scatteredness and better correlation. Krumholz et al. (2012) observed a linear relation between Σ_{SFR} and Σ_{gas}/t_{ff} along with a free-fall efficiency of 0.01, which they suggested would be roughly constant with a dispersion of ~0.3 dex. The value of $\epsilon_{ff} \approx 0.01$ is also derived theoretically by Krumholz & McKee (2005) for any supersonically turbulent medium. For nearby clouds, Pokhrel et al. (2021) found a nearly constant ϵ_{ff} of ~0.026, and did not find any threshold density above which the ϵ_{ff} rises significantly. Figure 6.10 shows that although the best-fit slope (~1.00) found here is fairly matching the linear relation of Krumholz et al. (2012) (shown by a solid black line), the ϵ_{ff} for our cluster sample is higher than their obtained value of 0.01. By fixing the slope of $\Sigma_{SFR} - \Sigma_{gas}/t_{ff}$ relation for our cluster sample to unity, the best-fit ϵ_{ff} value from the ODR regression fit comes around 0.20 (shown by a dashed black line in Figure 6.10), which is 20 times higher than the theoretical ϵ_{ff} value of ~0.01 (Krumholz & McKee, 2005). Pokhrel et al. (2021) in their study of nearby clouds also tested the volumetric star formation relation for individual clouds, and found best-fit slopes close to unity for each cloud, with a mean around 0.94 and a spread of 0.21 in log Σ_{SFR}. The relation of Pokhrel et al. (2021) is also shown in Figure 6.10 by a dashed red line. The obtained slope of the volumetric star formation relation for the cluster sample of this work is almost the same as their value; however, it is apparent from the figure that the trend line for our cluster sample lies above that of Pokhrel et al. (2021)'s relation by a factor of ~9.

Overall, it is apparent that our cluster sample shows significantly higher star formation rate surface densities than most of those found by previous studies (see Figure 6.9 and 6.10). Although the power law index in $\Sigma_{SFR} - \Sigma_{gas}$ relation for our cluster sample is somewhat comparable with the previous studies within the uncertainty, especially in volumetric star formation relation, but the surface density values of SFR and gas mass are noticeably higher. These high values of Σ_{SFR} and Σ_{gas} for our cluster sample can be explained by the following reasons: (i) the regions studied in this work are relatively much smaller and younger than those at extragalactic scales (Kennicutt, 1998b; Bigiel et al., 2008), (ii) our sample consists of cluster forming regions, i.e. active star-forming regions, however, at extragalactic and cloud scales, those regions are also included that are quiescent but have gas mass (atomic and molecular). As a consequence, regions

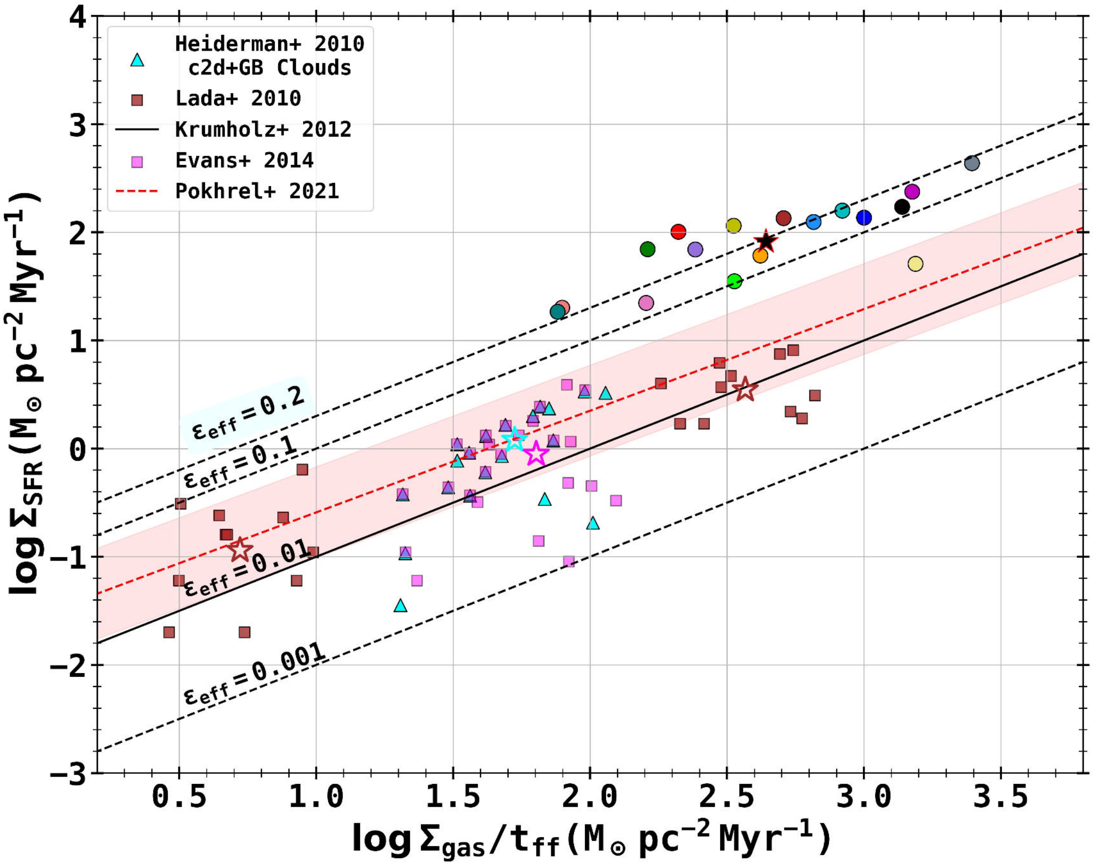

Figure 6.10: Comparison of $\log \Sigma_{SFR}$ with $\log \Sigma_{gas}/t_{ff}$. The colored symbols, red dashed line and red shaded region, are the same as in Figure 6.9. The black solid line shows the relation of Krumholz et al. (2012) and denotes the ϵ_{ff} of 0.01, and the black dashed lines show the ϵ_{ff} of 0.001, 0.1, and 0.2.

in our sample have higher SRFs within smaller plane-of-sky projected surface areas, hence larger Σ_{SFR}. A less scatteredness and better correlation in the SFR−gas mass relation found here can be explained by the adopted methodology to calculate the total stellar mass and age of the cluster. In some of the previous studies, a single average mass and age for all stars were adopted (Evans et al., 2009; Lada et al., 2010; Heiderman et al., 2010; Evans et al., 2014). In this work, to get the total stellar mass, we sampled the initial mass function down to the low mass limit of ~0.1 $M_\odot$ and calculated the age of the cluster as a whole by comparing it with synthetic clusters of different ages. Apart from that, in our cluster sample, except NGC 2282 and IRAS 06117+1901, all other clusters have gas mass surface densities greater than 110 $M_\odot$ pc^{-2}. A density threshold of ~110−130 $M_\odot$ pc^{-2} (or $7A_V$−$8A_V$) has been suggested in the literature above which the SFR varies linearly with the mass of dense gas and is better correlated than with the total mass (Lada et al., 2010; Heiderman et al., 2010; Evans et al., 2014). In fact, 13 out of 17 clusters in our sample have gas surface mass densities $\gtrsim$ 130 $M_\odot$ pc^{-2}, which could also be a reason for a better correlation of SFR with gas mass in the present work. However, as also discussed in Section 1.5.3.1, some other studies did not find any density threshold for star formation and explained the observational threshold density just as a mere consequence of increasing gravitational influence with increasing density (Gutermuth et al., 2011; Burkhart et al., 2013; Sokolov et al., 2019). Here, it is important to point out that Evans et al. (2014) clearly mentioned that threshold density, as indicated by Heiderman et al. (2010) and Lada et al. (2012), is just a limit above which SFR becomes linear and better correlated to gas mass density, it is not a limit for star formation to occur. The authors also suggested that a particular threshold applicable to nearby clouds may not necessarily apply in other regions, like in extreme conditions of the central molecular zone (for details, see Longmore et al., 2013) or low metallicity regions.

Figure 6.11 shows the plot of SFE with gas mass surface density of clouds, clumps, and cores. The mean SFE at the cloud scale is taken from the studies of nearby clouds (Evans et al., 2009; Heiderman et al., 2010; Lada et al., 2010; Evans et al., 2014), which are based on the star count method. The SFE at the molecular cloud scale is around 2.8 ± 1.0%. At the clump scale, the mean and median SFE are around 27% and 22%, respectively, as obtained in this work from a sample of 17 clumps active in star or star cluster formation. While the median standard deviation is around 8%. At the core scale, the SFEs are indirectly anticipated from the similarity between the shape of the dense core mass function and the stellar initial mass function (Alves et al., 2007; Könyves et al., 2010, 2015). Based on these studies, there is a one-to-one correlation between core and stellar masses, and the core-to-star formation efficiency is around 30 ± 10%.

6.5.2 Implication on cluster formation

In Chapter 1, we discussed the possible scenarios to form an intermediate-to-massive stellar cluster, i.e. either a high-gas mass reservoir with high SFE is needed, or a continuous supply of matter along with the merger of small subclusters or a combination of both (Longmore et al., 2014; Banerjee & Kroupa, 2015; Vázquez-Semadeni et al., 2019; Krumholz et al., 2019). Recently Guszejnov et al. (2022), simulated a molecular cloud of mass $\sim 2 \times 10^4$ $M_\odot$ and surface density $\sim$60 $M_\odot$ pc^{-2} and investigated its evolution over time by considering different physical factors

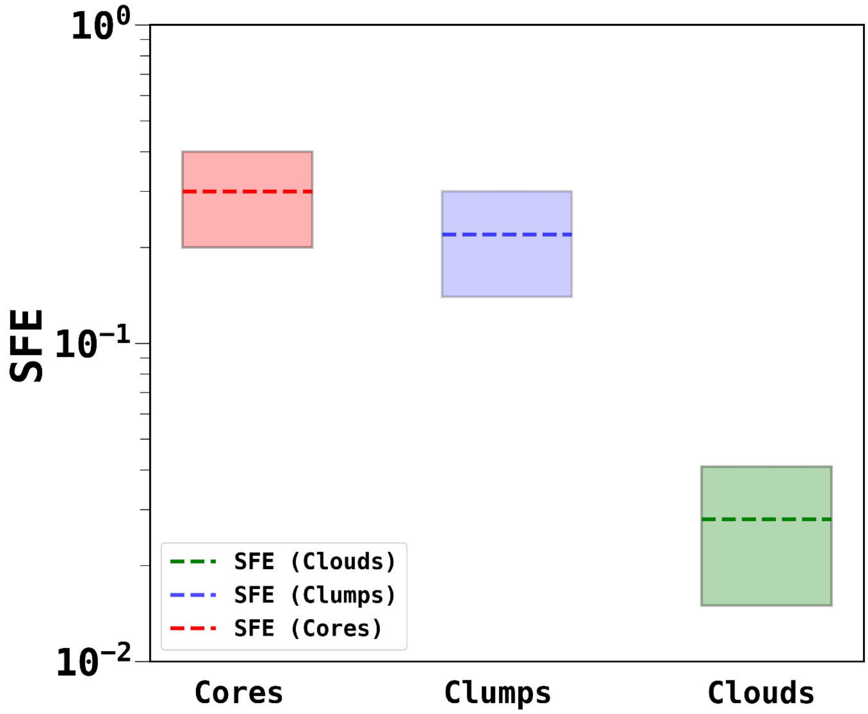

Figure 6.11: The star formation efficiencies at cloud, clump, and core scale. The red line shows the SFE of 30 ± 10% at the core scale (Alves et al., 2007; Könyves et al., 2010, 2015), the blue line shows the SFE of 22 ± 8% at the clump scale found in this work, and the green line shows the SFE of 2.8 ± 1.3% at the cloud scale (Evans et al., 2009; Heiderman et al., 2010; Lada et al., 2010; Evans et al., 2014). The corresponding colored shaded regions show the upper and lower limits of SFE at the respective scales.

like gas pressure, magnetic field, turbulence, and stellar feedback. The authors found that the cloud is able to form a cluster of mass $\sim 1.4 \times 10^3$ $M_\odot$ with an efficiency of around 7% in 4 Myr of time through the hierarchical assembly of gas, stars, and sub-clusters. Around 6 Myr, the feedback starts to affect the cloud significantly and disrupt the cloud in 8 Myr (Guszejnov et al., 2022). On the other hand, Polak et al. (2023) in their simulations found that a molecular cloud of mass $\geq 10^5$ $M_\odot$ and surface density ≥ 100 $M_\odot$ pc^{-2} can form a bound cluster of mass $\sim 10^4$ $M_\odot$ with an efficiency of around 65% in just one free-fall time. Also, the authors found that even a lower mass cloud is able to form a bound cluster but with a bound mass fraction of ~60%.

For the studied cluster-forming clumps, the SFE is found to be somewhat less than 0.3. As discussed above, most simulations suggest a high SFE (≥ 30%) is necessary to form a bound stellar cluster (Hills, 1980; Bastian & Goodwin, 2006; Goodman et al., 2009; Longmore et al., 2014; Krumholz et al., 2019). Thus, if these simulations are to be believed, the low efficiency found in the studied clumps suggests that the clusters within these clumps will likely become gravitationally unbound after a few million years of evolution, as most clusters are situated in isolated clumps. This could be the possible region of the "infant mortality" inferred from the statistics of embedded to open clusters (Lada & Lada, 2003), where a high fraction of young clusters/protoclusters dissolve in the Galactic field, and only a few per cent remain as bound clusters for a longer period.

6.6 Summary

This chapter presents the work done to test the star formation rate and gas mass relation at the clump scale by studying the gas and stellar properties of a sample of cluster-forming clumps. For this work, a sample of 17 clumps was selected that are located at a distance of < 2.5 kpc. The UKIDSS NIR photometric data and *Herschel* dust continuum-based column density maps were used to derive various properties of the clusters like extinction, age, stellar and gas mass, SFR, and SFE. The mean SFR and SFE in our sample are $\sim$187 $M_\odot$ Myr^{-1} and $\sim$0.27, respectively. The mean and median Σ_{gas} of the clumps are $\sim$282 $M_\odot$ pc^{-2} and $\sim$215 $M_\odot$ pc^{-2}, respectively.

It is found that Σ_{SFR} varies with Σ_{gas} as $\Sigma_{SFR} \propto \Sigma_{gas}^{(1.60\pm0.29)}$ in the studied sample of cluster-forming clumps, and both quantities are well correlated. The $\Sigma_{SFR} - \Sigma_{gas}$ relation in this work lies well above most of the previously obtained relations at extragalactic, cloud, and clump scales, which might be due to the fact that we have studied the scaling relation at the smaller scale, i.e. clumps that have high surface densities and chosen only the active star-forming clumps. The volumetric star formation relation is found to be of the form $\Sigma_{SFR} \propto (\Sigma_{gas}/t_{ff})^{(1.00\pm0.16)}$, which is well correlated and also lies above the previously obtained relations at the cloud scale. The mean ϵ_{ff} of clumps found in this work is around 15%, and with the slope fixed to unity ($\Sigma_{SFR} \propto \Sigma_{gas}/t_{ff}{}^{1.0}$), ϵ_{ff} is found to be $\sim$20%, which is significantly higher than the constant free-fall efficiency reported for nearby molecular clouds (Krumholz & McKee, 2005; Krumholz et al., 2012). Most of the clumps in our sample have $\Sigma_{gas} \gtrsim 110$ $M_\odot$ pc^{-2}, and the SFR−gas mass relations show a good correlation and less scatteredness, which favours the conclusions of Lada et al. (2010), Heiderman et al. (2010), and Evans et al. (2014), that the SFR−gas mass relations become better correlated above a certain threshold density. However, to conclusively comment on that, a larger sample needs to be studied, including more clumps at lower gas surface densities and using data of similar sensitivity.

Overall, from the results of this work, it seems that there is no universal relation between star formation rate and gas mass that can explain the star formation process from large scale, i.e. galaxies and GMCs, to small scale, i.e. clouds and clumps. It suggests that star formation is mostly affected and regulated by the local environment and properties of the gas in the localized regions rather than some global galactic scale process.

This page was intentionally left blank.

Chapter 7

Summary, conclusion, and future prospects

The star clusters serve as vast astrophysical laboratories to study the early stages of star formation, stellar evolution, and their impact on the parental cloud. However, the formation process of bound stellar clusters and the role of different physical factors in that process is still not well understood. Especially the young massive stellar clusters, which are rare in the Milky Way despite having several massive molecular clouds. Simulations and models suggest two broad mechanisms for intermediate-to-massive cluster formation, *monolithic collapse* and *conveyor-belt collapse*, along with the hierarchical merger of sub-clusters under the influence of global gravity (Longmore et al., 2014; Banerjee & Kroupa, 2015; Vázquez-Semadeni et al., 2019). Disentangling the aforementioned models of cluster formation and understanding the potential of a cloud in making a bound massive cluster requires detailed characterization and analysis of massive clouds. This analysis should encompass several aspects, including the cloud's boundness, structure, fractalness, role of different physical factors, gas assembly processes, and star formation efficiency and rate over all scales, as well as the interlink between these factors at different scales.

The aim of this thesis was to find observational evidence of massive cluster formation scenarios in GMCs and to compare them with the predictions of the aforementioned models.

To do this, the thesis delves into understanding the role of different physical and gas-to-star conversion factors involved in the star and star cluster formation process. The work conducted in this thesis is broadly divided into two parts. In the first part, a detailed case study is done on the massive GMC, G148.24+00.41, to understand its likely cluster formation mechanism and also its potential to form a massive cluster. In the second part, a statistical analysis of a sample of cluster-forming clumps is done in order to estimate the star formation rate and efficiency and examine the star formation scaling laws at the clump scale. These results are then discussed in the context of the emergence of bound clusters in molecular clouds.

The key findings and highlights of the thesis are as follows:

- G148.24+00.41 is a massive and gravitationally bound molecular cloud with an estimated mass of $\sim 10^5$ $M_\odot$, an effective radius of $\sim$26 pc, and a dust temperature of $\sim$14.5 K. The mass of the cloud was calculated using *Herschel* dust continuum based H_2 column density map, dust extinction map, and CO (J = 1−0) isotopologues based H_2 column density maps. The mass of the cloud from all these column density maps is within a factor of 2, which is comparable, keeping the note of uncertainty associated with each tracer. The gas mass surface density is also similar, $\sim$52 $M_\odot$ pc^{-2}, from dust and CO based H_2 column density maps. The dense gas fraction of G148.24+00.41 is around 18 per cent, which is comparable to Orion-A and higher than all other molecular clouds. Considering only the dense gas fraction (concentrated over an effective radius of $\sim$6 pc), the cloud has the potential to form a $\sim$1000−2000 $M_\odot$ cluster in 1−2 Myrs of time according to the SFR−dense gas relation. Including the overall census of YSOs from *Herschel* point source and SFOG catalogues, the cloud is presently capable of making a 2000−3000 $M_\odot$ cluster.

- The protostellar distribution over the whole G148.24+00.41 cloud indicates that the clustering structure of the protostars is fractal and also shows the signature of mass segregation, with a degree of mass segregation, $\Lambda_{MSR} \approx 3.2$. The gas mass surface density profile of the central compact structure of the cloud is found to be shallower than the stellar density profile of existing young massive clusters (e.g. Arches). Also, the compact and dense structure seen in the centre of the cloud is connected to the extended gas reservoir through filamentary structures. All these evidence suggests that the *monolithic collapse* scenario is not likely possible in G148.24+00.41, instead, the fractal nature of the cloud inferred from the distribution of the protostars and the presence of filamentary features indicates that an intermediate-to-massive star cluster may form in the cloud via *conveyor belt* type model.

- The cloud possesses a hub filamentary system. From CO isotopologues molecular line data, six likely velocity coherent large-scale filamentary structures were identified in the cloud. At the junction of these structures, a massive clump (C1) of mass ~2100 $M_\odot$ is located. Apart from this central massive clump, there are other 6 clumps identified in various intersection points of filaments, mostly in the dense ridge of the cloud. Most of the filaments are gravitationally unstable, especially the ridge in which most of the stars are forming. The filaments in G148.24+00.41 are found to be supplying the matter longitudinally towards the central region of the cloud with a rate of 26 to 264 $M_\odot$ Myr^{-1}. Three filaments are found to be directly connected to the massive clump located at the hub and supplying the matter with a combined accretion rate of ~675 $M_\odot$ Myr^{-1}. This combined accretion rate is comparable to and higher than the filamentary accretion rates of some of the well-known hub-filamentary systems, e.g. Mon R2, Serpens, and Orion. The sonic Mach number of the clumps mostly lies in the range of ~2.6−4.5, which shows that the clumps are supersonic.

  Under the scenario of *conveyor belt* or *GHC* model, the global collapse will be towards the gravitational potential minima, i.e. the central potential. In the present case, it is the location of the hub with a massive clump inside. As found in this work, the inflow of matter towards the clump is high, so under this picture, the G148.24+00.41 cloud may give rise to an intermediate-to-massive stellar cluster through a continuous supply of matter from the filaments towards the centre/hub/protocluster. In fact, in *Spitzer* images, the central region of the cloud is found to be associated with an embedded cluster. After studying the global dust and gas properties of G148.24+00.41, we investigated the central clump/hub region of the cloud in order to study the relative role of magnetic field, gravity, and turbulence in the star and star cluster formation process of the clump.

- The central region (size ~12′) of the cloud was observed from the JCMT SCUBA-2/POL-2 to detect dust polarization signals. However, the observed data shows high sensitivity up to 3 arc min diameter around the central area of the cloud, and then gradually decreases towards the edges of the map. The high-resolution images of JCMT at 850 μm have resolved multiple substructures in the central region/C1 clump of the cloud, namely the

CC, WC, and NES. The CC is the central clump located in the hub region, nearly at the geometric centre of the cloud.

- The overall B-field morphology of the hub region is complex. However, comparing the relative orientations of B-fields, intensity gradients, and local gravity vectors, the three factors are mostly found to be correlated in the CC and WC regions, while the difference in orientations is higher in the NES region. This correlation suggests a possibility that gravity is driving the intensity gradients in the direction of the B-fields, and matter is following the magnetic field lines in the dense regions. The POS magnetic field strengths of CC and NES regions are found to be around 24 and 20 μG, respectively. At present, the magnetic field and total kinetic energies, i.e. thermal plus non-thermal, are found to be not enough to support the central clump against the gravitational collapse. In fact, both the CC and NES regions are found to be magnetically transcritical/supercritical, depending upon the geometric corrections. Therefore, under the effect of gravity, the cluster, which is observed in the near-IR images of *Spitzer* in the central region of G148.24+00.41, would continue to grow in mass. Similar to CC at the hub of G148.24+00.41, gravity has also been found to be dominant in most of the HFSs studied with JCMT. However, a large sample of hub-filamentary clumps of various evolutionary stages (e.g. from pre-stellar clumps to clumps hosting emerging clusters of different ages) would be valuable to study the time evolution of various physical processes that govern star formation and its evolution.

- Finally, the young cluster, FSR 655, found at the hub location of G148.24+00.41, is observed in NIR JHK_s bands through the TANSPEC instrument mounted on the 3.6-m Devasthal Optical Telescope. The mean visual extinction of the cluster is estimated to be ~11 mag, whereas the foreground visual extinction in the direction of the cluster is found to be ~4 mag. The approximate age of the cluster is found to be around 0.5 Myr. The present-day total stellar and gas mass of the FSR 655 cluster is around 180 $M_{\odot}$ and 750 $M_{\odot}$, respectively, which gives the SFE of ~19% and SFR of ~360 $M_{\odot}$ Myr^{-1}. Assuming a constant SFR for a time span of 2 Myr and considering the continuous supply of matter through the filaments towards the central clump, where this cluster is forming, it was found that the cluster has the potential to grow further to become a 1000 $M_{\odot}$ cluster. This is the potential of the most massive clump. In Chapter 3, it was suggested that each individual clump has the potential to form a stellar cluster. Thus, we hypothesize that in G148.24+00.41, the individual clumps might not emerge as massive clusters, but a hierarchical merging of individual smaller clusters may result in the formation of a single massive cluster within the cloud.

- In the second objective of the thesis, the connection between star formation rate and gas mass at the clump scale was examined. Our statistical work on a sample of 17 cluster-forming clumps shows a good correlation between $\Sigma_{\rm SFR} - \Sigma_{\rm gas}$ with a best-fit power-law index of ~1.6. The volumetric scaling law, i.e. the relation between $\Sigma_{\rm SFR} - \Sigma_{\rm gas}/t_{\rm ff}$ shows even a better correlation with a best-fit power-law index of ~1.0. Comparing the $\Sigma_{\rm SFR} - \Sigma_{\rm gas}$ relation obtained in this work with the existing relations at the extragalactic and cloud scales, it was found that though the power-law index value is similar within the uncertainty, the trend line ($\Sigma_{\rm SFR}$ values) is relatively much higher than what has been found from extragalactic and cloud-scale relations for similar gas mass surface density. After normalizing with the free-fall time scale, i.e. the volumetric scaling law suggested by Krumholz et al. (2012), the power-law index is almost the same as found in extragalactic and cloud-scales, but the trend line of $\Sigma_{\rm SFR} - \Sigma_{\rm gas}/t_{\rm ff}$ relation is still higher. Also, the free-fall efficiency, which is generally found to be around 0.01−0.02 in nearby molecular clouds, is found to be much higher, i.e. 0.2 in our sample of cluster-forming clumps. From this work, a median star formation efficiency of ~22% was found at the clump scale. It was found that the scaling laws at the clump scale do not follow the KS relation, which indicates that the star and star cluster formation process is more influenced by the local environment of the region rather than a galactic scale global process.

Overall, based upon the detailed case study done over G148.24+00.41, this thesis work shows that a single massive clump within a massive cloud like G148.24+00.41 may not be able to form a massive cluster *in-situ* or *monolithically*. While a flow-driven mass assembly process, like *conveyor belt* or *global hierarchical collapse*, seems to be a more viable mode for forming a massive cluster in the cloud. The cluster formed in the hub region of G148.24+00.41 can evolve to become a massive cluster through filamentary accretion flows from the extended gas environment and the hierarchical merger of small subclusters. Also, the median SFE found in this work for a sample of 17 cluster-forming clumps is somewhat lower than the expected high SFE required to make a bound stellar cluster in a clump, as suggested by simulations. Thus, the studied clusters might not survive violent gas expulsions to remain bound for a longer time.

7.1 Future work

1. Young clusters formed in molecular clouds evolve and become unbound over time due to tidal disruptions, dynamical interactions, and stellar feedbacks (Krumholz et al., 2019). In the early evolutionary stage, studies suggest that only those clusters will survive the gas expulsions and remain bound that have high SFE (> 30−40%, Hills, 1980; Lada et al., 1984; Goodwin & Bastian, 2006). The dynamical evolution and fate of the cluster can be studied by comparing the kinematics of gas and the motions of young stars in the cluster. The cluster's fate, remaining bound or expanding, depends upon the fact that whether its virial state is still dominated by gas or stellar motions. This can be evaluated by comparing the cluster's velocity dispersion to the dispersion predicted by virial equilibrium, taking into account the gravitational potential energy of both gas and stars. Also, the type of mass segregation, primordial or dynamical, can be analysed by studying the velocity dispersion of young stellar members. In this thesis, we could not study the virial (or boundness) status of the clusters. Investigating the boundness status of clusters of different ages and the effect of feedback on it, is an interesting topic to understand the early cluster evolution.

   In future, I plan to examine the stellar kinematics and dynamics of young clusters to better understand their dynamical status and boundness status. To do so, I plan to use the radial velocity information of young stars using the Apache Point Observatory Galactic Evolution Experiment (APOGEE) spectroscopic data. APOGEE is a near-infrared (H band; 1.51−1.70 μm) and high resolution (~22500) stellar spectroscopic survey within Sloan Digital Sky Survey (SDSS) (Majewski et al., 2017). The instrument has the capability of taking around 300 spectra simultaneously and has observed a number of young clusters in APOGEE and APOGEE2 extension surveys (Blanton et al., 2017). The APOGEE2 data can be used to measure the radial velocity of young stars in clusters in order to compare them with the gas kinematics. Although the GAIA satellite observes in visible bands and thus mostly detects the evolved stars, it can also be used to trace the overall motion of bright stars in the evolved clusters by studying their proper motion data.

2. In this thesis work, we thoroughly studied a GMC from the cloud-to-clump scale. Next, I plan to study the gas kinematics and fragmentation at the clump-to-core scales using high-resolution and high-density tracer data. At these scales, I plan to investigate the initial stages of protostellar formation, core mass function, mass inflow towards individual cores within the clump, and the role of magnetic field and turbulence in the dynamics of clumps/cores. For such studies, I plan to use high-resolution data sets from interferometers, like ALMA, which has large spectral coverage, making it optimum to study gas kinematics and dynamics of both clumps and cores using various molecular line tracers. This will be able to shed light on how individual cores gain mass and grow in the clustered environment of the clump.

3. I also plan to understand the dynamical interaction among the sub-groups/clusters within a cloud to explore the merger scenario of sub-groups/clusters in molecular clouds like G148.24+00.41 with N-body simulations. Simulations show that the smaller sub-groups of stars can also merge together to make a big cluster in just 1 Myr (see Figure 7.1, Sills et al., 2018a). The results of G148.24+00.41 studied in this work can be given as an input to run the simulation, like the gas mass of clumps, young stellar sources, velocity dispersion, fractal distribution, virial parameter, sonic Mach number, and other factors. For this type of simulation, I plan to explore the *AMUSE* (Portegies Zwart et al., 2018), an Astrophysical Multipurpose Software Environment, which is a Python-based environment that consists of a variety of codes, like gravitational dynamics and hydrodynamical modelling.

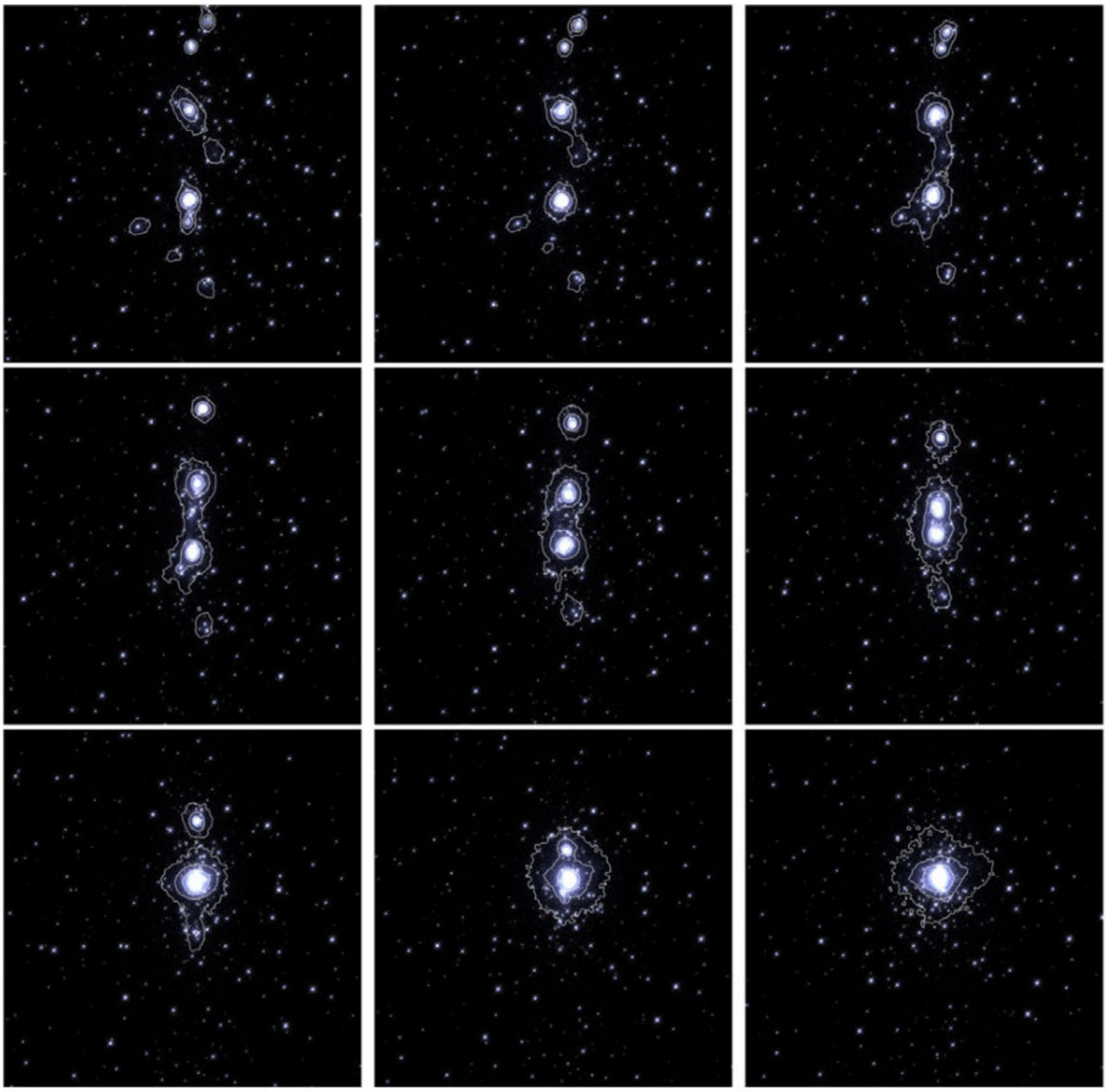

Figure 7.1: The figure is adopted from Sills et al. (2018a), which shows the snapshots of the evolution of DR21 in 1 Myr. The snapshots are taken at an interval of 0.1 Myr starting from 0.1 Myr (for details, see Sills et al., 2018a).

Appendix A

RadFil output of other filaments

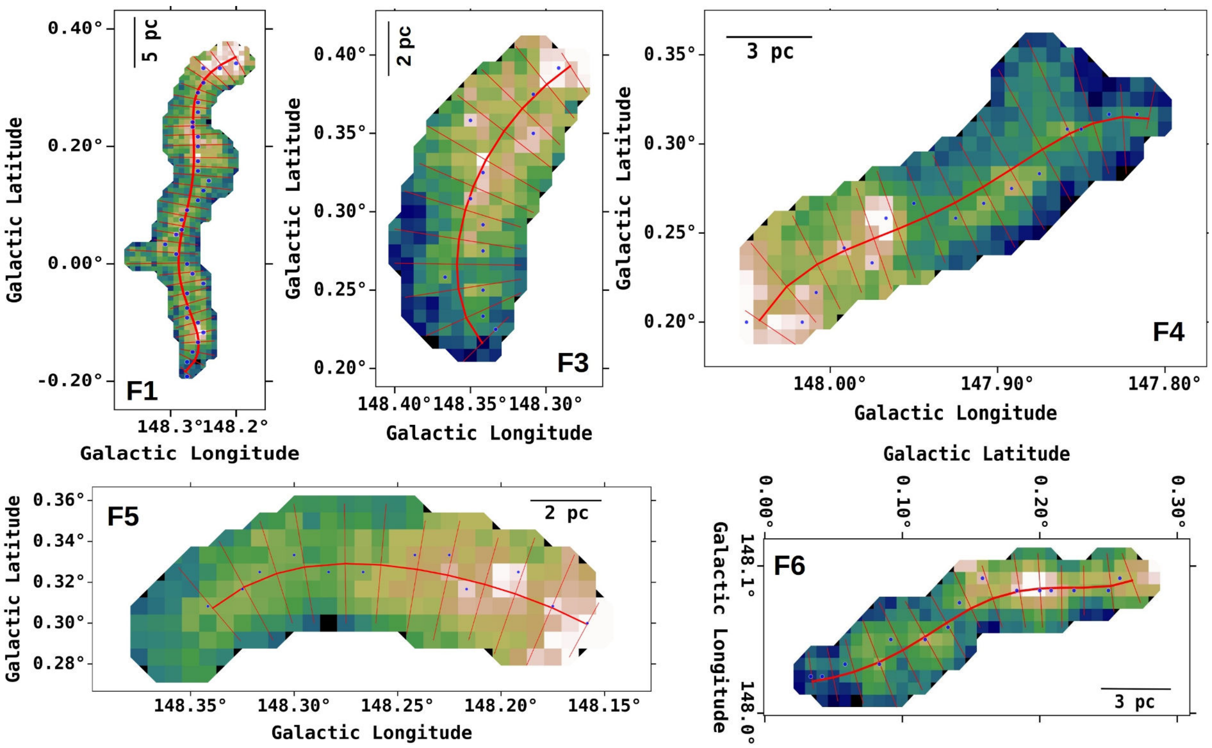

Figure A.1: The filaments spines (red solid curve) of F1, F3, F4, F5, and F6 shown over there ^{13}CO integrated intensity emission. The blue dots and perpendicular cuts (red solid lines) are the same as in Fig. 3.13a.

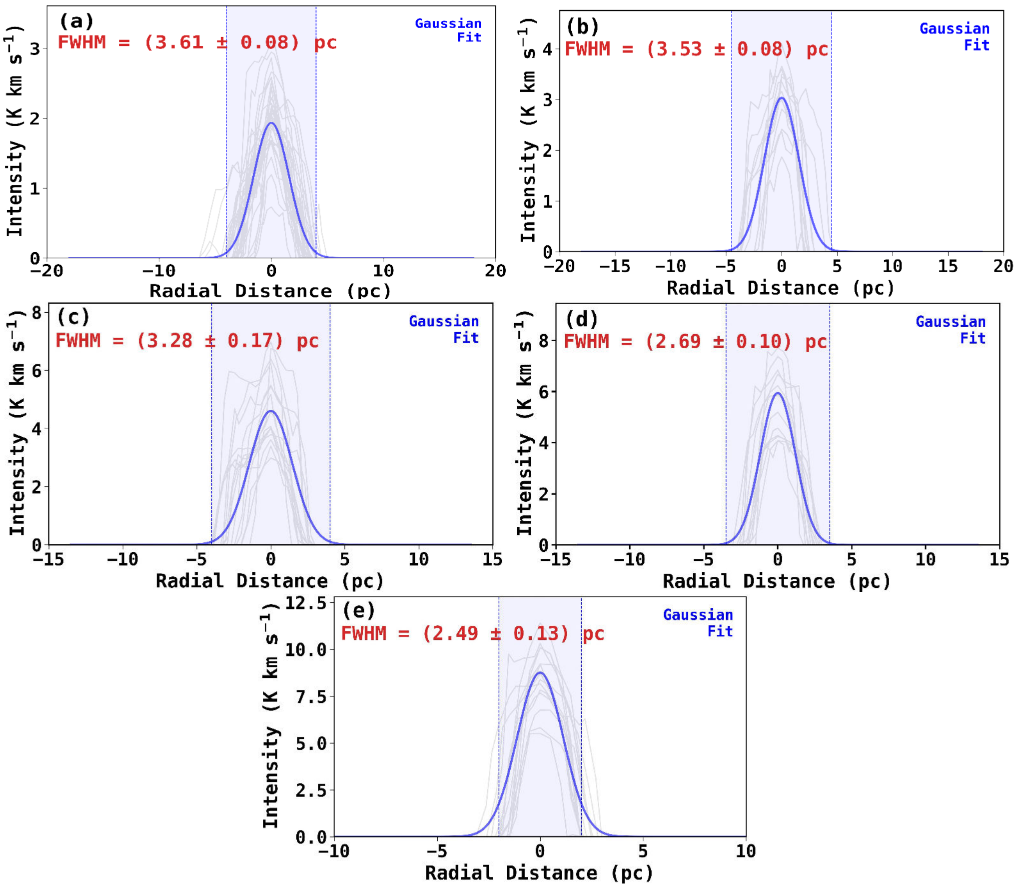

Figure A.2: The radial profiles of perpendicular cuts along the filament spines of (a) F1, (b) F3, (c) F4, (d) F5, and (e) F6, with details same as in Figure 3.13b.

Appendix B

Disk bearing members of the FSR 655 cluster

B.1 NIR excess sources

For deriving cluster properties, the identification of cluster members is crucial. The near and mid-infrared color-color (CC) diagrams are useful tools to identify the cluster members having NIR−excess emission due to circumstellar disk from young stars. However, other dusty objects along the line of sight may also appear as NIR−excess sources in the CC diagram. Without proper motion or radial velocity information, it is difficult to separate the member sources from the reddened field sources. One possible way to separate out the members from the field sources is to compare the CC diagram of the cluster with that of the field sources of the same area and photometric depth. Thus, we made the CC diagrams for the cluster as well as population synthesis model stars and did a comparative analysis of the distribution of the sources. Figure B.1a and Figure B.1b show $J-H$ vs. $H-K_s$ CC (JHK_s-CC) diagrams of the cluster as well as model field sources, respectively. In both diagrams, the main-sequence dwarfs' locus is shown

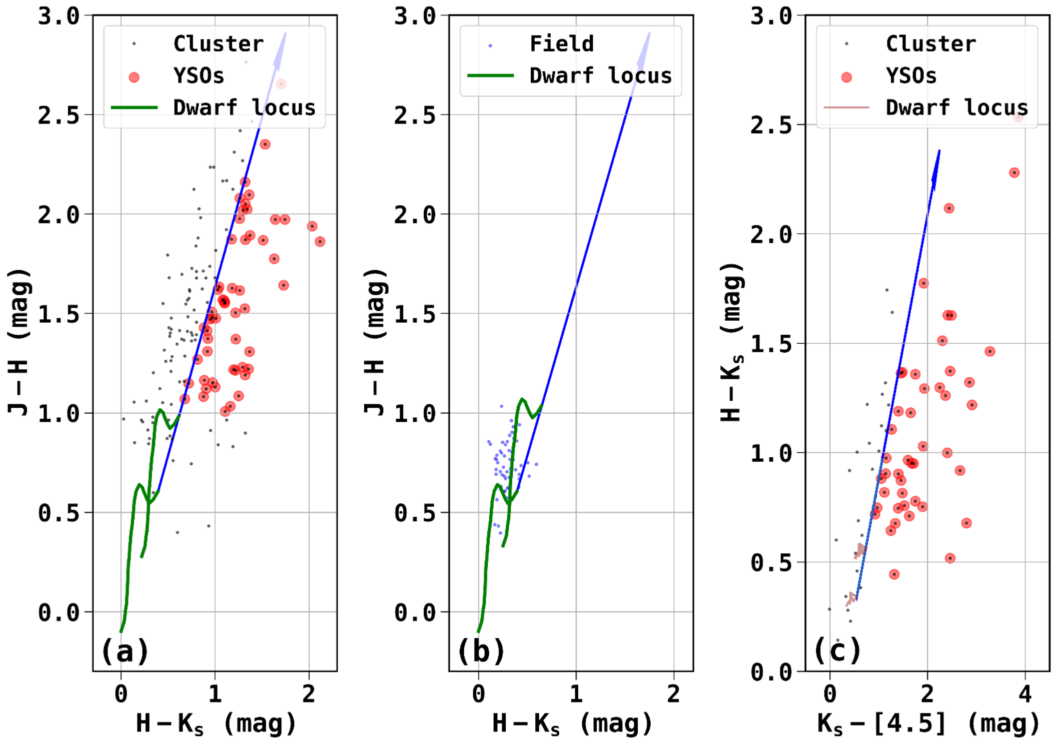

Figure B.1: The ($J-H$, $H-K_s$) CC diagram for the (a) cluster region and (b) for the modeled control field region. The green curves are the intrinsic dwarf locus from Bessell & Brett (1988). The blue dots in panel-b show the modeled field population. (c) The ($H-K_s$, K−[4.5]) CC diagram for the cluster region. The brown curves are the intrinsic dwarf locus of late M-type dwarfs (Patten et al., 2006). In panel-a and -c, the black dots show all the sources observed towards the cluster, and the red dots show the YSOs identified in the cluster, based on their NIR−excess in JHK_s and HK_s[4.5] CC diagrams, respectively. In all the plots, the blue line represents the reddening vector drawn from the location of the M6 dwarf.

by a green curve, and the reddening vector from the location of the M6 dwarf is shown by a blue arrow. In the NIR CC diagram, sources right to the M6-dwarf reddening vector are, in general, considered as pre-main-sequence (PMS) sources with NIR−excess (Lada & Adams, 1992; Lada & Lada, 1995; Haisch et al., 2001).

As can be seen in Figure B.1, compared to the cluster region, the NIR−excess zone of the field population is mostly devoid of sources, implying the presence of true NIR−excess sources in the cluster region. From the figure, it can also be noticed that most of the control field sources are distributed in the color-color space of $J-H$ < 1.0 mag and $H-K_s$ < 0.4 mag. A similar distribution with $J-H$ color less than 1.2 mag can also be seen for a group of sources in the cluster CC diagram. This group seems to be separated from the group of reddened cluster sources in the $J-H$ and $H-K_s$ color space. A comparison of CC diagrams leads us to suggest that the former group of sources in the cluster region is likely the field population along the line of sight. Figure B.1a and b also show the location of the dwarf locus reddened by $A_V = 4$ mag, which fairly matches with the distribution of control field sources and also the likely field population of the cluster region, implying that foreground extinction in front of cluster hosting cloud is around 4 mag. Comparing the CC diagrams, we selected sources with $(J-H)$ color greater than 1.0 mag as NIR−excess sources.

It is well known that circumstellar emission from young stars dominates at longer wavelengths, where the spectral energy distribution (SED) significantly deviates from the pure photospheric emission. Thus, by incorporating the *Spitzer* longer wavebands' data into the analysis, a more accurate census of the fraction of stars still surrounded by circumstellar material (i.e., optically thick accretion disks) can be obtained. We thus used the $H-K_s$ vs. $K_s-[4.5]$ CC ($HK_s[4.5]$-CC) diagram to identify extra NIR−excess sources (e.g., Samal et al., 2014), which is shown in Figure B.1c. Similar to the JHK_s-CC diagram, we selected NIR−excess sources whose $(H-K_s)$ color is greater than 0.5 mag and located right to the reddening vector drawn from the M6 dwarf star.

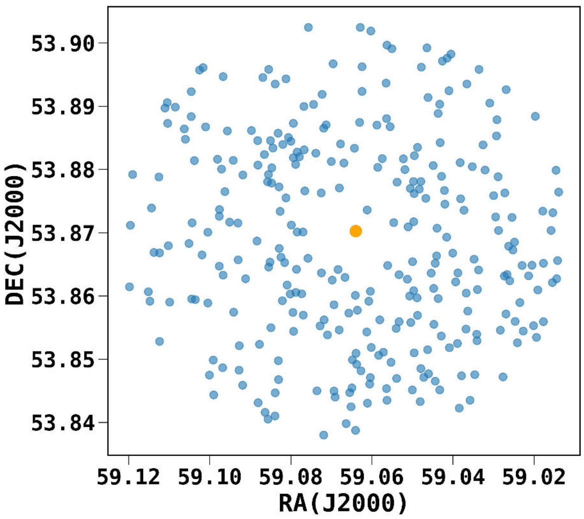

Figure B.2: Spatial distribution of the sources visible in 4.5 μm band, in the cluster direction within 2 arcmin radius from the cluster center. The location of the central massive YSO is marked by a yellow dot.

In summary, with the above approaches, we identified 56 and 47 NIR−excess sources from the JHK_s and $HK_s[4.5]$ CC diagrams, respectively. Including common sources, in total, we identified 82 disk-bearing sources in the cluster region.

B.2 Disk fraction

The disk fraction, which is the frequency of stars with disks within a young cluster, has been widely studied for various star-forming clusters in the solar neighbourhood. In general, it has been found that the disk fraction decreases exponentially with the age of the cluster, and the typical lifetime of an optically thick circumstellar disk is around 2−3 Myr (Haisch et al., 2001). Using the JHK_s and $HK_s[4.5]$ CC diagrams discussed in Appendix B.1, we estimate the disk fraction of FSR 655 to be around 47 ± 7% and 70 ± 8%, respectively, where the errors are due to Poisson statistics. However, if we include the photometric error of the cluster members and select only those sources which have excess 1σ (where σ is the color error) above the reddening vector, the disk fraction changes to ~38 ± 6% and ~57 ± 8%, respectively. To further confirm the disk-bearing cluster members, we determine the Q parameter, $Q = (J - H) - 1.7 \times (H - K_s)$, which gives the deviation from the reddening vector in the JHK_s CC diagram (Comerón et al., 2005; Messineo et al., 2012), following the Rieke & Lebofsky (1985) extinction law. Following the criteria of Comerón et al. (2005), i.e., a star having a Q value of less than − 0.10 is an NIR-excess source, we estimated the JHK_s disk fraction of FSR 655 to be around 43%. We also find that using a higher alpha value of 1.9 in the extinction law (discussed in Section 5.2.2.1), the disk fraction of FSR 655 based on Q value estimation changes by only 2%. A similar analysis of Q value for $HK_s[4.5]$-CC based disk fraction shows comparable results within 1σ uncertainty.

Comparing the disk fractions of FSR 655 with those of the NGC 2024 cluster, which is of similar age ~0.3 Myr (Haisch et al., 2000), we find that the JHK_s and $HK_s[4.5]$ disk fractions of FSR 655 are comparable to the JHK_s and JHK_sL disk fractions of NGC 2024 (i.e., ~58% and ~86%, respectively) within the limits of uncertainty. However, we want to point out that the $HK_s[4.5]$-CC based disk fraction estimated for FSR 655, is likely a lower limit. This is due to the presence of a high infrared diffuse background in the vicinity of the cluster center at 3.6 μm and 4.5 μm, which can potentially affect the detection of the faint point sources in these bands. This can be readily seen in Figure B.2, as a lack of point sources in the vicinity of the central massive star, shown by a yellow dot, compared to the overall distribution of point sources in the area. Deeper and high-contrast observations are required to determine the true JHK_sL or $HK_s[4.5]$ based disk fraction of the cluster.

Furthermore, it has been suggested that the gas and dust in the disk are affected by the stellar radiation of the host stars, thus, the disk fraction also depends on stellar mass. For example, larger disk fractions among lower-mass stars, compared to massive stars, have been found both in simulations (Johnstone et al., 1998; Hollenbach et al., 2000; Pfalzner et al., 2006; Pfalzner & Dincer, 2024) and observations (Balog et al., 2007; Kennedy & Kenyon, 2009; Stolte et al., 2010; Yasui et al., 2014; Ribas et al., 2015; Damian et al., 2023). It is thus important to estimate the disk fraction in a limited mass range. In this line, Fang et al. (2012) estimated inner-disk fraction based on H, K_s, 3.6 and 4.5 μm data for a number of nearby clusters with stellar members massive than 0.5 $M_\odot$ and found the dependence of disk fraction ($f_{\rm disk}$) on age as $f_{\rm disk} = e^{-t/2.3}$, where t is the age in Myr. They also found that for clusters having a higher number of OB stars, the disk dispersal is faster compared to the moderate number of OB stars. We thus estimated disk fraction using the mass-extinction limited sample, which is fairly complete, down to 0.5 $M_\odot$. Doing so, we find the JHK_s-CC and $HK_s[4.5]$-CC disk fraction to be around 45 ± 7% and 65 ± 8%. This may be a lower limit considering that our data is not fully complete down to 0.5 $M_\odot$.

Comparing the $HK_s[4.5]$-CC disk fraction of FSR 655 with the samples of Fang et al. (2012) (see their Figure 16), we find that the likely age of the cluster is not more than a Myr. To our knowledge, no disk fraction in the literature has been estimated for cluster members of mass above 0.5 $M_\odot$ using only JHK_s data, so a direct comparison of JHK_s disk fraction with other clusters is not possible. However, in general, it is comparable to the disk fraction (∼50−60%) of nearby clusters of age 0.5−1 Myr such as NGC 2024 and ONC (Haisch et al., 2000; Lada et al., 2000), for which disk fraction has been estimated for member stars down to 0.1 $M_\odot$.

This page was intentionally left blank.

References

Adamo A., et al., 2020, Space Sci. Rev., 216, 69 [Cited on page 25.]

Allard F., Freytag B., 2010, Highlights of Astronomy, 15, 756 [Cited on page 170.]

Allison R. J., Goodwin S. P., Parker R. J., Portegies Zwart S. F., de Grijs R., Kouwenhoven M. B. N., 2009a, MNRAS , 395, 1449 [Cited on pages 70 and 71.]

Allison R. J., Goodwin S. P., Parker R. J., de Grijs R., Portegies Zwart S. F., Kouwenhoven M. B. N., 2009b, ApJ , 700, L99 [Cited on page 185.]

Allison R. J., Goodwin S. P., Parker R. J., Portegies Zwart S. F., de Grijs R., 2010, MNRAS , 407, 1098 [Cited on page 70.]

Alves J. F., Lada C. J., Lada E. A., 2001, Nature, 409, 159 [Cited on pages xiii and 8.]

Alves J., Lombardi M., Lada C. J., 2007, A&A , 462, L17 [Cited on pages xxv, 214, and 215.]

Andersen M., Meyer M. R., Robberto M., Bergeron L. E., Reid N., 2011, A&A , 534, A10 [Cited on page 182.]

Andersson B. G., Lazarian A., Vaillancourt J. E., 2015, ARA&A, 53, 501 [Cited on pages 131 and 132.]

André P., et al., 2010, A&A , 518, L102 [Cited on pages 10, 14, 44, 58, 61, 90, and 109.]

André P., Di Francesco J., Ward-Thompson D., Inutsuka S. I., Pudritz R. E., Pineda J. E., 2014, in Beuther H., Klessen R. S., Dullemond C. P., Henning T., eds, Protostars and Planets VI. p. 27 (arXiv:1312.6232), doi:10.2458/azu$_{u}apress_{9}$780816531240 $-$ ch002 [Cited on pages 14, 56, 109, and 111.]

André P., 2017, Comptes Rendus Geoscience, 349, 187 [Cited on pages 27 and 90.]

Arzoumanian D., et al., 2019, A&A , 621, A42 [Cited on pages 109 and 121.]

Ascenso J., 2018, in Stahler S., ed., Astrophysics and Space Science Library Vol. 424, The Birth of Star Clusters. p. 1 (arXiv:1801.09940), doi:10.1007/978-3-319-22801-3_1 [Cited on pages 20 and 21.]

Attia O., Teyssier R., Katz H., Kimm T., Martin-Alvarez S., Ocvirk P., Rosdahl J., 2021, MNRAS , 504, 2346 [Cited on page 16.]

Baba D., et al., 2004, ApJ, 614, 818 [Cited on page 183.]

Baldeschi A., et al., 2017, MNRAS , 466, 3682 [Cited on pages xvi, 73, and 74.]

Ballesteros-Paredes J., Hartmann L., Vázquez-Semadeni E., 1999, ApJ, 527, 285 [Cited on page 12.]

Ballesteros-Paredes J., Klessen R. S., Mac Low M. M., Vazquez-Semadeni E., 2007, in Reipurth B., Jewitt D., Keil K., eds, Protostars and Planets V. p. 63 (arXiv:astro-ph/0603357), doi:10.48550/arXiv.astro-ph/0603357 [Cited on pages 27, 142, and 161.]

Ballesteros-Paredes J., et al., 2020, Space Sci. Rev., 216, 76 [Cited on pages 5, 10, and 12.]

Balog Z., Muzerolle J., Rieke G. H., Su K. Y. L., Young E. T., Megeath S. T., 2007, ApJ, 660, 1532 [Cited on page 235.]

Banerjee S., Kroupa P., 2015, MNRAS , 447, 728 [Cited on pages 25, 26, 29, 72, 214, and 219.]

Banerjee S., Kroupa P., 2018, in Stahler S., ed., Astrophysics and Space Science Library Vol. 424, The Birth of Star Clusters. p. 143 (arXiv:1512.03074), doi:10.1007/978-3-319-22801-3_6 [Cited on page 26.]

Barentsen G., et al., 2014, MNRAS , 444, 3230 [Cited on page 47.]

Barnard E. E., 1907, ApJ, 25, 218 [Cited on page 88.]

Barnes P. J., Hernandez A. K., Muller E., Pitts R. L., 2018, ApJ, 866, 19 [Cited on page 124.]

Barnes A. T., et al., 2019, MNRAS , 486, 283 [Cited on pages 26, 72, 83, and 124.]

Bastian N., Goodwin S. P., 2006, MNRAS , 369, L9 [Cited on page 215.]

Bastian N., Lardo C., 2018, Annual Review of Astronomy and Astrophysics, 56, 83 [Cited on page 22.]

Bastian N., Covey K. R., Meyer M. R., 2010, ARA&A, 48, 339 [Cited on page 185.]

Battersby C., et al., 2011, A&A , 535, A128 [Cited on pages 49 and 150.]

Baumann M., Boch T., Pineau F.-X., Fernique P., Bot C., Allen M., 2022, in Ruiz J. E., Pierfedereci F., Teuben P., eds, Astronomical Society of the Pacific Conference Series Vol. 532, Astronomical Data Analysis Software and Systems XXX. p. 7 [Cited on page 195.]

Beasley M. A., 2020, in Kabáth P., Jones D., Skarka M., eds, , Reviews in Frontiers of Modern Astrophysics; From Space Debris to Cosmology. pp 245–277, doi:10.1007/978-3-030-38509-5$_9$ [Cited on page 22.]

Beck A. M., Lesch H., Dolag K., Kotarba H., Geng A., Stasyszyn F. A., 2012, MNRAS , 422, 2152 [Cited on page 16.]

Beltrán M. T., et al., 2019, A&A , 630, A54 [Cited on page 17.]

Beltrán M. T., Rivilla V. M., Kumar M. S. N., Cesaroni R., Galli D., 2022, A&A , 660, L4 [Cited on page 90.]

Bertoldi F., McKee C. F., 1992, ApJ, 395, 140 [Cited on pages 61 and 163.]

Bessell M. S., Brett J. M., 1988, PASP, 100, 1134 [Cited on pages xxvi and 232.]

Beuther H., Vlemmings W. H. T., Rao R., van der Tak F. F. S., 2010, ApJ , 724, L113 [Cited on page 28.]

Beuther H., et al., 2018, A&A , 614, A64 [Cited on page 28.]

Beuther H., et al., 2020, The Astrophysical Journal, 904, 168 [Cited on pages 28 and 159.]

Bica E., Dutra C. M., Soares J., Barbuy B., 2003, A&A , 404, 223 [Cited on page 196.]

Bigiel F., Leroy A., Walter F., Brinks E., de Blok W. J. G., Madore B., Thornley M. D., 2008, AJ, 136, 2846 [Cited on pages xxv, 6, 30, 33, 209, 211, and 212.]

Blanc G. A., Heiderman A., Gebhardt K., Evans Neal J. I., Adams J., 2009, ApJ, 704, 842 [Cited on page 30.]

Blanton M. R., et al., 2017, AJ, 154, 28 [Cited on page 224.]

Bloemen J. B. G. M., et al., 1986, A&A , 154, 25 [Cited on page 6.]

Boggs P. T., Spiegelman C. H., Donaldson J. R., Schnabel R. B., 1988, Journal of Econometrics, 38, 169 [Cited on page 207.]

Bohlin R. C., Savage B. D., Drake J. F., 1978, ApJ, 224, 132 [Cited on pages 8, 9, 49, and 54.]

Bolatto A. D., Wolfire M., Leroy A. K., 2013, ARA&A, 51, 207 [Cited on pages 5, 6, 98, and 100.]

Bonnell I. A., Bate M. R., 2006, MNRAS , 370, 488 [Cited on pages 70 and 192.]

Bourke T. L., et al., 1997, ApJ, 476, 781 [Cited on page 97.]

Braun R., Thilker D. A., Walterbos R. A. M., Corbelli E., 2009, ApJ, 695, 937 [Cited on page 30.]

Bressan A., Marigo P., Girardi L., Salasnich B., Dal Cero C., Rubele S., Nanni A., 2012, MNRAS , 427, 127 [Cited on pages 70 and 78.]

Bressert E., Ginsburg A., Bally J., Battersby C., Longmore S., Testi L., 2012, ApJ , 758, L28 [Cited on page 74.]

Brodie J. P., Strader J., 2006, ARA&A, 44, 193 [Cited on page 22.]

Bromm V., 2013, Reports on Progress in Physics, 76, 112901 [Cited on page 1.]

Bromm V., Larson R. B., 2004, ARA&A, 42, 79 [Cited on page 1.]

Burkert A., Hartmann L., 2004, ApJ, 616, 288 [Cited on pages 43 and 122.]

Burkhart B., Lazarian A., Goodman A., Rosolowsky E., 2013, The Astrophysical Journal, 770, 141 [Cited on pages 32 and 214.]

Busquet G., 2020, Nature Astronomy, 4, 1126 [Cited on page 159.]

Caldwell S., Chang P., 2018, MNRAS , 474, 4818 [Cited on pages 75 and 189.]

Calzetti D., Liu G., Koda J., 2012, ApJ, 752, 98 [Cited on page 33.]

Cambrésy L., 1999, A&A , 345, 965 [Cited on page 54.]

Cao Y., Qiu K., Zhang Q., Li G.-X., 2022, ApJ, 927, 106 [Cited on page 105.]

Cardelli J. A., Clayton G. C., Mathis J. S., 1989, ApJ, 345, 245 [Cited on pages 7 and 8.]

Carpenter J. M., Snell R. L., Schloerb F. P., Skrutskie M. F., 1993, ApJ, 407, 657 [Cited on page 196.]

Carroll-Nellenback J. J., Frank A., Heitsch F., 2014, ApJ, 790, 37 [Cited on page 116.]

Cartwright A., Whitworth A. P., 2004, MNRAS , 348, 589 [Cited on pages 64, 65, and 67.]

Casali M., et al., 2007, A&A , 467, 777 [Cited on page 38.]

Casewell S., Hambly N., 2013, in Thirty Years of Astronomical Discovery with UKIRT. p. 291, doi:10.1007/978-94-007-7432-2$_2$7 [Cited on page 194.]

Castets A., Langer W. D., 1995, A&A , 294, 835 [Cited on page 97.]

Cazaux S., Tielens A. G. G. M., 2002, ApJ , 575, L29 [Cited on page 10.]

Chabrier G., 2003, PASP, 115, 763 [Cited on page 36.]

Chandrasekhar S., 1961, Hydrodynamic and hydromagnetic stability [Cited on page 19.]

Chandrasekhar S., Fermi E., 1953, ApJ, 118, 113 [Cited on page 155.]

Chapin E. L., Berry D. S., Gibb A. G., Jenness T., Scott D., Tilanus R. P. J., Economou F., Holland W. S., 2013, MNRAS , 430, 2545 [Cited on page 132.]

Chapman N. L., Mundy L. G., Lai S.-P., Evans Neal J. I., 2009, ApJ, 690, 496 [Cited on page 54.]

Chapman N. L., Goldsmith P. F., Pineda J. L., Clemens D. P., Li D., Krčo M., 2011, ApJ, 741, 21 [Cited on page 157.]

Chen M. C.-Y., et al., 2020, ApJ, 891, 84 [Cited on pages 102 and 114.]

Chen Y., Li H., Vogelsberger M., 2021, MNRAS , 502, 6157 [Cited on pages 60 and 192.]

Choi J., Dotter A., Conroy C., Cantiello M., Paxton B., Johnson B. D., 2016, ApJ, 823, 102 [Cited on pages xxiii, 179, 184, 185, and 203.]

Chomiuk L., Povich M. S., 2011, AJ, 142, 197 [Cited on page 14.]

Chung E. J., Lee C. W., Kwon W., Yoo H., Soam A., Cho J., 2022, AJ, 164, 175 [Cited on page 165.]

Chung E. J., Lee C. W., Kwon W., Tafalla M., Kim S., Soam A., Cho J., 2023, The Astrophysical Journal, 951, 68 [Cited on pages 28, 139, and 140.]

Clark P. C., Bonnell I. A., 2004, MNRAS , 347, L36 [Cited on page 60.]

Clark P. C., Whitworth A. P., 2021, MNRAS , 500, 1697 [Cited on page 75.]

Clark P. C., Bonnell I. A., Zinnecker H., Bate M. R., 2005, MNRAS , 359, 809 [Cited on page 60.]

Clarke S. D., Whitworth A. P., 2015, MNRAS , 449, 1819 [Cited on pages 43 and 124.]

Clarke S. D., Whitworth A. P., Hubber D. A., 2016, MNRAS , 458, 319 [Cited on page 121.]

Comerón F., Schneider N., Russeil D., 2005, A&A , 433, 955 [Cited on page 234.]

Commerçon B., Launhardt R., Dullemond C., Henning T., 2012, A&A , 545, A98 [Cited on page 67.]

Cooper H. D. B., et al., 2013, MNRAS , 430, 1125 [Cited on pages 35 and 75.]

Cox N. L. J., et al., 2016, A&A , 590, A110 [Cited on pages 27 and 105.]

Crutcher R. M., 2012, ARA&A, 50, 29 [Cited on pages 18, 157, and 164.]

Crutcher R. M., Nutter D. J., Ward-Thompson D., Kirk J. M., 2004, ApJ, 600, 279 [Cited on pages 160 and 161.]

Crutcher R. M., Wandelt B., Heiles C., Falgarone E., Troland T. H., 2010, ApJ, 725, 466 [Cited on page 157.]

Cudlip W., Furniss I., King K. J., Jennings R. E., 1982, MNRAS , 200, 1169 [Cited on page 18.]

Currie M. J., Berry D. S., Jenness T., Gibb A. G., Bell G. S., Draper P. W., 2014, in Manset N., Forshay P., eds, Astronomical Society of the Pacific Conference Series Vol. 485, Astronomical Data Analysis Software and Systems XXIII. p. 391 [Cited on page 132.]

Cutri R. M., et al., 2003, VizieR Online Data Catalog: 2MASS All-Sky Catalog of Point Sources (Cutri+ 2003), VizieR On-line Data Catalog: II/246. Originally published in: 2003yCat.2246....0C [Cited on page 194.]

Dame T. M., Hartmann D., Thaddeus P., 2001, ApJ, 547, 792 [Cited on pages 6, 45, and 98.]

Damian B., Jose J., Samal M. R., Moraux E., Das S. R., Patra S., 2021, MNRAS , 504, 2557 [Cited on pages 171, 183, and 186.]

Damian B., Jose J., Biller B., Paul K. T., 2023, Journal of Astrophysics and Astronomy, 44, 77 [Cited on page 235.]

Davis L., 1951, Physical Review, 81, 890 [Cited on page 155.]

Deharveng L., et al., 2012, A&A , 546, A74 [Cited on pages 49 and 150.]

Deharveng L., et al., 2015, A&A , 582, A1 [Cited on page 62.]

Dewangan L. K., Ojha D. K., Sharma S., Palacio S. d., Bhadari N. K., Das A., 2020, ApJ, 903, 13 [Cited on page 102.]

Dib S., Henning T., 2019, A&A , 629, A135 [Cited on page 64.]

Dobashi K., 2011, PASJ, 63, S1 [Cited on page 44.]

Dobashi K., Uehara H., Kandori R., Sakurai T., Kaiden M., Umemoto T., Sato F., 2005, PASJ, 57, S1 [Cited on page 35.]

Dobbs C. L., Bonnell I. A., Clark P. C., 2005, MNRAS , 360, 2 [Cited on page 81.]

Dobbs C. L., Burkert A., Pringle J. E., 2011, MNRAS , 413, 2935 [Cited on page 60.]

Doi Y., et al., 2020, ApJ, 899, 28 [Cited on page 27.]

Domínguez R., Fellhauer M., Blaña M., Farias J. P., Dabringhausen J., 2017, MNRAS , 472, 465 [Cited on page 70.]

Donkov S., Stefanov I. Z., 2018, MNRAS , 474, 5588 [Cited on page 60.]

Draine B. T., 2003, ARA&A, 41, 241 [Cited on page 7.]

Draine B. T., 2011, Physics of the Interstellar and Intergalactic Medium [Cited on page 10.]

Dunham M. M., et al., 2006, ApJ, 651, 945 [Cited on pages 61 and 67.]

Dunham M. M., Crapsi A., Evans Neal J. I., Bourke T. L., Huard T. L., Myers P. C., Kauffmann J., 2008, ApJS, 179, 249 [Cited on page 67.]

Dunham M. M., et al., 2013, The Astronomical Journal, 145, 94 [Cited on page 31.]

Dutra C. M., Bica E., 2001, A&A , 376, 434 [Cited on page 196.]

Dutta S., Mondal S., Jose J., Das R. K., Samal M. R., Ghosh S., 2015, MNRAS , 454, 3597 [Cited on pages 183 and 196.]

Dutta S., Mondal S., Samal M. R., Jose J., 2018, ApJ, 864, 154 [Cited on page 80.]

Elia D., et al., 2017, MNRAS , 471, 100 [Cited on pages 67 and 196.]

Elia D., et al., 2022, The Astrophysical Journal, 941, 162 [Cited on page 14.]

Ellerbroek L. E., et al., 2013, A&A , 558, A102 [Cited on page 183.]

Elmegreen B. G., Efremov Y. N., 1997, The Astrophysical Journal, 480, 235 [Cited on page 23.]

Espinoza P., Selman F. J., Melnick J., 2009, A&A , 501, 563 [Cited on page 23.]

Eswaraiah C., et al., 2020, ApJ, 897, 90 [Cited on pages 28 and 143.]

Eswaraiah C., et al., 2021, The Astrophysical Journal Letters, 912, L27 [Cited on pages 27 and 28.]

Evans Neal J. I., et al., 2009, ApJS, 181, 321 [Cited on pages xxv, 14, 24, 31, 43, 192, 193, 194, 208, 209, 211, 213, 214, and 215.]

Evans Neal J. I., Heiderman A., Vutisalchavakul N., 2014, ApJ, 782, 114 [Cited on pages xxv, 25, 31, 32, 34, 43, 56, 192, 193, 206, 208, 209, 210, 211, 212, 213, 214, 215, and 216.]

Fahrion K., et al., 2020, A&A , 637, A27 [Cited on page 22.]

Fang M., et al., 2012, A&A , 539, A119 [Cited on page 235.]

Federrath C., 2015, Monthly Notices of the Royal Astronomical Society, 450, 4035 [Cited on page 27.]

Federrath C., 2016, MNRAS , 457, 375 [Cited on page 109.]

Federrath C., Klessen R. S., 2012, The Astrophysical Journal, 761, 156 [Cited on page 28.]

Fiege J. D., Pudritz R. E., 2000, MNRAS , 311, 85 [Cited on pages 120 and 162.]

Foster J. B., et al., 2014, ApJ, 791, 108 [Cited on pages 33 and 75.]

Foster J. B., et al., 2015, ApJ, 799, 136 [Cited on page 70.]

Frerking M. A., Langer W. D., Wilson R. W., 1982, ApJ, 262, 590 [Cited on pages 6, 97, and 98.]

Friberg P., Bastien P., Berry D., Savini G., Graves S. F., Pattle K., 2016, in Holland W. S., Zmuidzinas J., eds, Society of Photo-Optical Instrumentation Engineers (SPIE) Conference Series Vol. 9914, Millimeter, Submillimeter, and Far-Infrared Detectors and Instrumentation for Astronomy VIII. p. 991403, doi:10.1117/12.2231943 [Cited on pages 37 and 132.]

Friesen R. K., Medeiros L., Schnee S., Bourke T. L., di Francesco J., Gutermuth R., Myers P. C., 2013, MNRAS , 436, 1513 [Cited on page 102.]

Friesen R. K., Bourke T. L., Di Francesco J., Gutermuth R., Myers P. C., 2016, ApJ, 833, 204 [Cited on page 115.]

Furlan E., et al., 2016, ApJS, 224, 5 [Cited on page 63.]

GLIMPSE Team 2020, GLIMPSE 360 Archive, doi:10.26131/IRSA205, https://catcopy.ipac.caltech.edu/dois/doi.php?id=10.26131/IRSA205 [Cited on page 171.]

Gao Y., Solomon P. M., 2004, ApJ, 606, 271 [Cited on pages 30 and 32.]

Garay G., Mardones D., Brooks K. J., Videla L., Contreras Y., 2007, ApJ, 666, 309 [Cited on page 60.]

Garden R. P., Hayashi M., Gatley I., Hasegawa T., Kaifu N., 1991, ApJ, 374, 540 [Cited on pages 94, 95, and 98.]

Gavagnin E., Bleuler A., Rosdahl J., Teyssier R., 2017, MNRAS , 472, 4155 [Cited on pages 83 and 85.]

Geen S., Hennebelle P., Tremblin P., Rosdahl J., 2015, MNRAS , 454, 4484 [Cited on page 24.]

Geen S., Hennebelle P., Tremblin P., Rosdahl J., 2016, MNRAS , 463, 3129 [Cited on page 24.]

Giannetti A., et al., 2017, A&A , 606, L12 [Cited on page 52.]

Ginsburg A., Bressert E., Bally J., Battersby C., 2012, ApJ , 758, L29 [Cited on pages xvi, 73, 74, and 75.]

Girart J. M., Rao R., Marrone D. P., 2006, Science, 313, 812 [Cited on pages 17 and 139.]

Girart J. M., Beltrán M. T., Zhang Q., Rao R., Estalella R., 2009, Science, 324, 1408 [Cited on page 28.]

Girart J. M., Frau P., Zhang Q., Koch P. M., Qiu K., Tang Y.-W., Lai S.-P., Ho P. T. P., 2013, The Astrophysical Journal, 772, 69 [Cited on page 28.]

Girichidis P., Federrath C., Banerjee R., Klessen R. S., 2012, MNRAS , 420, 613 [Cited on page 70.]

Goldsmith P. F., 2001, ApJ, 557, 736 [Cited on page 100.]

Goldsmith P. F., Langer W. D., 1999, ApJ, 517, 209 [Cited on page 115.]

Goldsmith P. F., Heyer M., Narayanan G., Snell R., Li D., Brunt C., 2008, ApJ, 680, 428 [Cited on pages 33 and 95.]

Gómez G. C., Vázquez-Semadeni E., 2014, ApJ, 791, 124 [Cited on pages 60, 81, 102, 126, and 134.]

Gómez G. C., Vázquez-Semadeni E., Zamora-Avilés M., 2018, MNRAS , 480, 2939 [Cited on pages 27, 102, 130, 134, and 158.]

Gómez G. C., Vázquez-Semadeni E., Palau A., 2021, MNRAS , 502, 4963 [Cited on page 160.]

Gontcharov G. A., 2012, Astronomy Letters, 38, 87 [Cited on page 170.]

Goodman A. A., Rosolowsky E. W., Borkin M. A., Foster J. B., Halle M., Kauffmann J., Pineda J. E., 2009, Nature, 457, 63 [Cited on page 215.]

Goodwin S. P., Bastian N., 2006, MNRAS , 373, 752 [Cited on page 224.]

Goodwin S. P., Whitworth A. P., 2004, A&A , 413, 929 [Cited on page 67.]

Griffin M. J., et al., 2010, A&A , 518, L3 [Cited on page 36.]

Guilloteau S., Lucas R., 2000, in Mangum J. G., Radford S. J. E., eds, Astronomical Society of the Pacific Conference Series Vol. 217, Imaging at Radio through Submillimeter Wavelengths. p. 299 [Cited on page 91.]

Guo W., et al., 2022, ApJ, 938, 44 [Cited on page 110.]

Guszejnov D., Markey C., Offner S. S. R., Grudić M. Y., Faucher-Giguère C.-A., Rosen A. L., Hopkins P. F., 2022, MNRAS , 515, 167 [Cited on pages 214 and 215.]

Gutermuth R. A., et al., 2008, ApJ , 673, L151 [Cited on page 77.]

Gutermuth R. A., Megeath S. T., Myers P. C., Allen L. E., Pipher J. L., Fazio G. G., 2009, ApJS, 184, 18 [Cited on pages 165 and 174.]

Gutermuth R. A., Pipher J. L., Megeath S. T., Myers P. C., Allen L. E., Allen T. S., 2011, ApJ, 739, 84 [Cited on pages 32, 34, 208, and 214.]

Gutermuth R., Dunham M., Offner S., 2019, in American Astronomical Society Meeting Abstracts #233. p. 367.10 [Cited on pages 33 and 193.]

Hacar A., Tafalla M., Kauffmann J., Kovács A., 2013, A&A , 554, A55 [Cited on pages 90, 104, 105, and 115.]

Hacar A., Alves J., Burkert A., Goldsmith P., 2016, A&A , 591, A104 [Cited on page 115.]

Hacar A., Alves J., Tafalla M., Goicoechea J. R., 2017, A&A , 602, L2 [Cited on pages 105, 106, 115, and 123.]

Hacar A., Tafalla M., Forbrich J., Alves J., Meingast S., Grossschedl J., Teixeira P. S., 2018, A&A , 610, A77 [Cited on pages 102 and 106.]

Hacar A., Clark S., Heitsch F., Kainulainen J., Panopoulou G., Seifried D., Smith R., 2022, arXiv e-prints, p. arXiv:2203.09562 [Cited on pages 74, 88, 90, and 114.]

Haisch Karl E. J., Lada E. A., Lada C. J., 2000, AJ, 120, 1396 [Cited on pages 234 and 235.]

Haisch Karl E. J., Lada E. A., Lada C. J., 2001, ApJ , 553, L153 [Cited on pages 232 and 234.]

Hall J. S., 1949, Science, 109, 166 [Cited on pages 10 and 130.]

Hartmann L., Ballesteros-Paredes J., Bergin E. A., 2001, ApJ, 562, 852 [Cited on page 27.]

Harvey P. M., et al., 2008, ApJ, 680, 495 [Cited on page 165.]

Heiderman A., Evans Neal J. I., Allen L. E., Huard T., Heyer M., 2010, ApJ, 723, 1019 [Cited on pages xiv, xxv, 14, 25, 31, 32, 48, 55, 56, 192, 193, 194, 206, 208, 209, 210, 211, 212, 213, 214, 215, and 216.]

Heigl S., Hoemann E., Burkert A., 2022, MNRAS , 517, 5272 [Cited on page 43.]

Heitsch F., Zweibel E. G., Mac Low M.-M., Li P., Norman M. L., 2001, ApJ, 561, 800 [Cited on page 156.]

Heitsch F., Hartmann L. W., Slyz A. D., Devriendt J. E. G., Burkert A., 2008, ApJ, 674, 316 [Cited on pages 14, 43, and 116.]

Hennebelle P., 2018, A&A , 611, A24 [Cited on page 28.]

Hennebelle P., André P., 2013, A&A , 560, A68 [Cited on page 121.]

Hennebelle P., Falgarone E., 2012, A&A Rev., 20, 55 [Cited on page 161.]

Hennebelle P., Inutsuka S.-i., 2019, Frontiers in Astronomy and Space Sciences, 6 [Cited on page 27.]

Hennemann M., et al., 2012, A&A , 543, L3 [Cited on page 102.]

Henning T., Cesaroni R., Walmsley M., Pfau W., 1992, A&AS , 93, 525 [Cited on page 196.]

Henshaw J. D., Barnes A. T., Battersby C., Ginsburg A., Sormani M. C., Walker D. L., 2023, in Inutsuka S., Aikawa Y., Muto T., Tomida K., Tamura M., eds, Astronomical Society of the Pacific Conference Series Vol. 534, Protostars and Planets VII. p. 83 (arXiv:2203.11223), doi:10.48550/arXiv.2203.11223 [Cited on pages 43 and 57.]

Hernandez A. K., Tan J. C., 2015, ApJ, 809, 154 [Cited on pages 95 and 114.]

Hernandez A. K., Tan J. C., Caselli P., Butler M. J., Jiménez-Serra I., Fontani F., Barnes P., 2011, ApJ, 738, 11 [Cited on page 97.]

Herschel Point Source Catalogue Working Group et al., 2020, VizieR Online Data Catalog, p. VIII/106 [Cited on pages xvii, xix, 62, 82, and 122.]

Heyer M., Dame T. M., 2015, ARA&A, 53, 583 [Cited on page 101.]

Heyer M. H., Corbelli E., Schneider S. E., Young J. S., 2004, ApJ, 602, 723 [Cited on page 30.]

Heyer M., Krawczyk C., Duval J., Jackson J. M., 2009, ApJ, 699, 1092 [Cited on pages 58, 100, and 101.]

Heyer M., Gutermuth R., Urquhart J. S., Csengeri T., Wienen M., Leurini S., Menten K., Wyrowski F., 2016, A&A , 588, A29 [Cited on pages xxv, 193, 210, and 211.]

Hildebrand R. H., 1983, QJRAS, 24, 267 [Cited on page 11.]

Hildebrand R. H., Kirby L., Dotson J. L., Houde M., Vaillancourt J. E., 2009, ApJ, 696, 567 [Cited on pages 155 and 156.]

Hillenbrand L. A., White R. J., 2004, ApJ, 604, 741 [Cited on page 71.]

Hills J. G., 1980, ApJ, 235, 986 [Cited on pages 191, 215, and 224.]

Hiltner W. A., 1949, Science, 109, 165 [Cited on pages 10 and 130.]

Hoang T., Lazarian A., 2008, MNRAS , 388, 117 [Cited on page 131.]

Hoang T., Lazarian A., 2014, MNRAS , 438, 680 [Cited on page 131.]

Hoemann E., Heigl S., Burkert A., 2023, MNRAS , 521, 5152 [Cited on page 43.]

Holland W. S., et al., 2013, MNRAS , 430, 2513 [Cited on pages 37 and 132.]

Hollenbach D. J., Werner M. W., Salpeter E. E., 1971, Astrophysical Journal, vol. 163, p. 165, 163, 165 [Cited on page 10.]

Hollenbach D. J., Yorke H. W., Johnstone D., 2000, in Mannings V., Boss A. P., Russell S. S., eds, Protostars and Planets IV. pp 401–428 [Cited on page 235.]

Hopkins A. M., 2018, PASA, 35, e039 [Cited on page 185.]

Hosek Matthew W. J., Lu J. R., Lam C. Y., Gautam A. K., Lockhart K. E., Kim D., Jia S., 2020, AJ, 160, 143 [Cited on pages 179 and 200.]

Houde M., Vaillancourt J. E., Hildebrand R. H., Chitsazzadeh S., Kirby L., 2009, ApJ, 706, 1504 [Cited on page 155.]

Howard C. S., Pudritz R. E., Harris W. E., 2018, Nature Astronomy, 2, 725 [Cited on pages 83, 84, 85, and 126.]

Hu B., et al., 2021, ApJ, 908, 70 [Cited on pages 105 and 108.]

Hubble E. P., 1922, ApJ, 56, 400 [Cited on page 3.]

Hull C. L. H., et al., 2017, ApJ, 847, 92 [Cited on page 28.]

Hwang J., et al., 2022, ApJ, 941, 51 [Cited on page 165.]

Immer K., Schuller F., Omont A., Menten K. M., 2012, A&A , 537, A121 [Cited on pages xvi, 73, and 75.]

Inutsuka S.-I., Miyama S. M., 1992, ApJ, 388, 392 [Cited on page 121.]

J. Rees M., 2005, Magnetic Fields in the Early Universe. Springer Berlin Heidelberg, Berlin, Heidelberg, pp 1–8, doi:10.1007/3540313966$_1$, https://doi.org/10.1007/3540313966_1 [Cited on page 16.]

Jeans J. H., 1902, Philosophical Transactions of the Royal Society of London Series A, 199, 1 [Cited on page 13.]

Jeffreson S. M. R., Kruijssen J. M. D., 2018, MNRAS , 476, 3688 [Cited on page 12.]

Johnstone D., Hollenbach D., Bally J., 1998, ApJ, 499, 758 [Cited on page 235.]

Jørgensen J. K., et al., 2006, ApJ, 645, 1246 [Cited on page 77.]

Jose J., et al., 2011, MNRAS , 411, 2530 [Cited on page 179.]

Jose J., et al., 2012, MNRAS , 424, 2486 [Cited on page 178.]

Jose J., Herczeg G. J., Samal M. R., Fang Q., Panwar N., 2017, ApJ, 836, 98 [Cited on pages 171 and 183.]

Jose J., et al., 2020, The Astrophysical Journal, 892, 122 [Cited on page 183.]

Kalberla P. M. W., Kerp J., 2009, ARA&A, 47, 27 [Cited on page 4.]

Karam J., Sills A., 2022, MNRAS , 513, 6095 [Cited on page 83.]

Kauffmann J., Pillai T., 2010, ApJ , 723, L7 [Cited on pages xvi, 73, and 74.]

Kauffmann J., Bertoldi F., Bourke T. L., Evans N. J. I., Lee C. W., 2008, A&A , 487, 993 [Cited on pages 50, 115, and 150.]

Kauffmann J., Pillai T., Goldsmith P. F., 2013, ApJ, 779, 185 [Cited on page 163.]

Kennedy G. M., Kenyon S. J., 2009, ApJ, 695, 1210 [Cited on page 235.]

Kennicutt Robert C. J., 1989, ApJ, 344, 685 [Cited on page 30.]

Kennicutt Robert C. J., 1998a, ARA&A, 36, 189 [Cited on page 194.]

Kennicutt Robert C. J., 1998b, ApJ, 498, 541 [Cited on pages xxv, 30, 192, 209, 211, and 212.]

Kennicutt R. C., Evans N. J., 2012, ARA&A, 50, 531 [Cited on pages xiv, 30, 31, 33, 193, and 194.]

Kennicutt Robert C. J., et al., 2007, ApJ, 671, 333 [Cited on page 30.]

Kharchenko N. V., Piskunov A. E., Schilbach E., Röser S., Scholz R. D., 2013, A&A , 558, A53 [Cited on page 22.]

Kim J.-G., Kim W.-T., Ostriker E. C., 2018, ApJ, 859, 68 [Cited on page 24.]

King I., 1962, AJ, 67, 471 [Cited on page 198.]

Kirk H., Myers P. C., Bourke T. L., Gutermuth R. A., Hedden A., Wilson G. W., 2013, ApJ, 766, 115 [Cited on page 123.]

Klessen R. S., Glover S. C. O., 2016, in Revaz Y., Jablonka P., Teyssier R., Mayer L., eds, Saas-Fee Advanced Course Vol. 43, Saas-Fee Advanced Course. p. 85 (arXiv:1412.5182), doi:10.1007/978-3-662-47890-5$_2$ [Cited on page 161.]

Klessen R. S., Heitsch F., Low M.-M. M., 2000, The Astrophysical Journal, 535, 887 [Cited on page 27.]

Koch E. W., Rosolowsky E. W., 2015, MNRAS , 452, 3435 [Cited on page 102.]

Koch P. M., Tang Y.-W., Ho P. T. P., 2012a, ApJ, 747, 79 [Cited on pages 142 and 149.]

Koch P. M., Tang Y.-W., Ho P. T. P., 2012b, ApJ, 747, 80 [Cited on pages 142 and 149.]

Koch P. M., Tang Y.-W., Ho P. T. P., 2013, ApJ, 775, 77 [Cited on pages 142, 143, and 158.]

Koch P. M., et al., 2014, The Astrophysical Journal, 797, 99 [Cited on page 27.]

Komugi S., Sofue Y., Nakanishi H., Onodera S., Egusa F., 2005, PASJ, 57, 733 [Cited on page 30.]

Könyves V., et al., 2010, A&A , 518, L106 [Cited on pages xxv, 214, and 215.]

Könyves V., et al., 2015, A&A , 584, A91 [Cited on pages xxv, 27, 34, 49, 90, 109, 214, and 215.]

Krause M. G. H., et al., 2020, Space Sci. Rev., 216, 64 [Cited on pages 24 and 25.]

Kroupa P., 2001, MNRAS , 322, 231 [Cited on pages 36, 78, 179, 185, 187, and 203.]

Kruijssen J. M. D., Longmore S. N., 2014, MNRAS , 439, 3239 [Cited on pages 31 and 33.]

Krumholz M. R., McKee C. F., 2005, ApJ, 630, 250 [Cited on pages 32, 33, 207, 212, and 216.]

Krumholz M. R., McKee C. F., 2020, MNRAS , 494, 624 [Cited on pages 25, 26, and 72.]

Krumholz M. R., Tan J. C., 2007, ApJ, 654, 304 [Cited on pages 32 and 33.]

Krumholz M. R., Dekel A., McKee C. F., 2012, ApJ, 745, 69 [Cited on pages xxv, 32, 58, 188, 207, 208, 212, 213, 216, and 223.]

Krumholz M. R., et al., 2014, in Beuther H., Klessen R. S., Dullemond C. P., Henning T., eds, Protostars and Planets VI. pp 243–266 (arXiv:1401.2473), doi:10.2458/azu$_{u}apress_{9}780816531240-ch011$ [Cited on page 33.]

Krumholz M. R., McKee C. F., Bland-Hawthorn J., 2019, ARA&A, 57, 227 [Cited on pages 20, 21, 24, 25, 29, 191, 192, 207, 214, 215, and 224.]

Kumar B., Sagar R., Melnick J., 2008, MNRAS , 386, 1380 [Cited on page 184.]

Kumar B., Sharma S., Manfroid J., Gosset E., Rauw G., Nazé Y., Kesh Yadav R., 2014, A&A , 567, A109 [Cited on page 178.]

Kumar B., et al., 2018, Bulletin de la Societe Royale des Sciences de Liege, 87, 29 [Cited on page 172.]

Kumar M. S. N., Palmeirim P., Arzoumanian D., Inutsuka S. I., 2020, A&A , 642, A87 [Cited on pages 90, 134, and 165.]

Kumar M. S. N., Arzoumanian D., Men'shchikov A., Palmeirim P., Matsumura M., Inutsuka S., 2022, A&A , 658, A114 [Cited on pages 79, 90, and 165.]

Kwon J., et al., 2018, ApJ, 859, 4 [Cited on page 133.]

Lada C. J., Adams F. C., 1992, ApJ, 393, 278 [Cited on page 232.]

Lada C. J., Dame T. M., 2020, ApJ, 898, 3 [Cited on page 52.]

Lada E. A., Lada C. J., 1995, AJ, 109, 1682 [Cited on pages 178 and 232.]

Lada C. J., Lada E. A., 2003, ARA&A, 41, 57 [Cited on pages 12, 20, 25, 179, and 216.]

Lada C. J., Margulis M., Dearborn D., 1984, ApJ, 285, 141 [Cited on page 224.]

Lada C. J., Muench A. A., Haisch Karl E. J., Lada E. A., Alves J. F., Tollestrup E. V., Willner S. P., 2000, AJ, 120, 3162 [Cited on page 235.]

Lada C. J., Alves J. F., Lombardi M., 2007, in Reipurth B., Jewitt D., Keil K., eds, Protostars and Planets V. p. 3 [Cited on pages xiii and 8.]

Lada C. J., Lombardi M., Alves J. F., 2010, ApJ, 724, 687 [Cited on pages xiv, xv, xxv, 14, 24, 32, 43, 44, 48, 55, 56, 57, 58, 192, 193, 194, 208, 209, 211, 212, 213, 214, 215, and 216.]

Lada C. J., Forbrich J., Lombardi M., Alves J. F., 2012, ApJ, 745, 190 [Cited on pages 32, 43, 48, 57, 84, 206, and 214.]

Lada C. J., Lombardi M., Roman-Zuniga C., Forbrich J., Alves J. F., 2013, The Astrophysical Journal, 778, 133 [Cited on pages 34, 193, 206, 209, and 210.]

Larson R. B., 1981, MNRAS , 194, 809 [Cited on pages 19 and 58.]

Lawrence A., et al., 2007, MNRAS , 379, 1599 [Cited on pages 35, 38, 44, and 194.]

Lazarian A., 2007, J. Quant. Spec. Radiat. Transf., 106, 225 [Cited on page 131.]

Lee E. J., Miville-Deschênes M.-A., Murray N. W., 2016, ApJ, 833, 229 [Cited on pages 14, 32, 75, and 188.]

Leisawitz D., Bash F. N., Thaddeus P., 1989, ApJS, 70, 731 [Cited on page 181.]

Levine J. L., Steinhauer A., Elston R. J., Lada E. A., 2006, ApJ, 646, 1215 [Cited on page 183.]

Lewis J. A., Lada C. J., Dame T. M., 2022, ApJ, 931, 9 [Cited on pages 98 and 101.]

Li G.-X., 2018, MNRAS , 477, 4951 [Cited on page 60.]

Li H.-b., Houde M., 2008, ApJ, 677, 1151 [Cited on page 27.]

Li H. B., Goodman A., Sridharan T. K., Houde M., Li Z. Y., Novak G., Tang K. S., 2014a, in Beuther H., Klessen R. S., Dullemond C. P., Henning T., eds, Protostars and Planets VI. pp 101–123 (arXiv:1404.2024), doi:10.2458/azu$_u apress_9 780816531240 - ch005$ [Cited on pages 27 and 165.]

Li Z.-Y., Krasnopolsky R., Shang H., Zhao B., 2014b, ApJ, 793, 130 [Cited on page 17.]

Li H., et al., 2015, The Astrophysical Journal Supplement Series, 219, 20 [Cited on page 97.]

Li S., et al., 2022, ApJ, 926, 165 [Cited on page 90.]

Lin S.-J., et al., 2023, arXiv e-prints, p. arXiv:2311.08026 [Cited on page 140.]

Liszt H. S., 2017, ApJ, 835, 138 [Cited on page 97.]

Liu H. B., Jiménez-Serra I., Ho P. T. P., Chen H.-R., Zhang Q., Li Z.-Y., 2012, ApJ, 756, 10 [Cited on pages 102 and 114.]

Liu H. B., Galván-Madrid R., Jiménez-Serra I., Román-Zúñiga C., Zhang Q., Li Z., Chen H.-R., 2015, ApJ, 804, 37 [Cited on page 165.]

Liu J., et al., 2019, ApJ, 877, 43 [Cited on pages 27 and 139.]

Liu T., et al., 2020, MNRAS , 496, 2790 [Cited on pages 124, 139, and 142.]

Liu X.-L., Xu J.-L., Wang J.-J., Yu N.-P., Zhang C.-P., Li N., Zhang G.-Y., 2021, A&A , 646, A137 [Cited on pages 90 and 110.]

Liu J., Zhang Q., Qiu K., 2022, Frontiers in Astronomy and Space Sciences, 9, 943556 [Cited on page 155.]

Liu H.-L., et al., 2023, MNRAS , 522, 3719 [Cited on page 102.]

Lombardi M., Alves J., Lada C. J., 2006, A&A , 454, 781 [Cited on page 6.]

Lombardi M., Alves J., Lada C. J., 2010, A&A , 519, L7 [Cited on page 58.]

Lombardi M., Lada C. J., Alves J., 2013, A&A , 559, A90 [Cited on page 55.]

Lombardi M., Bouy H., Alves J., Lada C. J., 2014, A&A , 566, A45 [Cited on page 55.]

Longmore S. N., et al., 2012, ApJ, 746, 117 [Cited on pages xvi, 73, and 75.]

Longmore S. N., et al., 2013, MNRAS , 433, L15 [Cited on pages xvi, 73, 75, and 214.]

Longmore S. N., et al., 2014, in Beuther H., Klessen R. S., Dullemond C. P., Henning T., eds, Protostars and Planets VI. pp 291–314 (arXiv:1401.4175), doi:10.2458/azu$_uapress_9780816531240-ch013$ [Cited on pages 24, 25, 26, 72, 76, 82, 214, 215, and 219.]

Lucas P. W., et al., 2008, MNRAS , 391, 136 [Cited on pages 44 and 194.]

Luhman K. L., Esplin T. L., Loutrel N. P., 2016, ApJ, 827, 52 [Cited on page 182.]

Lumsden S. L., Hoare M. G., Urquhart J. S., Oudmaijer R. D., Davies B., Mottram J. C., Cooper H. D. B., Moore T. J. T., 2013, ApJS, 208, 11 [Cited on pages 47 and 75.]

Mac Low M.-M., Klessen R. S., 2004, Reviews of Modern Physics, 76, 125 [Cited on pages 19, 28, and 161.]

MacLaren I., Richardson K. M., Wolfendale A. W., 1988, ApJ, 333, 821 [Cited on page 61.]

Mairs S., et al., 2021, The Astronomical Journal, 162, 191 [Cited on page 133.]

Maíz Apellániz J., 2024, arXiv e-prints, p. arXiv:2401.01116 [Cited on page 176.]

Majewski S. R., et al., 2017, AJ, 154, 94 [Cited on page 224.]

Mao S. A., Ostriker E. C., Kim C.-G., 2020, ApJ, 898, 52 [Cited on pages 61 and 163.]

Marsh K. A., Whitworth A. P., 2019, MNRAS , 483, 352 [Cited on pages 49 and 201.]

Marsh K. A., Whitworth A. P., Lomax O., 2015, MNRAS , 454, 4282 [Cited on pages 48 and 201.]

Marsh K. A., et al., 2017, Monthly Notices of the Royal Astronomical Society, 471, 2730 [Cited on pages 48, 51, 187, and 201.]

Martin C. L., Kennicutt Robert C. J., 2001, ApJ, 555, 301 [Cited on page 30.]

Martin-Alvarez S., Devriendt J., Slyz A., Teyssier R., 2018, MNRAS , 479, 3343 [Cited on page 16.]

Marton G., et al., 2017, arXiv e-prints, p. arXiv:1705.05693 [Cited on pages 62 and 66.]

Maschberger T., Clarke C. J., 2011, MNRAS , 416, 541 [Cited on page 70.]

Maschberger T., Clarke C. J., Bonnell I. A., Kroupa P., 2010, MNRAS , 404, 1061 [Cited on page 85.]

Mattern M., et al., 2018, A&A , 619, A166 [Cited on page 115.]

Maud L. T., Moore T. J. T., Lumsden S. L., Mottram J. C., Urquhart J. S., Hoare M. G., 2015, MNRAS , 453, 645 [Cited on pages 35, 75, and 196.]

McClure-Griffiths N. M., Stanimirović S., Rybarczyk D. R., 2023, ARA&A, 61, 19 [Cited on page 4.]

McKee C. F., Ostriker J. P., 1977, ApJ, 218, 148 [Cited on page 129.]

McKee C. F., Ostriker E. C., 2007, ARA&A, 45, 565 [Cited on pages 13 and 20.]

McKee C. F., Parravano A., Hollenbach D. J., 2015, ApJ, 814, 13 [Cited on page 20.]

Mège P., et al., 2021, A&A , 646, A74 [Cited on page 196.]

Megeath S. T., Herter T., Beichman C., Gautier N., Hester J. J., Rayner J., Shupe D., 1996, A&A , 307, 775 [Cited on page 178.]

Megeath S. T., Gutermuth R. A., Kounkel M. A., 2022, PASP, 134, 042001 [Cited on pages 204 and 210.]

Meingast S., Lombardi M., Alves J., 2017, A&A , 601, A137 [Cited on page 54.]

Méndez-Delgado J. E., Amayo A., Arellano-Córdova K. Z., Esteban C., García-Rojas J., Carigi L., Delgado-Inglada G., 2022, MNRAS , 510, 4436 [Cited on page 196.]

Messineo M., Habing H. J., Menten K. M., Omont A., Sjouwerman L. O., Bertoldi F., 2005, A&A , 435, 575 [Cited on page 176.]

Messineo M., Menten K. M., Churchwell E., Habing H., 2012, A&A , 537, A10 [Cited on page 234.]

Miville-Deschênes M.-A., Murray N., Lee E. J., 2017, ApJ, 834, 57 [Cited on pages 12, 35, 45, 91, and 101.]

Molinari S., et al., 2010, A&A , 518, L100 [Cited on pages 14, 44, 45, 48, 90, and 201.]

Montillaud J., et al., 2019, A&A , 631, A3 [Cited on page 80.]

Mookerjea B., Veena V. S., Güsten R., Wyrowski F., Lasrado A., 2023, MNRAS , 520, 2517 [Cited on page 123.]

Mooney T. J., Solomon P. M., 1988, ApJ , 334, L51 [Cited on page 31.]

Motte F., Bontemps S., Louvet F., 2018, ARA&A, 56, 41 [Cited on pages 90 and 102.]

Mottram J. C., et al., 2011, ApJ , 730, L33 [Cited on page 78.]

Mouschovias T. C., Tassis K., Kunz M. W., 2006, ApJ, 646, 1043 [Cited on page 28.]

Muench A. A., Lada E. A., Lada C. J., 2000, ApJ, 533, 358 [Cited on page 178.]

Muench A. A., Lada E. A., Lada C. J., Alves J., 2002, ApJ, 573, 366 [Cited on page 183.]

Muench A. A., Lada C. J., Luhman K. L., Muzerolle J., Young E., 2007, AJ, 134, 411 [Cited on page 183.]

Murray N., 2011, ApJ, 729, 133 [Cited on page 12.]

Murray N., Chang P., 2015, ApJ, 804, 44 [Cited on page 60.]

Myers P. C., 2009, ApJ, 700, 1609 [Cited on pages 14, 79, 90, 165, and 172.]

Myers P. C., 2012, ApJ, 752, 9 [Cited on page 77.]

Nakamura F., Li Z.-Y., 2008, The Astrophysical Journal, 687, 354 [Cited on page 27.]

Nakamura F., Li Z.-Y., 2014, ApJ, 783, 115 [Cited on page 25.]

Nakanishi H., Sofue Y., 2006, PASJ, 58, 847 [Cited on page 101.]

Naranjo-Romero R., Zapata L. A., Vázquez-Semadeni E., Takahashi S., Palau A., Schilke P., 2012, ApJ, 757, 58 [Cited on pages 102 and 134.]

Neichel B., Samal M. R., Plana H., Zavagno A., Bernard A., Fusco T., 2015, A&A , 576, A110 [Cited on page 168.]

Nishimura A., et al., 2015, ApJS, 216, 18 [Cited on page 94.]

Ochsenbein F., Bauer P., Marcout J., 2000, A&AS , 143, 23 [Cited on page 62.]

Ohlendorf H., Preibisch T., Gaczkowski B., Ratzka T., Ngoumou J., Roccatagliata V., Grellmann R., 2013, A&A , 552, A14 [Cited on page 171.]

Ojha D. K., et al., 2004, ApJ, 616, 1042 [Cited on pages 168 and 178.]

Ojha D. K., et al., 2011, ApJ, 738, 156 [Cited on pages xiii, 21, 22, and 178.]

Onodera S., et al., 2010, ApJ , 722, L127 [Cited on page 31.]

Ostriker J., 1964, ApJ, 140, 1056 [Cited on page 121.]

Ostriker E. C., Stone J. M., Gammie C. F., 2001, ApJ, 546, 980 [Cited on pages 155, 156, and 157.]

Padoan P., Nordlund Å., 2002, ApJ, 576, 870 [Cited on page 28.]

Padoan P., Goodman A., Draine B. T., Juvela M., Nordlund Å., Rögnvaldsson Ö. E., 2001, ApJ, 559, 1005 [Cited on pages 155 and 164.]

Padoan P., Pan L., Juvela M., Haugbølle T., Nordlund Å., 2020, ApJ, 900, 82 [Cited on pages 26, 60, 72, and 126.]

Pakmor R., Marinacci F., Springel V., 2014, The Astrophysical Journal Letters, 783, L20 [Cited on page 16.]

Palla F., Stahler S. W., 2002, ApJ, 581, 1194 [Cited on page 27.]

Pandey A. K., Mahra H. S., Sagar R., 1992, Bulletin of the Astronomical Society of India, 20, 287 [Cited on page 185.]

Panopoulou G. V., Psaradaki I., Skalidis R., Tassis K., Andrews J. J., 2017, MNRAS , 466, 2529 [Cited on page 109.]

Panopoulou G. V., Clark S. E., Hacar A., Heitsch F., Kainulainen J., Ntormousi E., Seifried D., Smith R. J., 2022, A&A , 657, L13 [Cited on page 109.]

Panwar N., Pandey A. K., Samal M. R., Battinelli P., Ogura K., Ojha D. K., Chen W. P., Singh H. P., 2018, AJ, 155, 44 [Cited on page 183.]

Parker R. J., 2018, MNRAS , 476, 617 [Cited on page 66.]

Parker R. J., Schoettler C., 2022, MNRAS , 510, 1136 [Cited on page 66.]

Parker R. J., Wright N. J., Goodwin S. P., Meyer M. R., 2014, MNRAS , 438, 620 [Cited on pages 64, 70, and 192.]

Parker R. J., Goodwin S. P., Wright N. J., Meyer M. R., Quanz S. P., 2016, MNRAS , 459, L119 [Cited on page 70.]

Patra S., II N. J. E., Kim K.-T., Heyer M., Kauffmann J., Jose J., Samal M. R., Das S. R., 2022, The Astronomical Journal, 164, 129 [Cited on page 101.]

Patten B. M., et al., 2006, ApJ, 651, 502 [Cited on pages xxvi and 232.]

Pattle K., et al., 2017, ApJ, 846, 122 [Cited on pages 27, 133, and 155.]

Pattle K., et al., 2018, The Astrophysical Journal Letters, 860, L6 [Cited on page 28.]

Pattle K., et al., 2019, The Astrophysical Journal, 880, 27 [Cited on page 140.]

Pattle K., Fissel L., Tahani M., Liu T., Ntormousi E., 2022, arXiv e-prints, p. arXiv:2203.11179 [Cited on pages 18, 19, 27, 142, and 157.]

Pecaut M. J., Mamajek E. E., 2013, ApJS, 208, 9 [Cited on page 175.]

Peretto N., et al., 2013, A&A , 555, A112 [Cited on page 80.]

Peretto N., et al., 2014, A&A , 561, A83 [Cited on pages 111 and 165.]

Pfalzner S., 2009, A&A , 498, L37 [Cited on pages xvi, 73, and 75.]

Pfalzner S., Dincer F., 2024, ApJ, 963, 122 [Cited on page 235.]

Pfalzner S., Olczak C., Eckart A., 2006, A&A , 454, 811 [Cited on page 235.]

Phillips J. P., 1999, A&AS , 134, 241 [Cited on page 15.]

Pillai T., Kauffmann J., Wyrowski F., Hatchell J., Gibb A. G., Thompson M. A., 2011, A&A , 530, A118 [Cited on page 163.]

Pillai T. G. S., et al., 2020, Nature Astronomy, 4, 1195 [Cited on page 159.]

Pineda J. E., Caselli P., Goodman A. A., 2008, ApJ, 679, 481 [Cited on page 95.]

Pineda J. L., Goldsmith P. F., Chapman N., Snell R. L., Li D., Cambrésy L., Brunt C., 2010, ApJ, 721, 686 [Cited on pages 95, 97, and 115.]

Pineda J. L., Langer W. D., Velusamy T., Goldsmith P. F., 2013, A&A , 554, A103 [Cited on pages 101 and 122.]

Pineda J. E., et al., 2022, arXiv e-prints, p. arXiv:2205.03935 [Cited on pages 72 and 90.]

Planck Collaboration et al., 2015, A&A , 576, A105 [Cited on pages xiii and 18.]

Planck Collaboration et al., 2016, A&A , 586, A138 [Cited on pages 27, 139, and 160.]

Planck Collaboration et al., 2020, A&A , 641, A12 [Cited on page 139.]

Plunkett A. L., Fernández-López M., Arce H. G., Busquet G., Mardones D., Dunham M. M., 2018, A&A , 615, A9 [Cited on page 72.]

Poglitsch A., et al., 2010, A&A , 518, L2 [Cited on page 36.]

Pokhrel R., et al., 2020, ApJ, 896, 60 [Cited on pages 33, 193, and 209.]

Pokhrel R., et al., 2021, ApJ , 912, L19 [Cited on pages xxv, 33, 34, 188, 193, 207, 208, 209, 211, and 212.]

Polak B., et al., 2023, arXiv e-prints, p. arXiv:2312.06509 [Cited on pages 25, 26, and 215.]

Pon A., Johnstone D., Heitsch F., 2011, ApJ, 740, 88 [Cited on page 122.]

Pon A., Toalá J. A., Johnstone D., Vázquez-Semadeni E., Heitsch F., Gómez G. C., 2012, The Astrophysical Journal, 756, 145 [Cited on page 43.]

Portegies Zwart S. F., McMillan S. L. W., Gieles M., 2010, ARA&A, 48, 431 [Cited on pages 22, 23, and 24.]

Portegies Zwart S., et al., 2018, AMUSE: the Astrophysical Multipurpose Software Environment, doi:10.5281/zenodo.1443252 [Cited on page 225.]

Qiu K., Zhang Q., Menten K. M., Liu H. B., Tang Y.-W., Girart J. M., 2014, The Astrophysical Journal Letters, 794, L18 [Cited on page 17.]

Ragan S. E., Heitsch F., Bergin E. A., Wilner D., 2012, ApJ, 746, 174 [Cited on page 67.]

Ragan S. E., Henning T., Tackenberg J., Beuther H., Johnston K. G., Kainulainen J., Linz H., 2014, A&A , 568, A73 [Cited on page 114.]

Rawat V., et al., 2023, MNRAS , 521, 2786 [Cited on page 40.]

Rawat V., et al., 2024a, MNRAS , 528, 1460 [Cited on page 41.]

Rawat V., et al., 2024b, MNRAS , 528, 2199 [Cited on page 41.]

Reid M. J., et al., 2019, ApJ, 885, 131 [Cited on page 46.]

Retes-Romero R., Mayya Y. D., Luna A., Carrasco L., 2017, ApJ, 839, 113 [Cited on page 210.]

Ribas Á., Merín B., Bouy H., Maud L. T., 2014, A&A , 561, A54 [Cited on page 77.]

Ribas Á., Bouy H., Merín B., 2015, A&A , 576, A52 [Cited on page 235.]

Rieke G. H., Lebofsky M. J., 1985, ApJ, 288, 618 [Cited on pages 48, 49, 174, 175, 176, 179, 203, and 234.]

Robin A. C., Reylé C., Derrière S., Picaud S., 2004, A&A , 416, 157 [Cited on page 170.]

Rodón J. A., Beuther H., Schilke P., 2012, A&A , 545, A51 [Cited on page 186.]

Rodriguez-Franco A., Martin-Pintado J., Gomez-Gonzalez J., Planesas P., 1992, A&A , 264, 592 [Cited on page 123.]

Roman-Duval J., Jackson J. M., Heyer M., Johnson A., Rathborne J., Shah R., Simon R., 2009, ApJ, 699, 1153 [Cited on page 45.]

Roman-Duval J., Jackson J. M., Heyer M., Rathborne J., Simon R., 2010, ApJ, 723, 492 [Cited on page 97.]

Romero G. A., Cappa C. E., 2009, MNRAS , 395, 2095 [Cited on page 94.]

Rosolowsky E. W., Pineda J. E., Kauffmann J., Goodman A. A., 2008, ApJ, 679, 1338 [Cited on page 117.]

Ryabukhina O. L., Zinchenko I. I., Samal M. R., Zemlyanukha P. M., Ladeyschikov D. A., Sobolev A. M., Henkel C., Ojha D. K., 2018, Research in Astronomy and Astrophysics, 18, 095 [Cited on page 80.]

Sadaghiani M., et al., 2020, A&A , 635, A2 [Cited on pages 64 and 72.]

Sadavoy S. I., et al., 2018, ApJ, 869, 115 [Cited on page 139.]

Sagar R., 2002, in Geisler D. P., Grebel E. K., Minniti D., eds, IAU Symposium Vol. 207, Extragalactic Star Clusters. p. 515 [Cited on page 185.]

Sagar R., Munari U., de Boer K. S., 2001, MNRAS , 327, 23 [Cited on page 184.]

Sagar R., Kumar B., Omar A., 2019, Current Science, 117, 365 [Cited on page 168.]

Sagar R., Kumar B., Sharma S., 2020, Journal of Astrophysics and Astronomy, 41, 33 [Cited on page 168.]

Saha A., et al., 2022, MNRAS , 516, 1983 [Cited on page 115.]

Salpeter E. E., 1955, ApJ, 121, 161 [Cited on page 185.]

Salvatier J., Wiecki T. V., Fonnesbeck C., 2016, PeerJ Computer Science, 2, e55 [Cited on page 140.]

Samal M. R., et al., 2014, A&A , 566, A122 [Cited on page 233.]

Samal M. R., et al., 2015, A&A , 581, A5 [Cited on page 171.]

Samal M. R., Chen W. P., Takami M., Jose J., Froebrich D., 2018, MNRAS , 477, 4577 [Cited on page 67.]

Sanhueza P., Jackson J. M., Zhang Q., Guzmán A. E., Lu X., Stephens I. W., Wang K., Tatematsu K., 2017, The Astrophysical Journal, 841, 97 [Cited on pages 52 and 164.]

Sanhueza P., et al., 2019, ApJ, 886, 102 [Cited on pages 64 and 126.]

Savage C., Apponi A. J., Ziurys L. M., Wyckoff S., 2002, ApJ, 578, 211 [Cited on page 100.]

Schisano E., et al., 2014, ApJ, 791, 27 [Cited on pages 90 and 109.]

Schisano E., et al., 2020, MNRAS , 492, 5420 [Cited on pages 49, 51, 150, and 202.]

Schmeja S., Klessen R. S., 2006, A&A , 449, 151 [Cited on pages 64 and 65.]

Schmidt M., 1959, ApJ, 129, 243 [Cited on page 30.]

Schneider N., Csengeri T., Bontemps S., Motte F., Simon R., Hennebelle P., Federrath C., Klessen R., 2010, A&A , 520, A49 [Cited on pages 90 and 123.]

Schneider N., et al., 2012, A&A , 540, L11 [Cited on page 14.]

Schneider N., et al., 2015a, A&A , 575, A79 [Cited on page 20.]

Schneider N., et al., 2015b, A&A , 578, A29 [Cited on page 20.]

Schneider N., et al., 2016, A&A , 587, A74 [Cited on page 20.]

Schuller F., et al., 2021, MNRAS , 500, 3064 [Cited on page 115.]

Seifried D., Walch S., 2015, MNRAS , 452, 2410 [Cited on page 27.]

Serkowski K., Mathewson D. S., Ford V. L., 1975, ApJ, 196, 261 [Cited on page 130.]

Shan W., et al., 2012, IEEE Transactions on Terahertz Science and Technology, 2, 593 [Cited on pages 37 and 90.]

Sharma S., Pandey A. K., Ogura K., Mito H., Tarusawa K., Sagar R., 2006, AJ, 132, 1669 [Cited on page 184.]

Sharma S., Pandey A. K., Ojha D. K., Bhatt H., Ogura K., Kobayashi N., Yadav R., Pandey J. C., 2017, MNRAS , 467, 2943 [Cited on page 183.]

Sharma S., et al., 2022, PASP, 134, 085002 [Cited on pages 38 and 168.]

Sharma S., et al., 2023, Journal of Astrophysics and Astronomy, 44, 46 [Cited on page 168.]

Shimajiri Y., et al., 2015, ApJS, 217, 7 [Cited on page 97.]

Shimajiri Y., André P., Palmeirim P., Arzoumanian D., Bracco A., Könyves V., Ntormousi E., Ladjelate B., 2019, A&A , 623, A16 [Cited on pages 27, 90, and 106.]

Sills A., Rieder S., Scora J., McCloskey J., Jaffa S., 2018a, MNRAS , 477, 1903 [Cited on pages xxv, 25, 29, 225, and 226.]

Sills A., Rieder S., Scora J., McCloskey J., Jaffa S., 2018b, MNRAS , 477, 1903 [Cited on page 83.]

Skrutskie M. F., et al., 2006, AJ, 131, 1163 [Cited on page 168.]

Smith R. J., Longmore S., Bonnell I., 2009, MNRAS , 400, 1775 [Cited on page 81.]

Smith R. J., Glover S. C. O., Klessen R. S., 2014, MNRAS , 445, 2900 [Cited on page 109.]

Soam A., et al., 2018, ApJ, 861, 65 [Cited on pages 27 and 139.]

Soam A., et al., 2019, ApJ, 883, 95 [Cited on page 27.]

Sokolov V., et al., 2019, ApJ, 872, 30 [Cited on page 214.]

Soler J. D., Hennebelle P., Martin P. G., Miville-Deschênes M. A., Netterfield C. B., Fissel L. M., 2013, ApJ, 774, 128 [Cited on page 27.]

Soler J. D., et al., 2017, A&A , 603, A64 [Cited on page 27.]

Solomon P. M., Rivolo A. R., Barrett J., Yahil A., 1987, ApJ, 319, 730 [Cited on page 6.]

Spilker A., Kainulainen J., Orkisz J., 2021, A&A , 653, A63 [Cited on page 49.]

Stahler S. W., Palla F., 2004, The Formation of Stars [Cited on pages xiii, 4, 5, 8, and 12.]

Stolte A., et al., 2010, ApJ, 718, 810 [Cited on page 235.]

Su Y., et al., 2019, ApJS, 240, 9 [Cited on pages 37, 45, 90, and 91.]

Suri S., et al., 2019, A&A , 623, A142 [Cited on page 109.]

Tan J. C., Kong S., Butler M. J., Caselli P., Fontani F., 2013, ApJ, 779, 96 [Cited on page 28.]

Tang Y.-W., Ho P. T. P., Koch P. M., Guilloteau S., Dutrey A., 2013, ApJ, 763, 135 [Cited on page 139.]

Tang Y.-W., Koch P. M., Peretto N., Novak G., Duarte-Cabral A., Chapman N. L., Hsieh P.-Y., Yen H.-W., 2019, ApJ, 878, 10 [Cited on pages 27, 142, 143, and 159.]

Thilker D. A., et al., 2007, ApJS, 173, 572 [Cited on page 30.]

Tigé J., et al., 2017, A&A , 602, A77 [Cited on page 102.]

Tody D., 1986, in Crawford D. L., ed., Society of Photo-Optical Instrumentation Engineers (SPIE) Conference Series Vol. 627, Instrumentation in astronomy VI. p. 733, doi:10.1117/12.968154 [Cited on page 168.]

Tody D., 1993, in Hanisch R. J., Brissenden R. J. V., Barnes J., eds, Astronomical Society of the Pacific Conference Series Vol. 52, Astronomical Data Analysis Software and Systems II. p. 173 [Cited on page 168.]

Treviño-Morales S. P., et al., 2019, A&A , 629, A81 [Cited on pages 78, 80, 90, 123, and 165.]

Trumpler R. J., 1930, PASP, 42, 214 [Cited on page 7.]

Urquhart J. S., et al., 2008, A&A , 487, 253 [Cited on pages 35, 46, and 91.]

Urquhart J. S., et al., 2013, MNRAS , 435, 400 [Cited on pages xvi, 73, 74, and 75.]

Vaillancourt J. E., 2006, PASP, 118, 1340 [Cited on page 133.]

Valdettaro R., et al., 2001, A&A , 368, 845 [Cited on page 196.]

Vázquez-Semadeni E., Gómez G. C., Jappsen A. K., Ballesteros-Paredes J., Klessen R. S., 2009, ApJ, 707, 1023 [Cited on pages 33, 75, and 126.]

Vázquez-Semadeni E., Palau A., Ballesteros-Paredes J., Gómez G. C., Zamora-Avilés M., 2019, MNRAS , 490, 3061 [Cited on pages 19, 26, 33, 72, 74, 75, 81, 83, 102, 116, 124, 126, 134, 158, 189, 214, and 219.]

Verley S., Corbelli E., Giovanardi C., Hunt L. K., 2010, A&A , 510, A64 [Cited on page 30.]

Vidali G., Li L., Roser J. E., Badman R., 2009, Advances in Space Research, 43, 1291 [Cited on page 10.]

Vutisalchavakul N., Evans Neal J. I., Heyer M., 2016, ApJ, 831, 73 [Cited on pages 31, 193, and 210.]

Wakelam V., et al., 2017, Molecular Astrophysics, 9, 1 [Cited on page 10.]

Walker D. L., Longmore S. N., Bastian N., Kruijssen J. M. D., Rathborne J. M., Jackson J. M., Foster J. B., Contreras Y., 2015, MNRAS , 449, 715 [Cited on pages xvi, 26, 73, 75, and 81.]

Walker D. L., Longmore S. N., Bastian N., Kruijssen J. M. D., Rathborne J. M., Galván-Madrid R., Liu H. B., 2016, MNRAS , 457, 4536 [Cited on pages 26, 72, 76, 81, and 82.]

Walker D. L., et al., 2018, MNRAS , 474, 2373 [Cited on page 76.]

Walter F. M., Sherry W. H., Wolk S. J., Adams N. R., 2008, in Reipurth B., ed., , Vol. 4, Handbook of Star Forming Regions, Volume I. p. 732 [Cited on page 183.]

Wang S., Jiang B. W., 2014, ApJ , 788, L12 [Cited on page 176.]

Wang K., Testi L., Ginsburg A., Walmsley C. M., Molinari S., Schisano E., 2015, MNRAS , 450, 4043 [Cited on pages 114 and 115.]

Wang K., Testi L., Burkert A., Walmsley C. M., Beuther H., Henning T., 2016, ApJS, 226, 9 [Cited on page 114.]

Wang J.-W., et al., 2019, ApJ, 876, 42 [Cited on pages 133, 140, 158, and 165.]

Wang J.-W., Lai S.-P., Clemens D. P., Koch P. M., Eswaraiah C., Chen W.-P., Pandey A. K., 2020a, ApJ, 888, 13 [Cited on page 159.]

Wang J.-W., Koch P. M., Galván-Madrid R., Lai S.-P., Liu H. B., Lin S.-J., Pattle K., 2020b, ApJ, 905, 158 [Cited on pages 27, 28, 142, 145, 159, and 165.]

Wang J.-W., et al., 2022, ApJ, 931, 115 [Cited on page 165.]

Ward-Thompson D., et al., 2017, ApJ, 842, 66 [Cited on pages 27 and 28.]

Weidner C., Kroupa P., Bonnell I. A. D., 2010, MNRAS , 401, 275 [Cited on pages 24 and 74.]

Weidner C., Kroupa P., Pflamm-Altenburg J., 2013, MNRAS , 434, 84 [Cited on page 24.]

Weisz D. R., et al., 2015, The Astrophysical Journal, 806, 198 [Cited on page 24.]

Wenger T. V., Balser D. S., Anderson L. D., Bania T. M., 2018, ApJ, 856, 52 [Cited on page 46.]

Whitney B., GLIMPSE360 Team 2009, in American Astronomical Society Meeting Abstracts #214. p. 210.01 [Cited on pages xvi and 79.]

Whitney B., et al., 2008, GLIMPSE360: Completing the Spitzer Galactic Plane Survey, Spitzer Proposal ID #60020 [Cited on page 171.]

Whittet D. C. B., Hough J. H., Lazarian A., Hoang T., 2008, ApJ, 674, 304 [Cited on pages 139 and 140.]

Wilson T. L., Rood R., 1994, ARA&A, 32, 191 [Cited on page 100.]

Winston E., Hora J. L., Tolls V., 2020, AJ, 160, 68 [Cited on pages xvii, 35, 65, 81, and 82.]

Wong T., Blitz L., 2002, ApJ, 569, 157 [Cited on page 30.]

Wouterloot J. G. A., Brand J., 1989, in Winnewisser G., Armstrong J. T., eds, , Vol. 331, The Physics and Chemistry of Interstellar Molecular Clouds - mm and Sub-mm Observations in Astrophysics. p. 97, doi:10.1007/BFb0119454 [Cited on page 35.]

Wu J., II N. J. E., Gao Y., Solomon P. M., Shirley Y. L., Bout P. A. V., 2005, The Astrophysical Journal, 635, L173 [Cited on pages 30 and 32.]

Wu J., Evans N. J., Shirley Y. L., Knez C., 2010, The Astrophysical Journal Supplement Series, 188, 313 [Cited on page 210.]

Xu J.-L., Xu Y., Zhang C.-P., Liu X.-L., Yu N., Ning C.-C., Ju B.-G., 2018, A&A , 609, A43 [Cited on page 94.]

Yadav R. K., et al., 2022, ApJ, 926, 16 [Cited on page 183.]

Yan C.-H., Minh Y. C., Wang S.-Y., Su Y.-N., Ginsburg A., 2010, ApJ, 720, 1 [Cited on page 183.]

Yan Z., Jerabkova T., Kroupa P., 2017, A&A , 607, A126 [Cited on page 24.]

Yan Z., Jerabkova T., Kroupa P., 2023, A&A , 670, A151 [Cited on page 24.]

Yang J., Jiang Z., Wang M., Ju B., Wang H., 2002, ApJS, 141, 157 [Cited on page 35.]

Yang D., et al., 2023, ApJ, 953, 40 [Cited on pages 90, 102, 111, 124, and 126.]

Yasui C., Kobayashi N., Tokunaga A. T., Saito M., 2014, MNRAS , 442, 2543 [Cited on page 235.]

Yasui C., Kobayashi N., Tokunaga A. T., Saito M., Izumi N., 2016a, AJ, 151, 50 [Cited on page 183.]

Yasui C., Kobayashi N., Saito M., Izumi N., 2016b, AJ, 151, 115 [Cited on page 183.]

Yuan J., et al., 2016, ApJ, 820, 37 [Cited on page 35.]

Yuan J., et al., 2018, ApJ, 852, 12 [Cited on page 124.]

Zamora-Avilés M., Vázquez-Semadeni E., Colín P., 2012, ApJ, 751, 77 [Cited on page 75.]

Zamora-Avilés M., Ballesteros-Paredes J., Hartmann L. W., 2017, Monthly Notices of the Royal Astronomical Society, 472, 647 [Cited on page 27.]

Zari E., Lombardi M., Alves J., Lada C. J., Bouy H., 2016, A&A , 587, A106 [Cited on page 55.]

Zavagno A., et al., 2023, A&A , 669, A120 [Cited on page 90.]

Zernickel A., 2015, PhD thesis, University of Cologne, Institute for Physics [Cited on page 114.]

Zhang Q., Fall S. M., Whitmore B. C., 2001, ApJ, 561, 727 [Cited on page 30.]

Zhang Q., et al., 2014, ApJ, 792, 116 [Cited on page 27.]

Zhang Q., Wang K., Lu X., Jiménez-Serra I., 2015, ApJ, 804, 141 [Cited on page 75.]

Zhang C.-P., et al., 2018, ApJS, 236, 49 [Cited on page 35.]

Zhang M., Kainulainen J., Mattern M., Fang M., Henning T., 2019, A&A , 622, A52 [Cited on page 114.]

Zhang S., et al., 2023, MNRAS , 520, 322 [Cited on page 90.]

Zhou J.-W., et al., 2022, MNRAS , 514, 6038 [Cited on page 114.]

Zhou J. W., et al., 2023, arXiv e-prints, p. arXiv:2305.12573 [Cited on page 114.]

Zucker C., Chen H. H.-H., 2018, ApJ, 864, 152 [Cited on pages 108 and 109.]

Zucker C., Battersby C., Goodman A., 2015, ApJ, 815, 23 [Cited on page 90.]

de los Reyes M. A. C., Kennicutt Robert C. J., 2019, ApJ, 872, 16 [Cited on pages 30 and 33.]